Large displacement numerical analysis of offshore pipe-soil interaction on clay

Deqiong Kong

Department of Engineering Science

University of Oxford

This dissertation is submitted for the degree of

Doctor of Philosophy

Lincoln College Trinity Term 2015

Acknowledgements

I would like to thank the following people for their generous support and gracious help during my four years of DPhil study.

First and foremost, my heartfelt thanks and deepest gratitude go to my supervisors, Professor Chris Martin and Professor Byron Byrne, for their professional guidance and support in planning and executing this work. I have been extremely fortunate to work with these highly talented people, and every discussion with them has been very inspirational. I am sincerely grateful to Chris for his invaluable advice on determining the scope of this thesis and his insightful suggestions throughout; and to Byron for offering me the opportunity to study in the Civil Engineering Research Group at Oxford and his encouragement which keeps driving me forward.

I gratefully acknowledge the funding I have received from the China Scholarship Council, which has enabled me to study at Oxford.

I am deeply indebted to my examiners, Professor Guy Houlsby and Professor Charles Augarde, for their scrutinous review of this thesis and their constructive comments which led to the improvement of it. I also appreciate the friendship and advice from my fellow colleagues in Jenkin Room 11. In particular, I want to thank Tao Zhao for his suggestion on choosing the visualization tool for the numerical results, and Giulia Macaro for her help which benefited me in the viva.

Finally, I want to thank my family for their unconditional love and support, especially my darling wife Lisa, without whom this thesis might have been completed half a year early but I could never have been half as happy.

I will always cherish my experience of studying here, where I met Lisa and so many wonderful people and learned so much from them. This memory will always be held dear to my heart and be an eternal source of encouragement in my future endeavors.

Abstract

Offshore on-bottom pipelines are vulnerable to lateral buckling caused by thermal- and pressure-induced axial expansion. A cost-effective solution is to allow for the buckling to occur in a controlled manner rather than to prevent it. This design approach requires an accurate assessment of the soil resistance experienced by the pipe during large cyclic lateral displacements.

The sequential limit analysis (SLA) method has been developed to study soil-structure interaction problems involving large displacements and large plastic strains in purely cohesive materials such as undrained clay. This approach was chosen because of its high computing efficiency as well as the robustness of limit analysis in solving plasticity problems. New techniques were developed to implement this approach, including model geometry updating routines, treatment of external model boundaries, periodic remeshing and interpolation methods as well as a constitutive model accounting for strain softening and strain rate effects. The SLA method was validated by benchmarking against known analytical solutions and physical model tests, as well as against output from complementary analyses performed using the coupled Eulerian-Lagrangian (CEL) approach in-built in Abaqus. The same constitutive model used in SLA was implemented into the CEL model via an Abaqus VUMAT subroutine to ensure comparability of results. Apart from these comparisons, the computing discrepancy between the lower and upper bound limit analysis solutions and the incompressibility of the deforming material were carefully examined to demonstrate the validity of the SLA approach.

Using the SLA method the vertical penetration behaviour of a pipe was investigated to an embedment of three diameters. The transition of soil failure mechanisms from shallow to deep embedment was examined carefully via a parametric study, and the strain softening effect was recognised to be extremely significant in determining the penetration resistance. A new simplified vertical penetration resistance calculation was developed, taking account of influences of interface roughness, soil strength gradient, soil unit weight and other parameters related to strain softening and strain rate.

Lateral pipe-soil interaction behaviour (monotonic and cyclic) was explored using the SLA method for lateral displacements up to twenty pipe diameters, with a focus on the soil resistance at the initial 'breakout' stage as well as the steady-state residual stage. In addition to the routine output of pipe load-displacement data (e.g. invert trajectory and lateral resistance), yield envelopes during the loading were also derived to provide more comprehensive understanding of the pipe-soil interaction. For monotonic loading, lower and upper bound estimates for the critical pipe weight that differentiates light pipe rising behaviour from heavy pipe diving behavior, were derived. Empirical equations were proposed to predict the residual resistance of a light pipe, accounting for the influences of pipe weight, initial pipe embedment, soil strength gradient, soil unit weight and finally strain softening effects. For cyclic loading, the numerical results for a number of different loading cases compared convincingly to corresponding centrifuge model test data, providing confidence in the numerical modelling approach. Parametric studies were completed exploring the influences of initial pipe embedment, pipe weight, soil strength gradient, soil unit weight, as well as the strain softening effect.

Table of contents

List of figures

List of tables

Notation

Roman Symbols

A_{min}	Minimum element size used in the model	m^2
c	Shear strength of Tresca material	kPa
D	Pipe diameter	m
E	Young's modulus	kPa
H	Lateral resistance of pipe	kN/m
H_{res}	Residual lateral resistance of pipe	kN/m
k	Shear strength gradient of soil	kPa/m
f_b	Soil buoyancy factor	
f_r	Equivalent strength enhancement factor	
S_t	Sensitivity of soil	
s_u	Operative shear strength of soil	kPa
$s_{u,0.5D}$	Initial shear strength at depth of half pipe diameter	kPa
$s_{u,avg}$	Initial shear strength at depth of half pipe diameter ($s_{u,0.5D}$)	kPa
s_{u0}	Initial shear strength of soil	kPa
s_{um}	Initial shear strength of soil at mudline	kPa
u	Current lateral displacement of pipe	m
V	Vertical load	kN/m
V_c	Vertical resistance of pipe	kN/m
V_g	Geotechnical resistance of pipe	kN/m
v_p	Vertical/horizontal loading rate of pipe	m/s
$V_{g,ideal}$	Geotechnical resistance of pipe in ideal soil	kN/m
W	Effective weight of pipe per meter	kN/m
w	Current embedment of pipe	m
w_{ini}	Initial embedment of pipe	m

Greek Symbols

α	Cohesion factor (roughness) of soil-structure interface

δ_{rem}	Remoulded strength ratio of soil, $1/S_t$	
$\dot{\gamma}_{max}$	Maximum shear strain rate	
$\dot{\gamma}_{ref}$	Reference shear strain rate	s^{-1}
γ'	Submerged unit weight of soil	kN/m^3
μ	Viscosity parameter	
ν	Poisson's ratio	
τ_{int}	Shear strength of soil-structure interface	kPa
$\dot{\varepsilon}$	Strain rate tensor	
$\dot{\varepsilon}^p$	Plastic strain rate tensor	
$\dot{\varepsilon}_1, \dot{\varepsilon}_3$	Major and minor principal strain rate	
$\varepsilon_1, \varepsilon_3$	Major and minor principal strain	
ξ	Accumulated plastic shear strain	
ξ_{95}	Accumulated plastic shear strain at which 95% soil strength reduction occurs by remoulding	
ξ_{eq}	Equivalent plastic shear strain	

Acronyms / Abbreviations

ALE	Arbitrary Lagrangian Eulerian
CEL	Coupled Eulerian Lagrangian
FELA	Finite element limit analysis
FEM	Finite element method
LB	Lower Bound
UB	Upper Bound
PIP	Pushed-in-place
RITSS	Remeshing and interpolation technique with small strain
SLA	Sequential limit analysis
WIP	Wished-in-place

Chapter 1

Introduction

1.1 Background

1.1.1 Offshore pipelines

Due to an increasing demand for energy, including for non-renewable energy products, as well as the depletion of fossil fuel reserves in shallow water, offshore hydrocarbon exploration and production must continually move into deeper and deeper water. Randolph and Gourvenec (2011) define 'deep water' as those sites where depths are greater than 500 m. These days, offshore hydrocarbon developments in water depths of 1000 m are not uncommon to find, and they can even reach 2500 m (Macaro, 2015). Development of these fields requires floating structures, a wide range of subsea facilities, as well as interconnecting systems.

Pipelines are widely used in these fields for transportation of hydrocarbon products such as oil and gas to either onshore locations or other interconnecting pipelines and facilities. These pipelines typically have an outer diameter D in the range of 100 mm to 750 mm, and a length up to a few hundred kilometres (Bruton *et al.*, 2005). Concrete or extruded polyethylene are often used as pipeline coatings to prevent corrosion and provide insulation. The effective unit weight of the pipe W (including pipe contents such as air, water, gas, etc.) typically varies from 2 kN/m to 8 kN/m (Lee, 2012), depending on the type and size of the pipeline used. More than 10000 offshore platforms have been constructed and installed worldwide since 1947 (Chakrabarti, 2005). Though the total

number of offshore pipelines are not clear, Beaubouef (2014) reported that over 11346 km of pipelines are to be built from 2014 to 2018.

The seabed sediments for many of these sites are generally very soft fine-grained deposits and are normally consolidated (Lee, 2012). It is often found that the undrained shear strength s_u of the sediments over the upper few metres below the seabed increases more or less proportionally with depth (Tani and Craig, 1995). This is usually expressed as $s_u = s_{um} + kz$, where s_{um} is the shear strength at the mudline, k is the strength gradient and z is the depth from seabed surface. Typically, s_{um} ranges from 0 kPa to 5 kPa and k ranges from 1 kPa/m to 2 kPa/m. However, it is not uncommon to find a higher strength surface crust at some locations. For example an undrained shear strength of 10 kPa to 15 kPa was found in the top few metres of soil off the West African coast (Borel *et al.*, 2005). Below the crust the soil reverts to the more standard normally consolidated profile. Offshore pipelines may be either buried in the soil using a trenching approach (either jetting or ploughing) or may be laid on the seabed surface. For many offshore sites, particularly in the deeper waters, it is more economical to lay the pipelines on the soil surface. However, it is usual for the pipelines to become partially embedded into the soil due to their weight or the dynamic motions applied during the pipe-laying process (Westgate *et al.*, 2010, 2009). It is observed that deepwater pipelines typically embed by between 10% and 50% of their diameter.

1.1.2 Lateral buckling of on-bottom pipelines

One of the key design challenges associated with oil pipelines is the control and understanding of thermally induced buckling. Oil pipelines are installed at ambient sea temperature but are operated at high temperatures and high pressures (HTHP) to ease the flow of the fluids and to prevent the solidification of wax fractions. These extreme operational conditions cause axial thermal expansion in the pipe, which leads to a vulnerability of the pipelines to buckling. Buckling occurs in the direction where the pipe is less constrained, and for surface pipelines this is usually in the horizontal (transverse) direction.

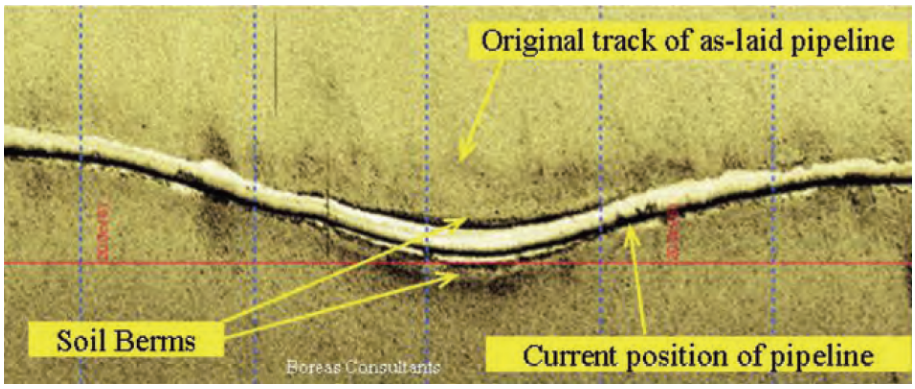

Figure 1.1 Lateral buckling of on-bottom pipelines (Bruton *et al.*, 2007)

A typical buckling event involves lateral displacements of up to 10 or 20 pipe diameters Bruton *et al.* (2005) and the length of the pipeline influenced by the buckling ranges from 100m to 300m (Bruton *et al.*, 2007). As the pipe scrapes progressively across the seabed surface, the soil around the pipe is remoulded and an active berm is formed in front of it (Figure 1.1). The magnitude of lateral displacement depends on both the pipe bending stiffness and on soil resistance, mainly contributed by the soil berm, to the pipe movement. There is a complex three dimensional interaction between these two elements. During the pipe's lifespan, there will be many cycles of loading due to start-up and shut-down for maintenance and cleaning. Consequently the pipeline experiences a range of cyclic loads due to the increase/decrease of both temperature and pressure. About 100-1000 cycles of motion can occur during the life span of a pipeline, which is typically 20 years (Cheuk *et al.*, 2007).

The buckling displacement leads to significant bending moments at the crown of the buckle, generating high bending stress, and introducing risks of a pipeline failure (Bruton *et al.*, 2007). The principal cause of failure relate to fatigue, and due to, in this instance, high stress low cycle fatigue. Despite the fact that various guidelines have been proposed for the design of pipelines, there are at least three known failures caused by lateral buckling, in the North Sea, West Africa and Brazil (Bruton *et al.*, 2005). Since any failure of the pipeline can result in containment loss and significant environmental hazard (Almeida *et al.*, 2001), great attention has to be paid to the design of pipelines. Pipeline costs can become a significant proportion of the development costs for deepwater hydrocarbon production.

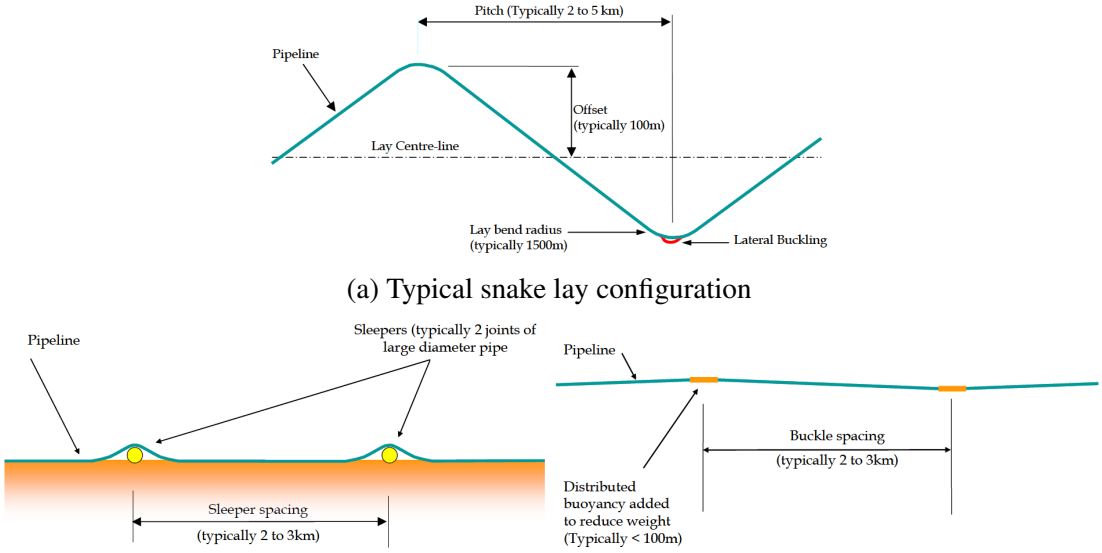

(a) Typical snake lay configuration

(b) Buckle initiation using sleepers

(c) Buckle initiation using distributed buoyancy

Figure 1.2 Buckle initiation techniques (Bruton *et al.*, 2005)

In 2002, Boreas Consultants, TWI and Cambridge University launched a joint industry project (JIP), named 'The Safe Design of Hot On-Bottom Pipelines with Lateral Buckling' (SAFEBUCK), with the aim of producing methods and guidance for the design of deepwater pipelines. The focus of the project was both on the structural design as well as the geotechnical design. Many studies referred to in this thesis formed part of this JIP. SAFEBUCK had three phases with the first and second phases completed in 2009. The third phase was launched in 2010, with Det Norske Veritas (DNV), who provide recommended design guidance (DNV, 2007, 2010), joining the same year with the aim of updating their guidance to reflect the new work. The third phase has now been completed. During the three phases of the JIP, both large-scale and small-scale model tests (e.g. Bruton *et al.*, 2005, 2007; Cheuk *et al.*, 2007; Rismanchian, 2014) were conducted exploring the behaviour of on-bottom pipelines under lateral buckling and axial movement. In addition detailed modelling has also been completed, though some of this is not yet in the public domain.

In the early days, the risk of buckling was minimised either by relieving the axial stress in the pipe using expansion spools, or by increasing the vertical and lateral restraint by trenching and burying. However, these methods are less cost effective for deepwater pipelines under more extreme conditions, where trenching is often technically infeasible

and the pipelines are generally laid directly on the seabed. An alternative and elegant solution is to work *with* rather than *against* the pipelines by controlling the formation of lateral buckles along them (Bruton *et al.*, 2005), namely controlled lateral buckling. As the temperature and pressures of pipelines increase further, this may be the only economic solution. This design strategy usually involves a number of buckle initiation techniques (shown in Figure 1.2) to encourage buckling at a controlled spacing, including snake-lay, vertical upset (sleepers), and distributed buoyancy. To ensure that the lateral buckles form as planned, and the pipe behaves as required, a comprehensive understanding of the in-plane interactions between a pipe segment and the seabed soil, namely the pipe-soil interaction, is required (Bruton *et al.*, 2005, 2007, 2006).

1.1.3 Pipe-soil interaction on clay soils

Pipe-soil interaction, especially in the lateral direction, is vital for understanding of the overall pipeline behaviour. However, it is impractical to develop an analytical pipe-soil interaction model that can be applied to design, taking into account the 3D nature of the pipeline problem. It is more usual to idealise the problem to a 2D plane strain problem, and then integrate up the behaviour along the pipe using a structural model. For the conceptual design stage the DNV design codes (2007 and 2010) adopt simplified independent elastic springs to represent the more complex pipe soil interactions. These models are excessively conservative and do not address the true design limit states (Bruton *et al.*, 2005).

In the detailed design stage, existing models of pipe-soil interactions are mainly derived for stability analyses, where design methods and acceptance criteria are provided by DNV (2007) and DNV (2010). These models do not take into account the changes to the seabed geometry, pipe-soil contact and soil strength (rate dependency and strain softening), and thus cannot be used to predict the soil resistance on pipelines undergoing large-amplitude displacements. To improve the safety and cost effectiveness of offshore hydrocarbon development, there is a need to establish a more rigorous design approach for on-bottom pipelines on the basis of better understanding of lateral pipe-soil interactions.

The popular macro-element model is a practical approach that can be used to describe more accurately 2D pipe-soil interaction. A typical macro-element is described by four components: (i) a yield surface in the $V-H$ loading space defining the allowable loading combinations; (ii) a hardening law determining the size of the yield surface; (iii) a description of the elastic behaviour for any load combinations within the yield surface; and (iv) a flow rule defining the direction of the incremental displacement vector upon plastic yielding. Development of such a model requires an extensive database of pipe-soil interaction results, especially soil resistances.

Pipe-soil interaction on clay can be simplified as illustrated in Figure 1.3. A pipe of diameter D, shallowly embedded into the seabed by w_{ini}, is moved laterally from the original position, represented by dashed lines, to the current position, under either constant vertical load or vertical position or some combination in between. The pipe is considered to be infinitely long so that plane strain conditions are assumed. The soil has submerged unit weight γ' and the initial shear strength profile is determined by $s_{u0} = s_{um} + kz$. Undrained conditions that generally prevail during pipe movements on fine-grained soils in deep water (Chatterjee *et al.*, 2013) are usually assumed. A soil berm is formed ahead of the pipe as it scrapes across the soil surface, and this material comes into progressively increasing contact with the pipe as the analysis proceeds. The pipe is assumed not to rotate as it moves laterally, as assumed in almost all the previous research on 2D pipe-soil interaction (e.g. Dingle *et al.*, 2008; Merifield *et al.*, 2008b; Wang *et al.*, 2010 and Rismanchian, 2014). The transient suction generated at the rear side of the pipe is often neglected, and thus no tensile force is permitted at the pipe-soil interface. Large deformations and strains are developed in the loading process and the soil around the pipe experiences severe remoulding, leading to degradation of the operative shear strength s_u. The loading rate has an influence of enhancing s_u due to the strain rate effect (viscosity). There may also be consolidation effects.

The key elements in the force-displacement response of the horizontally moving pipe are identified as: i) Initial break-out phase with elastic response defined by the mobilisation displacement and a peak response; ii) suction release phase and pipe elevation correction;

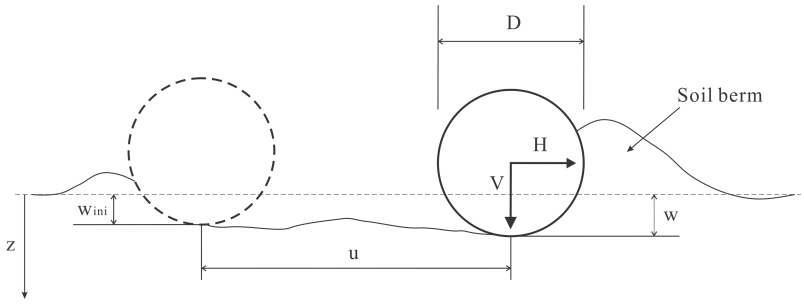

Figure 1.3 Schematic of pipe-soil interaction

and iii) steady accretion phase characterised by a gradual increase in friction, as an active berm builds up in front of the pipe (Bruton *et al.*, 2005). The soil deformation mechanisms at the three stages obtained from a centrifuge model test where particle image velocimetry (PIV) has been used are shown in Figure 1.4. The typical large displacement pipe-soil lateral responses under monotonic and cyclic loading are illustrated in Figure 1.5. Key design parameters are the peak resistance during the buckle initiation stage, and then the steady state resistance during subsequent cycles. The lateral reaction in Figure 1.5 can be interpreted as either the lateral soil resistance H (kN per metre length), or, for the sake of convenience, the equivalent friction ratio H/W, where W is the weight of the pipe per unit length. A 'normally penetrated pipe' represents a pipe that has experienced no greater historical vertical load than the current one, while an 'over-penetrated pipe' denotes otherwise. As shown in Figure 1.5a, a 'normally penetrated pipe' undergoes a downward movement with a hardening response after breakout while a heavily 'over-penetrated pipe' undergoes an upward movement with softening response. With further lateral movement, either light or heavy pipe behaviour is expected, depending on the pipe weight and soil properties. A light pipe can finally reach a residual stage where it steadily scrapes across the soil surface, with its elevation level and lateral resistance being kept almost constant; while a heavy pipe keeps diving into the soil and may not reach a residual stage within a reasonable displacement range (see Figure 1.6).

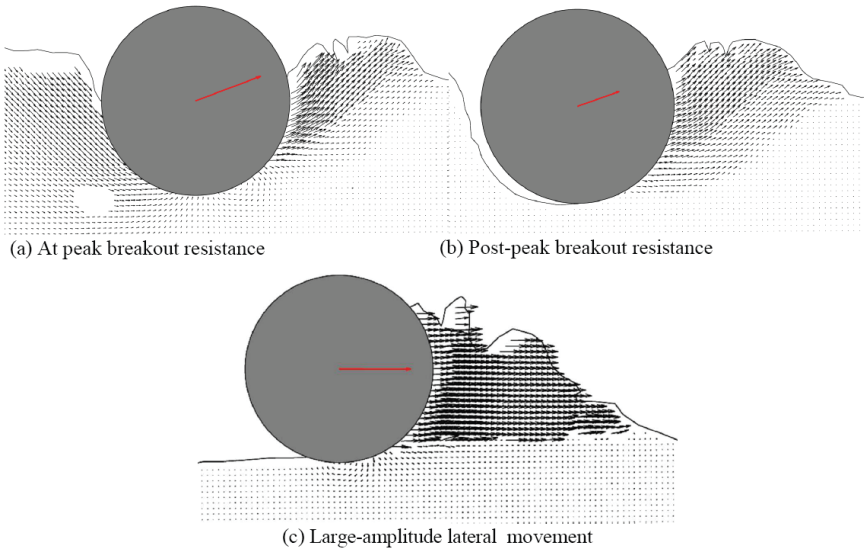

Figure 1.4 Soil deformation mechanism during lateral pipe movement from centrifuge modelling (Dingle *et al.*, 2008)

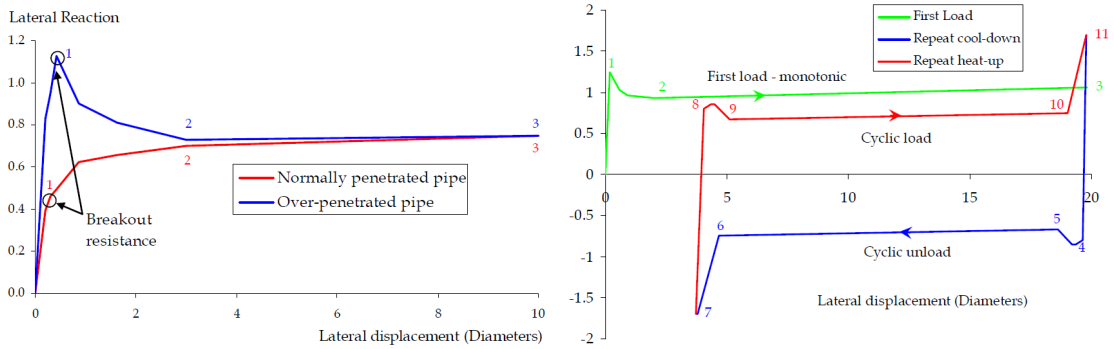

(a) Monotonic (b) Cyclic

Figure 1.5 Schematic of lateral force-displacement response (Bruton *et al.*, 2005)

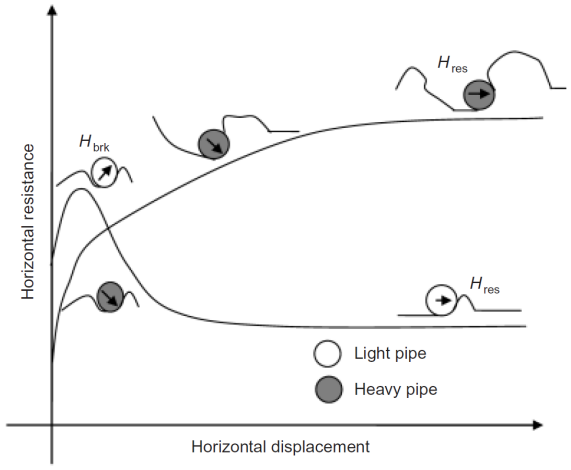

Figure 1.6 Idealisation of pipe response during lateral motion (Chatterjee *et al.*, 2012b)

1.2 Motivation

1.2.1 Vertical pipe-soil interaction: initial pipeline embedment

Pipelines in deep water are often laid on the seabed with the pipeline embedment determined by the pipe unit weight, soil strength and also the dynamic forces imposed on the pipeline at the seabed surface during the laydown process. This as-laid embedment is an important design element as it controls the subsequent lateral resistances exerted on the pipeline during lateral buckles caused by the thermal expansion. Pipelines with higher embedment will experience less convective heat loss, which leads to greater thermal expansion and axial stress in response, while shallowly embedded pipelines will operate with smaller thermal expansion but are more vulnerable to on-bottom stability risks. This contradictory influence makes conservative design impractical and denotes the necessity of an accurate estimation of the pipeline embedment for each specific project.

The dynamic loading effect is difficult to quantify due to the complexity of the problem with most studies of this effect being empirical (e.g. Cheuk and White, 2009, Westgate *et al.*, 2010), based on physical modelling or back-calculations using field measurements. The dynamic effect is often accounted for by a simple multiplier on the static embedment, so being able to assess the static embedment accurately is an essential part of predicting the initial embedment. As the pipe penetrates into a soft clay seabed, soil heave is generated at each side of the pipe (Figure 1.7b). As a result, the soil weight contributes an additional component of vertical load, exceeding nominal buoyancy, due to the distorted geometry of the soil surface. This effect should be treated carefully since the soil heave contributes not only to the vertical penetration resistance but also to the lateral capacity. Therefore,

(a) Wished-in-place (b) Pushed-in-place

Figure 1.7 Pipe-soil embedment cases (Merifield *et al.*, 2009)

the penetration process of a pipe should be considered as 'pushed-in-place' (Figure 1.7b) rather than 'wished-in-place' (Figure 1.7a) manner. Although recent studies have been carried out to look into this issue (e.g. Merifield *et al.*, 2009, Chatterjee *et al.*, 2013), the data are too limited for the quantification of the vertical resistance during pipe penetration, taking into account the geometry distortion, soil strength profile as well as rate-dependency and strain softening effects. Quantification of the dynamic loading effect is beyond the scope of this thesis.

1.2.2 Lateral pipe-soil interaction: controlled buckling of a pipeline

It is not possible to adopt a 'conservative' value for the prediction of soil resistance during lateral pipe movement. For the controlled buckling design, upper and lower bound values of soil resistance are both important. Uncertainty in soil behaviour and modelling approaches leads to a large range between upper and lower bound behaviour, which may preclude a design solution being obtained. Therefore, accurate assessment of lateral soil resistance, at initial break-out stage and residual stage, is very important for the controlled buckling design of pipelines.

Although many physical modelling tests have provided soil failure mechanisms during both vertical and lateral pipe movements, forming the basis for empirical force-displacement relationships (e.g. Cheuk *et al.*, 2007; Dingle *et al.*, 2008; Cheuk and White, 2009), the data are still very limited. For example, neither the vertical load nor displacement of a particular pipe segment can be considered to remain constant in the field due to 3D effects (i.e. interactions between interconnected pipe elements). However, much of the physical model testing involves either a constant vertical load or a constant vertical displacement. To develop the database further requires additional high quality testing at both small and large scale. This can involve a considerable cost, and importantly, the repeatability of physical tests cannot always be maintained.

For the reasons described above, numerical analyses become more attractive particularly for studies focused on undrained clay. A number of previous studies (e.g. Wang *et al.*, 2010; Chatterjee *et al.*, 2012b) have demonstrated the capacity of FEM to analyse lateral pipe-soil

interactions but have not systematically looked into the full range of detail necessary to establish rigorous design methods. Moreover, global numerical stability of FEM involving regular remeshing cannot be guaranteed. More effective and powerful numerical methods may need to be developed and employed to study pipe-soil interactions through extensive parametric studies.

1.3 Research purpose

This thesis reports a computational study exploring the interactions between pipelines and seabed soils, with the aim of developing guidance for the design of pipelines that undergo lateral buckling. Extensive parametric studies have been completed, due to the complexity of pipe-soil interactions under large deformations.

To facilitate this work, a powerful numerical model for the analysis of pipe-soil interactions has been developed. This model accounts for the change in seabed geometry and pipe-soil contact interface under extreme deformations. Rate-dependency and remoulding effects on the soil strength during shearing have also been incorporated into the modelling. The sequential limit analysis (SLA) technique was identified as a viable alternative to conventional FEM and other even more computationally expensive numerical approaches (e.g. distinct element method and material point method). The SLA method has been previously used to analyse relatively simple structural problems such as frames and plates (e.g. Yang, 1993, Raithatha and Duncan, 2008), where no contact or interface conditions need to be handled. To extend this method for the study of pipe-soil interaction problems, the external boundaries of the model have to be treated carefully, in addition to the consideration of hardening and softening behaviour of the material. Development of the SLA method in this thesis involves:

- The extension of the existing finite element limit analysis (FELA) software Oxlim (Makrodimopoulos and Martin, 2006, 2007, 2008) to handle large deformations. This involved software development to deal with the updating of model geometry and material properties.

- The validation of the proposed numerical method through a detailed benchmarking study. This was extremely important as the work described here represents the first attempt to apply limit analysis to solve large deformation problems involving soil-structure interactions. The study has demonstrated that the SLA model generates robust plasticity solutions; and, in conjunction with an appropriately chosen soil constitutive model, captures the right behaviour in analysing real pipe-soil interaction problems on undrained clay.
- The benchmarking of the proposed SLA method against a complementary numerical tool. The Coupled Eulerian-Lagrangian (CEL) method in-built in the finite element software Abaqus was chosen for this purpose. A subroutine VUMAT was developed to ensure the constitutive model used in the SLA was also used in the CEL model. Careful comparisons between CEL and SLA over a wide range of problems have been made to show the reliability of SLA in dealing with model geometry and field variables; and to illustrate the advantages of SLA over CEL (i.e. computation time).

For the study of pipe-soil interactions, the following contributions are described.

- The derivation of an enhanced approach to evaluate the vertical resistance of a pipe during penetration. The proposed approach quantified the influence of soil strength gradient, soil unit weight and other parameters related to the strain rate and strain softening effects of the soil.
- The derivation of yield envelopes for a pushed-in-place pipe at the initial break-out stage, taking into account the influence of soil strength properties and remoulding effect. Full and no tensile capacity has been assumed at the pipe-soil interface to bracket the real break-out resistance.
- The identification of empirical equations to evaluate the lateral soil resistance of the pipe during the steady-state residual stage based on a parametric study. The influence of pipe weight, initial pipe embedment, soil strength gradient and other parameters related to rate-dependency and strain softening effect on the residual resistance have been quantified.

- The derivation of lower and upper bounds of pipe weight to differentiate light and heavy pipes, considering the influence of soil strength gradient and strain softening effects.
- The development of yield envelopes for pipes during monotonic and cyclic lateral movements, which can be added to the existing database, benefitting the development of force-resultant pipe-soil models.

1.4 Layout of the thesis

This thesis consists of eight chapters. The first chapter has described the background and the objectives of this study.

Chapter 2 (*Review of pipe-soil interaction models*) presents a review of previous relevant research on pipe-soil modelling to evaluate pipe-soil interaction. The literature review covers both experimental and numerical findings on the vertical and lateral interactions between on-bottom pipelines and seabed soil.

Chapter 3 (*Numerical modelling methodology*) describes the development of the SLA method based on the FELA software OxLim. The whole computational scheme, with OxLim serving as a core solver for each increment of the analysis, is introduced in detail, including the update of model geometry, soil-structure contact and the treatment of field variables. A complementary numerical tool, the CEL method in Abaqus, which is accepted as a powerful numerical tool for solving large deformation geotechnical problems, is also introduced. This is followed by the description of how a modified Tresca material model, proposed by Einav and Randolph (2005), is incorporated into CEL via subroutine VUMAT. The main aim of introducing CEL is to provide more perspective on the advantages and disadvantages of SLA via comparisons. The parametric study results presented in this thesis were mainly obtained from SLA modelling due to high computing efficiency.

Chapter 4 (*Validation of the numerical method*) presents a detailed validation study of the SLA model for large deformation problems with benchmarking against either theoretical solutions or physical modelling results. Careful comparisons between SLA and CEL results are also provided for most of the problems presented. This chapter thoroughly

illustrates the capability of SLA in analysing pipe-soil interactions under various loading scenarios, including penetration, extraction, monotonic lateral loading with large amplitude, cyclic vertical loading with large amplitude, cyclic lateral loading with small amplitude but large number of oscillations and cyclic lateral loading with large amplitude.

Chapter 5 (*Vertical pipe-soil interaction: prediction of pipe embedment*) presents a numerical study of the vertical penetration behaviour of a rigid pipe into soft clay. The influence of strength gradient, unit weight and other parameters related to the strain rate and remoulding effects of the soil on the failure mechanism is examined. The corresponding effects of these parameters on the penetration resistance are then quantified and equations are presented for the ease of application.

Chapter 6 (*Lateral pipe-soil interaction: monotonic*) presents a numerical study of the monotonic loading response for a pipe undergoing very large-amplitude lateral movement (up to eight pipe diameters). The effects of various soil and pipe parameters on the pipe behaviour are examined through extensive parametric studies. The parameters varied include pipe weight, initial pipe embedment, soil strength gradient, soil unit weight and other parameters related to the strain rate and strain softening effects. This study focuses on the evaluation of lateral pipe resistance during the initial break-out stage and the steady-state residual stage. Failure mechanisms, in addition to soil resistances, at different loading stages are provided. The evolution of yield envelopes during the pipe movements is also presented to provide a more comprehensive insight into the pipe behaviour. For the estimation of break-out resistance, yield envelopes are derived with and without tensile capacity at the pipe-soil interface to consider the effect of soil suction at the rear of the pipe. For the evaluation of residual resistance, when applicable, simple equations are extracted from parametric results and the influencing factors on the residual resistance are quantified.

Chapter 7 (*Lateral pipe-soil interaction: cyclic*) describes a numerical study of the cyclic loading response of a pipe subjected to very large-amplitude lateral movements. The total loading distance of the pipeline in this study is more than twenty pipe diameters. Case studies of several problems are presented first. Comparisons of the numerical results with corresponding centrifuge model tests are provided, in terms of invert trajectory and

lateral resistance of the pipe. In addition, comparisons between these case studies are also made to examine the loading characteristics on the lateral resistance. The main features of the cyclic loading are discussed via the help of yield envelopes derived at different loading stages. Finally, a short parametric study is presented to explore the effects of soil and pipe parameters on the response. This chapter thoroughly demonstrates the capability of SLA in modelling the cyclic loading behaviour of pipelines during large-amplitude lateral buckling.

Chapter 8 (*Conclusions*) summarises the main findings obtained from the present study, based on which recommendations for further work are presented.

Chapter 2

Review of pipe-soil interaction models

2.1 Introduction

During the past few decades a considerable amount of research attention has been directed to pipe-soil interaction, covering installation issues, as well as the axial and transverse responses to internal and external loads. Two of the major tasks in design are to estimate the as-laid embedment of the pipelines and the consequent lateral resistance that the pipeline encounters when a buckle takes place.

A large majority of the existing work has considered plane strain conditions due to the very large length of a pipeline compared to the diameter. These studies have largely been conducted in clay soils, which dominate in the regions of deepwater development. A detailed review of the previous research, focusing on, but not limited to, the vertical penetration resistance and lateral resistance of a rigid pipe in clay, is summarised in this chapter, forming the background to the research carried out. The penetration mechanism of a pipe segment and the corresponding soil resistance, which is relevant to the estimation of pipe embedment, is first discussed. This is followed by the lateral loading behaviour of partially embedded pipes, which is a key aspect of designing pipes to undergo lateral buckling.

2.2 Pipe embedment

Pipelines in deepwater are often laid on the seabed with the pipeline embedment determined by the pipe unit weight as well as the dynamic motions during the laydown process. The as-

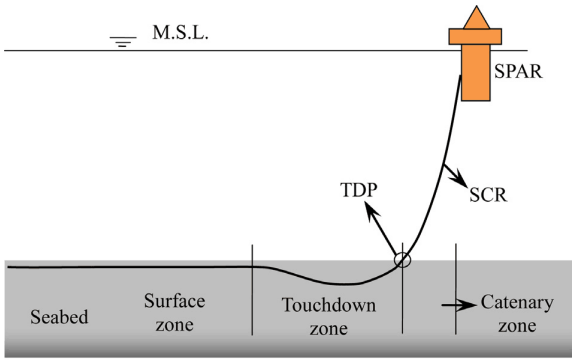

Figure 2.1 Schematic of the touchdown zone (TDZ) (Wang *et al.*, 2014)

laid embedment is a very important element of the pipeline design for on-bottom stability, axial resistance during thermal expansion and lateral resistance during thermally induced buckles (Bruton *et al.*, 2006). An accurate assessment of the pipe embedment requires reliable prediction of the vertical resistance of a pipe during penetration.

The studies reviewed here relate to pipes with embedment of less than half a diameter, as these directly relate to an on-bottom pipeline, which is the main focus of the thesis. However, studies at deeper embedments, up to several diameters, are also discussed to provide a wider perspective on general pipe-soil interaction. From an industrial perspective, the deep penetration behaviour of a pipe is also relevant to a steel catenary riser (SCR) at the touchdown zone (TDZ), as illustrated in Figure 2.1.

2.2.1 Physical modelling

Verley and Lund (1995) conducted a number of small- and large-scale laboratory tests to investigate the pipe penetration response. Based on the test results, a formula was proposed to predict the pipe embedment:

$$\frac{w}{D} = 0.0071(S_{VL}{G_{VL}}^{0.3})^{3.2} + 0.062(S_{VL}{G_{VL}}^{0.3})^{0.7} \tag{2.1}$$

in which w is the pipe embedment and two dimensionless parameters were defined as:

$$S_{VL} = \frac{W'_p}{Ds_u} \tag{2.2}$$

$$G_{VL} = \frac{s_u}{D\gamma} \tag{2.3}$$

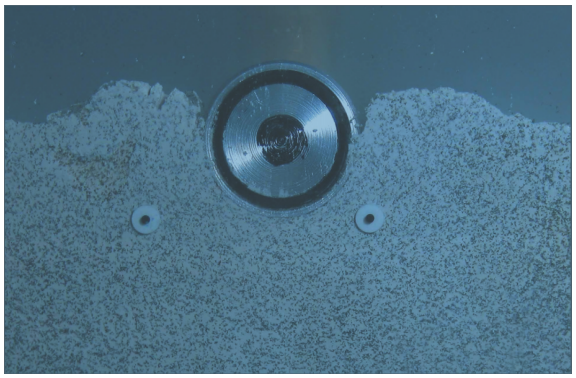

Figure 2.2 Soil deformation around a pipe at shallow embedment (Dingle *et al.*, 2008)

where W_p' is the effective weight of the pipe and γ is the total unit weight of the seabed soil. This equation is currently used in the design guideline DNV-RP-F109 (DNV, 2010) for pipelines. However, the adoption of total rather than effective soil unit weight leaves its theoretical basis open to question. Although Verley and Lund (1995) did not specify whether the resistance component contributed by soil heave was accounted for when the experimental data were collected, this component might have been included automatically (Cheuk, 2005).

Bruton *et al.* (2006) proposed an alternative equation, calibrated against limited model test results obtained from the SAFEBUCK JIP, accounting for remoulding effect of the soil:

$$\frac{w}{D} = \frac{S_t}{15}\left(\frac{W_p'}{Ds_u}\right)^2 \tag{2.4}$$

in which S_t is the sensitivity of soil.

These equations are empirical. More reliable evaluation of the vertical resistance of a pipe requires a better understanding of the pipe-soil failure mechanism during penetration. Dingle *et al.* (2008) conducted centrifuge modelling aimed at evaluating the vertical penetration resistance and lateral resistance of on-bottom pipelines. A digital image analysis technique, using particle image velocimetry (PIV), was implemented to observe the soil deformation mechanism (for example see Figure 2.2). The vertical embedment mechanisms were found to closely match known plasticity solutions, although the soil heave during penetration increased the pipe-soil contact perimeter by about 25%.

Lee (2012) reported a series of 1g physical model tests investigating the deep penetration behaviour of pipes in clay. High quality measurements of the soil deformation during the penetration process were obtained using image analysis. Based on these images, the geometry of the soil was extracted for back-analysis using upper bound limit analysis via the Discontinuity Layout Optimisation (DLO) approach, implemented in the software 'LimitState:GEO' (LimitState, 2009). Therefore the numerical modelling for this work was carried out with the pipe 'wished-in-place', but with the pipe-soil embedded geometry observed in the experiment. Good agreement was observed between the experimental and numerical results. The change in failure mechanism from 'soil heave' at shallow embedment to 'local flow-around' at deeper pipe embedments was also reported. A parametric study identified that the depth for which the full flow-around failure mechanism developed, depended strongly on the soil strength profile and the tensile capacity at the pipe-soil interface.

During the laydown process in the field, the real pipe embedment is much deeper compared with that predicted from static penetration analyses. This is due to additional loading arising from stress concentrations near the touchdown point (as shown in Figure 2.1) as well as dynamic forces incurred due to the movement of the pipe-lay vessel (Westgate *et al.*, 2009). For a deepwater pipeline on soft soil the dynamic effect could be significant (White and Randolph, 2007), compounded by the occurrence of both vertical and lateral motions of the pipeline at seabed level. These induced dynamic pipe motions lead to a reduction of the undrained strength of the surface soil, due to remoulding, also moving the soil to form an identifiable trench. As a result, the pipeline becomes embedded to a much greater depth compared to that assessed from a quasi-static resistance calculation.

The additional pipe embedment caused by dynamic laydown effects is usually ignored in pipeline design. However, recent studies propose that the dynamic lay effect can be assessed by multiplying the embedment due to static loading by an empirical dynamic embedment factor, f_{dyn}. This factor has been found to increase with the number of cycles and amplitude of the pipe motions (Lund, 2000; Morris *et al.*, 1988) and the sensitivity of

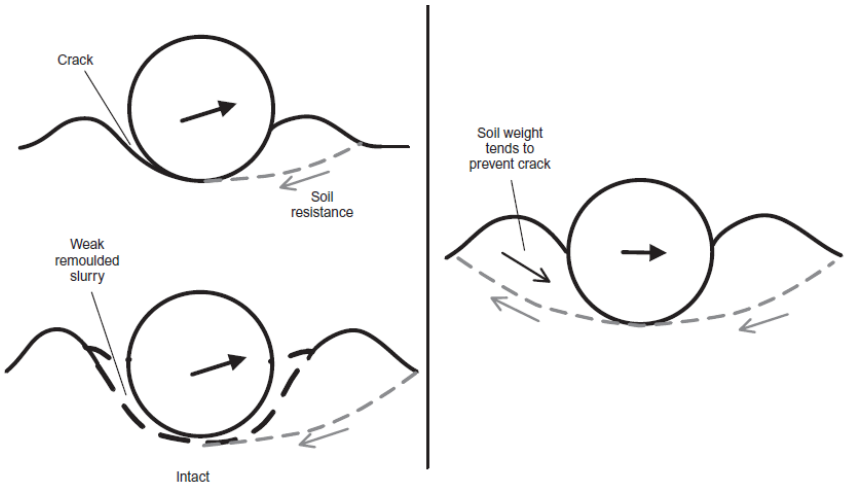

Figure 2.3 Mechanisms that affect tendency towards bonded and unbonded behaviour (Cheuk and White, 2009)

the soil (Cheuk and White, 2009). Typical values, ranging from 1 to 8, were suggested by Lund (2000) and Bruton *et al.* (2006) based on observations of field and model tests.

Cheuk and White (2009) reported an investigation into the influence of dynamic effects on pipeline embedment during the laydown process using centrifuge model testing. The results showed that only a few cycles of small amplitude lateral oscillation were sufficient to double or triple the static pipe embedment. This was attributed to the combined effects of lateral ploughing and strain softening. It was also found that during the cyclic lateral loading, the pipe-soil contact conditions changed from unbonded to bonded as the soil around the pipe softened, collapsing onto the pipe (as shown in Figure 2.3). A new pipe-soil interaction model incorporating a combined load failure envelope was proposed to take account of lateral loading in the estimation of the dynamic pipe embedment.

2.2.2 Numerical modelling

There is a reasonably long history of numerical and theoretical modelling of the vertical loading of pipes in undrained clay. The approaches can be classified into small-strain analyses (known as 'wished-in-place') where installation effects are not considered, that is the pipe is assumed to be placed in the soil at the appropriate location and changes in geometry are not considered. The second approach, 'pushed-in-place', involves large-strain

analyses where installation effects, including geometry changes and strain softening, are accounted for.

2.2.2.1 Small-strain analyses (wished-in-place)

Randolph and Houlsby (1984) gave the first rigorous theoretical solution for the limiting pressure on a circular pile moving laterally through undrained clay. This solution applies to other deeply buried cylindrical objects, such as a pipeline, where the capacity is independent of the pipe embedment and the direction of loading, assuming that the distribution of the soil strength is homogenous and isotropic. Both lower and upper bound solutions were derived in this study based on classical plasticity theory, with the solutions considered exact (with equal upper and lower bounds) at the time of publication.

The work of Murff *et al.* (1989) adapted the solutions of Randolph and Houlsby (1984) to the case of an unburied pipeline, relating the vertical penetration resistance to pipe embedment at shallow depths, assuming the pipe is 'wished-in-place' (Figure 2.4a). The soil is assumed to be a homogeneous and isotropic rigid-plastic material. Pipes with different interface roughness α were considered, with $\alpha = 0$ and 1 denoting fully smooth and fully rough interfaces, respectively. Murff *et al.* (1989) found that the solution proposed by Randolph and Houlsby (1984) was only exact in the case of a fully rough pipe with $\alpha = 1$. For other cases there was a localised discrepancy between the strain rate field and the stress field. Divergence of lower and upper bound solutions were found by Murff *et al.* (1989), with a maximum discrepancy of 9.1% for the extreme smooth case. Additionally a study using the lower bound solution revealed the potential effect of soil heave on bearing capacity, by assuming an inclined wedge of soil adjoining the pipe.

Martin and Randolph (2006) explored the discrepancy between lower and upper bound solutions for laterally loaded piles in undrained clay. They proposed a new solution, referred to as the Martin mechanism, consisting of a crescent-shaped block of soil, undergoing rigid body rotation about a point located on the axis of the pipe, perpendicular to the direction of motion. This solution works satisfactorily for small values of α. By combining this new mechanism with the one proposed by Randolph and Houlsby (1984)

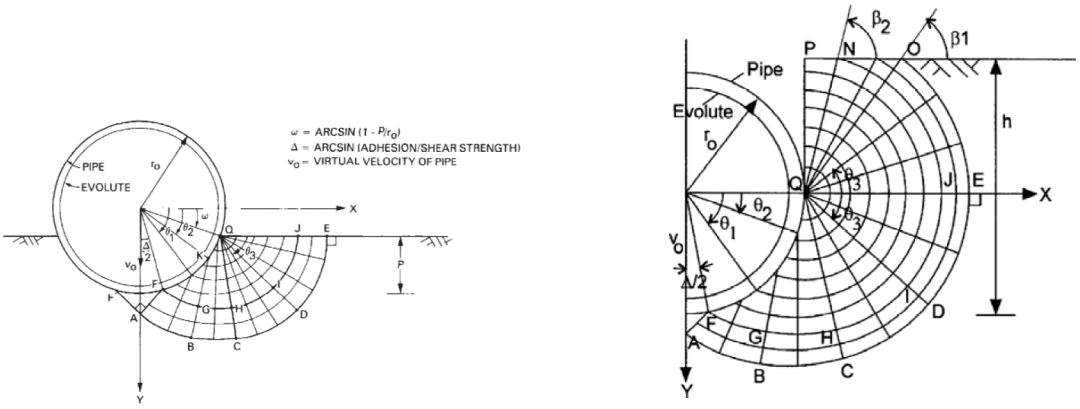

(a) $w/D < 0.5$ (Murff *et al.*, 1989) (b) $w/D > 0.5$ (Aubeny *et al.*, 2005)

Figure 2.4 Velocity fields of different plasticity solutions based on Randolph and Houlsby (1984)

a third mechanism was developed, giving very close results between upper and lower bound solutions for all values of α. The maximum discrepancy between the upper and lower bound solutions, for the fully smooth case, was reduced to 0.65% compared to 9.1% produced by Murff *et al.* (1989).

These plasticity solutions provide a basis for the assessment of the as-laid embedment of pipelines on clay for a uniform strength profile and with pipe embedment less than $0.5D$. Aubeny *et al.* (2005) extended the solutions of Murff *et al.* (1989) by considering a linearly varying strength profile, as well as pipe embedments greater than $0.5D$. Small-strain finite element analyses were conducted, assuming a perfect trench existed above the pipe as shown in Figure 2.4b. The computed results were compared with approximate lower and upper bound solutions. A simplified equation was developed, based on curve fitting of the FE results, to relate the vertical bearing capacity (V_c) to pipe embedment (w) and the soil strength at the pipe invert. This equation in normalised form is given as

$$\frac{V_c}{Ds_u} = a\left(\frac{w}{D}\right)^b \tag{2.5}$$

where a and b are fitting parameters and s_u is the undrained shear strength at the pipe invert. In Aubeny *et al.* (2005) the strength variation, characterised by a dimensionless parameter $\bar{k} = kD/s_{um}$, was found to hardly influence the normalised vertical penetration resistance.

The effect of the adhesion factor at the pipe-soil interface, α, was evaluated in this study and found to be dominant in determining the values of a and b.

Merifield *et al.* (2008a,b) conducted a series of FE analyses to examine the ultimate resistance of a shallowly embedded wished-in-place pipeline ($w \leq 0.5D$), finding that the relation between vertical resistance and pipe embedment was almost identical to that given by Aubeny *et al.* (2005). Best estimate values of the fitting parameters ($a = 7$ and $b = 0.3$) were suggested by Randolph and White (2008a) for design purposes.

Lee (2012) found that the empirical fits described in Equations 2.1 and 2.4 estimated a greater pipe embedment compared with the plasticity based solutions (Aubeny *et al.*, 2005; Murff *et al.*, 1989) for a given vertical load. This discrepancy was attributed to errors in quantification of the undrained strength of the soft sediments at and near the soil surface, as well as possible consolidation and installation effects in the experiments (Bruton *et al.*, 2006; Randolph and White, 2008a).

The work described above provides solutions for the penetration resistance of a pipe with shallow embedment ($w < 0.5D$) or extremely deep embedment ($w \to \infty$). The solutions for intermediate embedments proposed by Aubeny *et al.* (2005) have been based on the unrealistic existence of a vertical trench. To explore this further Martin and White (2012) conducted a more theoretically robust study using the FE limit analysis program OxLim (Makrodimopoulos and Martin, 2006, 2007, 2008) to obtain lower and upper bound plasticity solutions for a wide range of embedment depths (zero to five pipe diameters). In this study the soil was modelled as a rigid-plastic Tresca material, with shear strength either uniform or proportional to depth. Closely bracketed lower and upper bound solutions were derived. Martin and White (2012) systematically studied the effect of soil unit weight, interface roughness and interface tensile capacity on the undrained bearing capacity of a plane-strain pipe segment. The change of the failure mechanism from shallow to deep embedment was also reported based on the upper bound results.

The modelling described above assumes the clay behaves in a fully undrained manner, ignoring consolidation effects. Krost *et al.* (2011) studied consolidation around partially embedded pipelines via small-strain FE analysis. The development and dissipation of pore

water pressure at different pipe embedments was studied. A good match of the results compared to available field data was observed, although the response of the soil around the pipe in the study was assumed to be elastic. An increase in the average normal effective stress, and hence axial resistance, by up to 35%, due to the dissipation of pore pressure under partially embedded pipes, was identified.

2.2.2.2 Large-strain analyses (pushed-in-place)

Due to the higher density of the seabed soil relative to seawater, the pipeline becomes buoyant when it is penetrated into the seabed. In the wished-in-place case, the buoyancy reduces the effective pipe weight by $\gamma' A_s$, where γ' is the effective unit weight of the soil and A_s is the nominal area of the pipe section embedded below the soil surface. The latter can be expressed as:

$$A_s = \frac{D^2}{4}[\arcsin\sqrt{4w'(1-w')} - 2(1-2w')\sqrt{w'(1-w')}] \tag{2.6}$$

where w' is the normalised pipe embedment, w/D.

During continuous penetration of the pipe, heave is generated adjacent to the pipe, which increases the buoyancy effect. The analyses described in Section 2.2.2.1 assumed the pipe to be 'wished-in-place' thereby neglecting the change in geometry due to the large deformations associated with vertical penetration. In a state-of-the-art review of interactions between pipelines and seabed soils, Cathie *et al.* (2005) stated the importance of soil heave in raising the penetration resistance compared to wished-in-place analysis, and highlighted the scope for further work on this issue.

Randolph and White (2008a) proposed a buoyancy factor f_b to account for the enhancement on the pipe penetration resistance due to soil heave. The penetration resistance is expressed as the sum of geotechnical resistance and soil buoyancy:

$$\frac{V_c}{Ds_u} = a(\frac{w}{D})^b + f_b\frac{A_s}{D^2}\frac{\gamma' D}{s_u} \tag{2.7}$$

The resistance calculated by using Equation 2.7 was compared to results from large deformation finite element (LDFE) analyses reported by Randolph *et al.* (2008), where the

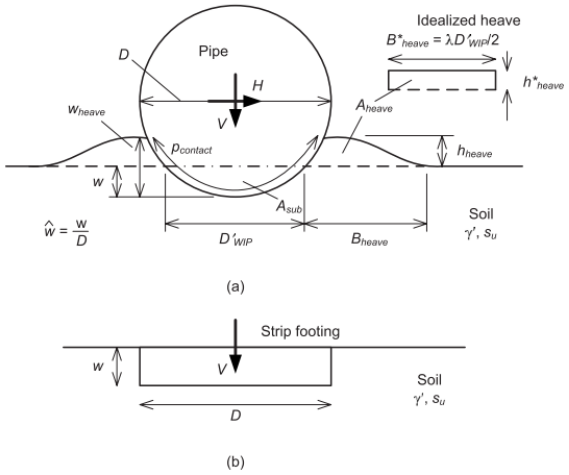

Figure 2.5 Nomenclature of Merifield *et al.* (2009)

pipe was pushed-in-place. The results showed that a buoyancy factor, f_b, of 1.5 gave the best approximation to the LDFE calculations, with the buoyancy component contributing up to 16% of the total resistance for a pipe embedded to $0.5D$. For very deeply buried pipes, once flow-around failure occurred, the buoyancy effect reduced to Archimedes' principle (i.e. f_b equal to 1).

The effects of soil weight and soil heave generated during continuous pipe penetration were further explored by Merifield *et al.* (2009). This study was conducted using the Arbitrary Lagrangian Eulerian (ALE) approach to address the mesh distortion problems found in traditional Lagrangian FE modelling. However, computing accuracy cannot be guaranteed when extreme displacements are involved (i.e. deep penetration of the pipe), as the remeshing technique does not change the mesh topology (elements and connectivity). The maximum penetration depth of this study was limited to $0.5D$. An analytical solution for penetration resistance was proposed, and involved approximating the circular geometry of the partially embedded pipe as a strip footing of width D embedded below the soil surface (Figure 2.5). This approach has also been suggested by the American Gas Association (AGA) in their pipeline design guidelines. The key equation is expressed as:

$$\frac{V_c}{Ds_u} = N_c + N_{sw}\frac{\gamma' w}{s_u} \tag{2.8}$$

where the two factors, bearing capacity factor N_c and self-weight factor N_{sw}, are defined to link the soil strength and soil unit weight to the average bearing stress.

The work described above has not considered either the remoulding of the soil or strain rate effects on the undrained strength of the clay. Wang *et al.* (2010) developed the work further by considering strain softening and strain rate effects on the pipe penetration resistance. This study made use of the FE approach 'remeshing and interpolation technique with small strain' (RITSS), proposed by Hu and Randolph (1998), where a series of small-strain FE calculations are conducted, with regular remeshing of the deformed regime to avoid mesh distortion. Interpolation of field variables (e.g. stress, strain and material properties) from the old mesh to the new one is performed every time the deformed regime is remeshed. The newly remeshed model is then submitted to the FE solver to perform a further small-strain incremental analysis. By repeating this process, the required displacement can be achieved using only small strain analyses but with a continuously updated geometry. The maximum penetration depth in Wang *et al.* (2010) was limited to $0.5D$. Shown in Figure 2.6 is an overview of the RITSS technique.

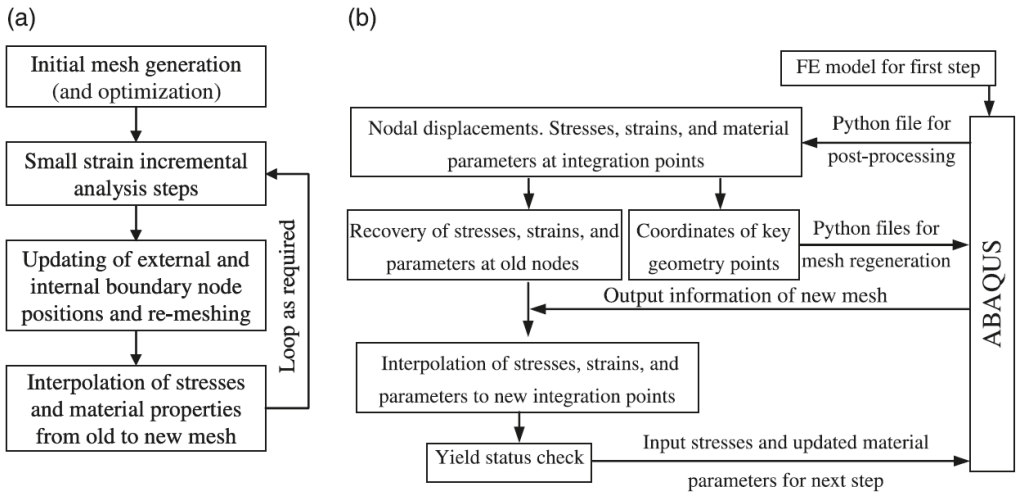

Figure 2.6 Procedure of Abaqus-based LDFE analysis (Wang *et al.*, 2010): (a) overall scheme; (b) implementation in Abaqus.

As the simulation progresses the soil strength is modified to account for reduction due to strain softening and enhancement due to strain rate effects, according to the model

proposed by Einav and Randolph (2005) and Zhou and Randolph (2007):

$$s_u = s_{u0} \times [\delta_{rem} + (1 - \delta_{rem})e^{-3\xi/\xi_{95}}] \times [1 + \mu log(\frac{max(\dot{\gamma}_{max}, \dot{\gamma}_{ref})}{\dot{\gamma}_{ref}})] \tag{2.9}$$

where s_{u0} denotes the intact shear strength of the soil. The second part of Equation 2.9 relates to the strength decrease caused by accumulated plastic shear strain (ξ) while the third relates to the strength increase due to strain rate $\dot{\varepsilon}$. The parameter δ_{rem} is the inverse of the sensitivity, S_t, of the soil, and denotes the ratio between the fully remoulded and initial shear strengths. S_t ranges from 2 to 5 for typical soft marine clays (Randolph, 2004). The ductility parameter ξ_{95} corresponds to the plastic shear strain (ξ) at which the soil has undergone 95 percent of the reduction in strength due to remoulding. Typical values of ξ_{95} ranges from 10 to 50, as suggested by Randolph (2004). The reference shear strain rate, $\dot{\gamma}_{ref}$ is usually taken as 0.01/h. The viscosity parameter, μ, represents the rate of strength increase per decade of strain rate and is typically in the range 0.05 to 0.2 (Biscontin and Pestana, 2001; Lunne and Anderson, 2007). The maximum shear strain rate, $\dot{\gamma}_{max}$, is defined by

$$\dot{\gamma}_{max} = \dot{\varepsilon}_1 - \dot{\varepsilon}_3 \tag{2.10}$$

where $\dot{\varepsilon}_1$ and $\dot{\varepsilon}_3$ are major and minor principal strain rates respectively. The numerical results computed by Wang *et al.* (2010) were compared to the available centrifuge test data reported by Dingle *et al.* (2008), showing a very close match. This study was further extended by Chatterjee *et al.* (2012a,c), with the pipe vertically penetrated to an embedment of one diameter. Based on a parametric study, simple expressions were developed for estimating the vertical penetration resistance of the pipe, taking into account the effect of strain softening, strain rate and soil heave.

To further extend the work Chatterjee *et al.* (2013) conducted a series of FE analyses using the RITSS method to study the coupled consolidation behaviour of soil around partially-embedded seabed pipelines. This work extended that reported by Krost *et al.* (2011) by using the Modified Cam Clay constitutive model, as well as taking into account the soil heave during pipe penetration. Due to the subsequent consolidation after the vertical penetration process, further embedment was observed of an amount dependent on

the level of drainage that occurred during penetration. The yield envelopes constructed by Chatterjee *et al.* (2013) were found to differ markedly from those derived by assuming undrained behaviour without consolidation-induced strength gain.

Following the work conducted at the University of Western Australia, Dutta *et al.* (2015) used the CEL method to study the behaviour of partially embedded pipelines. The soil followed the behaviour expressed in Equation 2.9 (Einav and Randolph, 2005), through the use of the Abaqus subroutine VUSDFLD. A validation study against centrifuge data was conducted with good agreement being found. This model was also used to conduct a validation study against the dynamic embedment of a pipe section (Dutta and Phillips, 2013) with the results finding close agreement with the centrifuge data reported by Cheuk *et al.* (2008). Hawlader *et al.* (2015) extended the work by studying the penetration behaviour of a pipe to a depth of $5D$. The extreme deformation of soil caused by the pipe penetration was found to be handled satisfactorily by the CEL model.

Ansari *et al.* (2014) presented a numerical study on quantifying offshore pipeline resistance during vertical penetration and axial movement, where both wished-in-place and pushed-in-place analyses were conducted. This work was conducted based on coupled pore pressure and displacement finite element analysis, with the Modified Cam Clay model being employed.

2.3 Lateral pipe-soil interaction

2.3.1 Physical modelling

Current design for the evaluation of the lateral breakout resistance of a partially embedded pipe uses empirical equations calibrated from model test results. The pipe weight, pipe embedment and the soil strength profile are generally used as inputs to these prediction models. Most of the calibration model tests were conducted with a focus on lateral stability, with the model pipe segment required to maintain a stationary position or allowed only a very small displacement before breakout might occur (Brennodden *et al.*, 1986, Morris *et al.*, 1988 and Verley and Lund, 1995). The lateral breakout resistance was assumed to

consist of a frictional component proportional to the pipe weight, and a passive resistance component linked to the pipe embedment and the soil strength, expressed as:

$$H_{brk} = \mu_s V + \lambda_s s_u w \tag{2.11}$$

where μ_s is the equivalent friction factor and λ_s is the coefficient for the passive component.

Bruton *et al.* (2006) recalibrated the general form of Equation 2.11, adopting dimensionless groups such as the ratio of soil strength to weight $s_u/\gamma' D$, giving:

$$\frac{H_{brk}}{Ds_u} = 0.2\frac{V}{Ds_u} + \frac{3}{\sqrt{s_u/\gamma' D}}\frac{w}{D} \tag{2.12}$$

For soils having strength variation with depth, Bruton *et al.* (2006) suggested adopting the shear strength at the pipe invert for the calculation. The displacement required to mobilise this breakout resistance, H_{brk}, is usually assumed to be 0.05 to $0.1D$ (Lee, 2012).

DNV-RP-F109 (DNV, 2010) recommended values of μ_s and λ_s in the ranges of 0.2 to 1.0 and 0.5 to 2.0, respectively, depending on the soil type. It is noteworthy that the data used for deriving Equation 2.12 was largely obtained from tests on light pipes with normalised pipe weight W/Ds_u below 2.5 (Merifield *et al.*, 2009). Therefore a more robust solution is needed for reliable prediction of the breakout resistance of pipes with moderate or heavy weight ($W/Ds_u > 2$), which are common for deepwater (Lee, 2012).

Verley and Lund (1995) proposed a nonlinear equation to predict lateral breakout resistance based on small- and large-scale laboratory tests, taking into account the effect of soil unit weight:

$$\frac{H_{brk}}{Ds_u} = 4.13{G_{VL}}^{-0.392}(\frac{w}{D})^{1.31} \tag{2.13}$$

where the definition of G_{VL} is the same as that in Equation 2.3. This model is currently used in DNV-RP-F109 (DNV, 2010) for the on-bottom stability analysis of pipelines. However, as discussed before, the use of total rather than effective soil unit weight makes the model questionable from a theoretical point of view.

Cheuk (2005) conducted a number of centrifuge and large-scale model tests to explore horizontal response for pipes with different weights:

$$\frac{H_{brk}}{Ds_u} = 3.8\sqrt{\frac{2w}{D}} - 0.08\left(\frac{V}{Ds_u}\right)^2 \tag{2.14}$$

This equation was found to predict satisfactorily the breakout resistance of a pipe buried in kaolin clay, but typically over-estimated the breakout resistance for pipes in West African clay by a factor of about 1.6 (Cheuk, 2005).

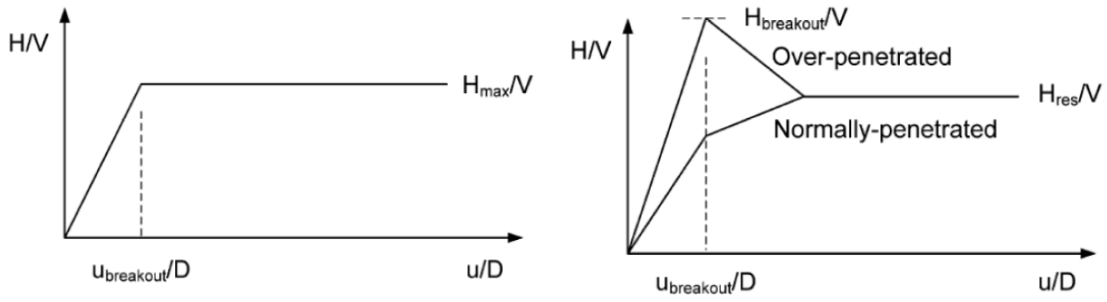

(a) bi-linear (b) tri-linear

Figure 2.7 Models for lateral movement of a partially embedded pipe (Cheuk *et al.*, 2008)

The models above (Equations 2.11 to 2.14) describe the initial breakout resistance and can be used in a 'bi-linear' model (e.g. Figure 2.7a) to capture the pipe-soil interaction behaviour for large deformations. Such large deformation analyses are required for modelling the lateral buckling of pipelines where the pipe can displace laterally by several diameters, even up to 10 diameters. However, this leads to the creation of an active berm ahead of the pipe. In turn this leads to a gradual increase in the lateral soil resistance, governed by the amount of soil scraped away by the laterally moving pipe. More sophisticated models are therefore required to assess the lateral resistance at large displacements.

The main reason that this resistance should be carefully assessed is that it significantly influences the pipeline structural response such as the bending moment distribution (Bruton *et al.*, 2005; Yu and Konuk, 2007), leading to significant implications for the pipeline fatigue design. Based on centrifuge and large-scale model test results, Cheuk (2005) suggested that an equivalent residual friction factor H_{res}/V being adopted between 0.3 and 1.2 could reasonably be used to assess the residual resistance during the first sweep. However, this range is too wide for design of controlled pipeline buckling.

Compared to the bi-linear approaches (see Figure 2.7a) derived based on stability analysis, a more sophisticated tri-linear model can be used to describe the loading behaviour of a laterally moving pipe as shown in Figure 2.7b. This shows different responses, hardening or softening, being identified. The pipe undergoing a downward movement after breakout often shows a hardening response ('normally penetrated') due to the increase in the pipe embedment, while the pipe undergoing upward movement shows a peak response followed by softening response ('over-penetrated') caused by a decrease in the pipe embedment. This tri-linear model uses two independent parameters, breakout resistance H_{brk} and residual resistance H_{res}, where the latter is always assumed to be constant at large displacement. Bruton *et al.* (2006) proposed an empirical approach, taking account of the strength and unit weight of the soil, to predict H_{res}:

$$\frac{H_{res}}{V} = 1 - 0.65[1 - \exp(-\frac{1}{2}\frac{s_u}{\gamma' D})] \tag{2.15}$$

where s_u is quantified at a depth of one pipe diameter to reduce the uncertainty involved in measurement of the seabed surface strength.

Cheuk *et al.* (2007) reported results of full scale model tests to study pipe-soil interactions due to cyclic lateral movements. Two types of soil, kaolin clay and West African soft offshore clay, were used in this study. Four stages of the loading response were identified: breakout, suction loss, steady berm growth and berm collection. A simple upper-bound plasticity mechanism was developed which showed reasonable agreement with the experimental results.

Dingle *et al.* (2008) reported a set of centrifuge model test investigating the lateral response of an on-bottom pipeline subject to cyclic large amplitude movements up to three pipe diameters. Soil mechanisms during the lateral sweeping were provided with the help of digital image analysis using PIV (Figure 1.4). The breakout resistance, as shown in Figure 2.8, involved a strong peak followed by a sharp drop due to the loss of soil suction at the pipe rear. The suction release was found to take place before slip surfaces at the rear of the pipe were fully developed.

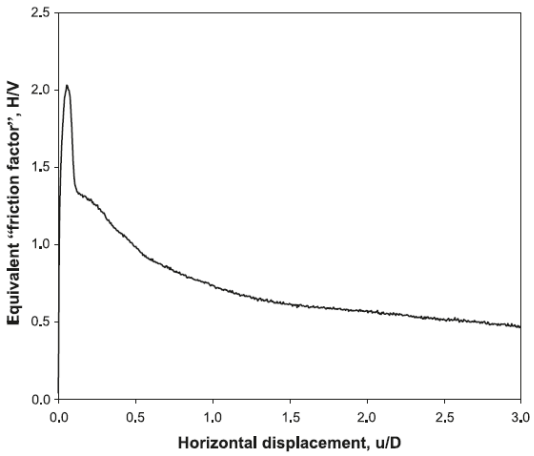

Figure 2.8 Equivalent friction factor during lateral movement (Dingle *et al.*, 2008)

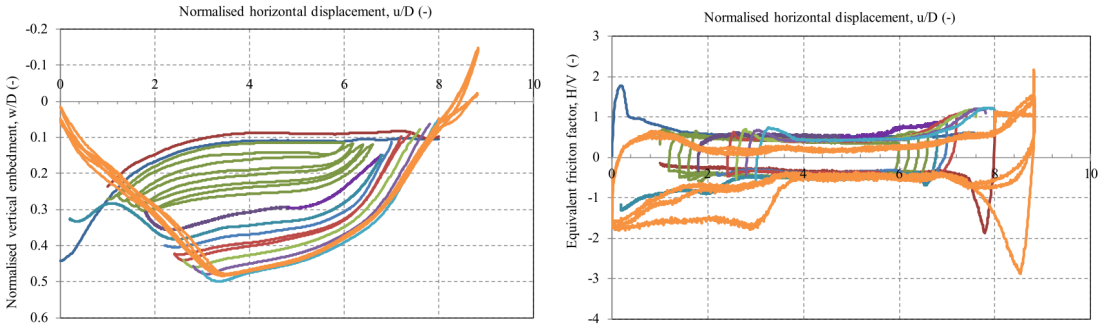

(a) Pipe invert trajectory

(b) Equivalent friction factor

Figure 2.9 Typical loading response of a pipe under lateral cyclic movements (Rismanchian, 2014). Curves in blue correspond to the first few sweeps of the cyclic loading.

Cardoso and Silveira (2010) reported results of a number of full scale model tests to study lateral pipe-soil interaction under large deformations. A wide range of pipe weights were chosen to cover both heavy and light pipes. Simple expressions for breakout resistance, residual resistance and berm resistance were presented using dimensionless groups.

Youssef *et al.* (2013) performed centrifuge modelling to explore the loading response of an on-bottom pipeline, on calcareous sand, under equivalent wave and current loading. The lateral pipe displacement in the study was up to five pipe diameters. The test results highlighted the different stages of the pipe-soil interaction behaviour, and were used to assess a macro-element plasticity model (Zhang *et al.*, 2002a,b) describing pipe-soil interaction.

Rismanchian (2014) reported a systematic study of the cyclic loading response of pipelines subject to very large lateral displacements up to eight pipe diameters, also obtained using centrifuge model testing. Different load paths and cyclic displacement histories were chosen to simulate the behaviour of pipeline segments at the crown and shoulder of a lateral buckle. The development of lateral soil resistance and the pipe invert trajectory (Figure 2.9), as well as development and dissipation of pore pressure around the pipe, were examined in detail. The test results were back-analysed using the FELA software OxLim developed at the University of Oxford. The numerical results were found to be in good agreement with the centrifuge data.

2.3.2 Numerical modelling

2.3.2.1 Lateral resistance at breakout

More theoretically based models, compared with the empirical approaches described above, have also been pursued to describe lateral pipe-soil interactions. The plasticity-based yield envelope approach has commonly been used to assess the bearing capacity of shallow foundations under combined vertical and horizontal loading.

The yield envelope approach was applied by Schotman and Stork (1987) to pipelines but not picked up more widely until Zhang *et al.* (2002a,b) applied the approach to the combined loading response of a partially embedded pipe in sand, calibrated against centrifuge test data. Although the model was calibrated for sand, it demonstrated the applicability of the yield envelope approach to describe the behaviour of pipes in other soil types.

Randolph and White (2008b) developed a series of yield envelopes using upper bound plasticity solutions for pipes partially embedded ($w \leq 0.5D$) in clay. The plasticity solutions were based on a generalisation of the mechanism proposed by Martin and Randolph (2006), with the rotation centre of the main block of the soil not constrained to lie on the diameter normal to the direction of pipe motion. The effects of different interface roughness (fully smooth or rough), and strength profiles (homogeneous or linearly increasing with depth) were examined for pipe embedments increasing from $0.1D$ to $0.5D$ with an interval of

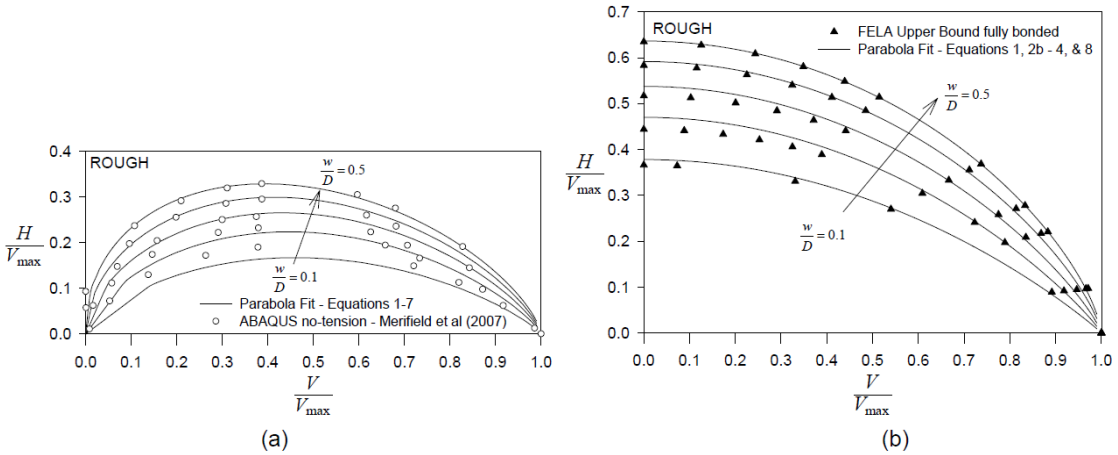

Figure 2.10 Yield envelopes of a shallowly embedded pipe (Merifield *et al.*, 2008a): (a) no-tension case (Abaqus); (b) full-tension case (FELA)

0.1D. Generally, it was found that the breakout resistance of a fully smooth pipe was 10% to 20% lower than that of a fully rough one. The direction of the pipe movement at breakout could also be conveniently determined from the yield envelopes based on the assumption of associated flow.

Merifield *et al.* (2008b) reported a finite element study on the breakout response of partially embedded pipes under combined vertical and lateral loading. The results were compared with the yield envelopes derived from upper bound plasticity solutions (Randolph and White, 2008b), with the limiting loads obtained using both methods being in good agreement. The curves of the yield envelopes were fitted with simple expressions to assess the ultimate resistance of partially embedded pipes.

Both Randolph and White (2008b) and Merifield *et al.* (2008b) allowed for separation at the rear of the pipe, so that no tensile force could be mobilised when breakout occurred. Merifield *et al.* (2008a) derived alternative yield envelopes assuming full tensile capacity at the pipe-soil interface. The breakout resistance was found to be significantly higher than the no-tension calculations (Figure 2.10), especially at low vertical loads, due to the two-sided failure mechanism. Such mechanisms were also observed in centrifuge modelling (Dingle *et al.*, 2008). In reality, a partially bonded condition would be more reasonable, which depends on the loading rate during breakout and the soil permeability.

Cheuk *et al.* (2008) and Oliveira *et al.* (2010) provided simple upper bound plasticity solutions for the combined vertical and lateral loading response of pipes by assuming

a slip circle failure mechanism. Both bonded and unbonded conditions at the interface were considered. The solutions were less optimal compared with those discussed above due to the simplification of the pipe-soil failure mechanism. However, they were still in good agreement with experimental results (and empirical expressions), demonstrating an alternative and simpler way to predict the breakout resistance of partially embedded pipes.

Hodder and Cassidy (2010) proposed a displacement hardening plasticity model which was derived on the basis of a series of centrifuge model tests exploring pipes partially embedded in clay. An increase in size and a change in shape of the yield envelopes with pipe embedment was reported. A flow rule and vertical elastic stiffness factor was introduced to allow prediction of the invert trajectory, and the corresponding vertical load of the pipe during lateral displacement across the soil. However, information for the flow rule at low values of normalised vertical load was not obtained.

As discussed in Section 2.2.2.1 Martin and White (2012) conducted a large number of FE limit analyses using OxLim (Makrodimopoulos and Martin, 2006, 2007, 2008) to explore the ultimate bearing capacity of a rigid pipe in undrained clay. The pipe was 'wished in place', with invert embedments varying from zero to five pipe diameters. Soil strength was either uniform or linearly increasing with depth. $V-H$ yield envelopes for the pipe were derived with the effect of soil unit weight, interface roughness and interface tensile capacity being systematically studied. Design guidelines were then suggested based on a comprehensive understanding of the failure mechanisms observed from upper bound results.

All of these studies described were conducted ignoring the surface heave generated as the pipe is penetrated into the soil. Merifield *et al.* (2009) conducted a series of LDFE analyses using ALE approach to investigate the effect of soil weight and surface heave on the lateral breakout resistance of a partially embedded pipe. The pipe was pushed-in-place to a specified embedment before being loaded laterally. The 'local' embedment of the pipe, due to the raised soil level adjacent to the pipe, was found to exceed significantly the nominal embedment relative to the original soil surface. This effect was also found to increase the lateral resistance component due to soil weight by almost 100%.

2.3.2.2 Lateral resistance following breakout

White and Cheuk (2008) considered the contribution of the active berm to the residual resistance, H_{res}, during the steady sweeping phase, by relating the amount of soil ploughed to the pipe embedment. The model adopted the simplification of the pipe moving at a constant elevation, ignoring the change of pipe embedment during the lateral sweep. This simplification will affect the assessment of the soil berm evolution and hence the lateral resistance.

Hesar (2004) made the first effort to study pipe-soil interaction numerically during large lateral movements in soft clay. The explicit approach built in Abaqus was used along with an adaptive meshing strategy to avoid mesh distortion. The study focussed on the effects of initial pipe embedment and pipe weight on the lateral soil resistance during the pipe movement. However, only results for a few specific cases were presented, and no general solutions were derived.

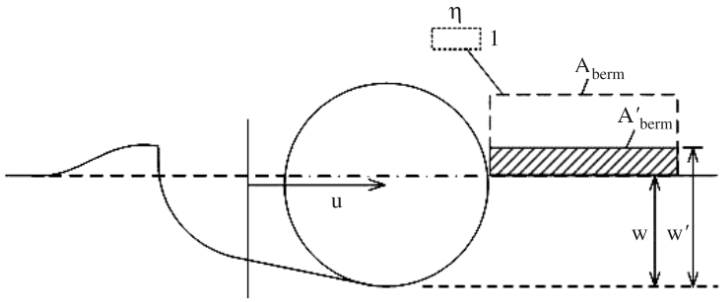

Figure 2.11 Effective embedment of a pipe (Wang *et al.*, 2010)

Wang *et al.* (2010) conducted a series of FE analyses using the LDFE strategy RITSS (Hu and Randolph, 1998) to examine the behaviour of a partially embedded pipe undergoing large lateral displacements. This study took into account the effect of strain softening and strain rate by using a modified Tresca constitutive model according to Equation 2.9. Comparison of the FE results with centrifuge data reported by Dingle *et al.* (2008) showed that the model could satisfactorily capture the loading behaviour of the pipe at large movement, in terms of the invert trajectory and the lateral soil resistance. However, the breakout resistance was largely underestimated due to the absence of tensile capacity at the pipe-soil interface. This study proposed the concept of an effective embedment w'

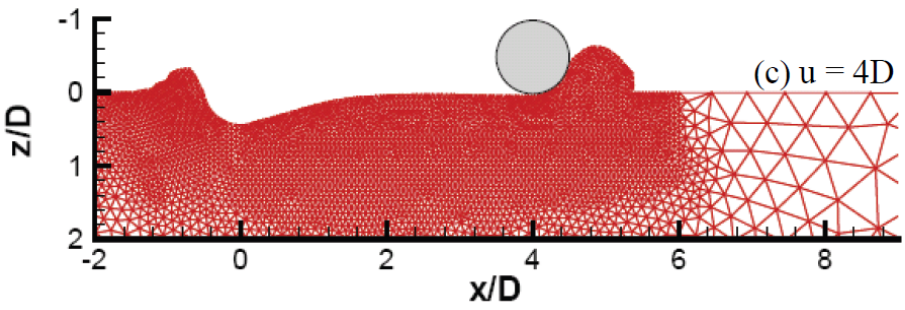

Figure 2.12 Typical mesh of the lateral pipe-soil interaction model using RITSS (Chatterjee, 2012)

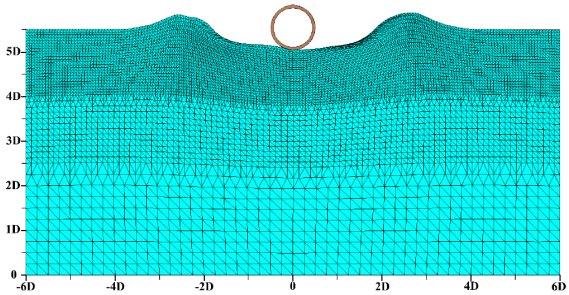

Figure 2.13 Deformed mesh at the end of the cyclic lateral loading of a pipe (Sabetamal, 2014)

to account for the presence of the soil berm ahead of the pipe (Figure 2.11). A power law function was developed, based on the FE results, to relate the residual resistance to the effective embedment. Chatterjee *et al.* (2012b) and Chatterjee (2012) further extended this work, systematically examining the effect of initial pipe embedment on the residual lateral resistance. Yield envelopes for a pipe at embedments ranging from $0.1D$ to $0.5D$ were constructed. Figure 2.12 shows a typical mesh for the pipe-soil model reported by Chatterjee (2012), where the RITSS method was also adopted. Chatterjee *et al.* (2013) extended the work to consider the coupled consolidation behaviour of soil around a partially-embedded pipe, finding a considerable enhancement of the lateral breakout response of the pipe due to consolidation effects.

All the preceding numerical work is limited to monotonic loading behaviour. In reality the pipe may experience thousands of cycles of motion during its service life (Cheuk *et al.*, 2008). For the study of cyclic lateral pipe behaviour Sabetamal (2014) constructed a numerical model using the FE code SNAC, developed at the University of Newcastle (NSW). The ALE mesh strategy was adopted to avoid mesh distortions in this

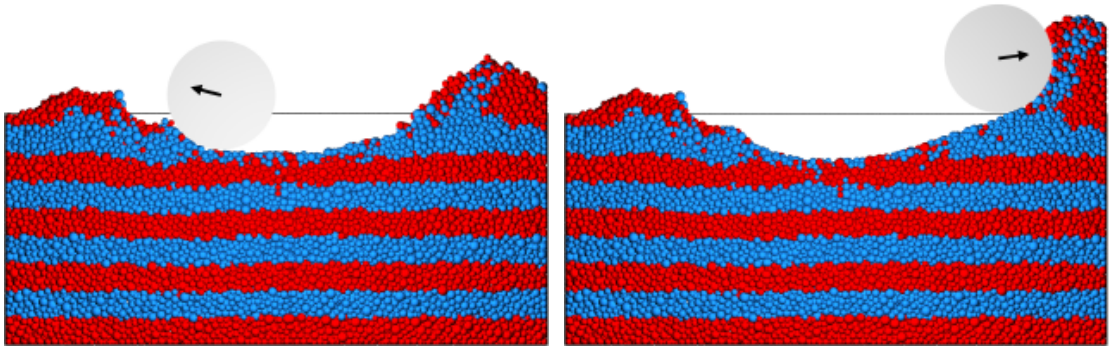

(a) Cycle 3, $u = 0.5D$ (b) Cycle 3, $u = 2.5D$

Figure 2.14 Distinct element method (DEM) model for pipe-soil interaction (Macaro, 2015)

study. The deformed mesh at the end of the cyclic lateral loading is illustrated in Figure 2.13. The model proved capable of simulating the generation and dissipation of pore pressure during the vertical penetration and the subsequent cyclic lateral motion of the pipe. However, comparisons with physical modelling results were not made. The study mainly focused on demonstrating the capability of the numerical model for a range of geotechnical applications, rather than detailed parametric analyses for the pipe-soil interaction problem.

Macaro (2015) performed a numerical study, using the Distinct Element Method (DEM) code Yade, into the cyclic loading behaviour of a pipe segment under large amplitude displacements. The pipe was loaded by 3 cycles of horizontal motion for amplitudes up to $2D$ (Figure 2.14). The simulation results were found to agree broadly with published experimental data. Insights into the mechanics of the soil at a particle level were provided. Although the analyses were limited, the study highlighted the possibilities of using methods other than FE analysis for studying pipe-soil interactions.

All the above work describes the results of 2D (plane strain) models, which do not take account of the global response of a pipeline during lateral buckling. Different displacement paths occur along the pipe length, with the structural response being strongly linked to the pipe-soil response. Konuk and Yu (2007) and Yu and Konuk (2007) studied large displacement pipe-soil interactions using an ALE approach in the explicit FE software LS-DYNA. Both two dimensional and three dimensional simulations were carried out with a cap plasticity soil model being employed. The drawbacks of conventional design

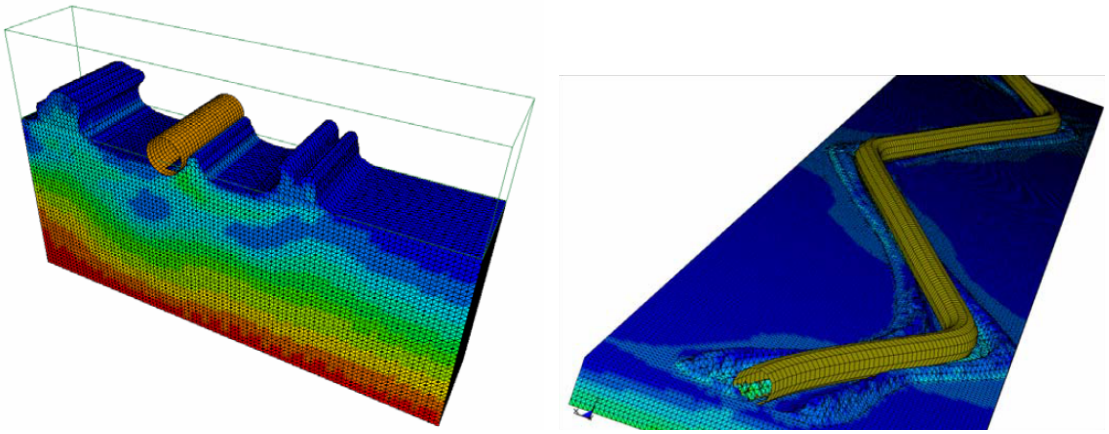

(a) 3D plane strain (b) Full 3D

Figure 2.15 Arbitrary Lagrangian-Eulerian (ALE) model for pipe-soil interaction (Yu and Konuk, 2007)

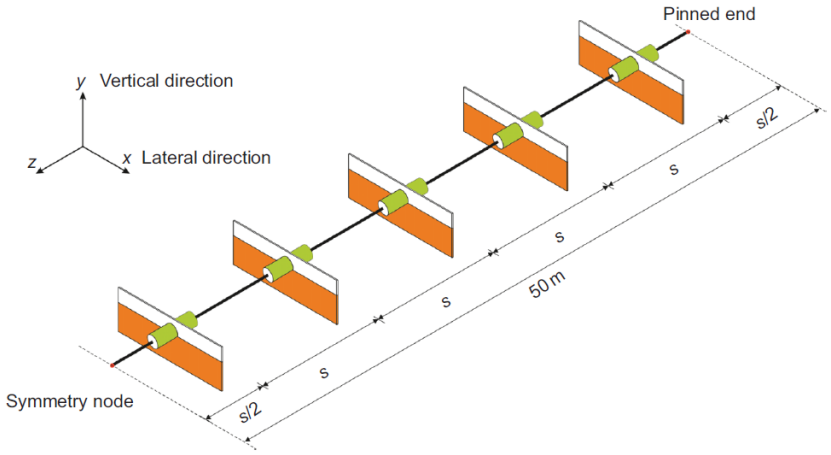

Figure 2.16 Coupled Eulerian-Lagrangian (CEL) model for pipe-soil interaction (Martin *et al.*, 2013)

approaches for lateral pipe-soil interaction, which are based on Winkler or Coulomb friction models, was emphasised in the study.

Martin *et al.* (2013) reported a numerical study of a pipeline undergoing lateral displacements with an amplitude of up to one pipe diameter. The analyses was performed using the CEL implementation in Abaqus. A 3D pipeline was modelled to interact with a number of soil slices (Figure 2.16). This modelling approach is still at an early stage and the soil used was an ideal elastic-plastic material without considering strain rate effects, strain-softening or strength increase with depth. The influence of the distance between

slices on the pipe response was studied and validity of this model was shown by checking the global force equilibrium of the pipeline.

2.4 Summary

Previous studies of the vertical and lateral pipe-soil interactions on clay, some of which formed part of the SAFEBUCK JIP, have been summarised in this chapter. The pipe-soil interaction models used in existing design approaches (e.g. DNV) for on-bottom pipelines are largely based on empirical expressions developed from a very limited database of experimental results.

The failure mechanisms relating to the vertical bearing capacity of a pipe in clay has been well studied with both physical and numerical modelling methods. However, apart from the physical modeling data which are limited to particular soil profiles, most of the numerical models neglect the effect of soil heave generated during the penetration process (i.e. installation effects). Moreover, the influences of rate-dependency and soil remoulding on the penetration resistance of a pipe have not been systematically examined or quantified.

For the loading behaviour of a pipe during lateral movement in soft clay, various models based on plasticity solutions and numerical studies have been developed, most of which focused on the soil resistance at the breakout stage. There is limited understanding of the lateral resistance of a pipe at large movements, especially under cyclic loading, taking into account the change in soil strength due to rate-dependency and remoulding effect.

It is clear that further studies are required to improve the understanding of both vertical penetration and lateral sweeping of a pipe segment, in an attempt to provide improved and robust guidelines for the design of offshore pipelines.

Chapter 3

Numerical modelling methodology

This chapter introduces the development of a sequential limit analysis (SLA) method to solve large deformation plasticity problems involving undrained soil under conditions of plane strain. The SLA method solves a large deformation problem by solving a consecutive series of small-strain limit analysis problems. This approach has been developed to analyse relatively simple problems such as frames and plates (e.g. Yang, 1993, Raithatha and Duncan, 2008), where no contact conditions need to be handled. To extend this method to study soil-structure interaction problems, the external boundaries of the model have to be treated with caution, and this will be described in detail.

After the development of SLA has been described, the CEL method in-built in Abaqus (Dassault Systémes, 2011) is introduced as a complementary tool. This method is nowadays commonly accepted as a powerful tool for solving problems involving large plastic deformations (Abadalla *et al.*, 2009; Andresen and Khoa, 2013; Dutta *et al.*, 2012; Grabe *et al.*, 2013; Hawlader *et al.*, 2015; Qiu and Grabe, 2011; Tho *et al.*, 2013). It will be used to compare with the newly developed SLA method to reveal the capability of SLA in handling the updating of model geometry as well as the material behaviour in Chapter 4 (*Validation of the numerical method*).

3.1 Classical limit analysis

The foundations of limit analysis for perfectly plastic structures are the lower and upper bound theorems of plasticity theory (Drucker *et al.*, 1952; Gvozdev, 1960), which allow

the exact collapse load to be bracketed in a robust manner. In formulating these theorems the following two types of fields are used:

- A statically admissible field of stresses, or an equilibrium system that satisfies: a) the conditions of equilibrium throughout the body; b) the boundary conditions for the stresses; and c) the yield condition is not violated at any point of the body.

- A kinematically admissible field of velocities, or a mechanism that satisfies: a) the velocity field is compatible; b) the boundary conditions for the velocities; and c) wherever deformations occur the strain rates satisfy the flow rule.

The true failure load is larger than the loads corresponding to an equilibrium system (lower bound theorem) and smaller than the loads corresponding to a mechanism that is calculated using the virtual work principle (upper bound theorem). Theoretically the maximum value of all lower bound solutions must equal the minimum values of all upper bound solutions. This exact value can only be obtained for very limited simple problems. In most cases, non-coincident lower and upper bound solutions are obtained numerically, either using bespoke stress and displacement fields, or via FELA (e.g. Lyamin and Sloan, 2002, Augarde *et al.*, 2003). FELA uses computational optimisation techniques to approach the corresponding maximum and minimum solutions simultaneously, and many complex problems can be solved with certainty of convergence and accuracy (e.g. Martin and White, 2012).

It may be noted that in the definition of the statically or kinematically admissible fields described above, the constitutive relations are not mentioned except for the statement that the stresses must satisfy the yield condition, and the strains must satisfy the associated flow rule. In this manner, limit analysis by-passes the tedium of keeping track of the details of elastic-plastic constitutive equations and thus can be implemented more simply than incremental FE methods, which depend heavily on the constitutive equations.

3.2 Finite element limit analysis (FELA) using OxLim

OxLim is a FELA program developed at Oxford University, with which strict lower and upper bound plasticity solutions can be obtained (Makrodimopoulos and Martin, 2006, 2007, 2008; Martin, 2011). In a standard OxLim analysis, the lower and upper bound theorems are formulated as standard second-order cone programming (SOCP) problems and then optimised by the software MOSEK (MOSEK APS, 2010). When the lower/upper bound theorem is formulated in OxLim, a piecewise continuous stress/deformation field is employed in which adjoining elements are separated by statically/kinematically admissible discontinuities. These discontinuities introduce additional degrees of freedom, yielding results generally much better than those obtained from a fully continuous field. In the SLA method, the OxLim software serves as the core solver to perform standard limit analysis for each problem in a sequence, allowing large plastic deformations to develop. This section gives a brief introduction to the interface between OxLim and the other parts of the SLA numerical code.

3.2.1 Input to OxLim

Two modes are supported in a standard OxLim analysis, the planar straight line graph (PSLG) mode and the mesh mode. Only the latter is introduced in this thesis because PSLG mode is not practical when there are field and history variables to be updated throughout a sequence of analyses. In a typical OxLim analysis in mesh mode, the simulation domain is comprised of a number of triangular elements, segments and nodes. Material properties are assigned to the elements while boundary conditions are applied to segments.

Figure 3.1a shows a simple example to analyse the vertical bearing capacity of a strip footing partially embedded in soil. The domain embraced by the rectangle *COPE* represents a rigid body. Segments FG and GH represent the edges constrained by fixed boundary conditions and segment EF represents the edge constrained by symmetry conditions. Segments EC and AC denote the interfaces where the rigid body and the soil domain are in contact. The whole domain meshed by the software Triangle (Shewchuk, 2002) is shown in Figure 3.1b. Apart from the coordinates of all the nodes and the element

connectivity, other necessary information to be passed to OxLim are the material properties (e.g. strength and body force) of the triangular elements and the boundary types (e.g. fixed, symmetry, etc.) of the external segments. It is worth noting that segments *AO*, *OP* and *PE* cannot be reflected in OxLim modelling and the full trace of a rigid body should be kept externally.

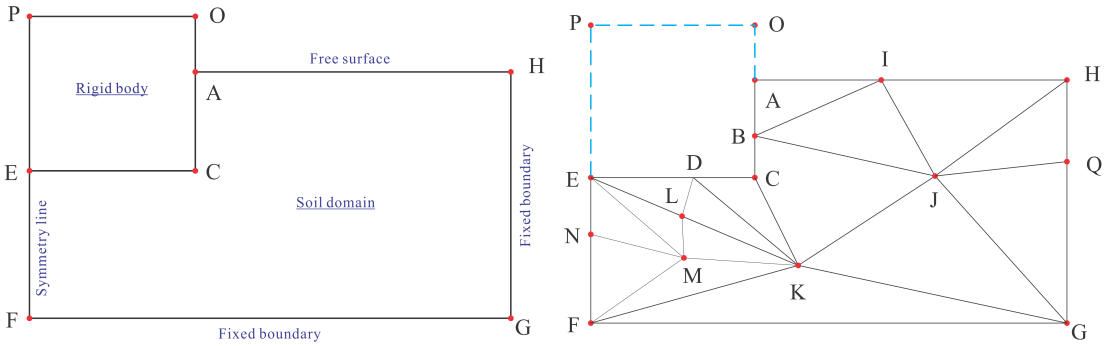

(a) PSLG (b) Mesh

Figure 3.1 Schematic of a typical OxLim model

3.2.2 Output from OxLim

The upper bound analysis in OxLim modelling provides all the necessary information to update the model configuration, namely the velocity vectors of all the nodes in the model. Nevertheless, lower-bound analysis is also performed to provide an error indicator for each analysis in the sequence, defined as

$$err\% = \frac{UB - LB}{UB + LB} \times 100 \tag{3.1}$$

where LB and UB are the failure loads obtained from lower and upper bound analyses, and err is the bracketing discrepancy between them.

3.3 Sequential limit analysis (SLA) based on FELA

This section introduces how the SLA method used in this thesis is developed as an extension of the FELA software OxLim. The problems to be studied in this thesis are more commonly studied via various methods such as incremental finite element (FE) analysis, which has

the drawback of lacking an automatic indication of proximity to the exact solution (Yang, 1993). In contrast, the lower bound and upper bound theorems in limit analysis allow the exact solution for a perfectly plastic structure to be bracketed rigorously. The SLA method introduced here is performed based on a series of limit analyses, via FELA, and thus has the advantage of global numerical stability.

3.3.1 Introduction of the SLA method

Using limit analysis, the instantaneous velocity field (or mechanism) of a deformable region undergoing plastic deformation is obtained from an upper bound solution for a given configuration of the model. The nodal velocity vectors can be integrated over a small time increment to yield the displacement field, which in turn updates the configuration of the deforming domain. The softening and hardening behaviour of the material can be included by updating the local material strength as a function of the cumulative plastic strain and estimated strain rate. A subsequent problem is then solved for the updated configuration. By repeating this process, a large deformation problem can be solved by a series of sequential limit analyses. Remeshing of the deforming domain is performed whenever necessary to eliminate the inaccuracy resulting from mesh distortion, which is a main concern of conventional FE modelling.

Accurate geometric updating can be achieved in SLA by choosing relatively large time increments compared with those used in incremental FE analysis, where complicated stress updating is also needed. This feature greatly improves computational efficiency (Raithatha and Duncan, 2008; Yang, 1993). Moreover, SLA remains globally stable under all material and geometrical nonlinearities. Certain behaviours of the material, such as the elastic response and consolidation, cannot be considered in SLA method. However, SLA can provide the most important information, at least for the problems to be investigated in this thesis, at a fraction of the cost of the incremental FE method, as will be shown in later chapters.

Based on the assumption of perfect plasticity, only the upper bound formulation is needed in the SLA method because each step of the sequence only involves geometric

updating. However, lower bound analysis is also performed simultaneously in this study to provide an indication of proximity to the exact solution. The main steps involved in the SLA method used in this thesis are as follows.

- 1. The initial model details are generated first and the software Triangle (Shewchuk, 2002) is then called to mesh the model. History variables (e.g. s_{u0}, ε^p, etc.) of all the nodes are initiated at the first analysis sequence and recorded. Meanwhile, every node on the external (e.g. IH and AB in Figure 3.1b) or internal (e.g. IJ and JK in Figure 3.1b) boundaries is assigned a boundary marker of its own. These boundary markers are used to decide the boundary types of nodes and segments in the OxLim analysis. All the information needed for a standard limit analysis is then written to an input file and submitted to OxLim for calculation.

- 2. After completion of the OxLim analysis, nodal velocities of the model are obtained from upper-bound results. A time increment Δt is then chosen based on these results to update the model configuration as well as the internal and external boundary conditions. More details of this process are given in Section 3.3.2.

- 3. The incremental plastic strain distribution is obtained from the nodal velocities and the cumulative plastic strain distribution is updated accordingly. The correct strength properties of each triangular element are then determined, as discussed in Section 3.3.3. This process is performed when the rate dependency or softening behaviour of the material is to be considered.

- 4. Remeshing is conducted if necessary and field variables are mapped from the old mesh (reference plane) to the new one (target plane). More details are given in Section 3.3.4.

- 5. Model details of the new remeshed domain are written to an input file and submitted to OxLim for computing again.

Steps 2-5 are taken as a complete 'analysis in the sequence' (increment) and repeated until the required displacement is achieved. The whole process is automatically processed

by a code written in Python without any intervention from the user. Figure 3.2 shows a simplified flow diagram describing the entire process, where it can be seen that the SLA method is similar to the RITSS method (Hu and Randolph, 1998) except that the RITSS method solves an elasto-plastic FE problem at each increment while SLA solves a pair of optimisation problems (LB, UB) using an interior-point solver.

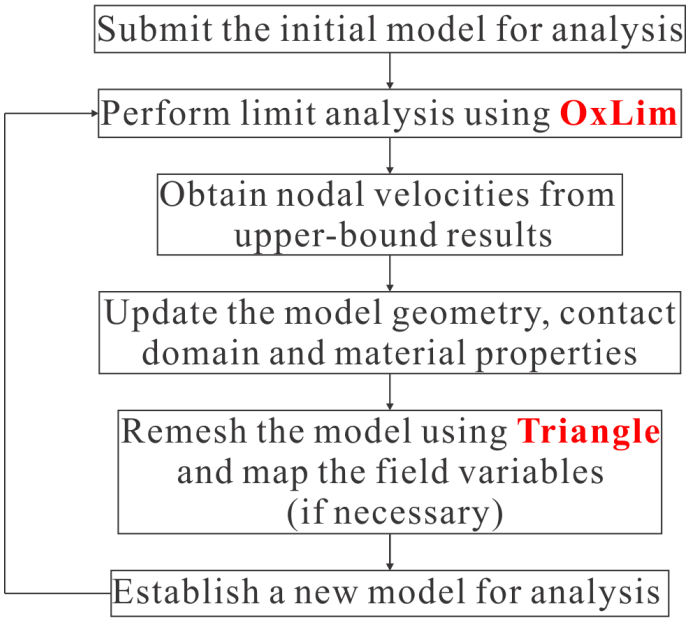

Figure 3.2 Overview of the SLA approach (without update of material properties)

In addition to the disadvantage of being unable to model the elastic loading/unloading, consolidation and other behaviours of the material, as discussed previously, a fundamental problem in sequential limit analysis makes it less competitive compared with other incremental methods (e.g. FEM and DEM). This lies in the fact that the mechanism (velocity field) of the model obtained from limit analysis is not unique, since in most cases optimisation problems are solved and the solutions are close but not identical to the exact solution. With the limit analyses being solved sequentially, whether the discrepancies in deformation tend to stabilise or accumulate, will be examined by a few numerical examples as presented in Chapter 4.

3.3.2 Update of the model configuration and boundary

An essential requirement in SLA modelling is the precise tracking of both free and constrained external boundaries. Free boundaries are treated by keeping a record of free surfaces in the model. A free surface in SLA modelling is comprised of a list of segments and the nodes forming them in consecutive order. Every time remeshing is performed, the newly generated nodes sitting on these segments and the old ones should be sorted in order again. This is extremely important in SLA modelling for the treatment of external boundaries when a complicated geometry update is involved, as will be introduced later in this chapter.

Concerning constrained external boundaries, the treatment of fixed and symmetric boundaries is quite straightforward. The challenging part is to deal with the contact between a rigid body and deforming material. This is achieved by tracking the nodes at the margin of contact (see Figure 3.3). The relative positions of these margin nodes to the rigid body are recorded throughout the analysis and the region between the two margin nodes is automatically recognised as the contact domain. This section introduces how these tasks are realised numerically in SLA modelling.

3.3.2.1 Determination of the nodal velocity

For an individual node at a given increment in the sequential limit analysis, its position is simply updated by

$$x_{(n)} = x_{(n-1)} + v_{(n)} \times \Delta t_{(n)} \tag{3.2}$$

where $x_{(n-1)}$ and $x_{(n)}$ are the coordinates of the node at the end of the $(n-1)^{th}$ and n^{th} increments, $v_{(n)}$ is the nodal velocity and $\Delta t_{(n)}$ is the time increment chosen to update the model configuration following the n^{th} analysis. The choice of $\Delta t_{(n)}$ will be further discussed in Section 3.3.2.3.

To obtain the nodal velocities in SLA modeling is not as straightforward as in conventional FE analysis since kinematically admissible velocity discontinuities are allowed in the upper bound analysis in OxLim (Makrodimopoulos and Martin, 2008), via the use of internal evaluation points. Each node may have several corresponding evaluation points

and the number depends on the local connectivity. Taking the mesh shown in Figure 3.1b for example, the node I has three evaluation points belonging to elements IAB, IBJ and IJH. All three points have the same coordinates as node I but can have different velocity vectors obtained from the upper bound solutions due to the assumption of kinematically admissible velocity discontinuities. For nodes inside the deforming domain or on the fixed boundaries, no special attention has to be paid since velocity continuity is enforced for them. While for nodes on the free surface or in contact with the rigid body, their velocity vectors should be treated carefully due to possible discrepancies.

Figure 3.3 shows three types of such nodes. Those on the free surface and not in contact with the rigid body are recognised and referred to as surface nodes hereafter; those in contact with the rigid body but adjacent to a surface node are recognised as margin nodes and others between the two margin nodes are interface nodes. When symmetry of the model is exploited, the interface nodes are those between the margin node and the symmetry line.

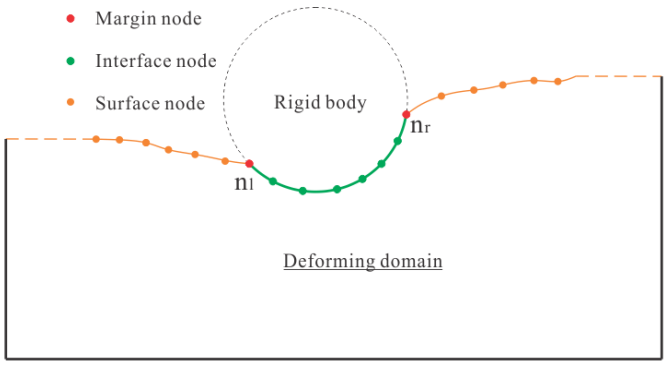

Figure 3.3 Nodes that might have velocity discrepancies on the external boundaries

To evaluate the velocity discrepancies between two arbitrary evaluation points of a node, the following equation is used:

$$\Delta v_{ij} = \frac{\|v_i - v_j\|}{\|v_i\| + \|v_j\|} \tag{3.3}$$

where $\|\cdot\|$ denotes the Euclidean norm of a vector. v_i and v_j are the velocity vectors corresponding to two arbitrary evaluation points of the node, and Δv_{ij} is the discrepancy between them.

For a surface node, its velocity is determined as the average of the velocity vectors corresponding to all of its evaluation points. It has been checked that the largest velocity discrepancy for a surface node is within an acceptable tolerance of 1%, for the problems investigated in this thesis.

A margin node should have at least one evaluation point that moves along the rigid body, that is, along the rigid body segment that the node sits on. Otherwise, breakaway will take place and a new margin node should be found based on this criterion. More information on how breakaway of a margin node from the rigid body is handled can be found in Section 3.3.2.2. Once a node is recognised to be a margin node, its velocity is determined by

$$v = \frac{\sum \|(v_i - v_r) \cdot s\|}{n\|s\|} \cdot \frac{s}{\|s\|} + v_r \tag{3.4}$$

where v_r is the velocity of the rigid body, n is the total number of evaluation points belonging to the node and s is the vector of the rigid body segment that the margin node sits on.

The position of an interface node is not updated directly on the basis of nodal velocities. Throughout the analysis, the position of the reference point of the rigid body is recorded and the coordinates of the margin nodes relative to the rigid body are also traced. Since the region between the two margin nodes (see Figure 3.3) is automatically recognised as a contact domain, the interface nodes can be conveniently reconstructed at the positions of rigid body vertices within the contact domain. This operation is reasonable based on the assumption that no crack takes place within the contact domain *between* the margin nodes (crack opening or closure *at* the margin nodes is covered in the following subsections).

Conservation of volume is automatically satisfied in the OxLim calculation when analysing an incompressible material, but the treatment of nodal velocities as introduced in this section might lead to some loss or gain of material after the model configuration is updated. This could be effectively avoided by using a fully continuous velocity field in the upper bound analysis, but less satisfactory solutions (in terms of bracketing discrepancy between LB and UB) will be obtained as a result. For all the problems investigated in this thesis, the inaccuracy of the material volume caused by adopting the strategy introduced

in this section is found to be rather limited, and this point will be further discussed in the validation studies presented in Chapter 4.

3.3.2.2 Breakaway of nodes from the rigid body

After the velocity field has been obtained from the upper bound solution, the margin nodes n_l and n_r as defined in Figure 3.3 are checked to see if they move along the rigid body segments S_m that they sit on, which are hereafter referred to as margin segments. For a specific margin node, referred to as n_m hereafter, this is achieved by checking if

$$\cos\theta = \frac{\|(v - v_r) \cdot s\|}{\|(v - v_r)\| \cdot \|s\|} \geq \cos\theta_{cri} \tag{3.5}$$

where s is the vector of the margin segment determined by the coordinates of its two endpoints, v is the velocity of n_m, v_r is the velocity of the rigid body and θ is the angle between $(v - v_r)$ and s. θ_{cri} is the tolerance of θ and a value of 10^{-4} rad is used here. Node n_m is determined to move along S_m if Equation 3.5 is fulfilled. Otherwise, breakaway of one or more interface nodes from the rigid body will take place.

If a margin node n_m is found to break away from the rigid body, other nodes in the contact domain near it are checked in a consecutive order as illustrated in Figure 3.4, until a node $n_{(e)}$ is found to move along the rigid body segment that it sits on. The previous n_m is the first node to be checked on the list and is denoted by $n_{(0)}$ in the figure. The searching order is counterclockwise if n_m is on the left side of the rigid body or clockwise if on the right. After the node $n_{(e)}$ has been detected, the nodes $n_{(0)}$ to $n_{(e-1)}$ are released from the contact boundary and recognised as surface nodes. Accordingly, segments $n_{(0)}n_{(1)}$ to $n_{(e-1)}n_{(e)}$ are recognised as free surface segments. Node $n_{(e)}$ is then defined as the new margin node n_m. Each node and segment is assigned an updated boundary marker which can be used to determine its boundary type in the subsequent OxLim input.

3.3.2.3 Evolution of the contact domain

After breakaway has been dealt with as described in Section 3.3.2.2, the positions of the margin nodes relative to the rigid body have to be updated to trace the evolution of the

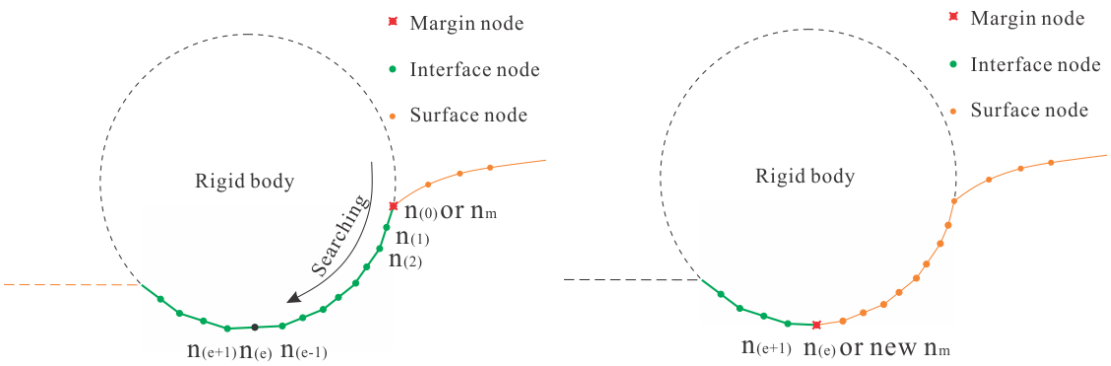

(a) Before break (b) After break

Figure 3.4 Schematic of interface nodes breaking away from a rigid body. Only a break from the right side is shown.

contact domain. In a SLA simulation, a rigid body is comprised of a series of nodes and segments as discussed in Section 3.2.1. Those parts of the rigid body that are not in contact with the deforming domain cannot be incorporated in an OxLim input. Therefore Oxlim can only provide information on whether a margin node moves along the rigid body segment it sits on, but cannot tell if a new segment will be involved in the next increment.

Figure 3.5a shows a margin node n_m sitting on $S_{(j)}$, which is the jth segment belonging to the rigid body. The end points of $S_{(j)}$ are denoted by $p_{(j),(1)}$ and $p_{(j),(2)}$. Since all the segments of the rigid body are constructed consecutively, $p_{(j),(1)}$ is identical to $p_{(j-1),(2)}$. To obtain the final position of this margin node after the model has been updated by a time step, it should be decided first which end point $p_{(j),(k)}$ the margin node moves towards. This is achieved by checking the sign of $(v - v_r) \cdot s$, where s is the vector of the margin segment determined by the coordinates of its two endpoints, v is the velocity of n_m and v_r is the velocity of the rigid body. A positive value indicates that $k = 2$ while a negative indicates that $k = 1$. The time dt taken for the margin node to move to the position of $p_{(j),(k)}$ can be calculated as

$$dt = \frac{\|x_p - x_m\|}{\|v - v_r\|} \tag{3.6}$$

where x_p and x_m are the coordinates of $p_{(j),(k)}$ and n_m. The time step Δt to update the nodal coordinates (and model configuration) is then determined by $\Delta t = \min(dt, \Delta t_{min})$, where Δt_{min} is a limiting value of the time step set by the user.

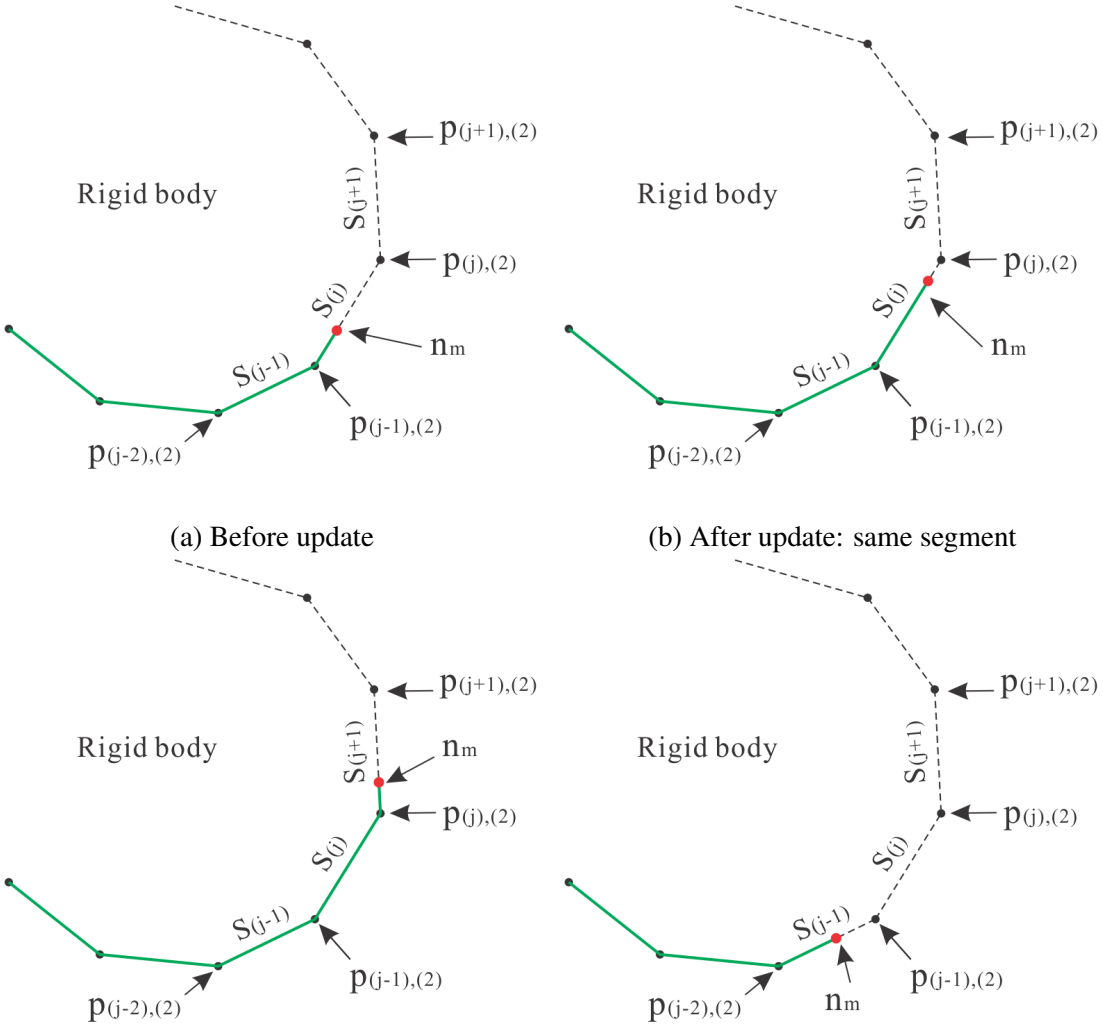

(a) Before update

(b) After update: same segment

(c) After update: new segment added

(d) After update: old segment removed

Figure 3.5 Determining the position of a margin node after coordinate update. Only the update of the right margin node is shown.

If Δt_{min} is chosen to update the nodal coordinates, the margin node will still stay on the segment $S_{(j)}$, though at different relative position after the coordinate update, as illustrated in Figure 3.5b. Otherwise, the margin node will move to overlap $p_{(j),(k)}$, which is exactly at the corner formed by segments $S_{(j)}$ and $S_{(j+d)}$, where $S_{(j+d)}$ is the potential margin segment that the margin node moves towards. The value of d is chosen in a way similar to that for k discussed above. A positive value of $(v - v_r) \cdot s$ produces $d = 1$ while a negative value indicates $d = -1$. However, if the margin node sits right on $p_{(j),(k)}$ after the updating of coordinates, $S_{(j+d)}$ can not be reflected in an OxLim input file for the next increment as discussed before. Therefore, after the model configuration has been updated by dt and the margin node overlaps $p_{(j),(k)}$, the margin node should then be forced to 'jump' by a very short distance to $S_{(j+d)}$ to indicate the existence of this segment to OxLim. The final coordinates of the margin node (X) can be determined by a linear interpolation $X = X_p + \zeta(X_q - X_p)$, where X_p and X_q are the updated coordinates of the two end points of $S_{(j+d)}$ ($p_{(j),(k)}$ and $p_{(j+d),(k)}$). The parameter ζ should be very small to avoid too much intervention to the model configuration and a value of 0.05 is used for all the analyses presented in this thesis. Figures 3.5c and 3.5d show the potential positions the margin node will be located when a 'jump' operation is performed.

Once the margin node is forced to 'jump' to another segment, remeshing should be performed to generate the new mesh. It should be noted that this operation is performed to pass to OxLim the information that a new rigid body segment will be involved in the next increment; and it does not necessarily force the margin node to move along this segment.

3.3.2.4 Inter-penetration of material into the rigid body

The upper bound results provide the velocity field rather than the displacement field of the deforming domain, and the time step chosen to update the nodal coordinates is not an infinitely small value. As a consequence, it is possible that some nodes on the free surface(s) near the rigid body might encroach into it after their coordinates have been updated.

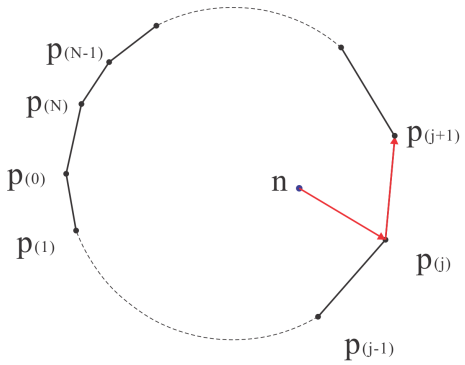

Figure 3.6 Determining encroachment of a node within a rigid body

To check whether an arbitrary node n is within the rigid domain, all N vertices of the rigid body are first sorted in counterclockwise order, as illustrated in Figure 3.6. After that, a vector $\overrightarrow{v_j}$ corresponding to an arbitrary pair of vertices, p_j and p_{j+1}, of the rigid body is generated by

$$\overrightarrow{v_j} = \overrightarrow{np_j} \times \overrightarrow{p_j p_{j+1}} \tag{3.7}$$

where the definition of the vectors $\overrightarrow{np_j}$ and $\overrightarrow{p_j p_{j+1}}$ is shown in Figure 3.6. In this equation, $j+1$ should be replaced by 0 when $j = N$. Node n is determined to be within the rigid domain if the following equation is fulfilled for all the values of j:

$$\frac{\overrightarrow{v_j}}{\|\overrightarrow{v_j}\|} > 0, j = 1,2,....N \tag{3.8}$$

This method is only valid when the rigid body is a convex shape, and a new strategy should be developed otherwise (e.g. for a spudcan foundation), which is beyond the scope of this thesis. The nodes on the free surface should be checked consecutively according to Equations 3.7 and 3.8 to see if they are within the rigid body domain. The searching order is from the node next to the margin node working outwards as shown in Figure 3.7a. Of all the nodes within the rigid body, the one at the end of the search is recognised as $n_{(e)}$. The nodes between $n_{(1)}$ and $n_{(e)}$ are forced to attach perpendicularly to the nearest rigid body segments. Additional contact is thus enforced and node $n_{(e)}$ will be taken as the new margin node (see Figure 3.7b).

The operation described above will introduce some minor change to the total volume of the deforming material. In practice, a small time step should be chosen to mitigate this effect. Taking the penetration of a pipe segment with diameter D into soil for example, in

this thesis the limiting time step is typically set as $0.002D/v_p$, where v_p is the penetrating velocity of the pipe.

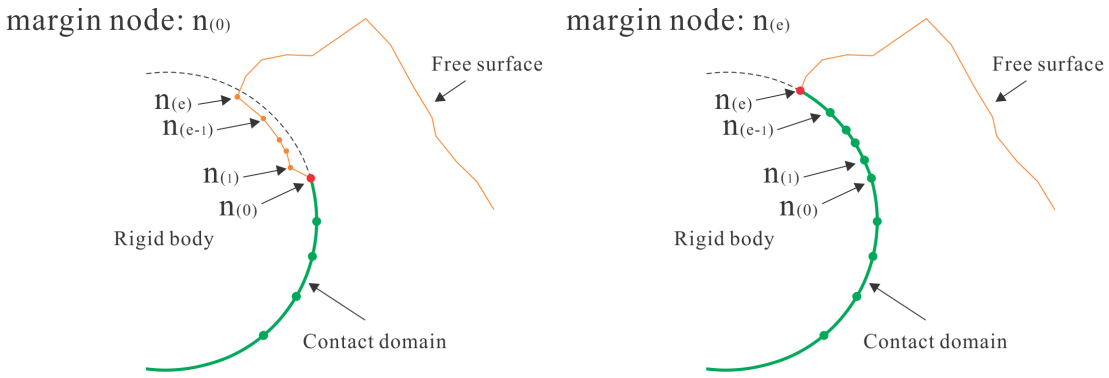

(a) Before treatment (b) After treatment

Figure 3.7 Treatment of nodes that penetrate into a rigid body

3.3.2.5 Self-contact behaviour of a free surface

After the coordinates of all the nodes of the model have been updated by a chosen time increment, it is possible that some nodes and segments on a free surface might penetrate into the free surface boundary formed by other nodes and segments of the surface, as illustrated in Figure 3.8a. This is the self-contact behaviour of a free surface, which is very typical in the modelling of lateral movement of a pipeline. If this happens, some nodes on the free surface should be removed to yield a new surface, which is conducted as follows.

A free surface in SLA modelling comprises a list of nodes and a list of segments, both of which are sorted in a consecutive order from the rigid body to the domain boundary. Each node or segment has an index, i, representing its position in the corresponding list. For an arbitrary segment $S_{(i)}$, its two nodes are denoted by $n_{(i)}$ and $n_{(i+1)}$.

One segment is chosen at a time, denoted by $S_{(p)}$ here, and all the segments before it ($S_{(0)}$ to $S_{(p-1)}$) are checked one by one to find a segment that intersects with $S_{(p)}$. Two arbitrary segments are found to intersect with each other only when the intersection point is within both segments rather than on the extension line of either. If several segments are found to intersect with $S_{(p)}$ (with nodes $n_{(p)}$ and $n_{(p+1)}$), the one with the smallest index number is recognised, which is denoted by $S_{(q)}$ (with nodes $n_{(q)}$ and $n_{(q+1)}$) here. A new node denoted by n_s is then generated at the intersection point, as illustrated in Figure 3.8a.

After that, all the nodes between $n_{(q)}$ and $n_{(p+1)}$ are removed from the node list while the node n_s is inserted in the node list after $n_{(q)}$. Based on the new node list of the surface, which is still in consecutive order, a new segment list is then generated and the new surface is as shown in Figure 3.8b. Successive similar operations are performed based on this new surface.

The operation described above is repeatedly processed from $p = 1$ to $p = L$, where L is the length of the segment list (which might keep reducing during the process). At the end of this operation, it can finally be guaranteed that any two arbitrary segments belonging to the free surface do not intersect with each other.

The approach introduced here can effectively deal with the self-contact behaviour of a free surface. Remeshing of the model is needed once self-contact takes place. Since no stress update or stress mapping is needed in SLA modelling, the operation of removing some nodes and segments from the old model does not introduce any numerical instability. However, it could result in minor volume loss in the material, which is represented by the area embraced by the dashed lines in Figure 3.8b. This effect is inevitable in SLA modelling but can be mitigated by adopting a small time step Δt to update the model.

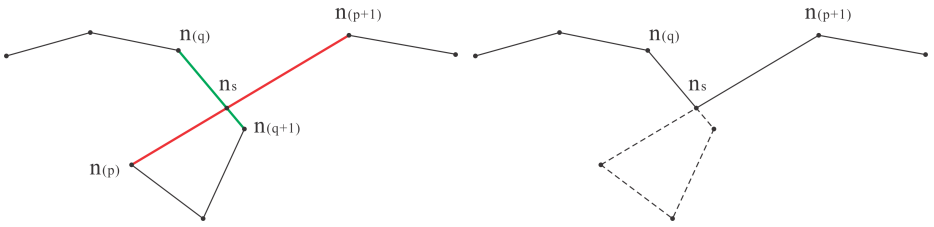

(a) Before node removal (b) After node removal

Figure 3.8 Removal of nodes when self-contact of a free surface takes place

3.3.2.6 Contact between two free surfaces

At very deep embedment of a rigid body, free surfaces at the two sides may come into contact. In SLA modelling, the nodes of the two surfaces will penetrate into each other, as illustrated in Figure 3.9a. Once the code detects that the segments of the two surfaces have intersections, all the nodes between these two critical intersection points are removed from the node lists belonging to the free surfaces. If more than two intersections are detected,

those with the lowest and highest vertical positions are chosen as critical intersection points. Two new nodes are then generated at the position of the two critical intersections, as shown in Figure 3.9a. New surfaces are constructed out of the nodes remaining in the node lists belonging to the free surfaces, and the two new generated nodes (Figure 3.9b).

After the operation described above has been completed, the simulation is continued with an inner free surface and an outer free surface. With further deformation, self-contact of the outer surface is likely, and the approach to deal with such behaviour has been discussed in Section 3.3.2.5. The area embraced by the inner surface and the rigid body boundary denotes a void in the simulation domain. This void is automatically eliminated once its area is found to be smaller than $5 \times 10^{-4} D^2$, where D is the characteristic size of the rigid body (e.g. diameter of a pipe). As a result, the rigid body is totally buried and the model is subsequently processed with only one free surface.

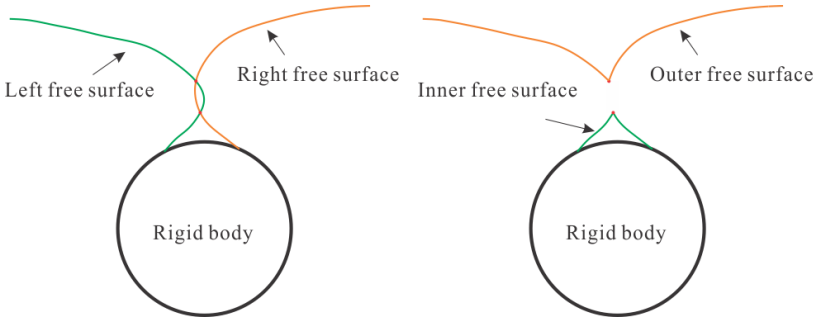

(a) Surfaces come into contact (b) New surfaces generated

Figure 3.9 Contact of two free surfaces

In problems where symmetry is exploited, the free surface will come into 'contact' with the symmetry line instead of another surface, as shown in Figure 3.10a. For all the intersections between the free surface and the symmetry line, those with the lowest and highest vertical position are chosen to be critical intersection points. Two intersection nodes are generated at the positions of these points. An inner free surface and an outer free surface are then constructed (Figure 3.10b). After remeshing, the nodes on the free surfaces are assigned free boundary conditions, while these on the symmetry line are assigned symmetry boundary conditions. With continuing sequential analysis, the inner and outer surfaces might again 'contact' the symmetry line, and this will be handled in the same way as described above. The void formed by the inner free surface and the rigid

body boundary is deemed to be filled once its area becomes smaller than $2.5 \times 10^{-4} D^2$, and the inner surface is then removed from the model.

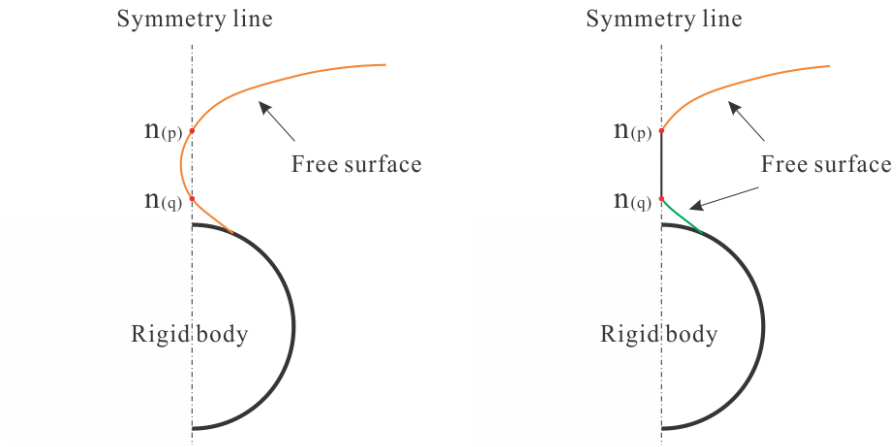

(a) Surface touches the symmetry line (b) New surface generated

Figure 3.10 Contact of a free surface and symmetry line

3.3.3 Update of material properties

During the SLA simulation, material properties have to be updated for each increment after the update of the model configuration. The history variables carrying necessary information to determine the strength properties of a particular material point are stored on the nodes of the triangular elements. Since a number of remeshing processes are performed during the analysis to avoid distortion of elements, second order triangular elements are used for the sake of reliable interpolation of field variables.

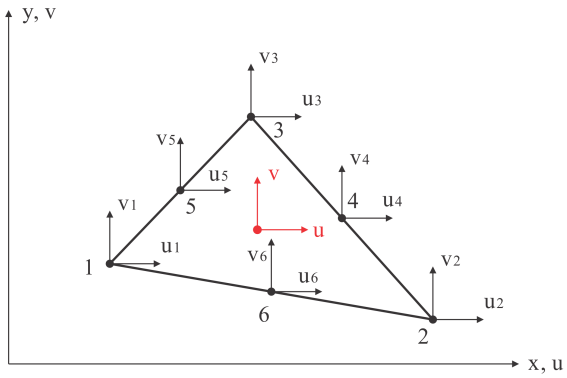

Figure 3.11 Velocity of the nodes of a linear strain element

3.3.3.1 Calculation of strain rate in linear strain element

The distribution of strain rate across the element can be directly evaluated from the velocities of its evaluation points as illustrated in Figure 3.11. For the determination of strain rate of an arbitrary point within the element, the velocity $[u,v]$ of this point is calculated first, where

$$\begin{aligned} u &= Ma \\ v &= Mb \end{aligned} \tag{3.9}$$

in which $M=[1,x,y,x^2,xy,y^2]$, $a=[a_1,a_2,a_3,a_4,a_5,a_6]$ and $b=[b_1,b_2,b_3,b_4,b_5,b_6]$. The coefficients x and y in M are the coordinates of the point. The vector a can be determined by substituting the horizontal velocities of the six nodal points into the equation and solving $a=X^{-1}\bar{u}$, where $\bar{u}=[u_1,u_2,u_3,u_4,u_5,u_6]^T$ and

$$X=\begin{bmatrix} 1 & x_1 & y_1 & {x_1}^2 & x_1y_1 & {y_1}^2 \\ 1 & x_2 & y_2 & {x_2}^2 & x_2y_2 & {y_2}^2 \\ 1 & x_3 & y_3 & {x_3}^2 & x_3y_3 & {y_3}^2 \\ 1 & x_4 & y_4 & {x_4}^2 & x_4y_4 & {y_4}^2 \\ 1 & x_5 & y_5 & {x_5}^2 & x_5y_5 & {y_5}^2 \\ 1 & x_6 & y_6 & {x_6}^2 & x_6y_6 & {y_6}^2 \end{bmatrix} \tag{3.10}$$

Similarly, b can be expressed as $b=X^{-1}\bar{v}$, where $\bar{v}=[v_1,v_2,v_3,v_4,v_5,v_6]^T$. Finally the two velocity components of the point can be expressed by

$$\begin{aligned} u &= MX^{-1}\bar{u} \\ v &= MX^{-1}\bar{v} \end{aligned} \tag{3.11}$$

The plastic strain rate over the triangle element can be expressed as

$$\dot{\varepsilon}^p=[\dot{\varepsilon}_x^p,\dot{\varepsilon}_y^p,\dot{\gamma}_{xy}^p]^T=[\frac{\partial u}{\partial x},\frac{\partial v}{\partial y},\frac{\partial u}{\partial y}+\frac{\partial v}{\partial x}] \tag{3.12}$$

where

$$\begin{aligned}\frac{\partial u}{\partial x} &= \frac{\partial M}{\partial x}X^{-1}\bar{u}\\ \frac{\partial v}{\partial y} &= \frac{\partial M}{\partial y}X^{-1}\bar{v}\\ \frac{\partial u}{\partial y} &= \frac{\partial M}{\partial y}X^{-1}\bar{u}\\ \frac{\partial v}{\partial x} &= \frac{\partial M}{\partial x}X^{-1}\bar{v}\end{aligned} \tag{3.13}$$

3.3.3.2 Update of plastic shear strain ξ of a node

In the SLA model using second order elements, the plastic strain rates calculated from the upper bound velocity field are discontinuous between elements, and the values at the common edges or points are not unique. Considering this feature, the plastic strain rates at a node are summed using an inverse distance weighting function according to the Inverse Distance Algorithm (IDA) method, as

$$\dot{\varepsilon}^p = \frac{\sum \dot{\varepsilon}^{p,i} w_r}{\sum w_r} \tag{3.14}$$

in which $\dot{\varepsilon}^{p,i}$ is the plastic strain rate at the centre of the ith element connected to this node and w_r is a weighting function defined as

$$w_r = d^{-e} \tag{3.15}$$

where d is the distance between points and e is an exponent usually taken in the range of 2 to 4. A value of 3.5 was recommended by TECPLOT (1992). After the model configuration has been updated by the time step Δt, the plastic shear strain of a node is updated by

$$\xi_{(t+\Delta t)} = \xi_{(t)} + (\dot{\varepsilon}_1^p - \dot{\varepsilon}_3^p)\Delta t \tag{3.16}$$

where $\dot{\varepsilon}_1^p$ and $\dot{\varepsilon}_3^p$ are the major and minor principal plastic strains respectively.

3.3.3.3 Determination of material strength

During the simulation, the operative strength at a node is modified to account for degradation due to strain softening and enhancement due to high strain rate, according to the

strength defined by Equation 2.9 (Einav and Randolph, 2005). In this equation, the parameters δ_{rem}, ξ_{95}, μ and $\dot{\gamma}_{ref}$ are related to soil properties and no update is needed. The parameters s_{u0} and ξ denote the initial shear strength and accumulated plastic shear strain respectively at the node and serve as history variables. Interpolations are conducted to obtain their values if remeshing is performed, as will be discussed in Section 3.3.4. $\dot{\gamma}_{max}$ is the maximum shear strain rate at the node, which is obtained based on the results of the last increment. Strictly speaking, $\dot{\gamma}_{max}$ should be the maximum shear strain rate from the current increment, rather than the one previous to it. However, it is reasonable to assume that the deforming patterns between any two consecutive analyses are extremely close to each other since the incremental time step is very small. The RITSS approach (Hu and Randolph, 1998; Wang *et al.*, 2009; Chatterjee *et al.*, 2012a) uses a similar strategy to obtain the value of $\dot{\gamma}_{max}$.

The values of shear strength corresponding to all the nodes of the model are calculated first. After that, the shear strength of each triangular element is determined by its three vertex nodes. The information carried by the mid-side nodes of the elements is only used for interpolation of field variables but not for determining the shear strength of the elements because a quadratic distribution of strength within an element is not supported in OxLim. The strength variation within an element can be expressed as $s_u = a + bx + cy$, where the constants a, b and c can be determined by substituting the shear strength corresponding to the three vertex nodes of the element into the above equation and solving

$$\begin{bmatrix} a \\ b \\ c \end{bmatrix} = \begin{bmatrix} 1 & x_1 & y_1 \\ 1 & x_2 & y_2 \\ 1 & x_3 & y_3 \end{bmatrix}^{-1} \begin{bmatrix} s_{u1} \\ s_{u2} \\ s_{u3} \end{bmatrix} \tag{3.17}$$

in which s_{ui} denotes the shear strength corresponding to the ith vertex of the element calculated by Equation 2.9.

3.3.4 Remeshing and interpolation of field variables

Apart from the situations discussed before, such as 'jump' of a margin node, breakaway of interface nodes from the rigid body, and interpenetration of material nodes into the rigid body, another criterion to perform remeshing of the model is based on the aspect ratios of elements. After the model configuration has been updated in each increment, all the elements are checked to see if any has an angle smaller than 20°. If so, remeshing is required to avoid excessive mesh distortion in the next increment.

Theoretically the model at the beginning of the $(n+1)$th increment has the same configuration as that at the end of the nth increment. Thus the new meshed domain and the old one overlap and they are referred to hereafter as the target plane and reference plane regarding interpolation of field variables. In the mapping step, all the nodes of the target plane should be located in the elements of the reference plane and then field variables are interpolated quadratically from the reference elements to the target nodes.

3.3.4.1 Determination of the position of a node

This section describes how to determine if a particular new node can be located inside a particular triangular element. Horizontal and vertical boundaries are drawn to pass through the extreme top and bottom points and the extreme left and right points of the triangle as illustrated in Figure 3.12. If the new node cannot be located between these boundary lines, it is recognized as outside the triangle and the check process will be terminated. Otherwise, three sub-triangles are generated (see Figure 3.12).

The order of the nodes belonging to the original triangle *ABC* is sorted counterclockwise. The nodes for the sub-triangle, *GAB*, *GBC* and *GCA* are then checked to see if they are also in counterclockwise order. If all the sub-triangles have nodes in counterclockwise order, node *G* is found to be inside the triangle (see Figure 3.12a). On the contrary, if a clockwise order is found, the check is terminated and the node is determined to be outside the triangle *ABC*. Taking the triangles in Figure 3.12b for example, triangle *GAB* is counterclockwise and the cross product of vectors $\overrightarrow{AB}$ and $\overrightarrow{BG}$ is a vector in the direction of z (x is the horizontal direction and y is the vertical direction in the figure). Triangle *GBC*

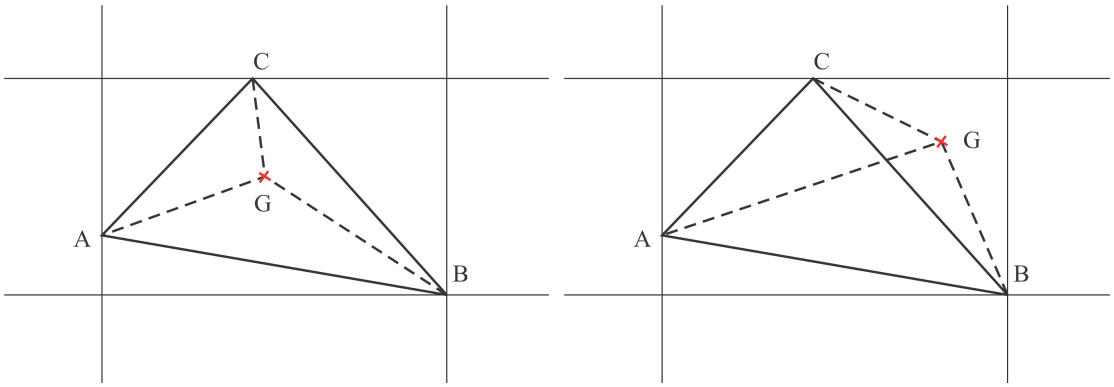

(a) Inside (b) Outside

Figure 3.12 Determining if a node is inside a triangle

is clockwise so the cross product of $\overrightarrow{GB}$ and $\overrightarrow{BC}$ is a vector in the opposite direction to z and the check is terminated immediately.

3.3.4.2 Interpolation of the whole domain

Typically the SLA simulations in this thesis involve 5000-10000 elements and significant time is needed to map field variables from the reference plane to the target plane, most of which is used to locate the nodes in the elements. To improve the computing efficiency, the whole domain is divided into a few auxiliary grids, after which the old elements as well as the new nodes are located in these grids. If a node is inside a grid or just on the boundary line of it, this node is added to the node list of the grid. If at least one vertex of an element is found to be inside a grid, the element will be added to the element list of the grid.

Once all the old elements and new nodes have been added to the element and node lists of the grids, the searching process is performed for each grid. One node is chosen at a time, and the search is continued until the element enclosing this node has been found. Then field variables are mapped quadratically from the six nodes of the old element to the new node. This strategy significantly reduces the computational cost for interpolation and typically it only takes around 10 seconds to perform the whole mapping process with both the reference and target plane having about 6000 elements. Without the auxiliary grids, the same interpolation process could be nearly 1 minute.

3.3.4.3 Adaptive meshing strategy

A simple but useful mesh generation strategy is adopted in SLA simulation. At the remeshing step, Triangle (Shewchuk, 2002) is called to generate a relatively coarse mesh at first, which will be further refined based on the distribution of plastic strains over the domain and an estimation of the areas that may experience intense shearing in the next increment.

It is reasonable to assume that the deformation pattern at the nth (current) increment, referred to as $\Omega_{(n)}$ hereafter, is similar to that at $\Omega_{(n-1)}$ because the time step between two consecutive increments is very small, even though it is much larger than that in FE modelling using the CEL method, for example. The attributes, plastic shear strain ξ and maximum shear strain rate $\dot{\gamma}_{max}$, of the old mesh at $\Omega_{(n-1)}$, denoted by $RM_{(n-1)}$ here, are mapped to the temporary coarse mesh at Ω_n, denoted by $CM_{(n)}$, following the steps described in Section 3.3.4.

To ensure that the region of mesh refinement is big enough to embrace the regions with intense shearing and severe softening, these attributes at analysis $\Omega_{(n-2)}$ are also mapped to $CM_{(n)}$. Although the reference plane of $\Omega_{(n-2)}$, denoted by $RM_{(n-2)}$ here, does not necessarily overlap the target plane of $\Omega_{(n)}$, it still provides useful information for most of the nodes in $CM_{(n)}$. For a particular variable, the larger value of that obtained from $\Omega_{(n-2)}$ and $\Omega_{(n-1)}$ is chosen. These attributes estimated for each node in $CM_{(n)}$ do not have to be extremely accurate since they will only provide information to refine the coarse mesh $CM_{(n)}$ rather than update the material properties.

After the mapping of these variables, each triangular region (element) in $CM_{(n)}$ can have its attributes set by

$$\phi_{est} = \max(\phi_1, \phi_2, \phi_3) \tag{3.18}$$

where ϕ_{est} are the estimated attributes (ξ and $\dot{\gamma}_{max}$) of a triangle, and ϕ_1, ϕ_2 and ϕ_3 are the estimated attributes at its vertices. The maximum target element area within a triangular region of $CM_{(n)}$ is then calculated by $A_{max} = f(\xi, \dot{\gamma}_{max})$.

The expression of the function used to obtain A_{max} varies with specific problems to be investigated. Here an example expression currently used in this thesis is introduced, which

is established based on a large number of preliminary analyses. The softening factor for the material strength is calculated first according to

$$f_{soften} = \delta_{rem} + (1 - \delta_{rem}) e^{-3\xi/\xi_{95}} \tag{3.19}$$

Details of this equation can be found in Section 2.2.2.2. If ξ is found to be larger than 0.05 or f_{soften} is smaller than 0.9, the maximum mesh area of this region is set as $A_1 = 0.01D^2$, where D is the characteristic size of the rigid body (e.g. diameter of a cylinder). This is set to ensure the accuracy of interpolation of field variables in the area with softening.

Concerning the shearing deformation that might take place at $\Omega_{(n)}$, the constraining area limited by the maximum shear strain rate is expressed as

$$A_2 = A_{min} \cdot \frac{\dot{\gamma}_{max,max}}{\max(\dot{\gamma}_{max}, 0.1)} \tag{3.20}$$

in which $\dot{\gamma}_{max,max}$ is the maximum value of $\dot{\gamma}_{max}$ for all the triangle regions in $CM_{(n)}$ and A_{min} is a minimum target element area set by the user. A typical value of $5 \times 10^{-4} D^2$ is adopted for A_{min} in most of the simulations presented in this thesis if not stated otherwise. The smaller value of A_1 and A_2 is adopted as A_{max} for the triangular region, based on which the Triangle software will refine this region. After the coarse mesh $CM_{(n)}$ has been refined to generate $RM_{(n)}$, field variables are mapped from $RM_{(n-1)}$ to $RM_{(n)}$ following the steps described in Section 3.3.4.

Martin (2011) uses a more reasonable approach, but without considering the necessity of mapping field variables, to refine the mesh in standard FELA. The objective of refining the mesh is to equalise $\int \dot{\gamma}_{max} dA$ throughout the whole domain, where $\dot{\gamma}_{max}$ is the maximum shear strain rate in a given element and is obtained from results calculated using a relatively coarse mesh of the model. By performing several iterations, a final mesh is generated to yield satisfactory results. This strategy can also be used in SLA modelling. However, the additional computational cost related to interpolation of field variables could be enormous since remeshing would need to be performed several times for each increment; therefore the pragmatic strategy introduced in this section is used instead. As a compensation, the minimum target element size A_{min} adopted in SLA modelling is excessively small, and

even the areas with small degrees of shearing ($\dot{\gamma}_{max}$) or softening (ε) are refined with fine meshes.

3.3.5 Dealing with numerical disturbance

In an SLA simulation, two factors might introduce numerical disturbance to the model. One is the update of model configuration, using explicit integration of the velocity field over a finite time step Δt. Another is the computing error generated in the remeshing and interpolation process. Such disturbances result in minor fluctuations in the calculated collapse load throughout the simulation. Moreover, they may even introduce numerical instability to the model which consequently means that the simulation cannot proceed.

For instance, in modelling the lateral movement of a pipe at the residual stage, the vertical dead load on the pipe is very close to the vertical bearing capacity. After remeshing and interpolation has been performed, it is possible that the vertical bearing capacity of the new model is lower than the dead load exerted on the pipe, which means that the model collapses under this load. Although OxLim can still do the calculation, the nodal velocities obtained from it are too large (e.g. $10^6 D$/s) and unreliable to update the model configuration. In this scenario, the pipe is temporarily in the current increment forced to penetrate into the soil at a downward velocity of $0.2v_p$, where v_p is the horizontal velocity.

During SLA modelling, collapse of the model is detected when the nodal velocities obtained from the upper bound results are unrealistically large ($10^6 D$/s). Apart from the over-loading phenomenon described above, another two matters related to slope stability may also cause collapse, namely an ill-shaped gap and steep slope above the crown of the rigid body. Once the code detects a collapse, it will try to handle it by forcing the rigid body to penetrate as described above. If collapse cannot be solved in this manner, the code will try to deal with the ill-shaped gap and then the steep slope, as will be discussed in Section 3.3.5.1 and Section 3.3.5.2.

3.3.5.1 An ill-shaped gap

When extremely large deformation takes place, a gap as illustrated in Figure 3.13 might be formed, with a risk that the soil above it might collapse due to slope instability. Although collapse of the soil does not necessarily happen when such a gap is generated during the simulation, it is necessary to develop a strategy to deal with it.

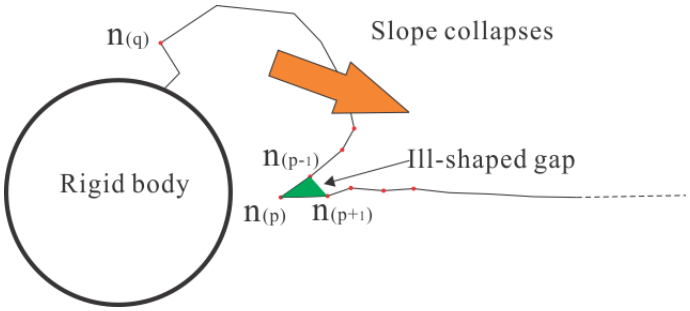

Figure 3.13 An ill-shaped gap that might introduce slope instability

Once the code detects a collapse of the model which might be caused by a 'gap', it begins to search for a critical node on the free surface. The criterion to determine such a node $n_{(p)}$ is that its horizontal position should be more close to the rigid body centre than the two nodes, $n_{(p-1)}$ and $n_{(p+1)}$, next to it. The index p denotes that the node is the pth node in the node list belonging to the surface. Apart from the basic criterion, the vertical coordinate of such a node should be lower than the centre of the rigid body. Otherwise, the node $n_{(q)}$ in Figure 3.13 will be mistakenly found to form a 'gap'. It should be noted that the method to search for $n_{(p)}$ introduced here is not theoretically robust or general, but very effective in the problems studied in this thesis. For other more complicated problems, new strategies should be developed.

When the critical node $n_{(p)}$ is found, it is removed from the node list of the surface and the surface is reconstructed. A new model is then generated for analysis. This process is repeated as necessary until the slope collapse problem has been solved or a new node that meets the criterion discussed above cannot be found.

3.3.5.2 Steep slope above the crown of rigid body

If a rigid body penetrates to a deep depth, a steep slope is formed above its crown, as illustrated in Figure 3.14. The slope tends to collapse if the region where the slip surface is most likely to take place is weakened due to the interpolation of field variables or the update of the model configuration. To handle this issue, an auxiliary domain slightly larger than the rigid body but of exactly the same shape is established and then all the nodes on the free surface are checked in consecutive order to see if they are located within this domain. If such a node is found (see $n_{(p-2)}$, $n_{(p-1)}$ and $n_{(p)}$ in Figure 3.14), it is projected perpendicularly onto the nearest rigid body segment, in order to restore the slope stability. Of all these nodes that meet the criterion, the one with the largest index number ($n_{(p)}$) is recognised as the new margin node. After that the surface is reconstructed and a new model is generated for another analysis.

Iterations are needed to handle this issue. The auxiliary domain starts from a size of $1.005D$, where D is the reference size of the rigid body (e.g. diameter of a pipe), and increases at an interval of $0.005D$ at each iteration. The iteration is terminated when the slope instability has been solved or the auxiliary domain reaches a size of $1.05D$. In some extreme cases such as deep penetration of a pipe into very soft soil ($S_t \geq 20$, $\xi_{95} = 10$), a satisfactory solution cannot be found and the analysis is terminated.

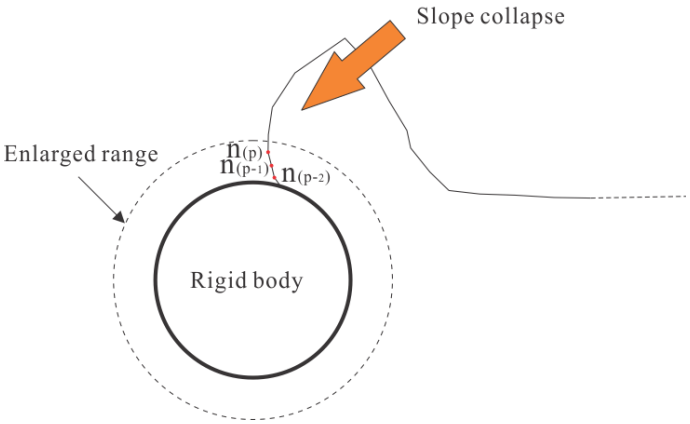

Figure 3.14 Steep slope above the crown of a rigid body

3.4 Complementary tool: CEL method

This section describes a CEL analysis method in-built in the Abaqus/Explicit FE program (Dassault Systémes, 2011), which is nowadays commonly accepted as a powerful tool for solving problems involving large plastic deformations (e.g. Abadalla *et al.*, 2009; Andresen and Khoa, 2013; Hawlader *et al.*, 2015). It will be used to compare with the newly developed SLA method to reveal the ability of SLA in handling the updating of model geometry as well as the material behaviour. To take into account the strength degradation and enhancement behaviour of the undrained clay material, a VUMAT material behaviour subroutine based on the Tresca yield criterion was developed to work in conjunction with the CEL method.

3.4.1 Explicit analysis in FE modelling

The solutions presented in this chapter are generated by explicit FE analysis using Abaqus (Dassault Systémes, 2011). Numerical methods for the solution of time-varying differential equations are generally implicit or explicit. In both methods the state of a model, $\Phi_{(t+\Delta t)}$, at time $t+\Delta t$ is determined from that at time t. An explicit method can be expressed as

$$\Phi_{(t+\Delta t)} = F(\Phi_{(t)}) \tag{3.21}$$

while an implicit method is expressed as

$$G(\Phi_{(t+\Delta t)}, \Phi_{(t)}) = 0 \tag{3.22}$$

From Equations 3.21 and 3.22 it can be seen that an explicit algorithm obtains quantities at $t+\Delta t$ using only the available values at time t while an implicit algorithm calculates these quantities based not only on the values at t, but also on these same quantities at $t+\Delta t$. Generally, for a single increment in implicit analysis, nonlinear equations must be solved and thus iterations are involved, which increases the computational cost. This can be avoided in an explicit analysis. However, the time steps Δt in an explicit analysis must be kept sufficiently small to ensure numerical stability. The optimum choice of solution strategy depends on the particular problem to be analysed.

In an explicit analysis of a dynamic problem in solid mechanics, the equations of motion of the body are integrated using the explicit central difference integration rule, expressed as

$$\dot{u}^{(i+\frac{1}{2})} = \dot{u}^{(i-\frac{1}{2})} + \frac{\Delta t^{(i+1)} + \Delta t^{(i)}}{2} \ddot{u}^{(i)} \tag{3.23}$$

$$u^{(i+1)} = u^{(i)} + \Delta t^{(i+1)} \dot{u}^{(i+\frac{1}{2})} \tag{3.24}$$

in which $\dot{u}$ is velocity and $\ddot{u}$ is acceleration. The superscript (i) refers to the increment number and $(i \pm \frac{1}{2})$ refers to midincrement values. According to Equations 3.23 and 3.24, the kinematic state can be updated using known values of of $\dot{u}^{(i-\frac{1}{2})}$ and $\ddot{u}^{(i)}$ from the previous increment. It can be seen that the integration operator is explicit and the state of the current increment can be advanced using known values from the previous increment.

For a dynamic problem, the acceleration at the beginning of an increment can be calculated by

$$\ddot{u}^{(i)} = M^{-1} \cdot (F^{(i)} - I^{(i)}) \tag{3.25}$$

where M is the mass matrix, F is the applied load vector and I is the internal force vector. The key to the computational efficiency of the explicit analysis is the use of diagonal element mass matrices, which makes the inversion of the mass matrix in Equation 3.25 trivial. Now it can be seen that each individual time increment in the explicit method is computationally inexpensive because the only matrix to be inverted is diagonal and this needs be done only once per increment.

The explicit method analyses a process by using many small time increments, and a conservative estimate of the stable time increment is determined by the Courant-Friedrichs-Lewy (CFL) condition (Courant *et al.*, 1967), expressed as

$$\Delta t \leq \Delta t_{cr} = \min(\frac{L_e}{c_d}) \tag{3.26}$$

where L_e is the characteristic element dimension and c_d is the current dilatational wave speed of the material, which can be calculated as

$$c_d = \sqrt{\frac{(\lambda + 2\mu)}{\rho}} \tag{3.27}$$

in which λ and μ are the first and second Lamé constants of the material and ρ is the density. Equation 3.26 indicates that refining the mesh of the model will have the most significant influence on the computational efficiency of an explicit analysis.

3.4.2 Large deformation modelling using CEL

3.4.2.1 Eulerian and Lagrangian approaches

In finite element formulations based on traditional continuum mechanics, two alternatives are usually used to describe the movement of a small volumetric element as a function of time, namely the Lagrangian and Eulerian frames (Figure 3.15). In a Lagrangian framework, the mesh is attached to the material and they move together throughout the entire computational process. The interface between two parts can be accurately tracked. This is the traditional approach used in conventional small strain finite element analysis. An obvious advantage of the Lagrangian formulation is that the history of field variables at a material point can be easily tracked. The main disadvantage is that the mesh deforms with the material and thus the accuracy of the solution can be severely affected when the mesh becomes heavily distorted. Moreover, in explicit analysis, the time increment controlled by the smallest element dimension can become extremely small and this leads to inefficiency for the time marching. On the contrary, in an Eulerian framework, the mesh is fixed in space and does not change with time, while the material can flow freely across element boundaries. Therefore, large deformations of the material do not cause any deformation to the mesh and distortion of the mesh can be avoided. However, the history of field variables at each moving material point becomes difficult to track, and to map these variables is computationally expensive. This approach is commonly used in fluid mechanics.

Due to the different but complementary features of these two frameworks, various techniques have been developed to combine them so as to strengthen their advantages while avoiding their disadvantages. This has led to the development of two categories of work that apply both the Lagrangian and Eulerian formulation: Arbitrary Lagrangian-Eulerian (ALE) and Coupled Eulerian-Lagrangian (CEL), both of which are available in Abaqus.

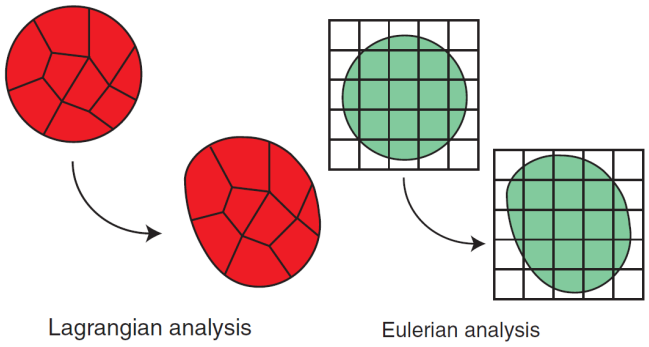

Figure 3.15 Deformation of a continuum in a Lagrangian analysis and an Eulerian analysis (Grabe *et al.*, 2013)

It is worth mentioning that the ALE method does not change the topology of the model and thus additional elements or boundary surfaces cannot be generated during the analysis, making it less powerful when extremely large plastic deformation takes place. A more practical method, the RITSS method of Hu and Randolph (1998) that was discussed in Section 2.2.2.2, can also be categorized as an ALE approach, but is not available in Abaqus. In this chapter, the application of CEL to solve large deformation problems involving rigid objects and undrained soil will be explored.

3.4.2.2 CEL analysis in Abaqus

CEL analysis is conducted by applying a 'Lagrange-plus-remapping' approach. A traditional Lagrangian phase is performed at first in each time increment, with the Eulerian elements temporarily fixed relative to the material, meaning that the Eulerian elements can temporarily 'deform' in this phase. To prevent unacceptable element distortions during the Lagrangian phase, the time step has to be sufficiently small. After that, in the Eulerian phase, all elements are checked to see if significant deformation has taken place. Those elements with large deformation are automatically remapped and the material flow through these elements is calculated accordingly. The movement of the material across the mesh is tracked by calculating its Eulerian Volume Fraction (EVF), representing the portion of an element filled with a material. The EVF is 1 if an Eulerian element is completely filled with a material and 0 if the element is void. Within each time increment, the boundary surfaces of the Eulerian material are reconstructed based on the EVF. The interface re-

construction algorithm in CEL approximates the material boundaries within an Eulerian mesh as simple planar facets. This generates a material surface that can be discontinuous between neighboring elements with EVF < 1. Fine mesh resolution is thus required in Eulerian analyses involving interfaces or boundary surfaces that are expected to undergo large deformations.

CEL analysis models interaction between Lagrangian elements and Eulerian material by using a general contact formulation based on a penalty method. A Lagrangian body can move through the Eulerian mesh without resistance until it encounters an Eulerian element filled with material (EVF $\neq 0$). The algorithm is less strict compared to the kinematic contact method used in pure Lagrangian analysis. Therefore, interpenetration of Eulerian material through the Lagrangian contact surface may happen, but it is limited to an area equal to the local Eulerian mesh size. The interpenetration can be minimized by refining the Eulerian mesh, which, however, will considerably increase the computational cost.

The application of the CEL method to large deformation problems has recently become quite common among researchers. Currently, CEL analysis in Abaqus must be performed in 3D, so a one-element thick mesh is usually used to approximate the plane-strain condition. Here a brief review of the application of CEL to solve large deformation problems in geotechnical engineering is given. This review is by no means exhaustive and only works directly related to the current study are discussed.

Abadalla *et al.* (2009) established a three-dimensional (3D) FE model using the CEL approach in Abaqus to predict the influence of iceberg scour on a pipe buried below the seabed. A systematic validation effort was carried out and the numerical results were found to overestimate the horizontal soil displacements compared to centrifuge results.

Qiu and Grabe (2011) incorporated a visco-hypoplastic constitutive model into Abaqus via subroutine VUMAT to study soil-structure interaction in clayey soil, investigating a strip footing problem. This CEL model in conjunction with the VUMAT was further extended to model the installation process of spudcan foundations in Qiu and Grabe (2012).

Dutta *et al.* (2012) used the CEL method to perform a validation study against the centrifuge data reported by Dingle *et al.* (2008). The soil was modelled as an elastic-

perfectly plastic material. Reasonable agreement between the numerical and centrifuge results was found. This model was further improved, together with a simplified version of the constitutive model in Equation 2.9, to model the dynamic embedment of a pipe (Dutta and Phillips, 2013). The numerical results were compared with the centrifuge data reported by Cheuk *et al.* (2008) and good agreement was observed. However, the means by which the constitutive model was incorporated into the CEL analysis was not discussed in this paper.

Andresen and Khoa (2013) conducted a numerical study into the installation of offshore anchor piles. Both ALE and CEL methods were employed for this problem, and the CEL method was found to be the most promising of the two. The CEL model was then used to model the penetration of a spudcan foundation and good agreement was obtained in terms of penetration resistance as well as the failure mechanism observed in a centrifuge test. The soil model used in this paper was ideal Tresca material.

Grabe *et al.* (2013) studied screwed pile installation and the deep vibration compaction process using CEL in Abaqus. A hypoplastic constitutive model was successfully implemented for this work.

Tho *et al.* (2013) investigated the vertical loading response of a spudcan foundation subject to extremely large displacement using CEL in the FE software LS-DYNA, where the backfilling of soil was successfully modelled. In this paper, validation study results against experimental data were also reported and very satisfactory agreement was found.

Hawlader *et al.* (2015) studied the deep penetration behaviour of a steel catenary riser to a very large depth of $5D$. The extreme deformation of soil caused by the pipe penetration was found to be handled satisfactorily by the CEL model.

3.4.3 Implementation of constitutive model

3.4.3.1 General stress return strategy

The integration of the equations that describe material behaviour is vital to an FE analysis. In this study, the radial return mapping method, first proposed by Wilkins (1964) and Maenchen and Sack (1964) for use with the von Mises yield criterion, was adopted. The

idea can be expressed as follows: the stress is first updated assuming the material is still elastic. If the elastic trial stress lies outside the yield surface, this stress will be projected onto the closest point on the yield surface. This stress return ensures that the updated stress does not violate the yield condition, and also ensures that the separation of strain increment into elastic and plastic parts is consistent with the final stress state. The scheme is illustrated in Figure 3.16, where f is the yield function and σ is the vector of stress components in Voigt notation.

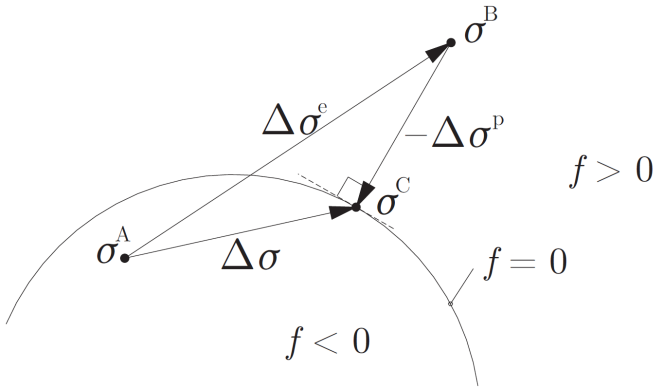

Figure 3.16 Schematic view of stress return (Hazell, 2008)

The stress vector at a point under consideration at the start of a time increment is σ^A, which lies inside or on the yield surface. For an incremental strain, $d\varepsilon$, to be imposed on the material, the elastic predictor increment can be calculated as

$$d\sigma^e = Dd\varepsilon \tag{3.28}$$

where D is the elastic constitutive matrix. The trial stress σ^B is then calculated as

$$\sigma^B = \sigma^A + d\sigma^e \tag{3.29}$$

If σ^B lies outside the yield surface, it is then corrected by $\Delta\sigma^p$ to be returned to point σ^C on the yield surface, such that BC is normal to the surface.

3.4.3.2 Implementation of a Tresca material into Abaqus

The user material subroutine VUMAT is used for implementing the chosen constitutive model into Abaqus/Explicit. In the VUMAT subroutine developed for this thesis, the

elastic constitutive matrix D is constructed first, which for linear elastic material in plane strain can be expressed as

$$D = \frac{E}{(1+\nu)(1-2\nu)} \begin{bmatrix} 1-\nu & \nu & \nu & 0 & 0 & 0 \\ \nu & 1-\nu & \nu & 0 & 0 & 0 \\ \nu & \nu & 1-\nu & 0 & 0 & 0 \\ 0 & 0 & 0 & 1-2\nu & 0 & 0 \\ 0 & 0 & 0 & 0 & 1-2\nu & 0 \\ 0 & 0 & 0 & 0 & 0 & 1-2\nu \end{bmatrix} \tag{3.30}$$

where E is the Young's modulus and ν is the Poisson's ratio.

The stress at the end of previous time increment, σ^A, and the strain increment to be applied to the material, $d\varepsilon$, are passed into the subroutine for processing. Then the trial stress σ^B is calculated according to Equations 3.28 and 3.29. The trial principal stresses σ_p^B and the corresponding transformation matrix N are then derived from σ^B with the help of Abaqus utility subroutines, where

$$\sigma_p^B = N\sigma^B \tag{3.31}$$

The Tresca yield criterion adopted in this thesis involves only linear functions of the principal stresses. The corresponding yield surface in principal stress place takes the form of a hexagonal prism aligned with the line $\sigma_1 = \sigma_2 = \sigma_3$, and can be defined by six linear yield functions

$$\begin{aligned} f_1(\sigma, s_u) &= \sigma_1 - \sigma_2 - 2s_u \qquad & f_2(\sigma, s_u) &= \sigma_2 - \sigma_1 - 2s_u \\ f_3(\sigma, s_u) &= \sigma_2 - \sigma_3 - 2s_u \qquad & f_4(\sigma, s_u) &= \sigma_3 - \sigma_2 - 2s_u \\ f_5(\sigma, s_u) &= \sigma_3 - \sigma_1 - 2s_u \qquad & f_6(\sigma, s_u) &= \sigma_1 - \sigma_3 - 2s_u \end{aligned} \tag{3.32}$$

The equation $f_i(\sigma, s_u)$ corresponds to a plane S_i in the principal stress space, as shown in Figure 3.17, where the stress region boundary planes for the Tresca criterion are also presented. The boundaries of the stress region associated with each face S_i are a pair of planes perpendicular to it, passing through the lines at its two edges. The stress region

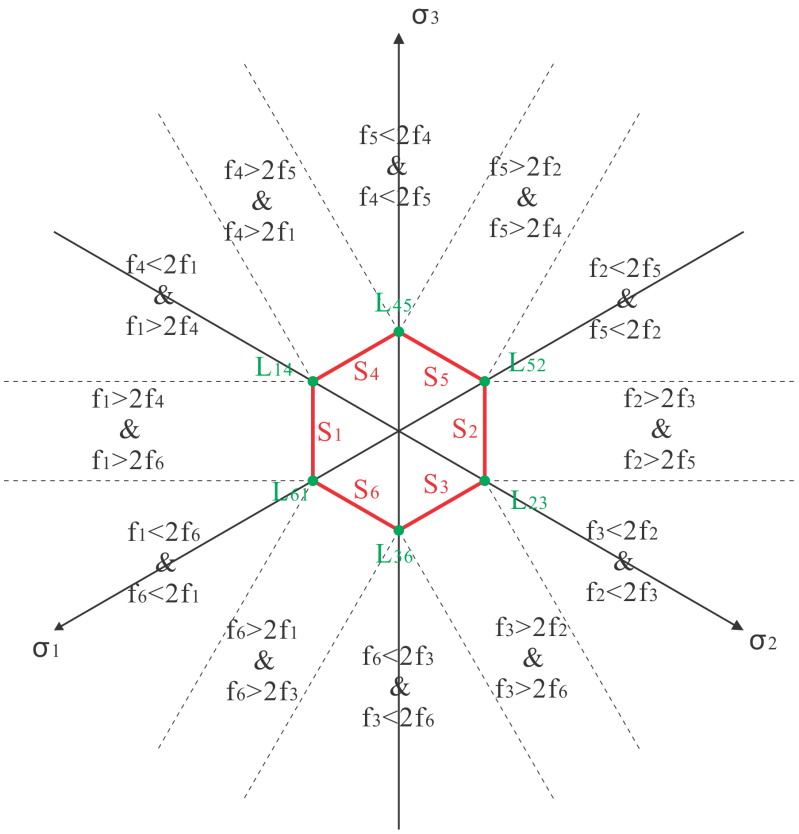

Figure 3.17 Plane surfaces that form the Tresca yield surface (after Hazell, 2008)

boundaries associated with each line L_{ij} are bounded by two planes passing through it, perpendicular to the two faces that intersect at that line.

The calculated trial principal stress σ_p^B is located within the stress boundaries illustrated in Figure 3.17 and returned to the relevant plane or line to obtain σ_p^C. After that the stress to be returned to Abaqus main program, σ^C, is obtained by $\sigma^C = N^{-1}\sigma_p^C$, where N is the transformation matrix mentioned above. More details of this subroutine can be found in Appendix 2 and in Hazell (2008), where a similar Tresca implementation for plane strain or axisymmetric analysis was developed.

3.4.3.3 Incorporation of the effect of strain softening and strain rate

The effects of strain rate and strain softening on soil shear strength were incorporated into the VUMAT by modifying the Tresca material according to Equation 2.9 (Einav and Randolph, 2005; Zhou and Randolph, 2007). In this equation, the parameters δ_{rem}, ξ_{95}, μ and $\dot{\gamma}_{ref}$ are related to soil properties and are fixed throughout the analysis. Two

variables, the accumulated plastic shear strain (ξ) and the maximum shear strain rate ($\dot{\gamma}_{max}$) have to be calculated/updated in the VUMAT. The accumulated plastic shear strain of the material point, ξ, is stored using solution dependent variables (SDVs) available in the VUMAT during the analysis. Every time the VUMAT is called by the Abaqus main program, it retrieves the value of ξ at the beginning of the time increment, ξ_t, and is given the incremental strain, $d\varepsilon$, to be imposed in the current time increment.

The virtual strain rate, $\dot{\varepsilon}'$, is then obtained by $\dot{\varepsilon}' = d\varepsilon/dt$, where dt is the time increment being used to update the model. It is noteworthy that for most cases the virtual loading rate used in the simulation was chosen to be extremely slow to mimic a static problem, and thus is not necessarily equal to the real rate to be simulated. Therefore a factor f should be introduced to scale $\dot{\varepsilon}'$ to a real strain rate, $\dot{\varepsilon}$, by $\dot{\varepsilon} = f\dot{\varepsilon}'$. For a loading process where the real loading speed is v and the loading speed used in the CEL simulation is v', the scaling factor can be calculated as $f = v/v'$. This scaling factor is passed from the Abaqus input into the VUMAT subroutine as a material property parameter, along with the other parameters (S_t, ξ_{95} and etc.).

Once $\dot{\varepsilon}$ has been obtained, the maximum shear strain rate, $\dot{\gamma}_{max}$, as required in Equation 2.9, can be calculated as $\dot{\varepsilon}_1 - \dot{\varepsilon}_3$. The currently applicable shear strength of the material is derived based on ξ and $\dot{\gamma}_{max}$ accordingly. After that, the VUMAT will check the yield condition of the material and return the stress to the yield surface whenever necessary by the method described in Section 3.4.3.2. If the material is found to yield, all the incremental strain in this increment is taken as plastic strain, and the cumulative plastic shear strain of the material is updated by

$$\xi_{t+dt} = \xi_t + (\dot{\varepsilon}_1 - \dot{\varepsilon}_3)dt \tag{3.33}$$

where ξ_{t+dt} is the plastic shear strain at the end of the time increment. This simplification saves the computational cost in differentiating plastic strain from elastic strain and might introduce some inaccuracy. However, the resulting inaccuracy is negligible in the problems studied in this thesis since the elastic strain is only a very small fraction (typically 0.002) compared with the plastic stain once the material starts to yield. The updated plastic shear

strain ξ_{t+dt} is stored via SDVs and will be used to calculate the shear strength at the next time increment.

3.4.3.4 Verification of the VUMAT

The loading response of an individual element undergoing pure shear is presented here. Since it was not practical to impose nonzero displacement to Eulerian nodes, conventional explicit analysis was conducted to do the verification instead of CEL analysis. The element used in the simulation was an 8 node linear brick element (Abaqus code C3D8R), with dimensions of 1m$\times$1m$\times$1m. Its four bottom nodes were fixed in all the three directions and the top four nodes were restrained from moving in the y and z directions. A velocity of 0.01 m/s in the x direction was applied to the top four nodes to reach a transverse displacement of 0.01 m.

Four different cases of the modified Tresca material were considered: rate-independent without strain softening, rate-dependent without strain softening, rate-independent with strain softening and rate-dependent with strain softening. E was set as $5000s_u$. This large value was chosen to ensure that plastic shear strain can take place at very small deformation. The softening parameters δ_{rem} and ξ_{95} in Equation 2.9 were chosen to be 0.01 and 0.05, respectively, so that the softening effect would become significant even for very small deformations. The viscosity parameter μ was set as 0.10 and the reference shear rate was 3×10^{-6} s^{-1}.

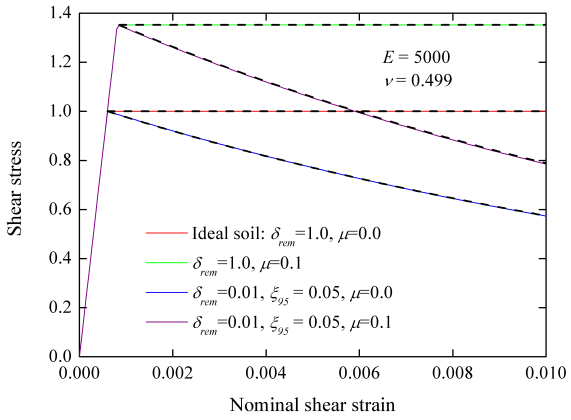

Figure 3.18 Verification of an individual element. Solid lines are Abaqus simulation results and dashed lines are values calculated from Equation 2.9.

Figure 3.18 shows the variation of shear stress against nominal shear strain. It can be seen that, for all cases, the numerical results coincide with the values calculated directly from Equation 2.9, indicating correct functioning of the VUMAT. This verification study is by no means exhaustive because the combined loading responses of the element are not presented. However, in the benchmark studies presented in Section 4.3 and Section 4.4, the VUMAT will be compared with the Abaqus in-built Tresca material to extend this verification, where more complicated loading conditions of the elements are involved.

3.5 Summary

This chapter has introduced the development of the sequential limit analysis (SLA) method for solving large deformation pipe soil interaction problems. This method is an extension of the finite element limit analysis (FELA) software OxLim developed at the University of Oxford. At each increment of time, upper bound results obtained from OxLim are used to construct the velocity field for the model, which then allows the model configuration to be updated. The treatments of external boundaries and material properties are discussed in detail. A constitutive model proposed by Einav and Randolph (2005) is adopted to take into account the hardening and softening behaviour of the soil (assumed to be undrained clay). The software Triangle (Shewchuk, 2002) is used as the mesh generator (and refiner) during the SLA modelling. The visualisation software Paraview (Ayachit, 2015) is used for viewing the results.

The CEL method, as built into Abaqus, is also introduced as an accepted numerical tool that can be used to provide comparisons with the newly developed SLA approach. This method is widely acknowledged as a powerful approach to the analysis of large deformation problems. A material model subroutine, VUMAT, is implemented into the CEL model to provide the same constitutive soil model as used in the SLA. The next chapter will present careful comparisons between the SLA and CEL simulations as well as comparisons with analytical solutions and model test results.

Chapter 4

Validation of the numerical method

4.1 Introduction

This chapter presents a detailed validation study of the SLA method introduced in Chapter 3. Two categories of problems were analysed. The first involves widely studied benchmark cases with analytical solutions available. These problems were examined to check the correct functioning of the SLA model as well as to provide evidence for choosing key parameters (e.g. minimum element size A_{min}, normalised incremental displacement $\delta d/D$, etc.) in readiness for parametric studies. The other category involves the vertical and lateral loading responses of seabed pipelines where physical modelling results have been published, since these are the research interests of this thesis. These problems were investigated to show that the SLA method, in conjunction with a constitutive model taking into account the effects of strain rate and strain softening, can yield reliable solutions for pipe-soil interactions on undrained clay. The CEL model introduced in Section 3.4 is also used to analyse most of these problems, and comparisons between the two methods are presented to provide a clearer insight into the newly developed SLA method. Tables 4.1 and 4.2 summarise the cases to be analysed.

Table 4.1 Summary of the validation tests against theoretical solutions

Loading tests	Comparisons	Notes
Anchor plate Section 4.2	Rowe and Davis (1982)	Without free surface update Theoretical solution: whole process
Wedge Section 4.3	Hill *et al.* (1945) CEL modelling	With free surface update Theoretical solution: whole process
Strip footing Section 4.4	Prandtl (1921) CEL modelling	With free surface update Theoretical solution: only at the surface

Table 4.2 Summary of the validation tests against physical modelling results of pipelines

Loading tests	Comparisons	Notes
Shallow penetration Section 4.5	Centrifuge (Dingle *et al.*, 2008) CEL modelling	Penetration depth: $0.45D$
Deep penetration Section 4.6	Small-scale test (Lee, 2012) CEL modelling	Penetration depth: $4.5D$
Monotonic lateral loading Section 4.7	Centrifuge (Dingle *et al.*, 2008) CEL modelling	Lateral displacement: $3.0D$
Cyclic lateral loading Section 4.8	Centrifuge (Cheuk *et al.*, 2008) CEL modelling	Amplitudes: $0.05-0.2D$. Up to 100 cycles
Cyclic vertical loading Section 4.9	Centrifuge (Hu *et al.*, 2011)	Amplitude: $3.0D$. 1.5 cycles

4.2 Vertical loading of a buried anchor plate

The undrained bearing capacity of a deep anchor plate is studied in this section. This problem was studied analytically by Rowe and Davis (1982) and a solution of $(2+3\pi)Dc$ was given for a plate with a rough interface, where D is the width of the plate and c is the shear strength of the soil. Since the plate is deeply embedded in the soil, no update of free boundaries is involved. This simple case is chosen to confirm the ability of SLA to derive reliable upper bound solutions using the meshing strategy introduced in Section 3.3.4.3.

4.2.1 Model details

Due to the symmetry of the problem, only the right half was analysed. The plate was modelled as a rigid rectangle with a half-width, $D/2$, of 0.5m and aspect ratio of 0.02, initially embedded at a depth of $2D$. The deforming domain was $3D$ in half-width and $5D$ in height. The configuration and initial mesh of the model can be seen in Figure 4.2a. The maximum shear strength of the interface (τ_{max}) was set to be c to model a fully rough condition. The left edge was assigned symmetry boundary conditions while the others were fixed. During the loading, the plate was displaced vertically by $1D$ using an incremental displacement of $0.005D$. Parametric studies were carried out to investigate the influence of mesh density on the loading response.

4.2.2 Results

Figure 4.1a shows the normalised resistance on the plate and Figure 4.1b shows the corresponding bracketing discrepancy between the lower and upper bound solutions throughout the sequential analysis. Four values of mesh density, $0.001D^2$, $0.002D^2$, $0.005D^2$ and $0.01D^2$, are considered here. The bracketing discrepancy decreases with mesh refinement as shown in Figure 4.1b. In the case with the default mesh quality ($A_{min} = 0.001D^2$), the discrepancy can be effectively limited to within 1.5%. The best solution is obtained when the finest mesh is used, where a normalised resistance of 11.45 can be observed in Figure 4.1a. This value is only slightly higher than the analytical solution of 11.42 reported by Rowe and Davis (1982). Considering that the rough plate used in this study has a thickness of $0.02D$, which might yield another component to the normalised bearing capacity of about 0.02, the calculated results presented here can be taken as extremely close to the analytical value.

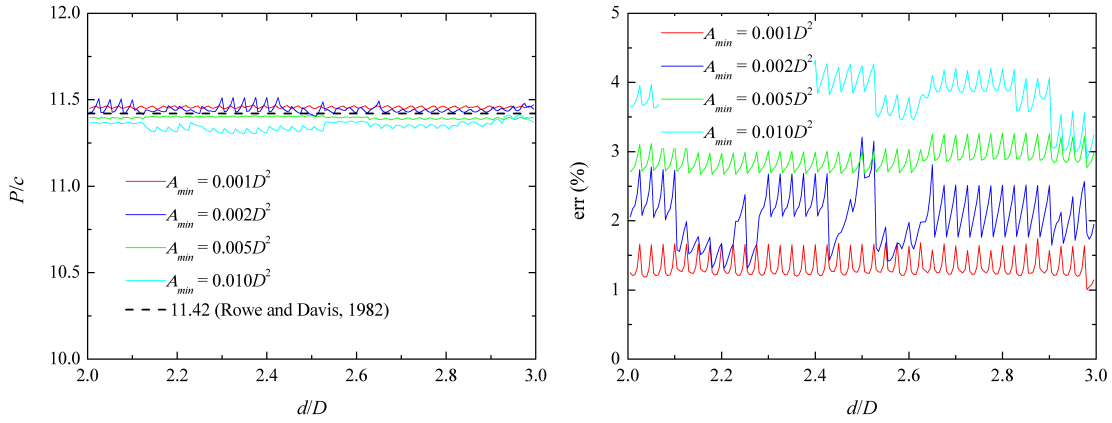

(a) Normalised resistance (b) Bracketing discrepancy

Figure 4.1 Load P against depth for buried plates

Figure 4.2 shows the soil failure mechanisms ($\dot{\gamma}_{max}D/v_p$) at the initial and final stages of loading, where $\dot{\gamma}_{max}$ is the maximum shear strain rate and v_p is the loading velocity of the plate. The failure mechanisms can be revealed by visualisation of this field variable, and are found to be identical at different stages of loading. The region with intense shearing is found to be contained within the finely meshed area throughout the analysis, revealing the reliability of the remeshing strategy introduced in Section 3.3.4.3.

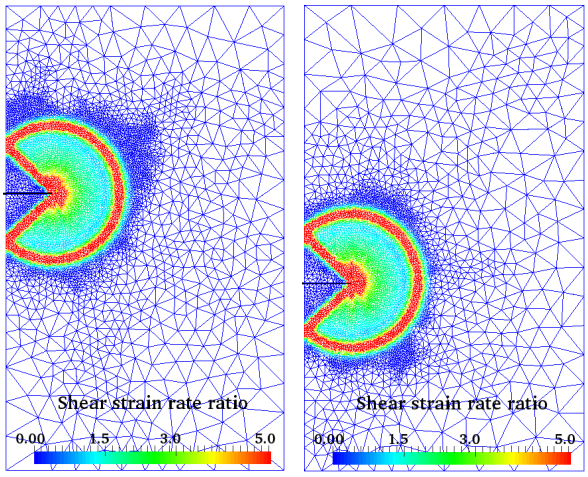

(a) d/D=0.0 (b) d/D=1.0

Figure 4.2 Soil failure mechanisms (showing $\dot{\gamma}_{max}D/v_p$) at the initial and final stages of loading of a rough anchor plate

4.3 Indentation of a smooth wedge

In this section the continuous indentation of a rigid plastic block by a smooth wedge (Figure 4.3) is studied. The theoretical solution of this problem was obtained by Hill *et al.* (1945) using the method of characteristics. Apart from the indentation resistance, the evolution of the free and contact boundaries can also be checked in detail against the solutions provided by Hill *et al.* (1945).

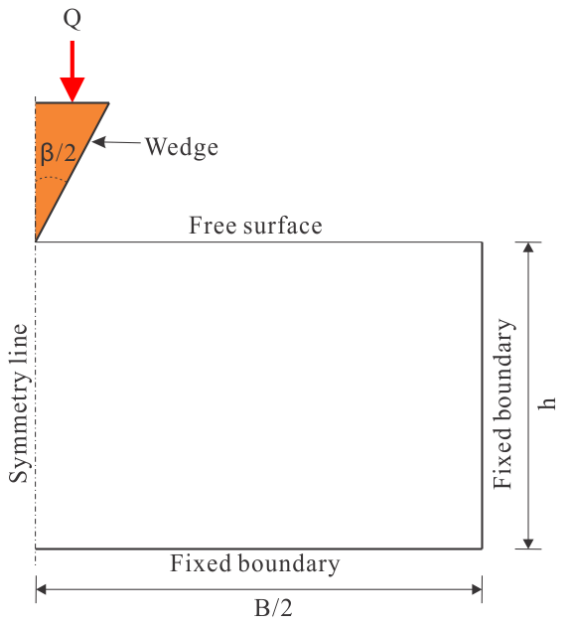

Figure 4.3 Indentation of a plane strain wedge

Figure 4.4 shows the mechanism for this problem given by Hill *et al.* (1945). Since symmetry can be exploited, only the right half is illustrated. The rigid-plastic material is indented downward by a smooth wedge at a constant velocity of v_p. The initial surface of the indented material lies horizontally on OC and the right face of the wedge is AB. With continuous penetration of the wedge, the free surface at the edge of the plastic region remains straight, denoted by line AC, of length l_{AC}. The material flows along parallel streamlines and the speed is the same throughout the deforming region, equal to $\sqrt{2}\sin(\beta/2)\cdot v_p$. The region ABD moves as a rigid block parallel to BD which is at 45° to the wedge face. ADE is a region of diffuse shear, with material moving on curved paths parallel to arc DE centred at A. AEC moves as a rigid block parallel to EC which is at 45° to AC.

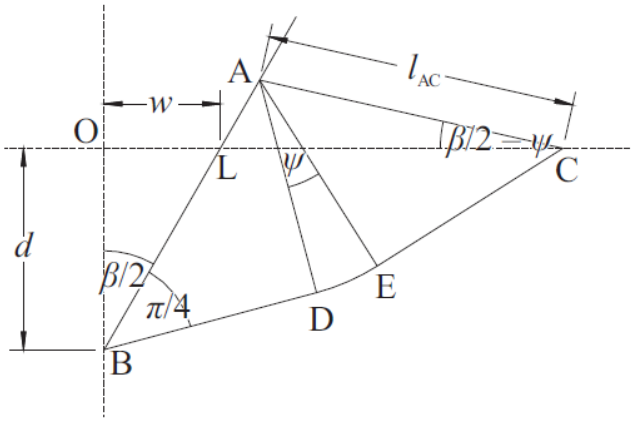

Figure 4.4 Mechanism for the indentation of a smooth wedge from Hill *et al.* (1945) (Hazell, 2008)

The relationship between the angles was derived by Hill *et al.* (1945) as

$$\cos(\beta-\psi)=\frac{\cos\psi}{1+\sin\psi} \tag{4.1}$$

The normal reaction pressure p on the wedge face is $2c(1+\psi)$ and the reaction load Q on the wedge can be expressed as

$$Q=2pl_{AC}\sin\frac{\beta}{2}=4cl_{AC}(1+\psi)\sin\frac{\beta}{2} \tag{4.2}$$

4.3.1 Details of the numerical model

4.3.1.1 CEL model

Considering that CEL analysis in Abaqus must be performed in 3D, a one-element thick (in direction z) mesh was used to model the plane-strain problem. Shown in Figure 4.5 is the model where symmetry has been exploited. The half-width ($B/2$) and depth (h) of the soil domain were 1.5 m and 2 m respectively. A void domain with height (h_0) of 0.5 m was created above the soil domain to allow for soil heave. The Eulerian domain encloses all materials and Lagrangian parts, and its dimension was chosen based on preliminary studies to ensure that boundary effects had been eliminated. The Eulerian mesh was modelled using 8-node brick elements (Abaqus code EC3D8R), which is the only element type supported in CEL analysis using Abaqus. The nodes on the bottom and side edge of the Eulerian domain were fixed by setting the velocity of these nodes in all directions to be zero, while the nodes on the symmetry plane were restrained from moving horizontally (x). The velocity in the out-of-plane direction (z) of all the nodes of the Eulerian mesh was set to be zero. The minimum element size near the footing was 0.02m$\times$0.02m$\times$0.02m and the total number of Eulerian elements in the model was 4897 (1121 for void and 3776 for soil).

The soil was modelled as an isotropic elastic-perfectly plastic Tresca material with a density of 0.1kg/m^3. Gravity was absent during the simulation to model a weightless material. A Poisson's ratio $\nu = 0.499$ and a Young's modulus $E = 400c$ were adopted to define the elastic behaviour. The shear strength, c, of the material was 1kPa and the wedge-soil interface was modelled as smooth by setting the coefficient of friction at the interface to be 0. The wedge was modelled as a rigid body using 4-node rigid surface elements (Abaqus code R3D4) initially positioned in an area of void within the Eulerian domain. The height and half-width of the wedge were 1m and $\tan(\beta/2)$m respectively. Two wedge angles, $\beta = 60^\circ$ and 90°, were adopted. The wedge was penetrated into the material to depths of 0.4m and 0.3m for wedge angles of 60° and 90°, respectively. A preliminary study showed that these simulations were very sensitive to the indentation rate due to the inertia effect. Thus the time step used to reach the required depth was 100 s for

both cases, to ensure that the simulation was conducted slowly enough to approximate quasi-static indentation.

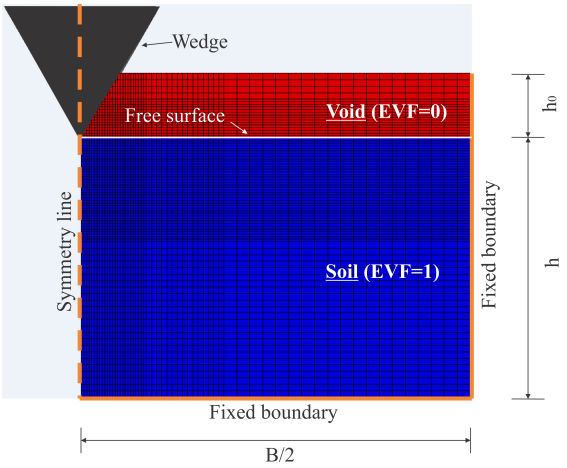

Figure 4.5 CEL model showing the mesh for the wedge indentation problem

4.3.1.2 SLA model

Three wedges with apex angles, β, of 30°, 60° and 90° were pushed to a final depth, D, of 0.5m. Only the right-hand half of the model was considered due to symmetry. The dimensions of the SLA model shown in Figure 4.3 were 2m in half-width ($B/2$) and 1.5m in depth (h). The self-weight of the indented material was not taken into account here because the results were compared with the theoretical solutions (Hill *et al.*, 1945), where weightless material was used. The shear strength of the material, c, was set to be 1kPa and the shear strength at the interface was zero to model a smooth wedge.

The default incremental displacement (δd) used to update each analysis was 0.005m, denoting an normalised incremental displacement $\delta d/D$ of 0.01. The default minimum element size A_{min} was set to be $0.001d^2$, representing a mesh density that varies with the indentation process. This reveals the advantage of using the meshing strategy introduced in Section 3.3.4.3 because adopting a constant mesh quality would yield less satisfactory results at very shallow indentation depths. Parametric studies were performed to investigate the influence of A_{min} and $\delta d/D$ on the solutions.

4.3.2 Results

4.3.2.1 Validation of the Tresca VUMAT in CEL analysis

Figure 4.6 shows the load-displacement curves obtained from CEL analysis, for both wedge angles. The analytical solutions obtained from Hill *et al.* (1945) are plotted as well for comparison. It can be observed that the curves obtained from the simulations using Abaqus, the in-built Tresca material and the Tresca VUMAT almost coincide and the 'saw-tooth' oscillations in the curves are within an acceptable range. Both numerical curves are in very good agreement with the analytical solutions. Exceptions are found at the initial stage of the case with a wedge angle of 60°, where the numerical results diverge significantly from the theoretical predictions. This can be attributed to the fact that the mesh was relatively too coarse when the indentation depth was very small.

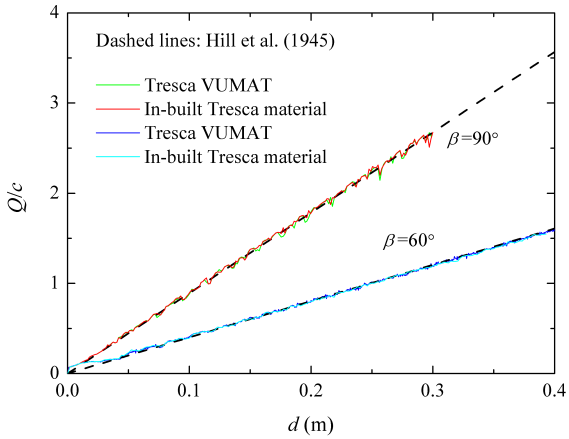

Figure 4.6 Influence of β on smooth wedge indentation in the CEL analyses

Figure 4.7 shows the deformation of the soil surface as well as the Tresca stress $(\sigma_1 - \sigma_3)$ of the soil in the CEL analyses with wedge angle $\beta = 60°$. The evolution of the surface near the wedge is in reasonable agreement with the analytical prediction, as the straight line *AC* shown in Figure 4.4 is reproduced here. This figure is presented to show the validity of the VUMAT via comparison with the Abaqus in-built Tresca material, and perfect agreement between the two parallel analyses can be found.

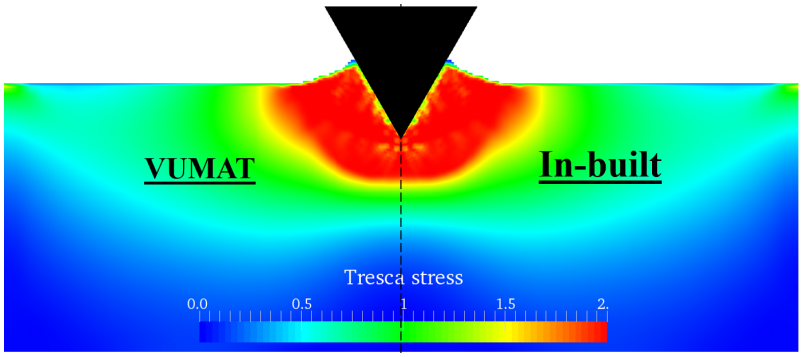

Figure 4.7 Tresca stress at the end of wedge indentation in the CEL analyses. $\beta = 60°$, $d = 0.40$m.

4.3.2.2 Validation of the SLA model

Figure 4.8 shows the load-displacement curves for wedges with different angles β. Also plotted are the solutions reported by Hill *et al.* (1945), and very good agreement between the numerical and analytical results for all cases can be observed .

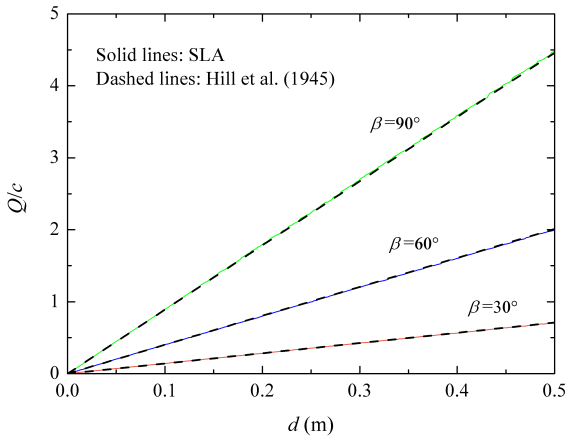

Figure 4.8 Influence of β on smooth wedge indentation in the SLA analyses. $\delta d/D = 0.01$, $A_{min} = 0.001d^2$.

Figure 4.9a shows the influence of mesh density on the loading response of a wedge with $\beta = 60°$. All the numerical curves are extremely close to the theoretical solution provided by Hill *et al.* (1945) and the 'saw-tooth' oscillation in these curves is within a satisfactorily small range even for the case with the coarsest mesh. Figure 4.9b illustrates the bracketing discrepancy between the lower and upper bound solutions throughout the indentation. The bracketing discrepancy is found to decrease with mesh density and can be limited to 2% by taking A_{min} below $0.005d^2$.

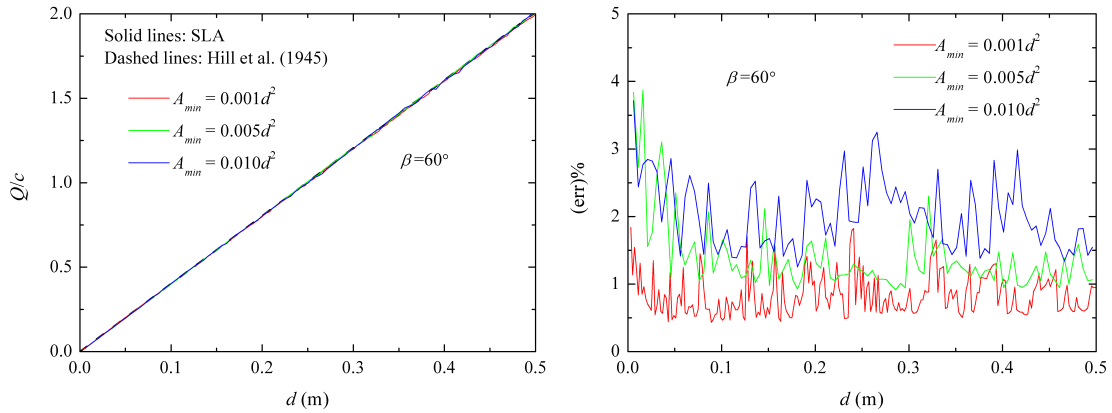

(a) Normalised indentation resistance (b) Bracketing discrepancy

Figure 4.9 Influence of mesh quality A_{min} on the wedge indentation response. $\beta = 60°$, $\delta d/D = 0.01$.

Figure 4.10a shows the influence of $\delta d/D$ on the indentation response of a wedge with β of 60°. The minimum element size in all the cases is $0.001d^2$ and four values of $\delta d/D$, 0.002, 0.004, 0.01 and 0.02 are considered. The CEL results are also provided for comparison, and very good agreement is observed in general. However, at the initial stage of loading, CEL produces higher resistance than the SLA results as well as the theoretical solution. This is because the CEL mesh is extremely coarse at very shallow penetration depths, considering the very small contact area between the wedge and the deforming material. The CEL curve also exhibits more severe 'saw-tooth' oscillation compared to all the SLA results, especially before the wedge reaches a depth of 0.15m. All the simulations were conducted using a 4 processor desktop and the computing time corresponding to these analyses are provided in the figure. It is noteworthy that typically 3-4 parallel SLA simulations were run at the same time so the computing time presented in Figure 4.10a is the real time divided by a factor of 2. The final indentation depth in the CEL model is 0.4m rather than 0.5m as used in the SLA model. It can be seen that for this problem, SLA generates more satisfactory results than CEL at a very small fraction of its computational cost.

Figure 4.10b shows the normalised volume change of material, $\Delta V/D^2$, during the indentation using SLA modelling, where ΔV is the current material volume minus that at the beginning of analysis. For all the analyses, $\Delta V/D^2$ is limited to 6×10^{-4}, demonstrating that the numerical induced volume change in the SLA procedure is extremely limited.

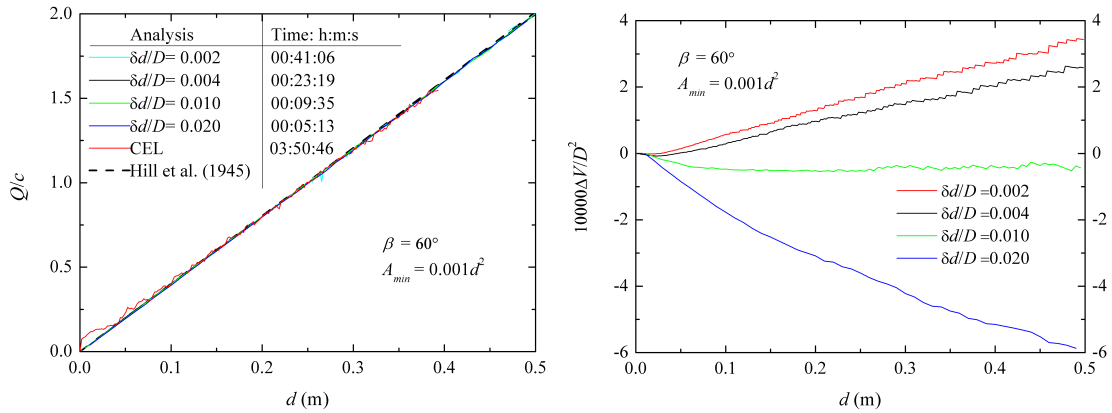

(a) Normalised indentation resistance (b) $\Delta V/D^2$

Figure 4.10 Influence of $\delta d/D$ on the wedge indentation response. $\beta = 60°$, $A_{min} = 0.001d^2$.

However, it can be seen in this figure that adopting a smaller value of $\delta d/D$ does not necessarily reduce the volume change, due to the fact that more increments are involved in solving the problem.

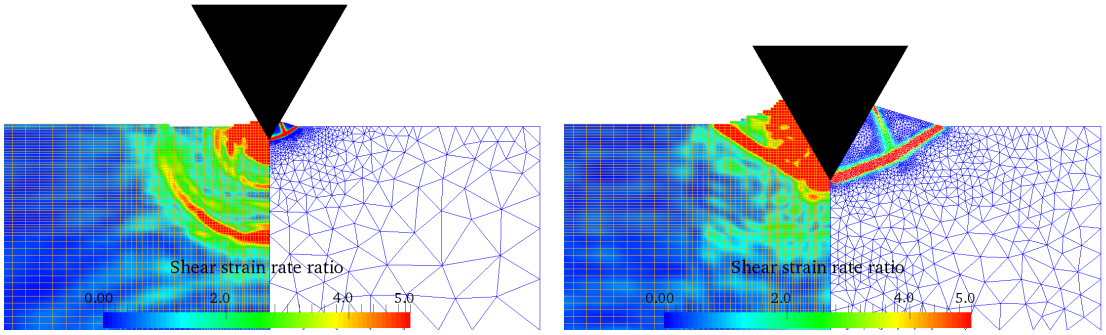

(a) d =0.1m (b) d =0.4m

Figure 4.11 Soil failure mechanisms (showing $\dot{\gamma}_{max}D/v_p$) of smooth wedge with $\beta = 60°$. Left half is from CEL analysis and right half is from SLA.

Figure 4.11 illustrates the normalised shear strain rate $\dot{\gamma}_{max}D/v_p$ as well as the mesh during the indentation. The left half of each image is obtained from CEL modelling and the right half is from SLA. Reasonable agreement between the two can be found in terms of the shape of the soil surface. However, a significant difference is observed at the initial loading stage, which might be attributed to the propagation of an elastic wave in the CEL model (see Figure 4.11a). This difference becomes less significant with increase of the indentation depth. The SLA results show a rigid block adjacent to the wedge and another at the surface, as well as a fan region of diffuse shear between the two rigid blocks, which

is consistent with the mechanism provided by Hill *et al.* (1945). More importantly, the free surface remains straight throughout the simulation, as predicted by the theoretical solution. In general, SLA produces more reasonable results compared with CEL. The region with intense shearing in the SLA model is found to be enclosed by fine meshes throughout the analysis, indicating very good performance of the meshing strategy introduced in Section 3.3.4.3.

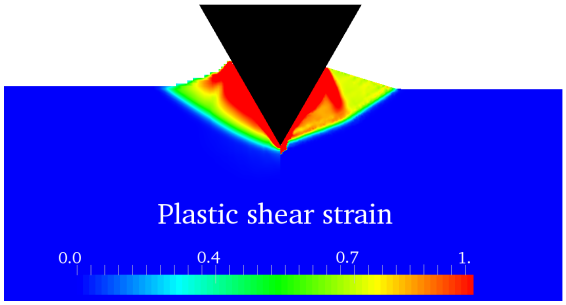

Figure 4.12 Accumulated plastic shear strain (ξ) at the end of wedge indentation. $\beta = 60^{\circ}$ and $d = 0.4m$. Left half is from CEL analysis and right half is from SLA.

Figure 4.12 shows the distribution of the cumulative plastic shear strain ξ at the end of loading. Theoretical solutions for the accumulated plastic strain are not readily available. However, the SLA results agree reasonably well with the CEL results (in magnitude if not in pattern), suggesting that history and field variables are handled reliably in the SLA model.

4.4 Indentation of a strip footing

The classic strip footing problem illustrated in Figure 4.13 is analysed in this section. The interface between the footing and the soil is fully rough. For an infinitesimal vertical displacement this problem has been analytically solved by (Prandtl, 1921) using slip line theory. The average punch pressure for this footing at soil surface is given by Prandtl as $p = (2+\pi)c$, where c is the shear strength of the soil. With further indentation of the footing, no analytical solution is available. Therefore, the resistance, soil mechanism and surface configuration obtained from SLA are to be compared with those from CEL. In

addition, the numerical results for this problem reported by Qiu *et al.* (2009), where both explicit and implicit analyses using Abaqus were presented, are used for comparison.

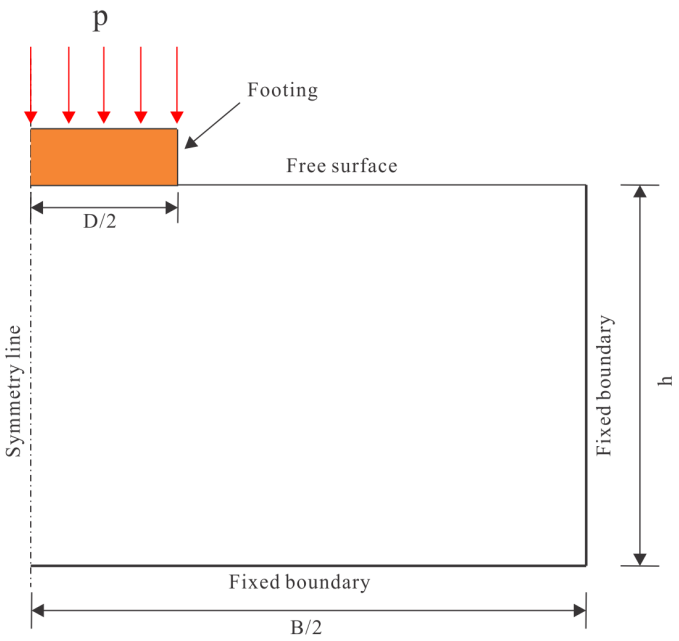

Figure 4.13 Indentation of a strip footing

4.4.1 Details of the numerical model

4.4.1.1 CEL model

In a similar way to the simulation for the loading response of a wedge as described in Section 4.3, a one-element thick mesh was used to model the plane-strain problem because Abaqus can only perform CEL analysis in 3D. The CEL model is illustrated in Figure 4.14. The strip footing used in the simulation was 1m in half-width ($D/2$) and 0.5m in height (L). The half-width ($B/2$) and depth (h) of the soil domain were $4D$ and $3D$ respectively. A void domain with height $0.5D$ was created above the soil domain to allow for soil heave. This dimension of the Eulerian domain was chosen based on preliminary studies to ensure that boundary effects had been eliminated. The strip footing was modelled as a rigid body using 4-node rigid surface elements (R3D4), initially positioned in an area of void within the Eulerian domain. The minimum element size of the Eulerian domain near the footing was $0.02D \times 0.02D \times 0.02D$ and the Eulerian domain had a total number of 7957 elements

(1387 for void and 6570 for soil). Details concerning the boundary conditions of the CEL model are the same as in Section 4.3.1.1.

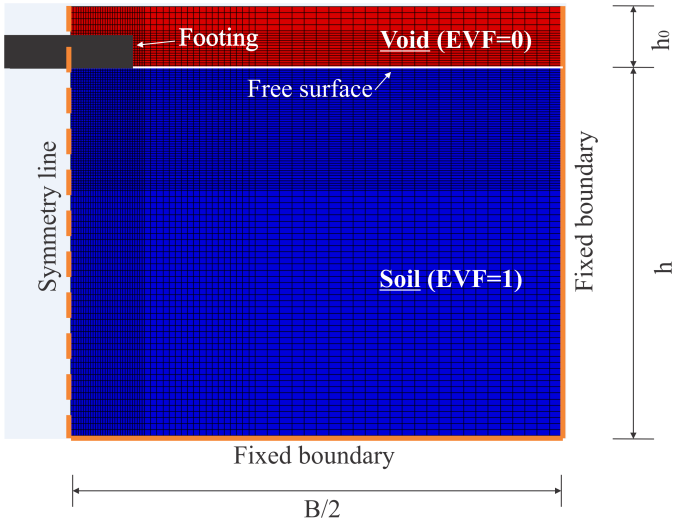

Figure 4.14 CEL model showing the mesh for the strip footing problem (only right side)

The soil was modelled as an isotropic elasto-perfectly plastic Tresca material with a density of 0.1 kg/m^3. Gravity was absent throughout the analysis to model a weightless material. A Poisson's ratio $\nu = 0.499$ and a Young's modulus $E = 400c$ were adopted to define the elastic behaviour, where c is the shear strength of the deforming material. The coefficient of friction at the soil-footing interface was set as 1 to model a fully rough interface and the maximum shear strength at this interface was c. No special treatment was given to the interface at the side of the footing because during the simulation no contact arises in this area due to the absence of gravity. During the loading process, the footing was vertically penetrated into the soil to the depth of $0.5D$ at a constant velocity $0.025D$/s. This velocity was chosen based on preliminary study results and found to be slow enough to eliminate inertia effects.

4.4.1.2 SLA model

Only the right half of the model was considered due to symmetry. The configuration can be seen in Figure 4.13. The half-width $D/2$ and height h of the footing were 1m and 0.5m respectively. The half-width, $B/2$, and depth, h, of the soil domain were determined by preliminary studies to be $4D$ and $3D$ respectively. The initial mesh of the model

can be seen in the right half of Figure 4.19a (the left half is the CEL model). The strip footing was modelled as a rigid body comprised of four segments and experienced no deformation during the penetration. The base of the footing was made totally rough by setting the cohesion factor α to be 1. The soil was modelled as ideal weightless material with homogeneous shear strength throughout the model, and the effects of strain rate and strain softening were not considered. The right edge and the bottom of the soil domain were fixed while the left side was assigned symmetry boundary conditions. The footing was initially positioned at a depth of $0.001D$ and then pushed to $0.5D$.

The minimum element size, A_{min}, was chosen to be $0.00025D^2$ by default and the normalised incremental displacement used to update each sequence of analysis, $\delta d/D$, was 0.002. A set of preliminary analyses was carried out to study the dependency of the solutions on A_{min} and $\delta d/D$. In these analyses, the footing was penetrated to a final depth of $0.25D$ instead of $0.5D$.

4.4.2 Results

4.4.2.1 Validation of the Tresca VUMAT in CEL analysis

The load-displacement curves from the CEL simulations are depicted in Figure 4.15, where the results of Qiu *et al.* (2009) are also provided. Note that the final indentation depth in Qiu *et al.* (2009) was $0.25D$ instead of $0.5D$ as adopted in the current study. The yield point for all the numerical curves is reached at an indentation depth of less than $0.05D$. The agreement between the numerical results and the analytical solution is quite satisfactory, with a difference of about 5%. After reaching the yield point the resistance of the numerical analyses increases continuously at a slow rate, which is attributed to the enlargement of the slip line mechanism as the soil heaves during loading. The CEL curves obtained from the Abaqus in-built Tresca material and the Tresca VUMAT almost coincide, indicating that the VUMAT has been implemented correctly. The curve from the implicit analysis of Qiu *et al.* (2009) exhibits stiffer deep penetration response than the CEL results, while that from the explicit analysis is very close to them. This is reasonable since the CEL analysis is in essence categorised as an explicit analysis.

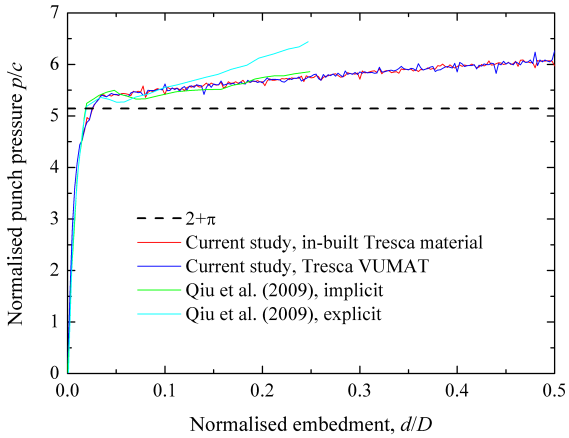

Figure 4.15 Punching response of a strip footing

Figure 4.16 shows the comparison of Tresca stress of the soil between results obtained from simulations with VUMAT and with in-built material. Two typical stages of the loading, shallowly and deeply embedded, are illustrated. It can be seen from Figure 4.16a that soil heave is generated before the material yields, which explains why the punch pressure at the point when the material starts to yield (see the turning point in Figure 4.15) is higher than the theoretical value. A very large plastic area around and beneath the footing can be observed in Figure 4.16b and the deformed shape is consistent with Prandtl's failure mechanism. The soil failure mechanism will be further discussed in Section 4.4.2.2 in comparison with the plasticity solutions obtained from SLA. In general, Figure 4.16 confirms that the stress fields obtained from the analyses with the two soil cases (VUMAT and in-built) are extremely close at both elastic (or almost elastic) and plastic stages.

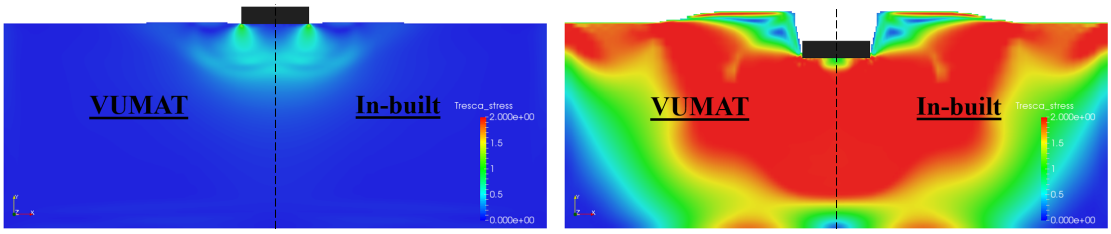

(a) d/D=0.05 (b) d/D=0.5

Figure 4.16 Tresca stress at different stages of punch

4.4.2.2 Validation of the SLA model

Figure 4.17a shows the influence of mesh density on the loading response of the strip footing. It can be observed that even the coarsest mesh case with A_{min} of $0.00125D^2$ can generate satisfactorily stable results with acceptable jaggedness in the curve, demonstrating the global stability of limit analysis in dealing with deep penetration problems. For all cases, the bearing capacity calculated at the initial stage of loading, where the footing is just below the soil surface, are extremely close to the theoretical value of $2+\pi$ reported by Prandtl (1921). The bearing capacity increases approximately linearly with further indentation. Since the soil was modelled as weightless, it is clear that this increase in indentation resistance is attributed to the enlargement of the plastic region with depth, and the additional effect of soil heave. The bracketing discrepancy between lower and upper bound results (Figure 4.17b) are strictly limited to 1.5% in all cases. For the case with the default mesh quality, this discrepancy is further reduced to 0.8%, indicating that extremely reliable results have been produced.

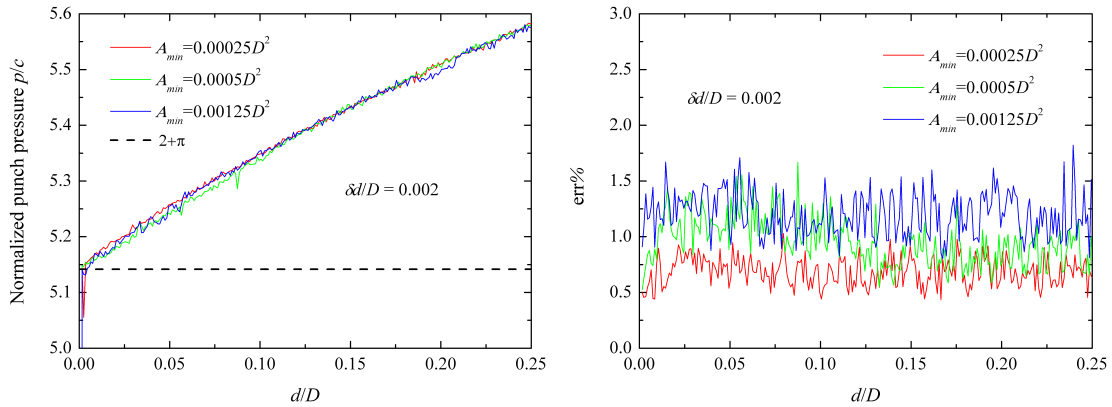

(a) Normalised punching pressure (b) Bracketing discrepancy

Figure 4.17 Influence of mesh density on loading response of the strip footing

Figure 4.18 shows the influence of $\delta d/D$ on the loading response, where the resistance curve obtained from CEL modelling is also provided. A fine mesh with A_{min} of $0.00025D^2$ was used to obtain all the SLA results presented here. As expected, the SLA loading curves agree very well with the theoretical solution at the initial loading step and then increase linearly. It can be seen that even the case with the largest $\delta d/D$ of 0.005 can yield reliable and stable results, as all the SLA curves coincide throughout the loading.

The CEL curve is obviously lower than the analytical value of $2+\pi$ as well as the SLA curves at the initial stage of loading. This is reasonable since the footing in the CEL model using elastic-plastic material needs to be pushed further to develop a global failure mechanism, while the footing in the SLA model using rigid-plastic material can develop a global mechanism immediately after the load is applied (see Figures 4.19a and 4.19b). After the CEL curve reaches its yield point, which indicates that a global mechanism has been developed, it starts to show a slightly stronger response than the SLA curves. In the CEL model the footing was pushed to the desired depth of $0.5D$ at a quasi-static rate, to ensure that the inertia effect had very limited influence on the loading response. Therefore, the reason why the CEL results show a stronger response could be that the plastic region in CEL is slightly larger than that in SLA due to elastic deformations (see Figure 4.19c). The discretisation error as well as the 'locking' phenomenon could also contribute to this difference.

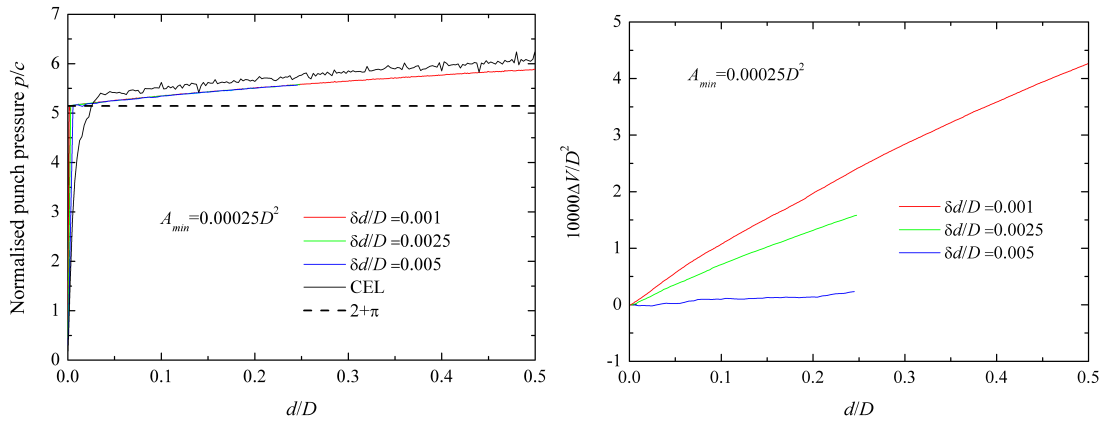

(a) Normalised punching pressure (b) $\Delta V/D^2$

Figure 4.18 Influence of $\delta d/D$ on the response of the strip footing

Figure 4.18b shows the change in material volume throughout the loading, which is expressed in a normalised form as $\Delta V/D^2$, where ΔV is the current material volume minus that at the beginning of analysis. The volume change is found to increase with the number of analyses in the sequences. This reveals the fact that SLA modelling does inevitably introduce some degree of non-physical volume change. However, even for the case with the largest number of analyses (and deepest embedment), the normalised volume change is limited to an extremely small value of 4.5×10^{-4}.

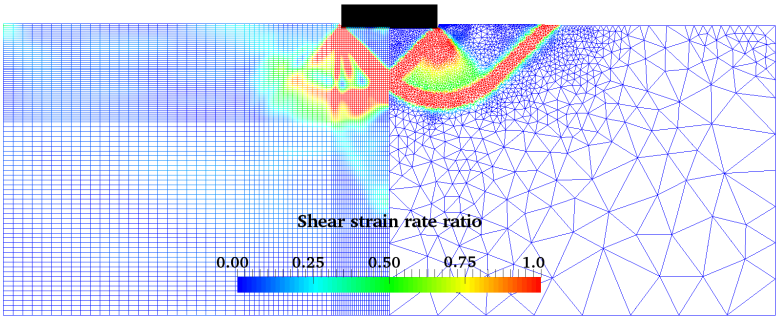

(a) $d/D = 0.03$

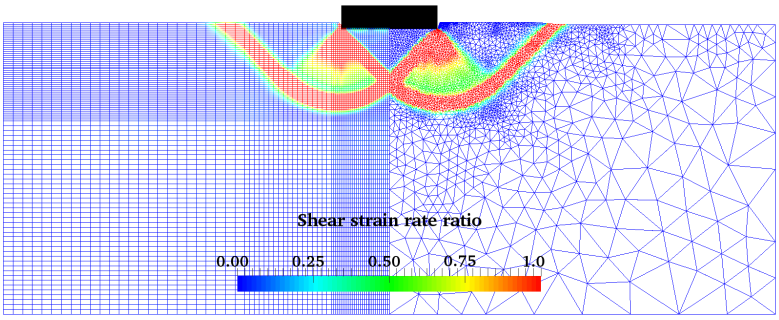

(b) $d/D = 0.05$

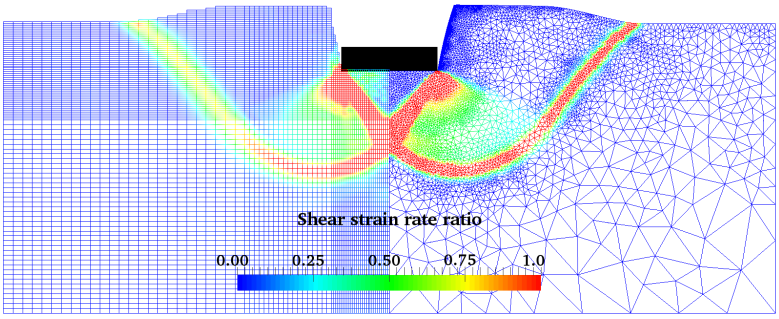

(c) $d/D = 0.50$

Figure 4.19 Soil failure mechanisms (showing $\dot{\gamma}_{max}D/v_p$) of the strip footing. Left half is from CEL analysis and right half is from SLA.

Figure 4.19 shows the soil failure mechanisms ($\dot{\gamma}_{max}D/v_p$) at different loading stages of the footing penetration. The CEL modelling results are also provided for comparison with the SLA results. Very good agreement is found throughout the loading process, except for the initial stage where a global failure mechanism has not yet been fully developed in the CEL model (Figure 4.19a). A rigid block beneath the footing and another at the surface are found to move with the footing. The fan region between the two rigid blocks and the slip line embracing the whole mechanism can also be observed, revealing a classical Prandtl-like mechanism. Throughout the loading process, very fine meshes can be seen to cover the area with intense shearing in the SLA model.

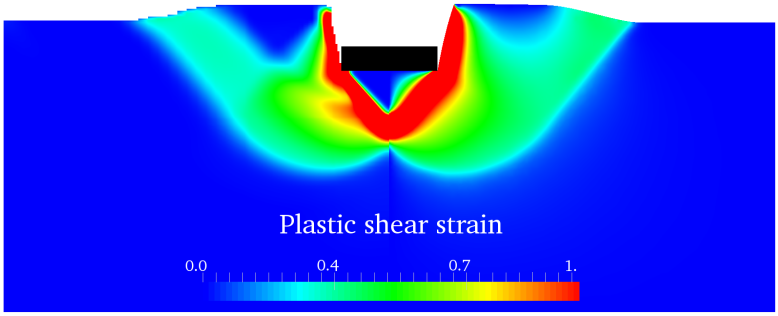

Figure 4.20 Accumulated plastic shear strain (ξ) at the end of punch. $d/D = 0.5$. Left half is from CEL analysis and right half is from SLA.

Figure 4.20 shows the accumulated plastic shear strain of the soil at the end of penetration, where very similar distribution pattern is observed in general between CEL and SLA. However, plastic strain can be observed within the rigid block beneath the footing in the SLA results, which is unrealistic because no shear strain should take place in this region throughout the loading process. The reason is that in this analysis first-order upper bound elements were used in the SLA modelling. Over hundreds of linear interpolations, regions experiencing no shearing gradually acquire non-zero values due to 'pollution' of field variables. In the following validation cases against physical modelling, as well as the parametric study results presented in subsequent chapters, second-order upper bound elements were used in the SLA model and this issue was effectively avoided. Typically an SLA simulation using second-order elements has about 3 times the total number of nodes of one using first-order elements, even though a relatively coarse mesh can be used for the

interpolation of field variables. This considerably increases the computational cost related to the interpolation steps.

4.5 Shallow penetration of a pipe

In this section, the SLA method is used to simulate one of the centrifuge model tests reported by Dingle *et al.* (2008), where a model pipe segment was vertically penetrated to a depth of $0.45D$. Basic parameters from Dingle *et al.* (2008) are tabulated in Table 4.3. The enhancement and degradation of soil strength caused by strain rate and strain softening was incorporated into the SLA model by modifying the rigid-plastic Tresca material according to Equation 2.9. The parameters concerning the effects of strain softening and strain rate were chosen according to the LDFE study reported by Chatterjee *et al.* (2012a), as given in Table 4.4. A CEL simulation was also conducted to make a comparison with the SLA simulation.

4.5.1 Details of the numerical model

4.5.1.1 SLA model

For all the analyses in this thesis concerning the vertical loading behaviour of a pipe, the dimensions and boundary conditions of the SLA model are same as those illustrated in Figure 4.21. A typical initial mesh of the model is also shown in this figure. The pipe with diameter D was initially positioned at a depth of $0.001D$. The pipe was considered

Table 4.3 Basic parameters from Dingle *et al.* (2008)

Parameter	Value
Pipe diameter, D: m	0.8
Shear strength of soil at mudline, s_{um}: kPa	2.3
Shear strength gradient, k: kPa/m	3.6
Submerged unit weight of soil, γ': kN/m^3	6.5
Initial pipe embedment, w_{ini}	$0.45D$
Lateral pipe displacement, u_{fin}	$3D$
Pipe weight during lateral movement, W: kN/m	3.3
Vertical penetration rate, v_p	$0.015D$/s
Lateral sweep rate, v_p	$0.050D$/s

Table 4.4 Soil parameters concerning the effects of strain rate and strain softening (Chatterjee *et al.*, 2012a)

Parameter	Value
Rate of strength increase per decade, μ	0.10
Reference shear strain rate, $\dot{\gamma}_{ref}$: s^{-1}	$3\times10^{-6}s^{-1}$
Sensitivity of soil, S_t	3.2
Ductility parameter of soil, ξ_{95}	10

as a rigid body composed of 60 straight-line segments, with freedom only in the vertical and lateral directions (i.e. rotation was prevented). Symmetry was exploited and only the right half of the soil domain was modelled, the half-width and depth of which are denoted by $B/2$ and h respectively. The bottom and right sides of the domain were fixed, while the left side was assigned a symmetric boundary condition. The top side of the domain was set as a free surface. The shear strength and tensile capacity of the pipe-soil interface were τ_{int} and T respectively see details below. During the vertical loading, a normalised incremental displacement, denoted by $\delta d/D$, was imposed on the pipe for each analysis of the sequence. This process was repeated until the required displacement had been reached. The minimum element size of the model was A_{min}.

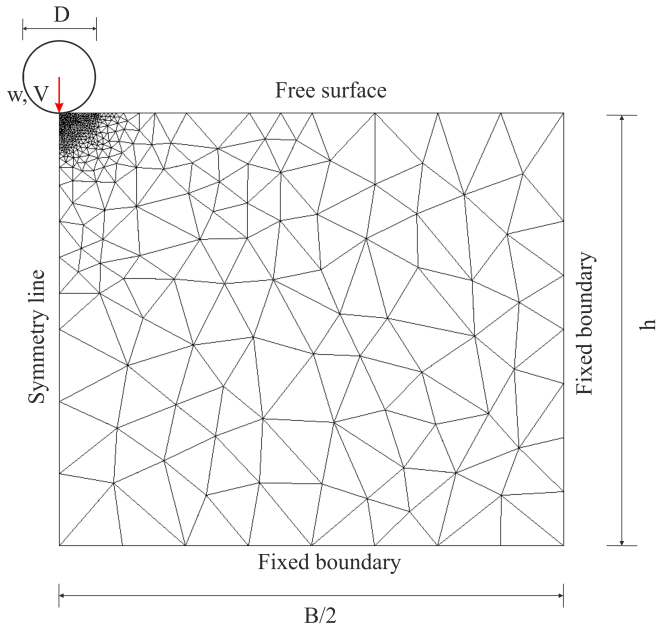

Figure 4.21 Dimension and initial mesh of the SLA model for pipe penetration

Two types of interface modelling were used in the SLA simulation by defining $\tau_{int} = \alpha s_{um}$ and $\tau_{int} = \alpha s_u$, where α is the roughness at the interface, s_{um} is the initial soil

strength at the mudline and s_u is the operative strength of the soil adjacent to the pipe. The latter took into account the variation of the current soil strength along the interface caused by strain softening and strain rate.

The settings described above provide most of the information on the SLA model used to investigate the vertical loading behaviour (monotonic and cyclic) of a pipe segment in this thesis, and they are kept the same if not stated otherwise. For the validation study presented here, $B/2$ and h were set as $5D$ and $4D$ respectively. A_{min} was $0.00025D^2$ and $\delta d/D$ was 0.002. τ_{int} was modelled as $0.5s_{um}$ and tensile capacity T was zero. These values were chosen based on preliminary studies to ensure reliable results. Other parameters concerning the soil and pipe were chosen according to Tables 4.3 and 4.4.

4.5.1.2 CEL model

The configuration of the CEL model is illustrated in Figure 4.22, where symmetry has been exploited. The half-width and depth of the soil domain were denoted by $B/2$ and h respectively. A void with height h_0 was created above the soil domain to allow for soil heave. The pipe with diameter D was modelled as a rigid body using 4-node rigid surface elements (R3D4), initially positioned in an area of the void. The Eulerian domain encloses all materials (soil and void) and Lagrangian parts (pipe). The soil domain as well as the void were modelled using 8-node brick elements (EC3D8R) and a one-element thick mesh was used to approximate the plane-strain problem. The nodes on the bottom and side edges of the Eulerian domain were 'fixed' by setting the velocity of these nodes in all directions to be zero, while the nodes on the symmetry plane were restrained from moving horizontally (x). The velocity in the out-of-plane direction (z) of all the nodes of the Eulerian mesh was set to be zero. The soil was modelled as an isotropic elastic-perfectly plastic continuum, with failure described by the Tresca-based VUMAT developed in Section 3.4.3. The Young's modulus and Poisson's ratio that define the elastic behaviour of the soil were denoted by E and ν, where $E = 400s_{u0}$ and $\nu = 0.499$ if not stated otherwise. The shear strength of the pipe-soil interface was set as αs_{um}.

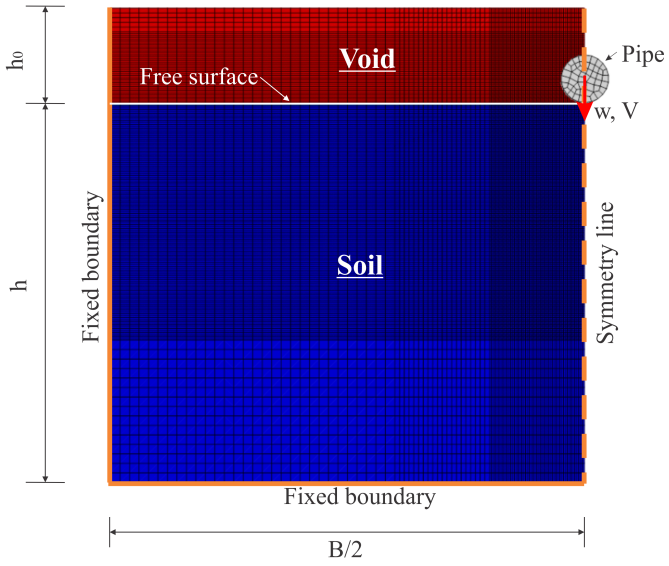

Figure 4.22 Dimension and mesh of the CEL model for pipe penetration

The settings described above provide most of the information on the CEL model used to investigate the vertical loading behaviour (monotonic and cyclic) of a pipe in this thesis, and they are kept the same if not stated otherwise. In this validation study, $B/2$ and h were set as $5D$ and $4D$ respectively and h_0 was $1D$. This dimension was chosen based on preliminary studies to eliminate boundary effects. Throughout the analysis, the minimum element size was chosen to be $0.02D \times 0.02D \times 0.02D$ and the Eulerian domain had a total of 18875 elements. Other parameters concerning the soil and pipe were chosen according to Tables 4.3 and 4.4. The analysis was conducted in three steps.

- Restrain the Eulerian material from flowing outside the predefined dimensions. The velocity was set to be zero in the normal direction at the bottom and all planar boundaries of the soil extending to the top of the Eulerian domain, while the top surface of the soil was left free to move within the void.
- Apply a body force that represents the submerged unit weight of the soil, and at the same time restrain the movement of the pipe in all directions. Although not directly controlled, the ratio of horizontal stress to vertical stress is approximately equal to 1 throughout this stage.
- Penetrate the pipe at a constant velocity to the required position of $0.45D$.

4.5.2 Results

Figure 4.23a shows the variation of the normalised penetration resistance V/Ds_{u0} with the normalised embedment of the pipe invert w/D, where s_{u0} is the initial shear strength at the current pipe invert level, calculated as $s_{u0} = s_{um} + kw$. It can be observed that the resistance corresponding to ideal soil is significantly less than that of the centrifuge results. Even less resistance is generated if only the softening effect is considered. When the effects of both strain rate and strain softening are taken into account, a reasonable match with the centrifuge results can be achieved (see the curve corresponding to $\mu = 0.10$). The CEL modelling results are also shown and are found to be very close to the SLA results. The bracketing discrepancy between lower and upper bound results throughout the sequential analysis is shown in Figure 4.23b for the case of $\mu = 0.10$. It is clear that satisfactory computing accuracy was achieved in the SLA simulation, with the bracketing discrepancy being kept within a reasonable range of $1\% - 2\%$. The normalised volume change $\Delta V/D^2$ shown in Figure 4.23c (again for $\mu = 0.10$) is found to be within 1.3×10^{-3} at the end of loading, which is considered reasonable for this type of problem.

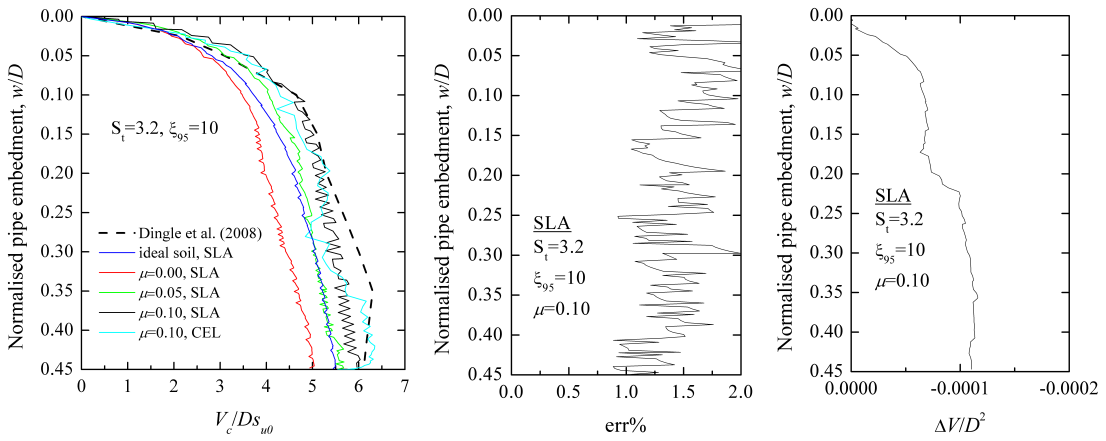

Figure 4.23 Shallow penetration response of a rigid pipe: (a) Normalised penetration resistance; (b) Bracketing discrepancy; (c) Normalised volume change.

Figures 4.24a and 4.24b show the comparison of soil failure mechanisms between SLA and CEL at normalised embedments of 0.1 and 0.3, where the left half is taken from CEL and the right half from SLA. Reasonably good agreement between the two models can be observed, despite the fact that CEL generates a stiffer soil berm than SLA. By comparing

to the deformed soil profile reported by Dingle *et al.* (2008) (Figure 2.2), it can be seen that SLA produces a more reasonable shape of soil berm. The region with intense shearing is contained within the fine mesh area throughout the analysis. Figure 4.24c shows the softening factor of the soil (i.e. the second term in Equation 2.9) at the end of loading. The distributions show a similar pattern except that the soil in the CEL analysis experiences less softening.

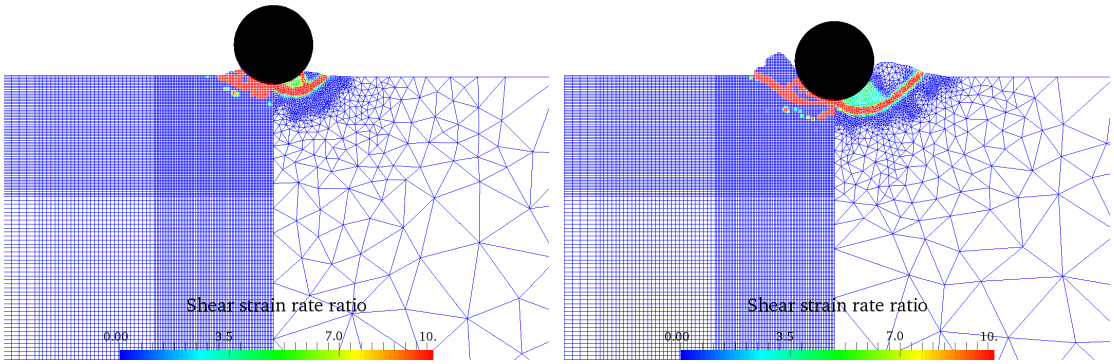

(a) w/D =0.10: $\dot{\gamma}_{max}D/v_p$ (b) w/D =0.30: $\dot{\gamma}_{max}D/v_p$

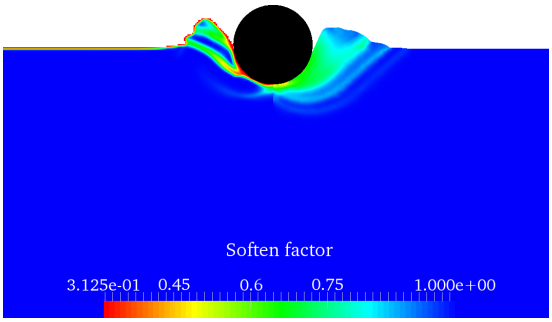

(c) w/D =0.45: Softening factor

Figure 4.24 Deformation of the soil during shallow penetration of a rigid pipe. Left half is from CEL and the right half is from SLA.

4.6 Deep penetration of a pipe

Physical modelling of the deep penetration behaviour of a pipe segment into kaolin clay is reported by Lee (2012). In the small-scale model tests, the pipe was vertically penetrated to a depth of more than 7D and a transition from global to localised failure mechanism was observed. Parameters related to the model test given by Lee (2012) are depicted in Table 4.5.

Table 4.5 Basic parameters from Lee (2012)

Parameter	Value
Pipe diameter, D: m	0.03
Shear strength of soil at mudline, s_{um}: kPa	1.1
Shear strength gradient, k: kPa/m	4.5
Submerged unit weight of soil, γ: kN/m^3	6
Final pipe embedment, w_{fin}	$7D$
Vertical penetration rate, v_p	$0.1D$/s
Pipe-soil interface roughness factor, α	0
Sensitivity of soil, S_t	1.7
Ductility parameter of soil, ξ_{95}	10

4.6.1 Details of the numerical model

4.6.1.1 SLA model

The configuration and boundary conditions of of SLA model for simulating the deep penetration behaviour of the pipe are illustrated in Figure 4.21. The half-width ($B/2$) and depth (h) of the soil domain in this study were both set to be $7D$. The pipe was penetrated to an invert embedment of $4.5D$ using a incremental displacement of $0.005D$. The minimum element size was chosen to be $0.00025D^2$. Other settings of the model were the same as those given in Section 4.5.1.1 and the pipe and soil parameters were chosen according to Table 4.5.

4.6.1.2 CEL model

The configuration and boundary conditions of the CEL model for this problem are illustrated in Figure 4.22 and the settings of the model are similar to those given in Section 4.5.1.2. Here only the different settings are provided. The half-width ($B/2$) and depth (h) of the soil domain were both $10D$ and the void above the soil had a height (h_0) of $2D$. The minimum element size was $0.04D \times 0.04D \times 0.04D$ and the total number of Eulerian elements was 21300. The pipe and soil parameters were as given in Table 4.5. During the vertical loading process, the pipe was penetrated at a velocity of $0.1D/$s to the depth of $4D$.

4.6.2 Results

Figure 4.25 shows the relationship between the normalised penetration resistance V_c/Ds_{u0} and the normalised embedment of the pipe w/D. The ideal soil case (no rate dependency, no strain softening) moderately overestimates the penetration resistance by about 12%. The rate-independent ($\mu = 0$) soil with softening can reasonably predict the loading response, especially at deep embedment, but underestimates the resistance at depths less than $2.5D$. With rate-dependence being incorporated into the model, a considerable increase in resistance can be achieved and the case with $\mu = 0.05$ best fits the experimental curve at depths less than $1D$. A perfect match with the experimental curve through the whole depth of penetration cannot be achieved by any of the SLA simulations presented here. It is noteworthy that the experimental curve shown in Figure 4.25 is the average of several model tests rather than the data of a specific test. This averaged curve was used in Lee (2012) when numerical modelling was performed to back-analyse the test results. Results from the CEL modelling using softening soil without any rate effect are presented in Figure 4.25 for comparison with the SLA data, and very good agreement between the two can be observed.

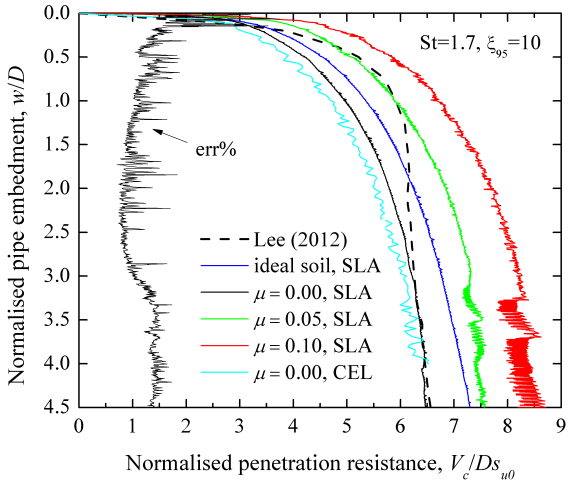

Figure 4.25 Normalised penetration resistance of a rigid pipe during deep penetration

The bracketing discrepancy corresponding to the SLA curve with $\mu = 0$ is shown in the figure, and it is within the range of 1.5% beyond an embedment of $0.5D$. This represents a high standard of computing accuracy considering that the material with non-homogeneous

initial strength becomes highly non-linear due to strain softening. The normalised volume change of material, $\Delta V/D^2$, is 2.41×10^{-3} at the end of the SLA simulation with $\mu = 0$, indicating a good approximation of constant-volume deformation.

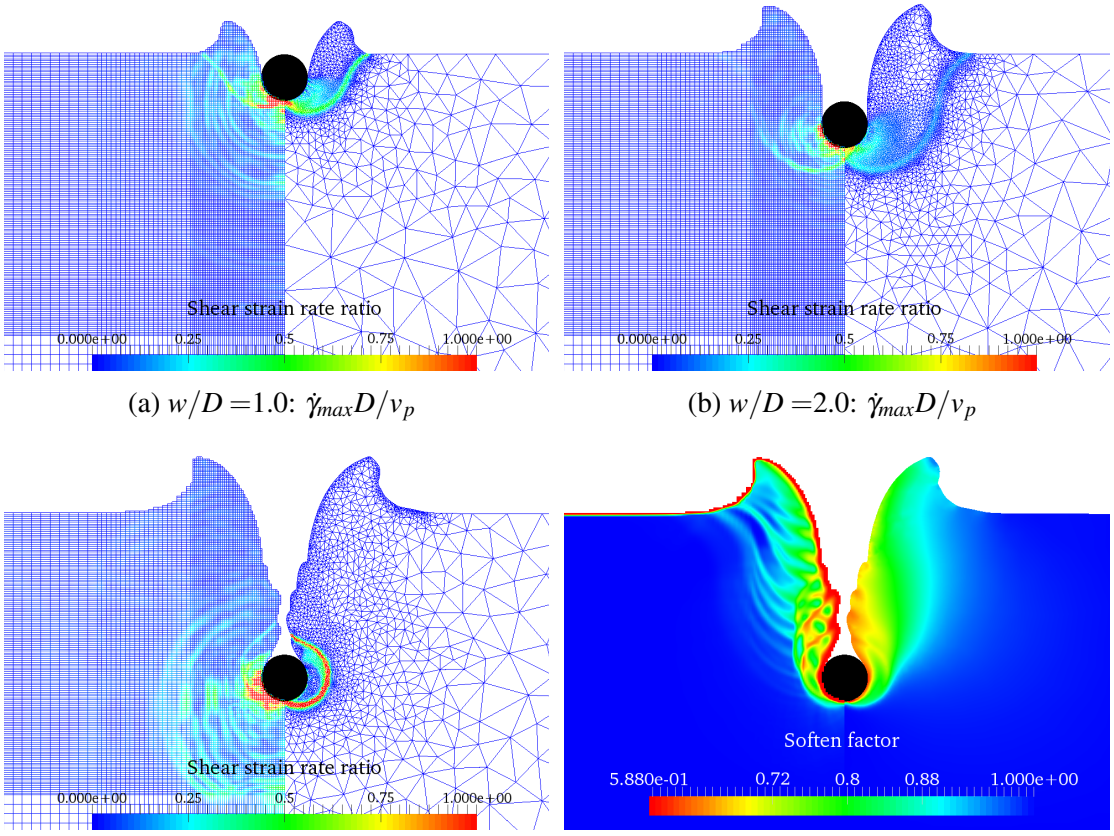

(a) w/D =1.0: $\dot{\gamma}_{max}D/v_p$ (b) w/D =2.0: $\dot{\gamma}_{max}D/v_p$

(c) w/D =4.0: $\dot{\gamma}_{max}D/v_p$ (d) w/D =4.0: Softening factor

Figure 4.26 Deformation of the soil during deep penetration of a rigid pipe. Left half is from CEL analysis and the right is from SLA.

Figures 4.26a to 4.26c provide comparisons of soil failure mechanisms in the SLA and CEL simulations at different penetration depths. The left and right halves are obtained from CEL and SLA respectively. The deforming patterns of the two numerical analyses are extremely close, given the different types of elements are used. After an embedment of $2D$, the global failure mechanism changes to a localised one, which can be observed in both sets of numerical results. Since the model test was conducted at 1g at a very small scale, the effect of the soil weight was not as significant as would be observed in the field. Backfilling of the soil is absent in both physical and numerical results. This backfilling behaviour is studied in Section 5.2, where comparisons between SLA and CEL results

are also made. Figure 4.26d shows the softening factor in the soil at the end of the deep penetration, and very good agreement between SLA and CEL can be observed.

4.7 Monotonic lateral loading of a pipe

A centrifuge model test investigating the monotonic lateral loading behaviour of a pipe segment was reported by Dingle *et al.* (2008). A validation study against this problem is presented here using both SLA and CEL methods. Basic parameters reported by Dingle *et al.* (2008) are tabulated in Table 4.3, and other parameters concerning the effect of strain rate and strain softening were chosen according to the LDFE studies of Wang *et al.* (2010) and Chatterjee *et al.* (2012a), as given in Table 4.4.

4.7.1 Details of the numerical model

4.7.1.1 SLA model

For all the analyses concerning the lateral loading behaviour of a pipe that are presented in this thesis, the general arrangement and boundary conditions of the SLA model are as illustrated in Figure 4.27. The invert of the pipe was initially positioned at a depth of $0.001D$. The pipe was considered as a rigid body composed of 60 straight-line segments with freedom only in the vertical and lateral directions. The distances of the left and right sides of the soil domain from the initial centre of the pipe were B_1 and B_2 respectively and the depth was denoted by h. Fixed boundary conditions were applied to the two sides and the bottom of the soil domain, while the top was set as a free surface. The shear strength and tensile capacity of the pipe-soil interface were τ_{int} and T respectively (see details below). The initial penetration depth before lateral loading was w_{ini}. The minimum element size was A_{min} and the normalised incremental displacement used to update the model configuration was $\delta d/D$.

Two types of interface modelling methods were used in the SLA simulation by defining $\tau_{int} = \alpha s_{um}$ and $\tau_{int} = \alpha s_u$, where α is the roughness at the interface, s_{um} is the initial soil strength at the mudline and s_u is the operative strength of the soil adjacent to the pipe. The

latter took into account the variation of soil strength along the interface caused by strain rate and strain softening.

The settings described above provide most of the information on the SLA model used to investigate the lateral loading behaviour (monotonic and cyclic) of a pipe in this thesis, and they are kept the same if not stated otherwise.

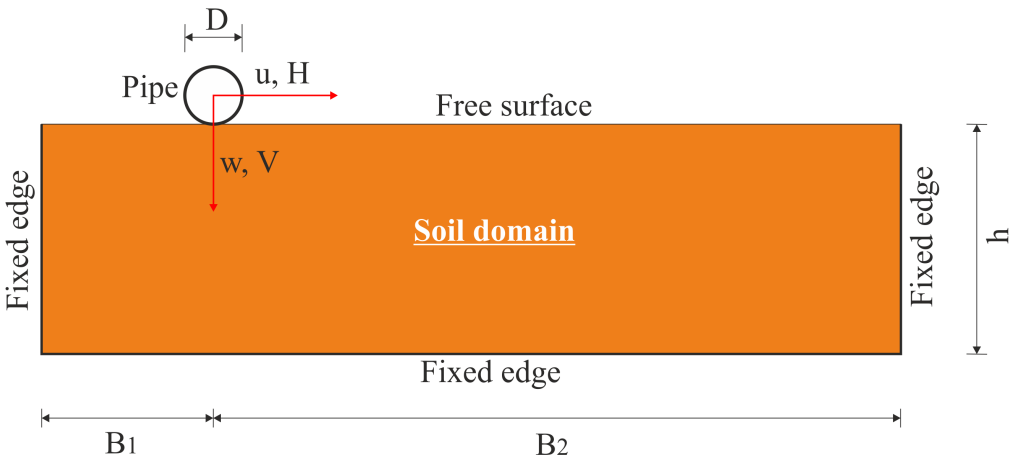

Figure 4.27 Configuration of the SLA model for lateral loading of a pipe

In this validation study, B_1, B_2 and h were chosen to be $3D$, $7D$ and $3D$ based on preliminary study results. A_{min} was set as $0.00025D^2$, and $\delta d/D$ was taken as 0.0025 and 0.005 for the vertical and lateral loading steps respectively. Tension was not allowed at the interface by default ($T = 0$) but one case with unlimited tension was also studied to model the initial lateral loading stage. The roughness factor α was set as 0.5. The pipe was initially pushed to a desired depth (w_{ini}) of $0.45D$, after which it was displaced horizontally by $3D$ under a constant vertical load of 3.3kN/m (Dingle *et al.*, 2008) throughout the lateral loading process.

4.7.1.2 CEL model

The configuration of the CEL model for lateral loading of a pipe is illustrated in Figure 4.28. The Eulerian domain is comprised of a soil domain and a void above it. The horizontal distances from the left and right edges to the pipe centre were denoted by B_1 and B_2 respectively and the depth of the soil domain was h. A void with height h_0 was created above the soil domain to allow for soil heave. The pipe with diameter D was modelled

as a rigid body using 4-node shell elements (R3D4), initially positioned in the void. The Eulerian domain encloses all materials (soil and void) and Lagrangian parts (pipe). The soil domain as well as the void were modelled using 8-node brick elements (EC3D8R) and a one-element thick mesh was used to approximate the plane-strain problem. The nodes on the bottom and side edges of the Eulerian domain were restrained vertically (y) and laterally (x) respectively. All the nodes of the Eulerian mesh were restrained from moving in the out-of-plane direction (z). The soil was modelled as an isotropic elastic-perfectly plastic continuum, with failure described by the Tresca-based VUMAT developed in Section 3.4.3. The Young's modulus and Poisson's ratio that define the elastic behaviour of the soil were denoted by E and ν, where $E = 400s_{u0}$ and $\nu = 0.499$ if not stated otherwise. The shear strength of the pipe-soil interface was set as αs_{um}.

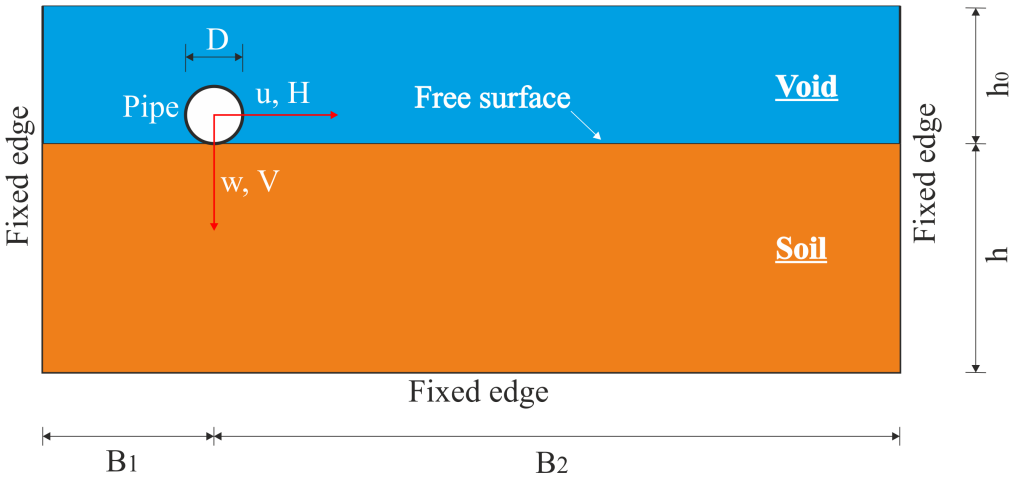

Figure 4.28 Configuration of the CEL model for lateral loading of a pipe

The settings described above provide most of the information on the CEL model used to investigate the lateral loading behaviour (monotonic and cyclic) of a pipe in this thesis, and they are kept the same if not stated otherwise. In this validation study, B_1 and B_2 were set as $3D$ and $6D$ respectively. h was $3D$ and h_0 was $1D$. This dimension was chosen based on preliminary studies to eliminate boundary effects. Throughout the analysis, the minimum element size was $0.025D \times 0.025D \times 0.025D$ and the total number of Eulerian elements was 30160. Other parameters concerning the soil and pipe were chosen according to Tables 4.3 and 4.4. The simulations were conducted in the following three steps.

- Restrain the Eulerian material from flowing outside the predefined dimensions. Apply a body force that represents the submerged unit weight of the soil, and at the same time restrain the movements of the pipe in all directions.
- Penetrate the pipe at a constant velocity to the required depth (w_{ini}) of $0.45D$.
- Release the vertical constraints on the pipe and laterally displace it without rotation at a constant velocity to a required distance of $3D$ with the pipe free to move vertically.

4.7.2 Results

Figure 4.29 shows the centrifuge test results as well as the numerical results obtained from both SLA and CEL analyses, in terms of the pipe invert trajectory and the lateral soil resistance. The lateral resistance was normalised by Ds_{u0}, where s_{u0} is the initial strength of the soil at the current pipe invert level. It can be observed that when the effects of both strain rate and softening are considered in the model, good agreement is found between the physical and numerical results. The SLA simulation with ideal soil largely overestimates the soil resistance. The softening soil case without rate effect moderately underestimates the soil resistance at the initial loading stage but yields the most satisfactory results near the end of loading. Different modelling assumptions for the soil-pipe interface strength seem to have a limited effect on the loading response of the pipe. Of all the SLA simulations presented here, the largest normalised volume change, $\Delta V/D^2$, at the end of lateral loading was about 5×10^{-3}.

At the initial lateral break-out stage, a sharp increase in lateral resistance is observed in the centrifuge results (Figure 4.29b), which can be attributed to tensile stresses mobilised at the rear of the pipe caused by suction. This behaviour was absent in the numerical results, where tensile normal stress was not permitted at the pipe-soil interface, and thus indicates a limitation of the present large displacement numerical work for certain design calculations. Figure 4.29b also shows the results of an SLA simulation of the initial phase of movement with unlimited tension being allowed at the interface, where it can be seen that the lateral break-out resistance is moderately over-estimated. The peak resistance measured in the centrifuge test is found to be between the two extreme cases of no tension and full tension

at the interface. CEL results are also provided in Figure 4.29 for comparison. It can be seen that CEL makes a better overall prediction of the trajectory of the pipe, but largely underestimates the residual lateral resistance.

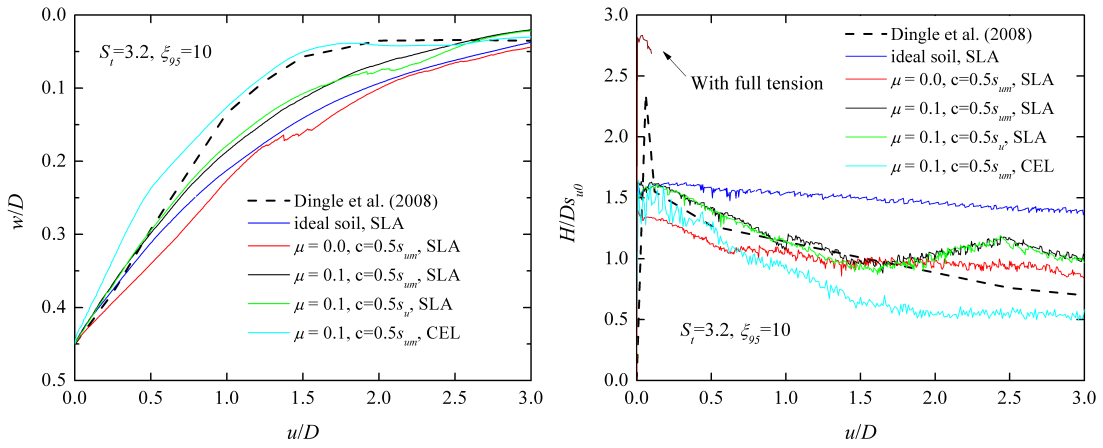

(a) Pipe invert trajectory (b) Normalised lateral resistance

Figure 4.29 Monotonic lateral loading behaviour of a rigid pipe

Figure 4.30 shows the strength enhancement factor of the soil due to strain rate (i.e. the third term of Equation 2.9) during the lateral loading, where the soil failure mechanisms can also be observed. Here the rate parameter μ is 0.1 which is the typical value suggested by Randolph (2004). The shear strength of the soil within the deforming region is largely enhanced by about 50%. It can be observed from Figure 4.30 that the area influenced by the strain rate effect is very localised. The shape of the soil berm at the end of loading (see Figure 4.30d) agrees reasonably with the deformed soil profile provided by Dingle *et al.* (2008) (see Figure 1.4c).

Figure 4.31 shows the softening factor of the soil (i.e. the second term of Equation 2.9) at different stages of loading. The soil within the active berm (see Figure 1.3) becomes severely softened after a lateral pipe displacement of $2D$. Of most importance in Figure 4.31 is that, with second order elements being used, 'pollution' of the field variables as seen earlier in Figure 4.20 can be hardly detected here.

Figure 4.32 shows the combined strength modification factor of the soil with both strain rate and strain softening effects being taken into account. It can be observed in Figures 4.30 and 4.31 that the regions being softened and those being enhanced hardly coincide.

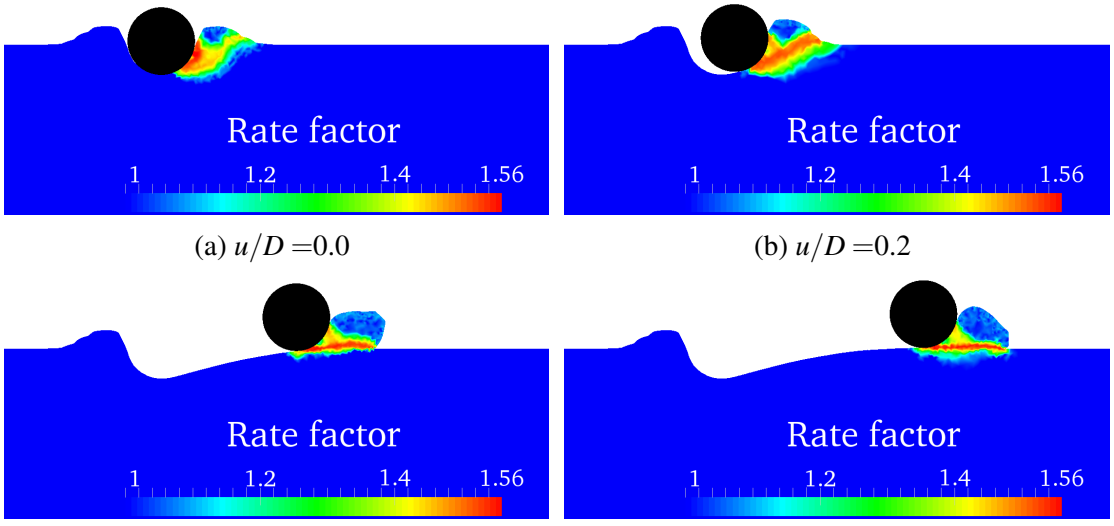

(a) u/D =0.0 (b) u/D =0.2

(c) u/D =2.0 (d) u/D =3.0

Figure 4.30 Rate factor of the soil during monotonic lateral loading of a pipe. Only part of the soil domain is visualised for clarity.

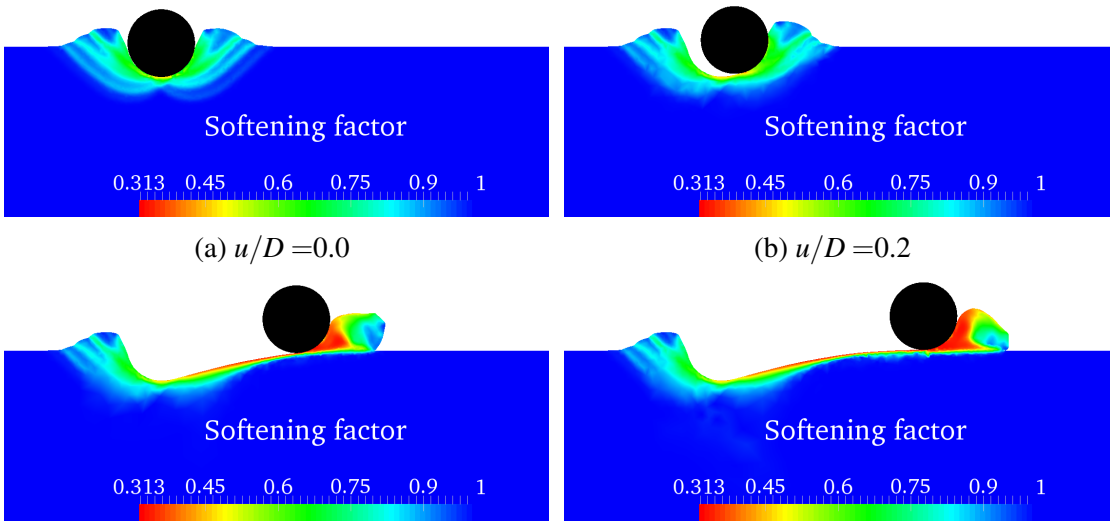

(a) u/D =0.0 (b) u/D =0.2

(c) u/D =2.0 (d) u/D =3.0

Figure 4.31 Softening factor of the soil during monotonic lateral loading of a pipe. Only part of the soil domain is visualised for clarity.

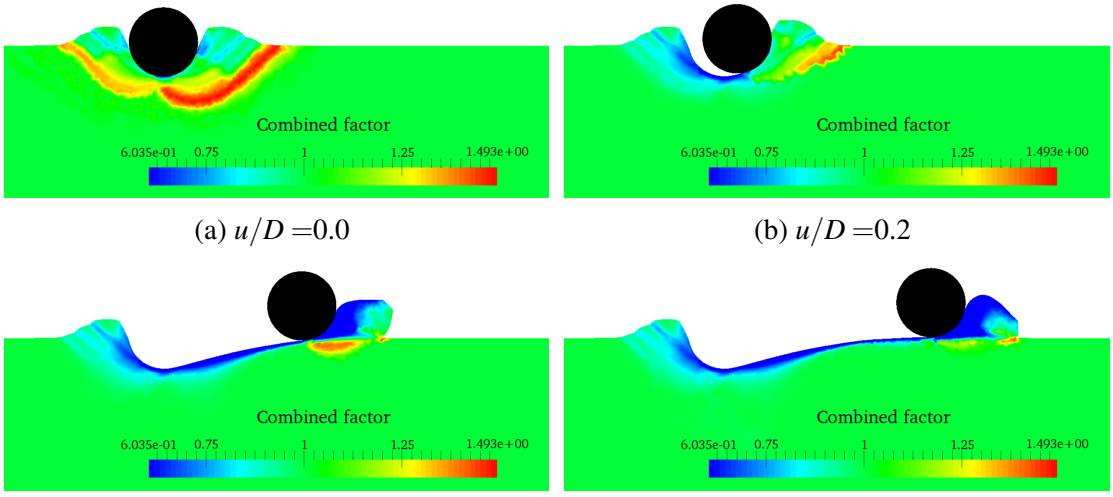

(a) u/D =0.0 (b) u/D =0.2

(c) u/D =2.0 (d) u/D =3.0

Figure 4.32 Combined strength modification factor of the soil during monotonic lateral loading of a pipe. Only part of the soil domain is visualised for clarity.

Therefore the combined factor in Figure 4.32 varies over a very wide range, suggesting that the influences of strain rate and strain softening cannot be easily taken as counterbalancing.

4.8 Cyclic embedment of a pipe segment

In this section, the cyclic embedment behaviour of a rigid pipe segment is simulated, and the results are compared with centrifuge model test results reported by Cheuk and White (2009). The soil used in the centrifuge modelling was kaolin clay with a strength profile defined by $s_{u0} = 0.75 + 1.6z$. The diameter of the pipe was 0.8m at prototype scale. Two types of cyclic loadings were studied, with fixed vertical load but variable amplitude of horizontal displacement (test KC05) and fixed amplitude of horizontal displacement but variable vertical load (tests KC06 and KC07). The horizontal loading rate was 0.1Hz. More details of the vertical loads and the amplitudes of horizontal displacement for each test are presented later.

For all the analyses conducted by both SLA and CEL, the following parameters were adopted. The sensitivity of the soil was chosen as 4 rather than 2.5 as provided by Cheuk and White (2009). This is because the T-bar penetrometer test results they provided are limited to very few cycles and the soil still shows a trend of degrading. The ductility parameter of the soil, ξ_{95}, was taken as 10 and the reference shear strain rate was 3×10^{-6}. Two values for the rate parameter, μ, were chosen as 0.00 and 0.10 to study the behaviour of both rate-independent and rate-dependent material. The maximum shear stress at the pipe-soil interface was $0.5s_{um}$ and no tension was allowed at the interface.

4.8.1 Details of the numerical model

4.8.1.1 SLA model

The configuration and boundary conditions of the SLA model for this problem are similar to those shown in Figure 4.27. Most of the model details are the same as in Section 4.7.1.1 where an SLA model for investigating the monotonic lateral loading behaviour of a pipe was established. Here only the different settings are provided. The values of B_1 and B_2 as illustrated in Figure 4.27 were both set to be $5D$ and the depth of soil h was $4D$. The minimum element area was $0.0005D^2$ and the incremental displacement for each analysis of the sequence was $0.002D$. The pipe was initially wished-in-place at a depth of $0.001D$

and then pushed vertically to the required depth. After that, small amplitude cyclic lateral motions were applied to the pipe. Only the first 80 cycles of loading in the centrifuge tests were simulated.

4.8.1.2 CEL model

The configuration and boundary conditions of the CEL model are similar to those shown in Figure 4.28. Most of the model details are the same in Section 4.7.1.2. Only the different settings are provided here. The values of B_1 and B_2 as illustrated in Figure 4.28 were both set to be $5D$ and the depth of soil h was also $5D$. The void above the soil had a height (h) of $1.25D$. The minimum element size was $0.05D \times 0.05D \times 0.05D$ and the total number of Eulerian elements in the model was 25000. The CEL simulations were conducted in the following four steps.

- Restrain the Eulerian material from flowing outside the predefined dimensions.
- Apply a body force that represents the submerged unit weight of the soil, and at the same time restrain the movement of the pipe in all directions.
- Apply a vertical force representing the weight of the pipe and release all the constraints (except for rotation) on the pipe to allow for penetration.
- Apply cyclic lateral motions to the pipe using an amplitude curve provided by Abaqus. The horizontal loading rate was 0.1Hz for all the tests.

4.8.2 Results: Cyclic lateral loading with fixed vertical load

The pipe in test KC05 was firstly pushed to an embedment of $0.1D$, after which two stages of cyclic loading were simulated. The constant vertical load during the cyclic lateral loading was kept as 2.17 kN/m in prototype scale and the amplitudes used for the lateral displacement cycles can be found in Figure 4.33a, where the trajectory of the pipe invert is plotted. The evolution of the pipe embedment during the lateral loading cycles is presented in Figure 4.33b, and very good agreement with the centrifuge data can be observed. With the strain softening effect incorporated into the model, SLA can make a satisfactory prediction of the pipe embedment. CEL results are also presented,

and are found to slightly underestimate the embedment of the pipe. Of interest is that the simulation using ideal soil largely overestimates the pipe embedment, even though much stronger soil should be present than in the softening soil case. This can be attributed to the fact that during the cyclic lateral loading, the pipe-soil contact conditions might change from unbonded to bonded as the soil around the pipe is softened and collapses onto the pipe. Such behaviour has been confirmed by observation of the centrifuge model tests reported by Cheuk and White (2009) (Figure 2.3). It can be observed in the SLA simulations using softening soil (Figures 4.34a and 4.34b), but cannot be captured in the ideal soil case (Figure 4.34c).

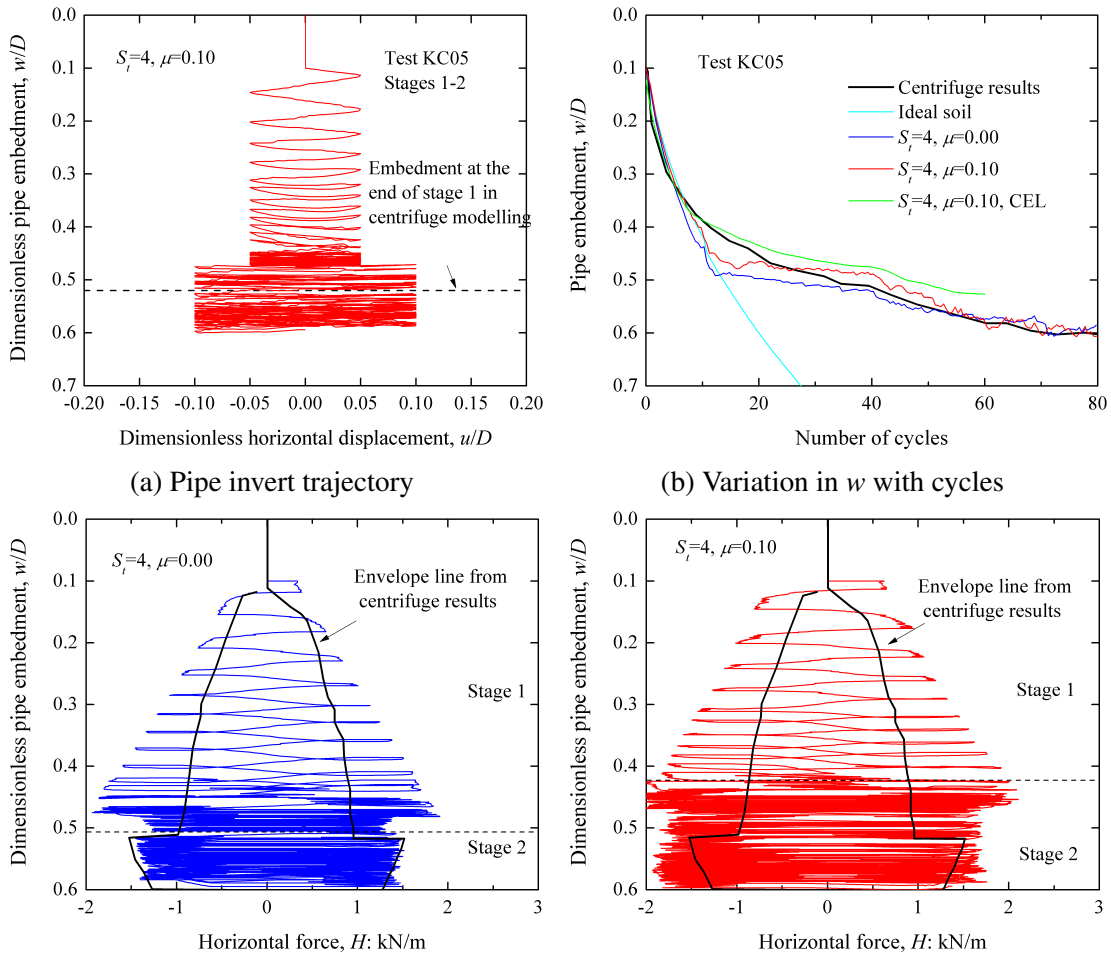

(a) Pipe invert trajectory

(b) Variation in w with cycles

(c) Variation in lateral load: rate-independent

(d) Variation in lateral load: rate-dependent

Figure 4.33 Loading response of the pipe in test KC05

Figures 4.33c and 4.33d show the horizontal load exerted on the pipe during the lateral oscillations. The lateral resistance increases gradually in the first 10 cycles as the pipe penetrates deeper into the soil. During this stage, SLA predicts much higher resistance

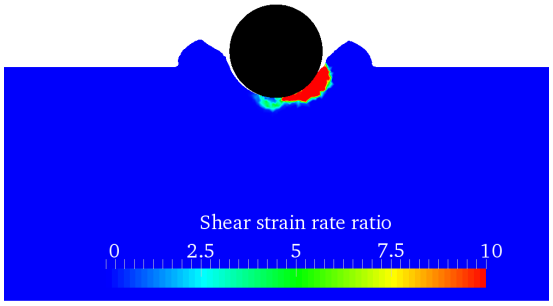

(a) 5 cycles: softening soil

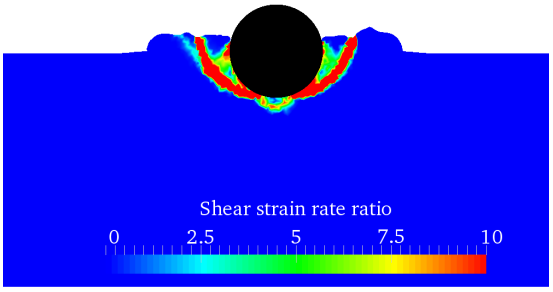

(b) 15 cycles: softening soil

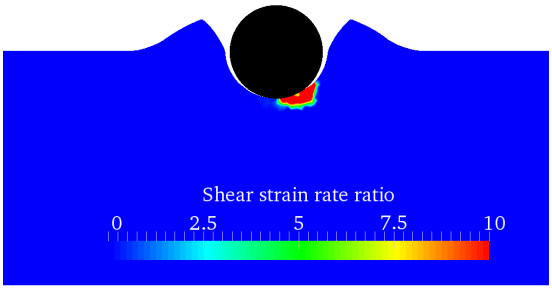

(c) 15 cycles: ideal soil

Figure 4.34 Soil failure mechanisms (showing $\dot{\gamma}_{max}D/v_p$) in test KC05 in SLA model. Only part of the soil domain is shown for clarity.

than the centrifuge results. Two factors might contribute to this. The first is that the intact strength of the soil at shallow depth in the SLA model (with its assumed linear variation of strength with depth) is much higher than that in the centrifuge test, according the T-bar test results. The second is that the transition of pipe-soil contact conditions from unbonded to bonded takes place much earlier in the centrifuge model test than in the SLA simulations due to the presence of weaker soil (see Figure 4.33b). Once bonded conditions have been achieved in the SLA simulations, the lateral resistance reduces with the number of loading cycles at the same oscillation amplitude, and a sharp increase can be seen when the lateral oscillation amplitude increases. After that, the lateral resistance reduces again with continuing loading cycles. This behaviour is consistent with that observed in the centrifuge modelling and it can be found from Figure 4.33c that the lateral resistance predicted by SLA is very close to that obtained in the centrifuge test for the remaining 70 loading cycles. The simulation with rate-dependent soil (Figure 4.33d) generates slightly higher soil resistance throughout the cyclic loading process.

4.8.3 Results: Cyclic lateral loading with variable vertical load

In tests KC06 and KC07, the pipe was pushed to an embedment of $0.05D$, after which constant amplitude lateral cyclic motions were applied. The oscillation amplitudes were $0.05D$ and $0.10D$ for KC06 and KC07 respectively. Four loading stages, each with 20 lateral cycles under a different vertical load, were applied. The same loading history as reported by Cheuk and White (2009) was used and the vertical loads for each stage are listed in Table 4.6. The predicted trajectory of the pipe invert for the two tests can be seen in Figures 4.35a and 4.36a.

Table 4.6 Vertical load on the pipe during the oscillations Cheuk and White (2009)

Tests	KC06, V: kN/m	KC07, V: kN/m
Stage 1, 20 cycles	0.39	0.41
Stage 2, 20 cycles	1.14	1.16
Stage 3, 20 cycles	2.08	2.11
Stage 4, 20 cycles	3.13	3.13

Figure 4.35b shows the embedment of the pipe with lateral loading cycles, and good agreement between SLA and the centrifuge results can be found. After the completion of each loading stage of 20 cycles, a rapid increase in the penetration rate can be observed due to the step increase of vertical load. Accordingly, the lateral resistance on the pipe, as shown in Figure 4.35c, increases gradually with the pipe embedment, which is attributed to the increase in soil strength with depth as well as the higher vertical load exerted on the pipe. The simulation with rate-dependent soil makes a better prediction of the pipe embedment, while that with rate-independent soil slightly overestimates it. The lateral resistance data from test KC06 in the centrifuge test is not available. The embedment of the rate-independent case is larger than the rate-dependent case, leading to higher intact soil strength at invert level. It is, however, found that the latter case still produces considerably higher resistance than the former.

Figure 4.36 shows the loading response of test KC07. Similar observations to test KC06 can be made. Again, the rate-dependent case gives a very satisfactory prediction of the pipe embedment history but yields lateral resistances about 20% higher than the centrifuge results as illustrated in Figure 4.36d. The lateral resistance in the rate-independent case

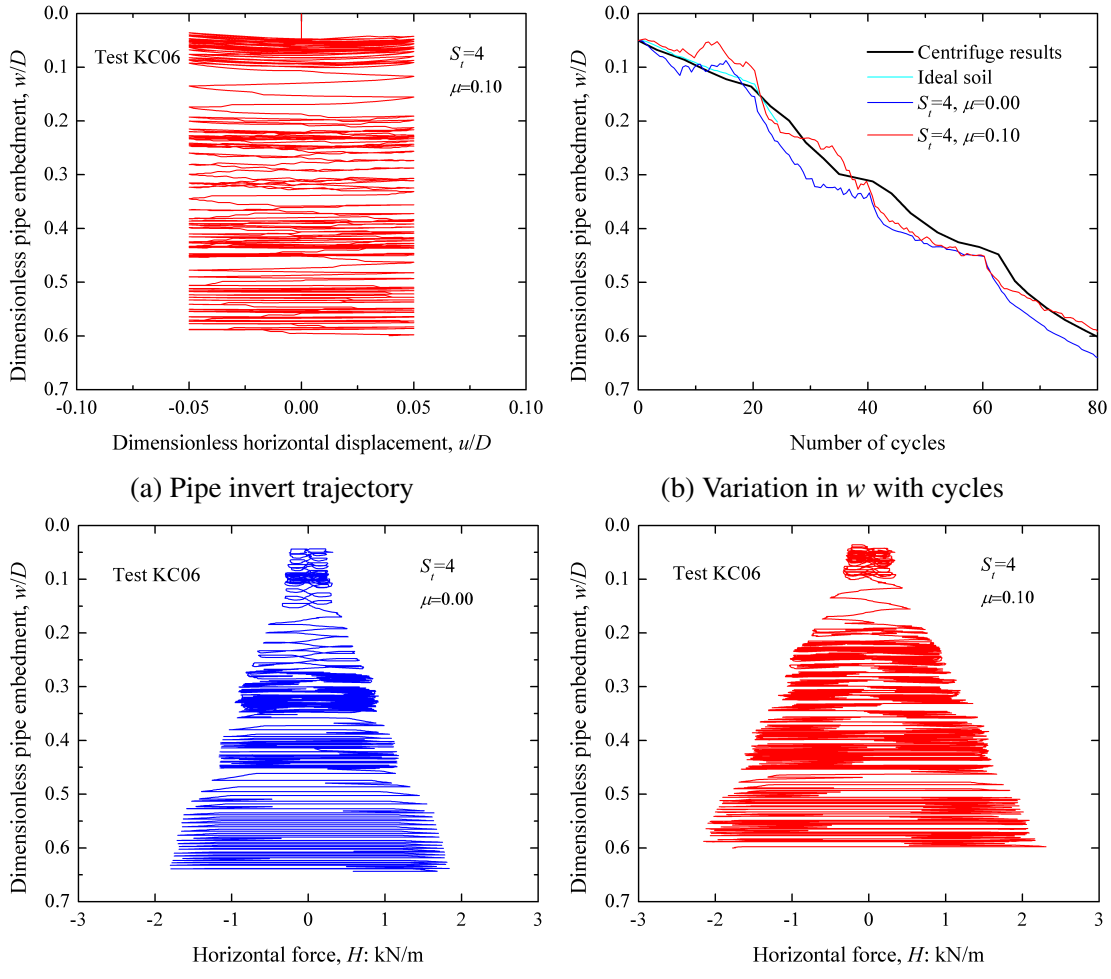

(a) Pipe invert trajectory

(b) Variation in w with cycles

(c) Variation in lateral load: rate-independent

(d) Variation in lateral load: rate-dependent

Figure 4.35 Loading response of the pipe in test KC06

(Figure 4.36c) provides more reasonable agreement with the centrifuge data. However, it can be seen in Figure 4.36b that the pipe in the rate-independent case dives very quickly into the soil at the last loading stage, indicating that the pipe might become buried at this stage.

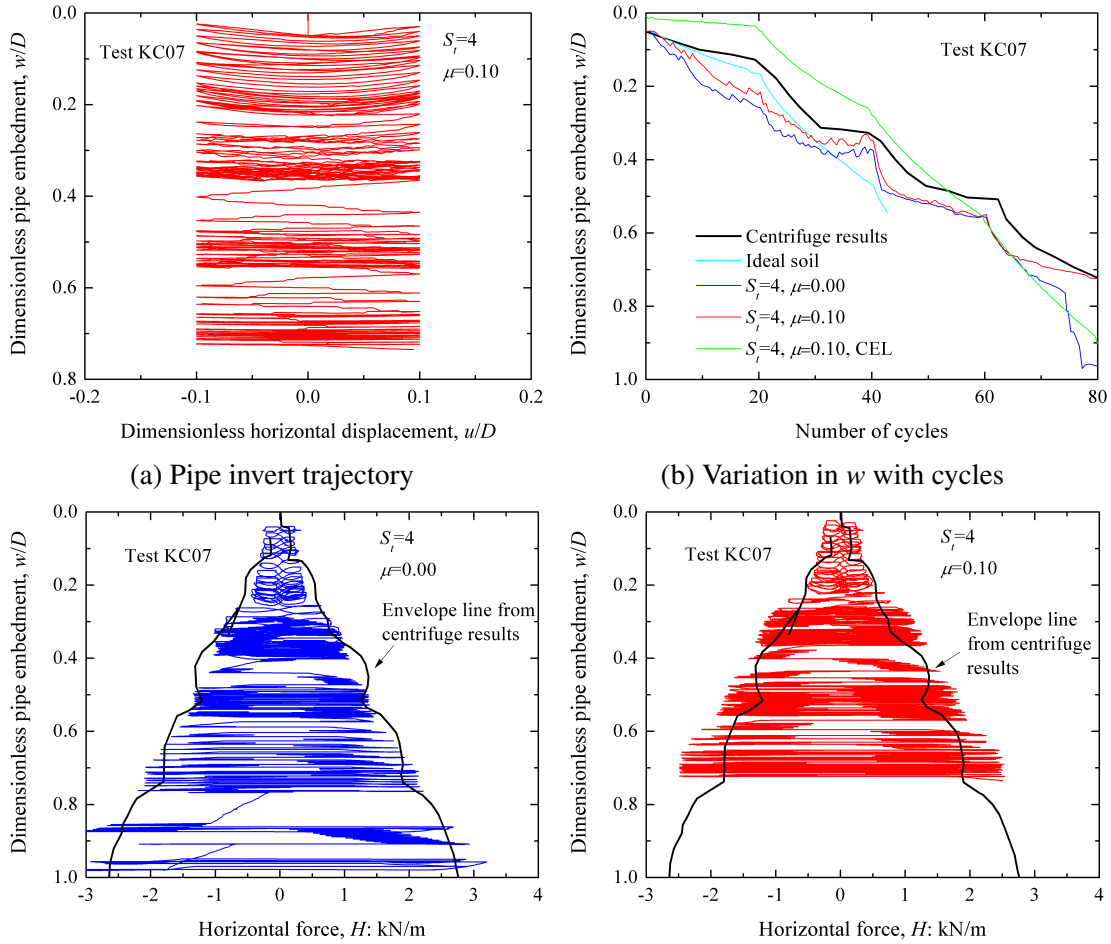

(a) Pipe invert trajectory

(b) Variation in w with cycles

(c) Variation in lateral load: rate-independent

(d) Variation in lateral load: rate-dependent

Figure 4.36 Loading response of the pipe in test KC07

Figure 4.37 presents the softening factor of the soil at different stages of the loading in test KC07. The SLA results obtained from both the rate-independent and rate-dependent analyses are provided for comparison. The soil around the pipe is fully remoulded (softening factor=$1/S_t = 0.25$) after the cyclic loading. It can be clearly seen that the deforming region with $\mu = 0.10$ is larger due to the rate effect (enlarged sliplines). A more profound difference can be observed at the end of the loading, where the pipe in the rate-independent case is totally buried by the surrounding soil, which also reveals the ability of SLA to deal with extreme deformations. Of interest is that the vertical force that drives the pipe to

be buried is 3.13kN/m, which is only slightly greater than the nominal soil buoyancy of 3.016kN/m.

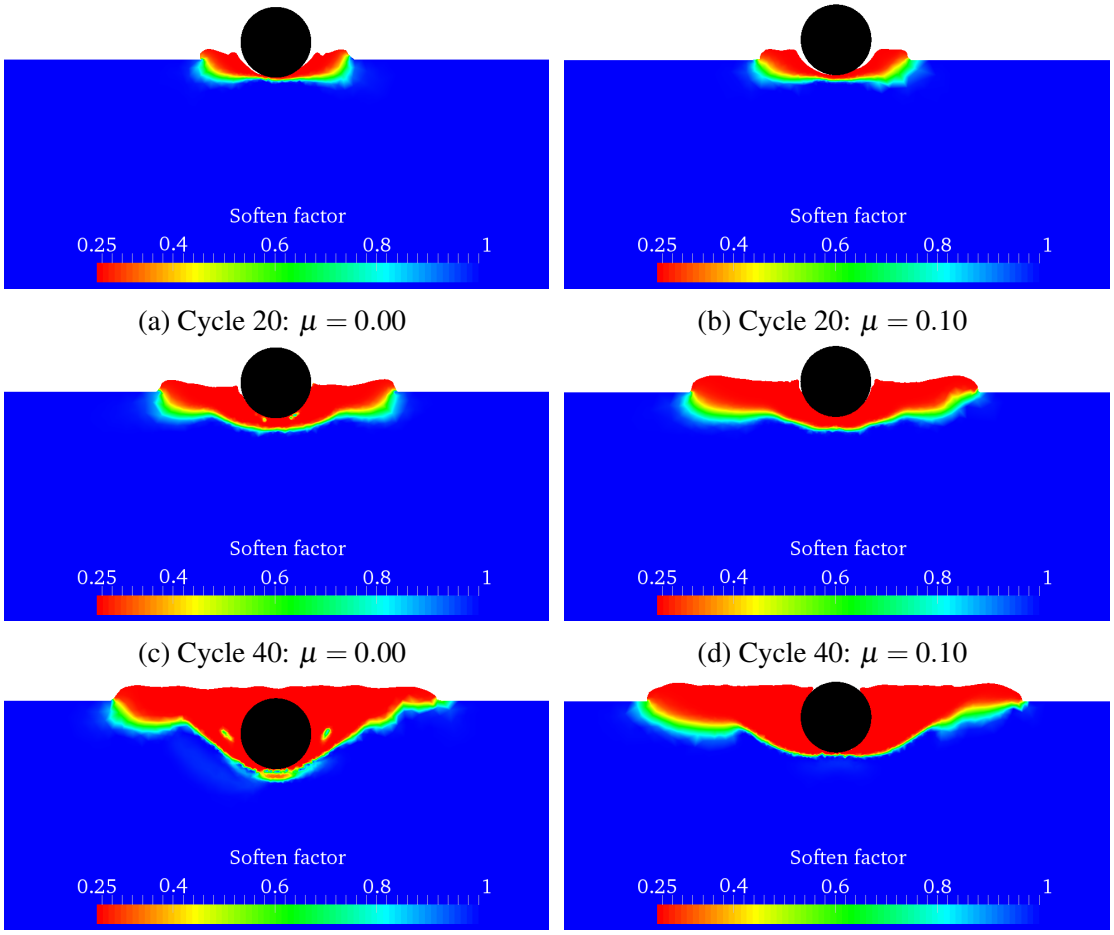

(a) Cycle 20: $\mu = 0.00$ (b) Cycle 20: $\mu = 0.10$

(c) Cycle 40: $\mu = 0.00$ (d) Cycle 40: $\mu = 0.10$

(e) Cycle 80: $\mu = 0.00$ (f) Cycle 80: $\mu = 0.10$

Figure 4.37 Softening factor of the soil in test KC07

4.9 Cyclic vertical loading of a pipe

This section presents a validation study on the cyclic vertical loading response of pipelines on clay. A centrifuge model test on the cyclic vertical loading behaviour of a pipe segment was reported by Hu *et al.* (2011). The pipe section used in this test had a prototype diameter of 1m. The strength profile of the soil obtained from T-bar testing was given as $s_{u0} = 5.19z$, where z is the depth of soil. The soil sensitivity (S_t) and effective unit weight (γ') were not provided by Hu *et al.* (2011). The pipe was vertically penetrated at a constant velocity of

$0.001D/\text{s}$ to a depth of $3D$ and then several cycles of vertical motion with an amplitude of $3D$ were applied at the same loading rate.

4.9.1 Numerical details of the SLA model

The configuration and boundary conditions of the SLA model are as previously illustrated in Figure 4.21. For this problem the half-width ($B/2$) and depth (h) of the soil domain were set to be $7D$ and $6D$ respectively. The shear strength of the pipe-soil interface was set as $c = 0.5s_u$. The tensile capacity at the interface was taken to be unlimited during extraction and zero during penetration. The soil strength ($s_{u0} = 5.19z$) given by Hu *et al.* (2011) was not suitable for SLA modelling since the strength at the mudline was zero. To avoid the numerical instability that might be caused by this, the soil strength in the SLA model was defined as $s_{u0} = 1 + 4.8z$. This approximation was chosen so that the initial unsoftened soil strength at the depth of $3D$ in the SLA model was the same as that in the centrifuge test. The soil was assigned a submerged unit weight of 6kN/m^3, which is a typical value for seabed soils in deep water. Three values of the rate parameter (μ) were chosen as 0.00, 0.05 and 0.10 to examine the effect of strain rate dependence in this test. The parameters concerning the strain softening effect were 3.3 and 10 for S_t and ξ_{95} respectively.

A normalised incremental displacement ($\delta d/D$) of 0.5% was imposed on the pipe during each penetration and extraction. The minimum element area used in the model was $0.0005D^2$. These values were chosen based on preliminary studies and are small enough for SLA to yield reliable results.

4.9.2 Results

Figure 4.38 shows the force-displacement relationship of the pipe involving cyclic penetration and extraction. Both model test and numerical results are presented for comparison. The numerical curve ($\mu = 0.05$) that best matches the centrifuge curve is presented in Figure 4.38a, with the data obtained from the whole cyclic loading process being provided; while Figure 4.38b presents test data for the initial penetration and extraction only, along with SLA simulations using various soil parameters. It is seen in Figure 4.38a that satis-

factory agreement between the numerical simulation and the centrifuge test results can be achieved almost throughout the loading. An exception can be seen at the initial stage of extraction, where a peak resistance is achieved by the pipe immediately in the SLA simulation due to the absence of any elastic response, and the assumption of unlimited tensile capacity at the pipe-soil interface.

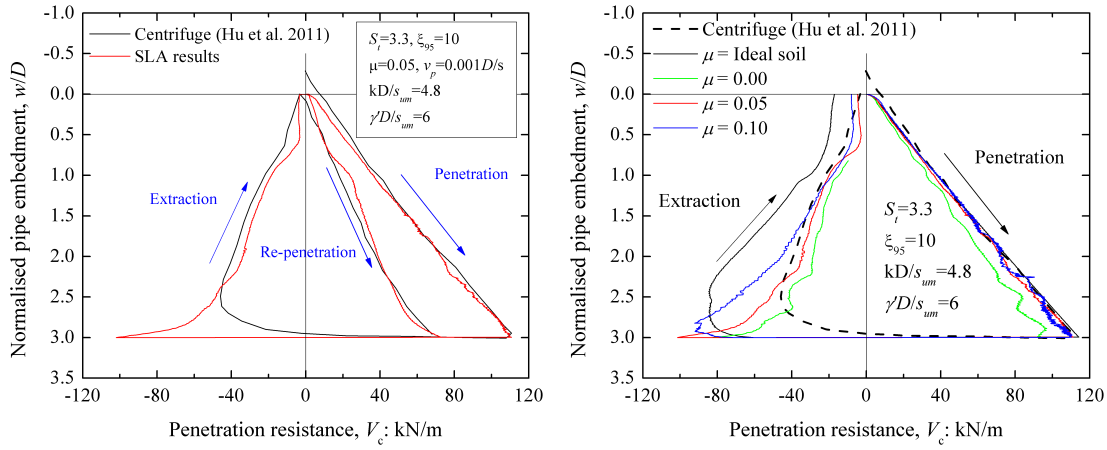

(a) $\mu = 0.05$ (b) Varied μ

Figure 4.38 Comparison of vertical cyclic loading results between centrifuge test and SLA

During the model test, a maximum resistance of 113 kN/m is achieved upon reaching the target embedment of $3D$. Before that, the penetration resistance almost increases linearly with embedment. All the numerical curves in Figure 4.38b, except that corresponding to the rate-independent soil with softening (denoted $\mu = 0$), agree very well with the centrifuge data at this stage. A slight difference is that, in the centrifuge test, non-zero vertical resistance is achieved by the pipe before any penetration takes place. Whether this resistance arises from buoyancy is not clear.

When the extraction begins, the curve corresponding to $\mu = 0.05$ provides the most satisfactory agreement with the centrifuge test data. However, a peak resistance is achieved by the pipe immediately in SLA modelling due to the reasons previously discussed. This leads to somewhat unrealistic behaviour compared to the centrifuge results, where a short distance of about $0.3D$ is needed to mobilise the peak resistance of about 46kN/m. After the pipe invert reaches an elevation of $2.4D$, the numerical curve ($\mu = 0.05$) starts to match the centrifuge curve satisfactorily. For all the cases with strain softening being considered (Figure 4.38b), the soil resistance is found to increase with the rate parameter μ throughout

the extraction process, and a peak resistance is achieved immediately when extraction begins.

Figure 4.39 shows the soil deformation at different stages during the extraction in the SLA simulation with $\mu = 0.05$. The left half of each figure shows the softening factor of soil while the right half shows the normalised shear strain rate $\dot{\gamma}_{max}D/v_p$ as well as the mesh. Localised failure mechanisms are observed until the pipe invert reaches a depth of $2.5D$ (Figures 4.39a to 4.39b). With further extraction, global mechanisms are developed with sliplines extending to the free surface. An almost vertical narrow band with intense shearing can even be observed in Figure 4.39c. After the pipe has been extracted to the mudline (Figure 4.39g), an area with almost fully remoulded soil is left beneath the pipe invert. Therefore, it is reasonable to expect that the soil resistance during re-penetration should be far less than that during initial penetration, and indeed this proves to be the case (Figure 4.38a).

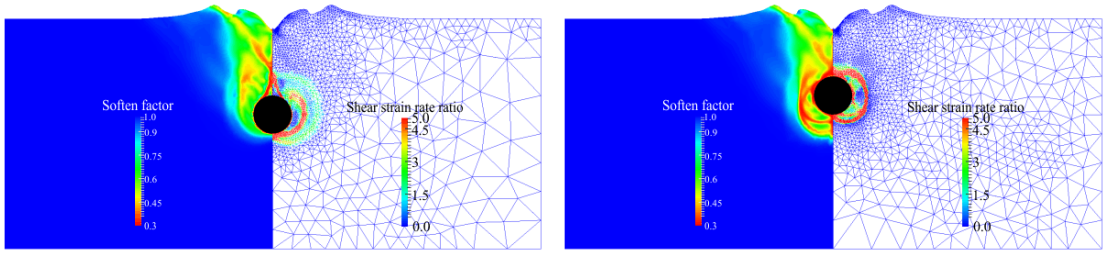

(a) w/D =3.0 (↑)

(b) w/D =2.5 (↑)

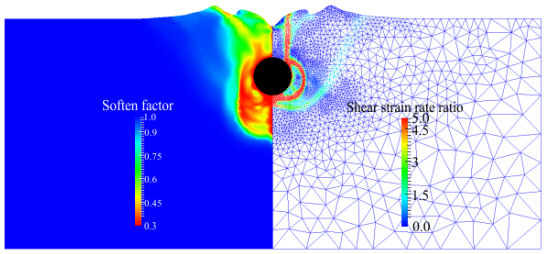

(c) w/D =2.0 (↑)

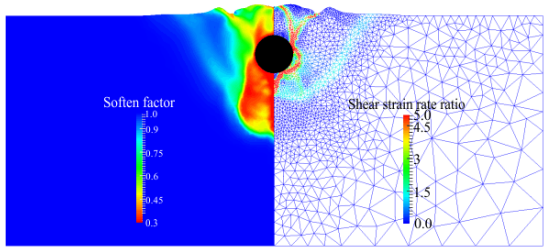

(d) w/D =1.5 (↑)

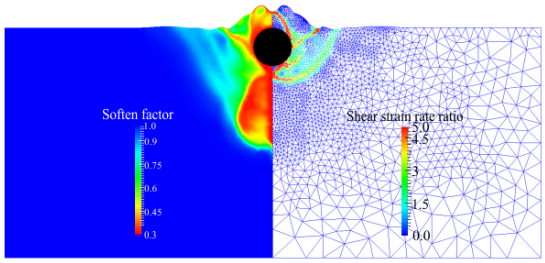

(e) w/D =1.0 (↑)

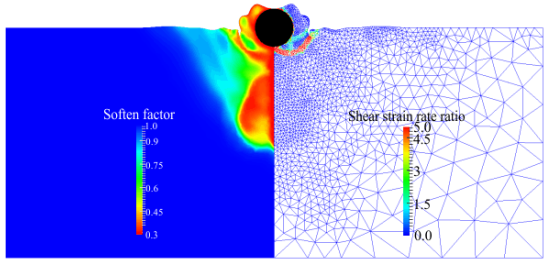

(f) w/D =0.5 (↑)

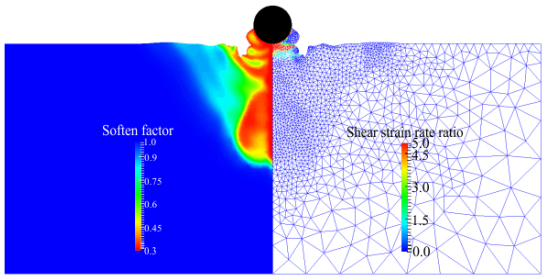

(g) w/D =0.0 (↑)

Figure 4.39 Deformation of the soil during cyclic vertical loading of a rigid pipe. Left half side shows softening factor and right half side shows the failure mechanism ($\dot{\gamma}_{max}D/v_p$) of the soil.

4.10 Summary

This chapter has presented a detailed validation of the SLA method introduced in Chapter 3. Two categories of large deformation problems were analysed. The first involved widely studied benchmark cases where analytical solutions have been produced, and included the buried plate problem and the wedge indentation problem. The second category involved the vertical and lateral loading response of surface pipelines where results of model tests, mostly centrifuge tests, have been published. The aim of the study is to demonstrate that the SLA model produces appropriate answers for both theoretical plasticity problems as well as for pipe-soil interactions on undrained clay. A complementary numerical tool, the CEL approach, was also used to analyse a number of these problems. Detailed comparisons were made between the two numerical tools to explore the potential of the SLA approach. The validation results are qualitatively assessed in Table 4.7 with computing times for the different analyses provided in Table 4.8. The analyses chosen for the comparison of computing time are the default cases for each problem studied. The main findings of this chapter are as follows.

- For the benchmark problems with analytical solutions, perfect agreement was found between the SLA simulation results and the theoretical solution indicating the approach is robust. Comparisons with the CEL results show that the field variables in the SLA method are treated reliably, providing confidence that effects such as strain softening of undrained clay can be handled appropriately.

- A constitutive model was implemented to take into account the effects of strain rate and strain softening on the undrained soil strength. The SLA approach generated very satisfactory results compared to model test results. This was demonstrated for both monotonic and cyclic loading behaviour of a pipe segment, subjected to vertical or lateral motions.

- For the parameters related to strain softening and strain rate effects, δ_{rem} $(1/S_t)$ can be conveniently obtained from penetrometer tests, while ξ_{95} and μ are relatively hard to quantify. The benchmark studies against centrifuge modelling results suggest

Table 4.7 Validation results

Loading tests	Compared with	Comparison results
Anchor plate	Analytical (Rowe and Davis, 1982)	Excellent
Wedge	Analytical (Hill *et al.*, 1945)	Excellent
	CEL	Very good
Strip footing	Analytical (Prandtl, 1921)	Excellent
	CEL	Very good
Pipe (shallow penetration)	Centrifuge (Dingle *et al.*, 2008)	Very good
	CEL	Very good
Pipe (deep penetration)	Small-scale test (Lee, 2012)	Good
	CEL	Very good
Pipe (monotonic lateral loading)	Centrifuge (Dingle *et al.*, 2008)	Very good
	CEL	Good
Pipe (cyclic lateral loading)	Centrifuge (Cheuk *et al.*, 2008)	Good
	CEL	Good
Pipe (cyclic vertical loading)	Centrifuge (Hu *et al.*, 2011)	Very good

Table 4.8 Computational times of SLA and CEL methods

Loading tests	SLA time, s [1]	CEL time, s [2]
Wedge	1399 (4 cores)	13846 (4 cores)
Pipe (shallow penetration)	780 (4 cores)	7935 (16 cores)
Pipe (deep penetration)	13661 (4 cores)	61520 (32 cores)
Pipe (monotonic lateral loading)	11094 (4 cores)	43364 (32 cores)

[1] 3 to 4 analyses running in parallel, 4 core PC, 2.93GHz Xeon(R), 4GB RAM, Windows 7.

[2] 1 analysis running at a time, 16/32 core supercomputer, 2.0GHz Xeon SandyBridge/Ivybridge, 64GB RAM, Red Hat Enterprise Linux 6.

that a value of 10 for ξ_{95} and a range of 0.05-0.10 for μ can yield the best results in numerical modelling.

- In general, the computational cost of the SLA method is a small fraction (2-10%) of that for the CEL approach. It was difficult to make an objective comparison of computing times between SLA and CEL for all problems investigated in this Chapter as, whilst the SLA analyses were performed on a desktop, most CEL analyses could only be completed on a supercomputer. Typically 3 to 4 parallel SLA simulations were performed at the same time on a 4-core desktop, whereas most CEL analyses were performed with the full use of 16 to 32 cores (see Table 4.8).

- Mesh distortion, which is one of the main concerns for conventional FE models for large deformation problems, could be avoided by regularly remeshing of the model. The meshing strategy used for the SLA approach proved to be highly reliable, and in particular the areas with intense shearing were targeted with higher mesh densities. Since no mapping of stresses is need for the interpolation stage, the SLA method has the significant advantage of being numerically stable.

- The treatment of the external boundary for the model in the SLA simulation inevitably introduces some change in volume for the (assumed) incompressible material. However, for all the problems investigated in the chapter, the resulting volume change introduced is found to be very limited, and unlikely to significantly influence the overall model response.

Chapter 5

Vertical pipe-soil interaction: prediction of pipe embedment

This chapter presents a numerical study investigating the vertical penetration behaviour of a rigid pipe into soft clay. The pipe is penetrated from the mudline to a very deep embedment of three pipe diameters to capture the pipe behaviour related to different types of failure mechanisms. The penetration resistance of the pipe at shallow embedments is relevant to the prediction of the embedment of on-bottom pipelines. Typically they are embedded by between 10% and 50% of their diameter due to self-weight and dynamic motions during laying (Westgate *et al.*, 2010, 2009). For deeper embedments, this study is more relevant to the pipe-soil interactions of steel catenary risers in the touchdown zone (TDZ, Figure 2.1), where the pipe embedments are much higher than on-bottom pipelines due to the stress concentration effect and the continuous dynamic motions during operation. Typically the pipe embedment at the TDZ can be more than one pipe diameter (Bridge and Howells, 2007; Wang *et al.*, 2014).

The influences of the undrained strength gradient, unit weight and other parameters related to strain softening and strain rate effects are examined. The aim of this chapter is to develop a simplified model for predicting pipe embedment under purely vertical loading, with the effects of the various influencing factors being quantified.

5.1 Description of the numerical model

Both sequential limit analysis (SLA) and coupled Eulerian-Lagrangian (CEL) methods were used in this study, although the parametric study results presented were mainly obtained from SLA modelling. Validation studies of these two methods for pipe penetration problems have been demonstrated in Sections 4.5, 4.6 and 4.9. In this chapter, detailed comparisons of typical pipe penetration results using the two methods are made to demonstrate the accuracy and robustness of the SLA modelling before the parametric study results are presented.

Table 5.1 Parameter values used for the parametric study

Parameter	Default value	Other values
Pipe diameter, D: m	1.0	-
Shear strength of soil at mudline, s_{um}: kPa	1.0	-
Shear strength gradient, k: kPa/m	0	1, 2, 3, 4, 5, 10, 20
Submerged unit weight of soil, γ': kN/m^3	3	0, 1, 2, 5, 10, 20
Pipe/soil interface shear strength, τ_{int}: kPa	0.5	0.0, 0.2, 0.8, 1.0
Remoulded strength ratio of soil, $\delta_{rem} = 1/S_t$	0.3	1, 0.5, 0.2, 0.1, 0.05, 0.02, 0.01
Ductility parameter of soil, ξ_{95}	20	10, 50
Viscosity parameter of soil, μ	0	0.05, 0.10, 0.15, 0.20
Pipe displacement rate, v_p: m/s	0.003	0.0003, 0.03
Reference shear strain rate, $\dot{\gamma}_{ref}$: s^{-1}	3×10^{-6}	-

The reference values of parameters used in the parametric study are given in Table 5.1, where other values that might be used are also provided. All of the results below are presented in dimensionless form so as to be generalised to other parameters. It is noteworthy that the parameters chosen for the default cases vary with the problems to be investigated, more details are provided in each section where parametric results are presented.

5.1.1 Numerical details of the SLA model

In the SLA simulations, a 2D plane strain model was used and only half of the model was considered, taking advantage of symmetry. The model configuration and boundary conditions are illustrated in Figure 4.21. Most of the SLA model details concerning the pipe penetration are as provided in Section 4.5.1.1. The half width ($B/2$) and depth (h)

of the soil domain were $7D$ and $6D$ respectively. These dimensions were chosen based on preliminary studies to ensure that the soil domain comfortably enclosed the failure mechanism throughout the analysis. The maximum shear stress at the pipe-soil interface (τ_{max}) was set as αs_u, where α is the interface roughness factor and s_u is the operative shear strength of the soil adjacent to the pipe. In this study s_u was used instead of s_{um}, which is the initial shear strength of the soil at the mudline, to consider the variation of shear strength of the pipe-soil interface. A value of 0.5 was adopted for α for all the parametric studies if not stated otherwise. The degradation and enhancement of the soil strength caused by strain softening and strain rate were incorporated into the model by modifying the rigid-plastic Tresca material according to Equation 2.9 (Einav and Randolph, 2005; Zhou and Randolph, 2007) as described in Section 2.2.2. The incremental displacement used to update the model configuration was taken as $0.005D$. This value was proven to be small enough for SLA to yield reliable results, as discussed in Chapter 4. The minimum element area (A_{min}) in the model was chosen to be $0.00025D^2$.

Most of the SLA simulations in this study were performed in a pushed-in-place (PIP) manner in order to consider the change in free surface geometry as well as the changing pipe-soil contact conditions. In addition to that, another type of loading behaviour was also studied, where the pipe was pre-embedded inside the soil domain and then vertically displaced through a distance of $5D$, as illustrated in Figure 5.1. This type of wished-in-place (WIP) analysis was performed to complement the PIP analyses in the 'residual' stage (where the pipe was fully covered by the surrounding soil) but without considering the influence of geometry change of the soil surface. The effects of strain rate and strain softening could thus be evaluated with stable and localised failure mechanisms being developed throughout the analysis.

5.1.2 Numerical details of the CEL model

These analyses use the CEL formulation in-built in Abaqus, as introduced in Section 3.4. A user subroutine VUMAT was developed to account for the variation in soil strength according to Equation 2.9 (Einav and Randolph, 2005; Zhou and Randolph, 2007). More

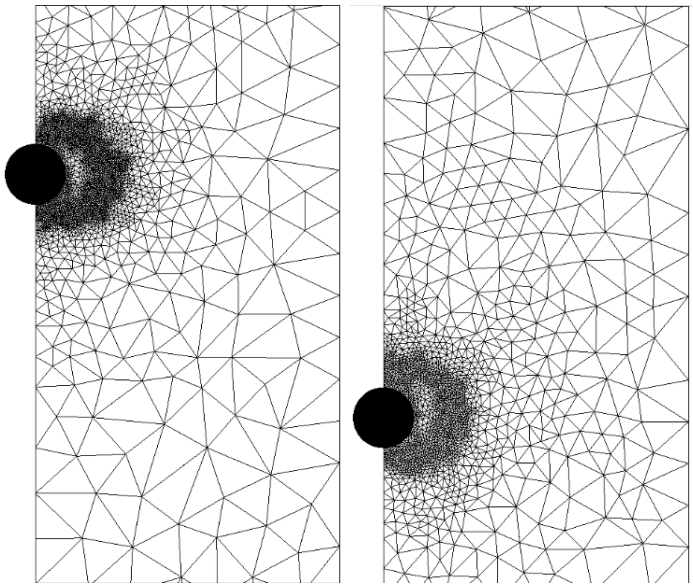

(a) Before displacement (b) After displacement

Figure 5.1 Initial and final configurations of the SLA model for wished-in-place case

details of this subroutine can be found in Section 3.4.3.2. The Eulerian domain, shown schematically in Figure 4.22, was $10D$ in half-width ($B/2$) and $8D$ in depth (h). These dimensions were chosen based on preliminary studies to evaluate and minimise boundary effects. Numerical details of the CEL model are provided in Section 4.5.1.2. The soil and pipe parameters were chosen according to Table 5.1. The minimum mesh size was chosen to be $0.04D \times 0.04D \times 0.04D$ and the penetration rate was set as $0.05D/\text{s}$, unless stated otherwise. The Eulerian domain had a total number of 18500 brick elements. The analysis was conducted in the following two steps.

- Apply a body force that represents the submerged unit weight of the soil, and at the same time restrain the movements of the pipe in all directions. This body force was absent if weightless soil was simulated. Although not directly controlled, the ratio of horizontal to vertical stress in the soil was approximately equal to 1 throughout this stage.

- Penetrate the pipe at a constant velocity to the required position.

5.2 Comparison between typical SLA and CEL results

Both SLA and CEL were used to run a large number of analyses to investigate the deep penetration behaviour of a pipe into undrained clay. For the sake of clarity, only the results obtained from SLA are systematically analysed and presented, while CEL results are only provided as a complement wherever necessary. Three typical cases are selected in this section to conduct a very careful comparison between SLA and CEL. The parameters adopted in these simulations are listed in Table 5.2, where the computing times for SLA and CEL analyses are also provided. Typically 3 to 4 parallel SLA simulations were performed at the same time on a 4-processor desktop while most CEL analyses were performed with full use of 16 processors. In general, for this kind of analysis, the advantage of SLA in terms of computational cost over CEL is not significant.

Table 5.2 Parameters used for comparison between SLA and CEL analyses

	μ	δ_{rem}	ξ_{95}	kD/s_{um}	$\gamma' D/s_{um}$	SLA time, s *	CEL time, s
Case 1	0	1	10	0	3	7841 (4 cores)	2261 (16 cores)
Case 2	0	1	10	3	3	6839 (4 cores)	7470 (16 cores)
Case 3	0	0.3	10	0	3	7199 (4 cores)	2136 (16 cores)

* 4 core PC, 3 to 4 analyses running in parallel

Figure 5.2 shows the comparison of penetration resistance for the three cases using both SLA and CEL results. The curves obtained from the two methods are very close for all three cases, though SLA generates much more stable resistances than CEL with the corresponding curves showing less jaggedness. There is a critical phase for the soil with $kD/s_{um} = 0$ where the normalised resistance drops and then rises again to a constant value, which differs from the published WIP simulation results presented by Martin and White (2012). More detailed comparisons are made in Sections 5.2.1 to 5.2.3 for the three cases in terms of normalised maximum shear strain rate $\dot{\gamma}_{max}D/v_p$, accumulated plastic shear strain ξ and intact shear strength s_{u0}.

5.2.1 Case 1

Figure 5.3 illustrates the distribution of $\dot{\gamma}_{max}D/v_p$ in the soil at different stages of pipe penetration in Case 1. The soil used in Case 1 is homogenous soil without softening. By

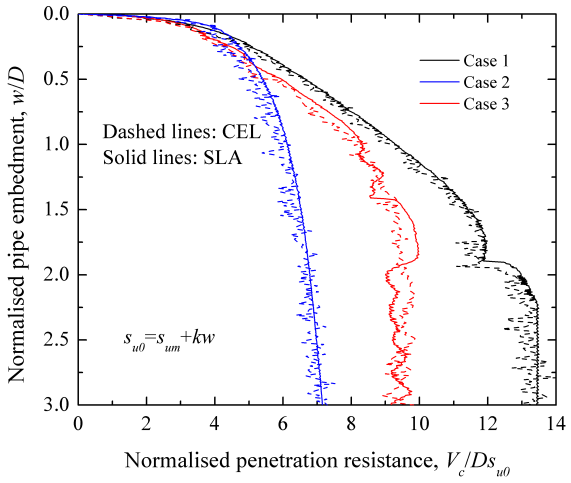

Figure 5.2 Comparison of penetration resistance between typical SLA and CEL results. $\mu = 0$, $\xi_{95} = 10$ and $\gamma' D/s_{um} = 3$.

visualising $\dot{\gamma}_{max}D/v_p$, the failure mechanisms can be conveniently observed. The deformed soil configuration as well as the failure mechanisms obtained from the two methods are extremely similar throughout the loading process. An exception is that in the CEL results, shear deformation can be seen in the area away from the region where intense shearing takes place. This difference is reasonable since elastic response is also modelled in the CEL simulation, which cannot be captured by the rigid-plastic material used in SLA modelling.

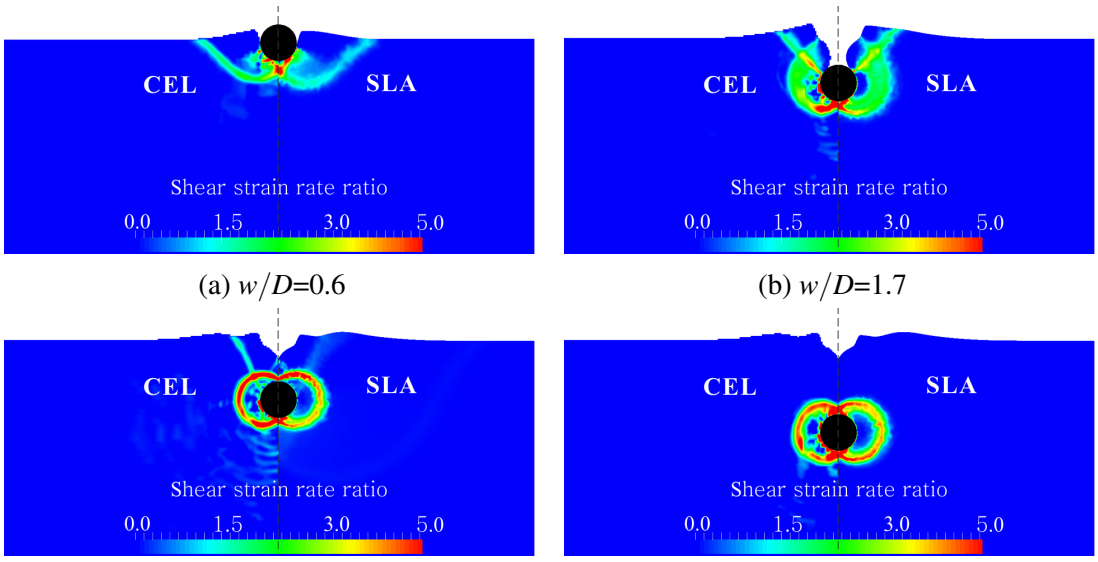

(a) w/D=0.6 (b) w/D=1.7

(c) w/D=2.0 (d) w/D=3.0

Figure 5.3 Soil failure mechanisms (showing $\dot{\gamma}_{max}D/v_p$) in Case 1

At shallow embedment, the failure mechanism (see Figure 5.3a) is very similar to Prandtl's mechanism for a strip foundation. As the soil around the pipe flows over and

gradually backfills the region above the pipe crown, the weight of the soil above the slip line (see Figure 5.3b) exerts a downward force on the pipe, leading to a moderate reduction in the penetration resistance as shown by the Case 1 curve in Figure 5.2. With further penetration, the soil surfaces at the two sides of the pipe gradually come into contact (see Figure 5.3c), reducing the downward force exerted on the pipe, and the pipe regains some bearing capacity in response. Finally the failure mechanism becomes totally localised and constant resistance is maintained throughout the rest of penetration. The backfilling behaviour that has been reported from field test observations (Bridge and Howells, 2007) is successfully reproduced here, revealing the great potential of SLA and CEL analyses to model large deformation problems.

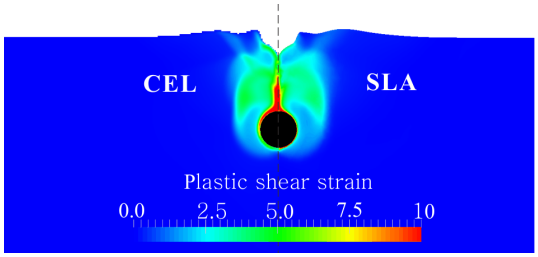

Figure 5.4 Accumulated plastic shear strain ξ at $w/D = 3$ in Case 1

Figure 5.4 shows the distribution of accumulated plastic shear strain at the end of penetration ($w/D = 3$), where an extremely similar pattern is observed between the SLA and CEL results. It is found that at shallow depth, the soil near the pipe (see the diffuse shear area in Figure 5.3a), hereafter referred to as 'surrounding soil', gains much more plastic strain compared with that in the relatively remote area (see the slip lines extending to the free surface in Figure 5.3a), hereafter referred to as 'remote soil'. For shallow pipe embedment where a global mechanism operates, both the 'surrounding soil' and 'remote soil' contribute to the bearing capacity (see Figure 5.3a); while for deep pipe embedment where the failure mechanism becomes localised, only the 'surrounding soil' contributes to the bearing capacity (see Figure 5.3d). This indicates that when the pipe penetrates deeply enough to develop a localised mechanism, strain softening will result in more significant reduction of the penetration resistance.

5.2.2 Case 2

Figure 5.5 shows the distribution of $\dot{\gamma}_{max}D/v_p$ of soil at two stages of penetration in Case 2. The soil used in Case 2 differs from Case 1 in that it has a normalised strength gradient kD/s_{um} of 3 (see Table 5.2). As shown in Figure 5.3, a global failure mechanism with slip extending to the soil surface is observed throughout the loading process. However, very satisfactory agreement is still achieved between SLA and CEL in terms of the failure mechanism as well as the shape of the deformed soil surface. The circumstances under which a localised failure mechanism can be obtained are discussed in Section 5.5.1.

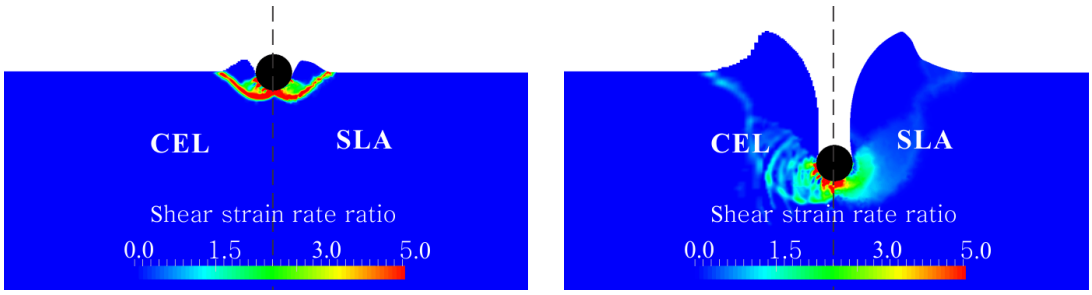

(a) w/D=0.5 (b) w/D=3.0

Figure 5.5 Soil failure mechanisms (showing $\dot{\gamma}_{max}D/v_p$) in Case 2

Figure 5.6a shows the cumulative plastic shear strain at the end of penetration in Case 2, and very good agreement between the two methods can be seen. In both analyses the area experiencing the most shearing is near the soil surfaces forming the trench beside the pipe.

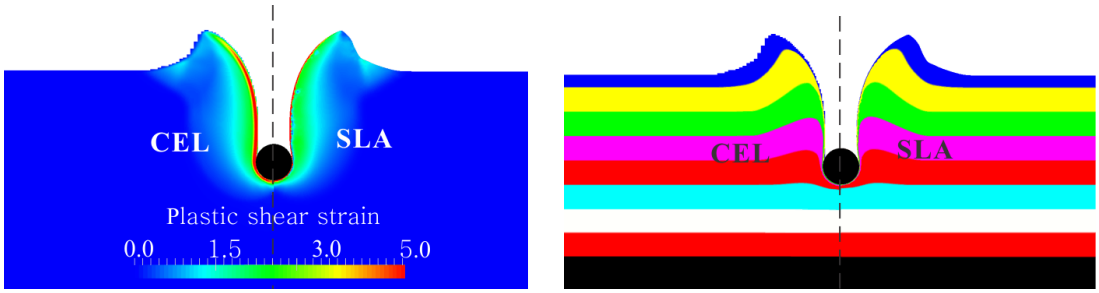

(a) Plastic shear strain (ξ) (b) Initial shear strength (s_{u0})

Figure 5.6 Distribution of field variables at $w/D = 3$ in Case 2

Figure 5.6b illustrates the distribution of intact soil strength s_{u0} of the model at $w/D = 3$. The soil is divided into several layers by s_{u0} with an interval of $2s_{um}$ from top to bottom. Each layer is assigned a different colour for visualisation. A similar pattern between the

SLA and CEL results is observed again, though the soil layers in the CEL analysis tend to be pushed downwards slightly more than in SLA. This is due to the presence of elastic deformation, which is absent in SLA modelling. Figure 5.6b also provides strong evidence that the surficial soil at the mudline is smeared onto the pipe and dragged downwards with it during the penetration. This behaviour is commonly assumed when considering the strength along the pipe-soil interface (Chatterjee *et al.*, 2012a,b; Wang *et al.*, 2009).

5.2.3 Case 3

Figure 5.7 shows the distribution of normalised shear strain rate $\dot{\gamma}_{max}D/v_p$ in Case 3, which uses a homogenous soil with the softening effect incorporated. By comparing Figure 5.7a and Figure 5.3b, backfilling of the surrounding soil is found to take place much earlier if strain softening is taken into account, indicating that strain softening helps to induce localised failure mechanisms. The agreement between the SLA and CEL results in this case is not as good as that in the ideal soil case (Case 1), but still very reasonable.

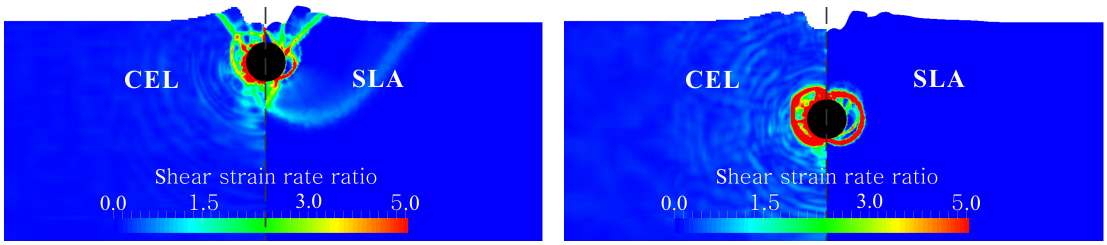

(a) w/D=1.5 (b) w/D=3.0

Figure 5.7 Soil failure mechanisms (showing $\dot{\gamma}_{max}D/v_p$) in Case 3

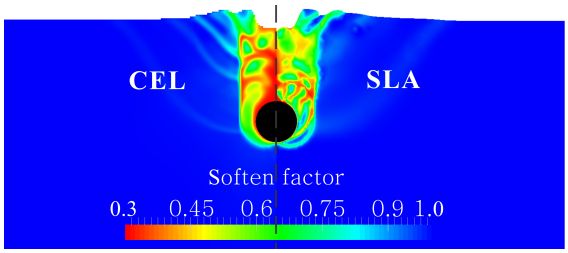

Figure 5.8 Softening factor of the soil at $w/D = 3.0$ in Case 3

Figure 5.8 shows the distribution of the soil strength softening factor at the end of penetration in Case 3. The pattern derived from SLA matches well with that from CEL in general.

5.3 Quantification of geotechnical resistance in ideal soil

The total resistance experienced by the pipe during vertical penetration may be considered as the sum of geotechnical resistance and soil buoyancy. The geotechnical resistance is usually expressed as a power law (Aubeny *et al.*, 2005) for use in routine design, so the total penetration resistance can be expressed as

$$\frac{V_c}{Ds_{um}} = a\left(\frac{w}{D}\right)^b + f_b \frac{A_s}{D^2}\frac{\gamma' D}{s_{um}} \tag{5.1}$$

where the first part of the right-hand side denotes normalised geotechnical resistance V_g/Ds_{um}; two different sets of fitting coefficients (a and b) should be used in the power law for a pipe with shallow embedment ($w/D \leq 0.5$) or deep embedment ($w/D > 0.5$), as recommended by Aubeny *et al.* (2005). The second part represents the normalised resistance contributed by buoyancy. A_s is the submerged cross-sectional area of the pipe section and $A_s\gamma'$ is the nominal buoyancy of the pipe. The buoyancy factor, f_b, is adopted to account for the enhanced buoyancy effect due to soil heave adjacent to the pipe, and a value around 1.5 is suggested by Merifield *et al.* (2009).

This section aims to propose a method to quantify the geotechnical resistance V_g of the pipe in ideal weightless soil, where V_g is only influenced by kD/s_{um} and α within the scope of this study.

5.3.1 Influence of interface roughness α

The pipe surface in the field may be smooth, for example if the pipe has an unroughened plastic insulation coating; or it may be extremely rough, for example if the pipe is coated with concrete to increase its weight and thus its on-bottom stability.

Figure 5.9a shows the variation of normalised penetration resistance V_c/Ds_{u0} with normalised embedment w/D. Five values of the roughness factor, $\alpha = 0.0$, 0.1, 0.3, 0.5 and 1.0 are considered. The soil used here has homogenous shear strength. The unit weight is set to be zero to eliminate the influence of soil buoyancy, therefore V_c equals V_g. As expected, the resistance curves show an increasing trend with α. Since it is common to quantify the geotechnical resistance using closed-form expressions suitable for use in

routine design, these curves are fitted using a power law equation as in Equation 5.1. The fitting coefficients a and b are illustrated in Figure 5.9b. Two linear expressions used to approximately quantify the effect of α on a and b are also provided in Figure 5.9b.

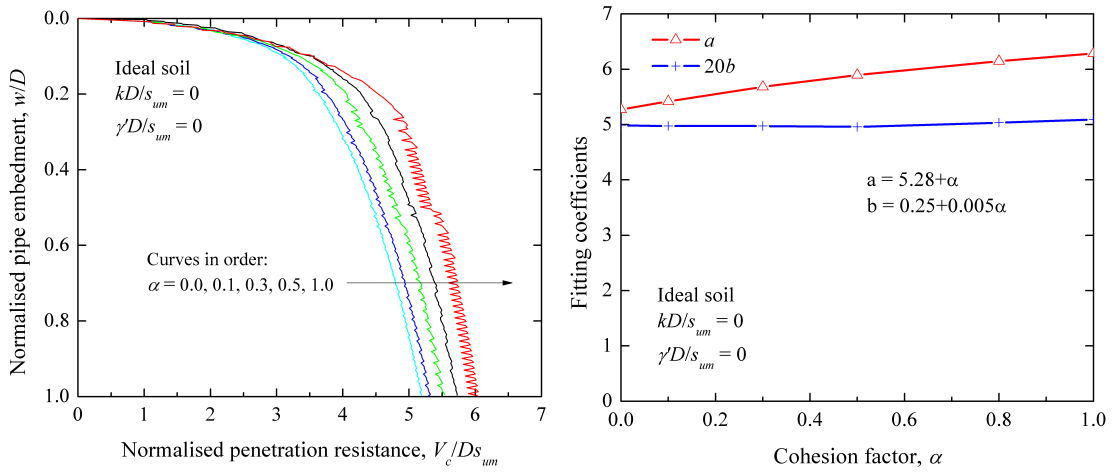

(a) Normalised resistance (b) Coefficients a and b

Figure 5.9 Influence of interface roughness on penetration resistance at shallow embedment

The coefficients a and b illustrated in Figure 5.9b are derived from data with w/D ranging from 0 to 1, and will be used to evaluate V_g in the model proposed later in this chapter. To make comparisons with previous research (Aubeny *et al.*, 2005; Merifield *et al.*, 2008b, 2009), another set of a and b are derived from data with w/D ranging from 0 to 0.5, since the results of these studies are mainly obtained from very shallow penetration modelling. The derived values of a and b are given in Table 5.3 for the extreme cases of fully smooth and fully rough interfaces. The results reported by Chatterjee *et al.* (2012a) with the effects of strain softening and strain effect accounted for are not presented for comparison, because only ideal soil (rate independent, perfectly plastic) is considered here.

Table 5.3 Comparison of coefficients a and b from literature and present study

	Smooth		Rough		Comments
	a	b	a	b	
Aubeny *et al.* (2005)	5.42	0.29	7.41	0.37	WIP
Merifield *et al.* (2008b)	5.66	0.32	7.40	0.40	WIP
Merifield *et al.* (2009)	5.30	0.25	7.10	0.33	PIP
Present study	5.53	0.27	7.07	0.32	PIP

For weightless soil, the pipe creates an open trench and it is impractical to use PIP analysis to derive the penetration resistance at very deep embedment when the pipe is buried by surrounding soil. WIP analysis was therefore conducted to provide information on pipe penetration at this stage, with the pipe pre-embedded at a depth of $3D$ and then displaced by $1D$. Since there is no change in soil geometry or strength, V_c/Ds_{um} for this sort of analysis remains constant throughout the loading (Figure 5.10). The calculated values corresponding to fully smooth and rough conditions are 9.30 and 12.01 respectively, which are consistent with the theoretical solutions of 9.20 and 11.94 derived by Martin and Randolph (2006) and Randolph and Houlsby (1984). For the default α of 0.5 adopted in the parametric study, the normalised vertical resistance is 11.06. The resistances corresponding to other values of α can be obtained to sufficient accuracy by performing quadratic or bi-linear interpolation.

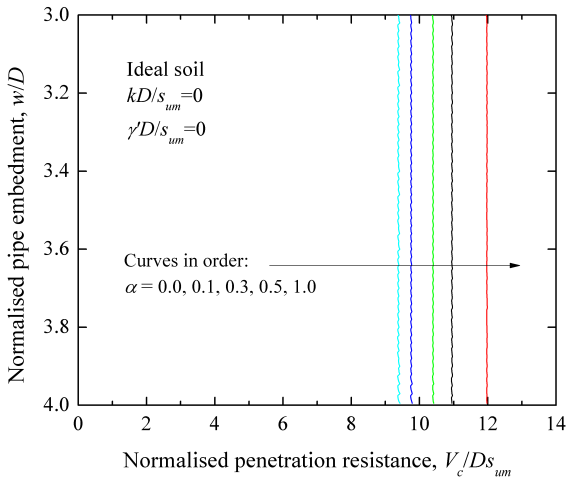

Figure 5.10 Influence of interface roughness on penetration resistance at deep embedment

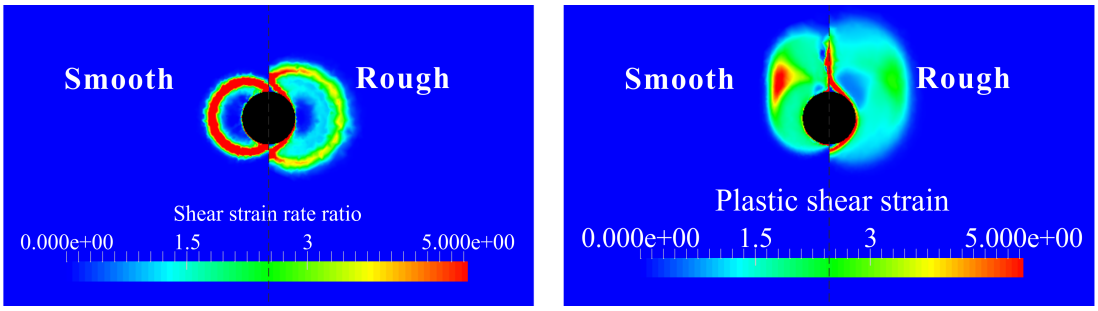

(a) Soil failure mechanism (showing $\dot{\gamma}_{max}D/v_p$) (b) Cumulative plastic shear strain ξ

Figure 5.11 Influence of interface roughness on soil deformation. Ideal soil, $k = 0$ and $\gamma' = 0$.

Figure 5.11 presents comparisons of soil deformation between the fully smooth and rough interface cases after a penetration distance of $1D$ in the WIP analysis. The pipe with the rough interface is found to develop a larger mechanism but the surrounding soil experiences less intense shearing. Small wedge blocks above and below the pipe are found to move with the rough pipe, which is consistent with the theoretical predictions mentioned above. As the surrounding soil keeps flowing around the pipe these blocks still show no shear strain at the end of loading, revealing the reliability of SLA in handling field variables when remeshing and interpolation are carried out.

5.3.2 Influence of strength gradient k

Figure 5.12a shows how the soil strength gradient, k, affects the geotechnical penetration resistance. Again, weightless soil is adopted to eliminate the soil buoyancy component of the resistance, and no strain softening or strain rate effect is considered. The roughness factor at the pipe-soil interface is 0.5. To avoid these curves spanning a very wide range, V is normalised by Ds_{u0} here rather than Ds_{um} as used in Equation 5.1; this was also done in Figure 5.2.

The normalised resistance at any given depth increases considerably with kD/s_{um} at the initial stage of loading ($w/D \leq 0.1$) and then shows a reduced rate of increase. For the cases with very large kD/s_{um}, a distinct turning point for this transition can be observed. These curves are fitted by the same power law function used in Section 5.3.1 and the coefficients are presented in Figure 5.12b, in which two expressions that approximately link these coefficients with k are also provided. The parameter $s_{u,0.5D}$ shown in Figure 5.12b denotes the intact soil strength s_{u0} at a depth of half a pipe diameter.

5.3.3 Determination of geotechnical resistance in ideal weightless soil

Based on the results presented in Sections 5.3.1 and 5.3.2, the contribution of soil strength to the bearing capacity of pipe can be evaluated approximately using power law functions, considering the influence of the roughness factor α and the soil strength gradient k. The

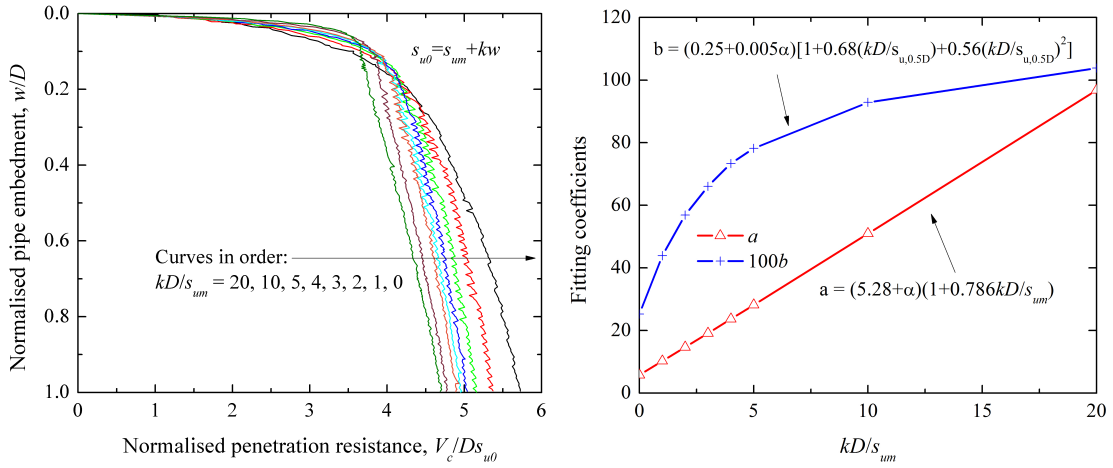

(a) Normalised resistance (b) Coefficients a and b

Figure 5.12 Influence of strength gradient on penetration resistance. Ideal soil, $\alpha = 0.5$ and $\gamma' = 0$.

fitting coefficients are expressed as

$$a = (5.28 + \alpha)[1 + 0.786(\frac{kD}{s_{um}})] \tag{5.2}$$

$$b = (0.25 + 0.005\alpha)[1 + 0.681(\frac{kD}{s_{um} + 0.5kD}) + 0.558(\frac{kD}{s_{um} + 0.5kD})^2] \tag{5.3}$$

Using a simple power law equation to predict the geotechnical resistance within the whole embedment range of 0 to 1D leads to a certain degree of inaccuracy. This issue will be further discussed in Section 5.7.1.

5.4 Quantification of soil buoyancy

This section aims to develop a method to quantify the soil buoyancy component of the pipe penetration resistance. The influence of soil unit weight γ' and strength gradient k are examined with both ideal and softening soil being considered. The soil behaviour is assumed to be rate-independent here, and the parameters used for this study are given in Table 5.4.

It is commonly assumed that the soil weight has very little influence on the penetration mechanism (Chatterjee *et al.*, 2012a; Merifield *et al.*, 2009). Therefore the buoyancy term in Equation 5.1 can be quantified by running parallel sets of analyses, with and without

Table 5.4 Parameters chosen for investigating soil buoyancy

δ_{rem}	ξ_{95}	kD/s_{um}	$\gamma' D/s_{um}$	Comments
1.0	20	0	0, 1, 3, 5, 10	Influence of γ' on soil buoyancy
0.3	20	0	0, 1, 3, 5, 10	Ideal and softening soil
1.0	20	0, 1, 2, 3, 4, 5, 10, 20	0, 3	Influence of k on soil buoyancy
0.3	20	0, 1, 2, 3, 4, 5, 10, 20	0, 3	Ideal and softening soil

consideration of soil unit weight. Figure 5.13 presents a comparison between two cases with $\gamma' D/s_{um}$ of 3 and 0, where a minor difference in the failure mechanism is found at a pipe embedment around $0.5D$ (Figure 5.13a). This difference becomes moderate with further penetration (Figure 5.13b) but a similar pattern is still observed.

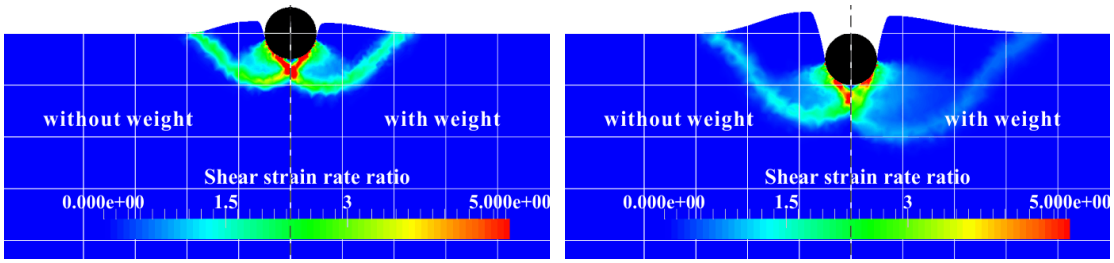

(a) $w/D = 0.5$ (b) $w/D = 1.0$

Figure 5.13 Comparisons of soil failure mechanisms (showing $\dot{\gamma}_{max}D/v_p$) between cases with ($\gamma' D/s_{um} = 3$) and without ($\gamma' D/s_{um} = 0$) unit weight. Ideal homogenous soil.

Based on this assumption, the value of $A_s f_b$ in Equation 5.1 can be evaluated by subtracting the geotechnical resistance V_g from the total resistance V_c for analyses with the soil unit weight being considered. This method is only valid at shallow embedments ($w/D \leq 1$) since at deeper embedment the weightless soil case might develop a totally different mechanism type compared with other cases with non-zero soil unit weight. In this scenario, f_b at deep embedment can be deduced by running two sets of analyses which have all the parameters fixed other than $\gamma' D/s_{um}$, where all the values of $\gamma' D/s_{um}$ are chosen to ensure that similar (localised) mechanisms are developed. Then f_b can be quantified as $f_b = \Delta V/A_s \Delta\gamma$,where ΔV and $\Delta\gamma$ are the differences of penetration resistance and effective unit weight between the two analyses. For instance, in Figure 5.14 all the curves can be used to quantify f_b at shallow depth while only the curves corresponding to $\gamma' D/s_{um}$ of 3, 5 and 10 can be used to evaluate f_b at deep embedments after the pipe has been buried and the resistance stabilises.

5.4.1 Effect of unit weight

Figure 5.14 illustrates the influence of normalised unit weight $\gamma' D/s_{um}$ on the penetration resistance of the pipe. Apart from the fact that the total resistance (geotechnical plus buoyancy) increases considerably with $\gamma' D/s_{um}$, the curves corresponding to lower values of $\gamma' D/s_{um}$ (0 and 1) show a different pattern from the rest. This is attributed to the fact that in heavy soil cases the soil tends to flow over and cover the pipe at relatively shallow embedments, followed by a localised failure mechanism and constant resistance as discussed in Section 5.2, while in light soil cases the soil is strong enough to sustain an open trench, resulting in a global failure mechanism throughout the displacement range investigated in this study.

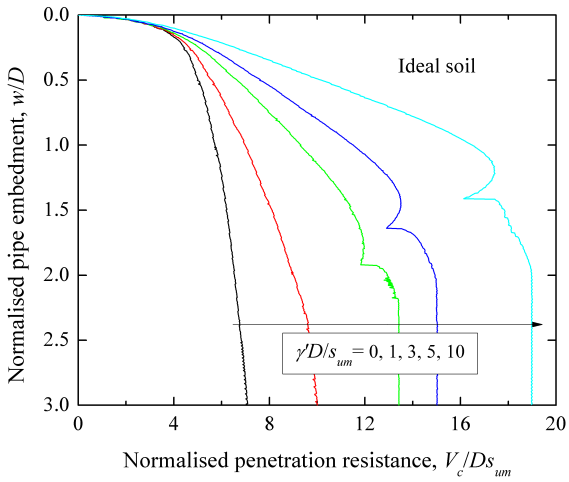

Figure 5.14 Influence of unit weight on penetration resistance. Ideal homogenous soil.

At deep penetrations, the values of $A_s \Delta\gamma f_b$ are quantified by reducing the resistances corresponding to $\gamma' D/s_{um}$ of 5 and 10 by that corresponding to $\gamma' D/s_{um}$ of 3 in Figure 5.14. The calculated results of f_b are 1.0058 and 1.0033 which are extremely close to 1, confirming that once the pipe becomes fully covered the consideration of soil buoyancy degrades to Archimedes' principle. This provides evidence that the soil weight does not influence the geotechnical resistance or the soil mechanism once a localised failure mechanism is developed.

Figure 5.15 shows the effect of soil unit weight on the buoyancy factor f_b at shallow embedment ($w/D \leq 1.0$). The results obtained from both ideal and softening soils are presented. Based on Figures 5.15a and 5.15b, it is assumed that f_b increases from 1.0 at

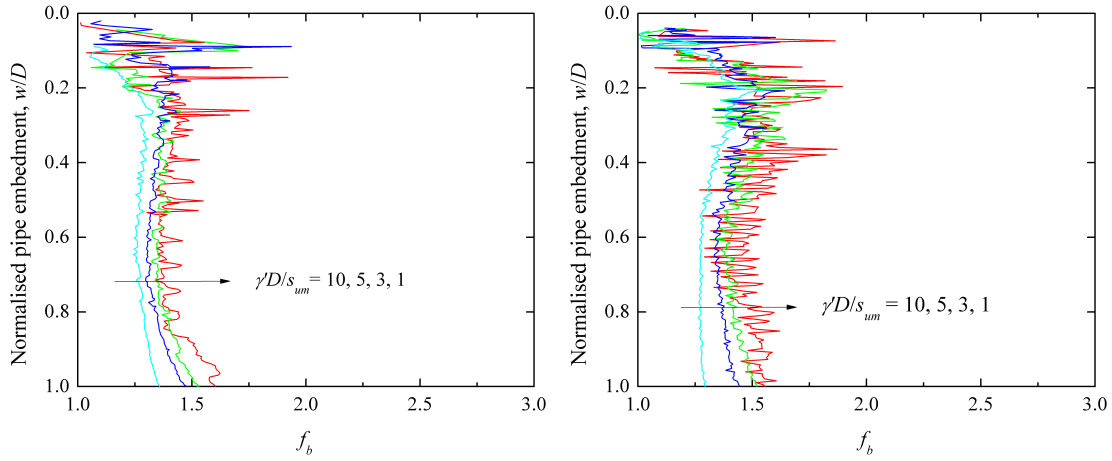

(a) Ideal soil (b) Softening soil (δ_{rem}=0.3, ξ_{95}=20)

Figure 5.15 Influence of unit weight on buoyancy factor. $k = 0$.

$w/D = 0$ to a relatively stable value $f_{b,s}$ at $w/D = 0.2$, and then remains constant until the pipe reaches a $w/D = 0.8$. The averaged values of f_b for each analysis at w/D ranging from 0.2 to 0.8, denoted by $f_{b,s}$, are plotted in Figure 5.17a, where a linearly decreasing trend with $\gamma' D/s_{um}$ can be observed. This is conceivable as with heavy soil less soil heave is expected to be generated during the penetration. For the sake of convenience, this constant value $f_{b,s}$ is adopted for quantifying the soil buoyancy of a pipe at penetrations of $0.2D$ to $1.0D$.

5.4.2 Effect of strength gradient k

Figure 5.16 shows the relationship between f_b and w/D for different values of kD/s_{um}. Soils with and without strain softening are used, and rate-dependence is not considered. The normalised unit weight $\gamma' D/s_{um}$ of the soil is chosen to be 0 and 3 in each parallel set of analyses for the quantification of f_b. In a similar way to the findings in Figure 5.15, f_b increases linearly at first and then reaches a stable value until a pipe embedment of $0.8D$. The averaged values of f_b from $w/D = 0.2$ to 0.8 are presented in Figure 5.17b, showing a linearly increasing trend with $kD/s_{u,0.5D}$, where $s_{u,0.5D}$ is the intact shear strength of the soil at the depth of $0.5D$.

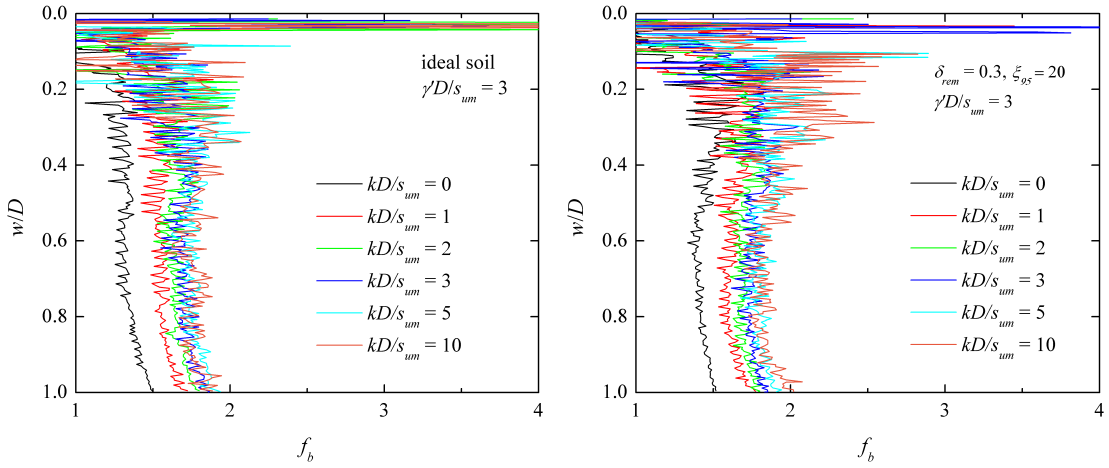

(a) Ideal soil (b) Softening soil (δ_{rem}=0.3, ξ_{95}=20)

Figure 5.16 Influence of soil strength gradient on buoyancy factor. $\gamma' D/s_{um} = 3$

5.4.3 Determination of f_b

Figures 5.17a and 5.17b illustrate the influences of unit weight and strength gradient on $f_{b,s}$, respectively, where linear equations are provided to link these parameters. Of interest is that strain softening has a positive influence on the buoyancy parameter f_b, which is in contrast to expectation since a smoother surface profile and less soil heave should be generated with weaker soil. The reason for this will be discussed in the next section, where the effect of strain softening is investigated.

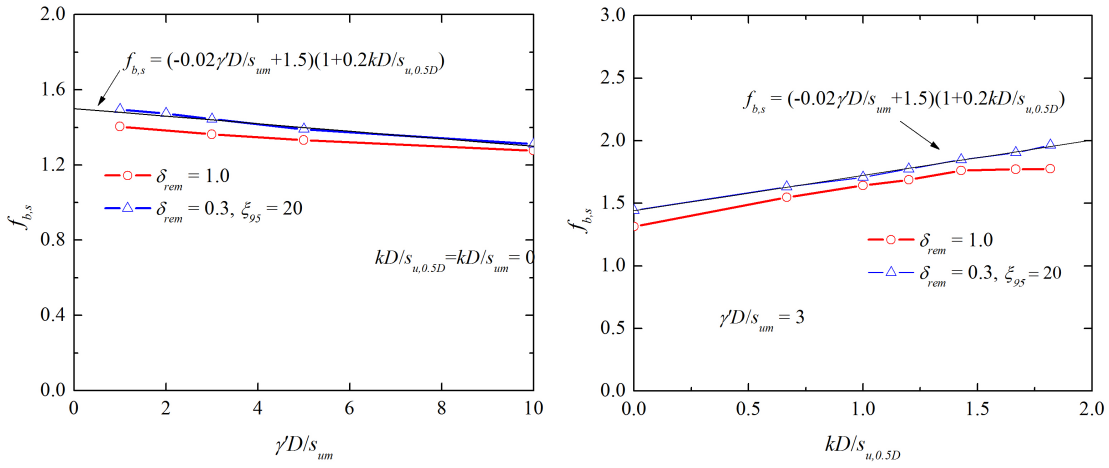

(a) Effect of unit weight (b) Effect of strength gradient

Figure 5.17 Averaged buoyancy factor at w/D ranging from 0.2 to 0.8, $f_{b,s}$

Based on the results presented in Figures 5.15 and 5.16, the buoyancy factor for $w/D \leq 1.0$ can be approximated as

$$f_b = \min\left(1 + 5(f_{b,s} - 1) \cdot \frac{w}{D}, f_{b,s}\right) \tag{5.4}$$

in which $f_{b,s}$, as presented in Figure 5.17, is expressed as

$$f_{b,s} = [-0.02(\frac{\gamma' D}{s_{um}}) + 1.5] \cdot [1 + 0.2(\frac{kD}{s_{um} + 0.5kD})] \tag{5.5}$$

Equations 5.4 and 5.5 quantify the effect of soil unit weight γ' and shear strength gradient k on soil buoyancy. The fitting coefficients are derived from rate-independent soil with strain softening parameters $\delta_{rem} = 0.3$ and $\xi_{95} = 20$. Since very little difference is found in Figure 5.17 between softening and ideal soils, these equations can be used to quantify soil buoyancy for soils with other softening parameters.

5.5 Effect of soil strength degradation

This section aims to look into the effect of strain softening on the vertical penetration behaviour of a pipe, and to propose an approach for quantifying the corresponding strength degradation. For all the results presented in this section, the strain rate effect is not considered by setting rate parameter $\mu = 0$. To achieve a comprehensive understanding of the effect of softening, both PIP (default) and WIP analyses were performed. Details of the tests are summarised in Table 5.5, in which Softenset1 is the main reference test set. In the PIP tests the pipe was pushed from the soil surface to a final embedment of w_{fin} while in the WIP tests, the pipe was embedded at a depth of $3D$ and then displaced through a further distance of w_{fin}. Apart from the tests illustrated in Table 5.5, another set of analyses was conducted to examine the influencing factors (kD/s_{um} and $\gamma' D/s_{um}$) that determine the mechanism type (global or localised) when strain softening is not considered. For the consideration of strain softening, the remoulded strength ratio δ_{rem} typically ranges from 0.2 to 0.5 and the ductility parameter ξ_{95} typically ranges from 10 to 50 (Randolph, 2004).

Table 5.5 Parameters chosen for investigating the effect of strain softening

Test set	$S_t = 1/\delta_{rem}$	ξ_{95}	kD/s_{um}	$\gamma' D/s_{um}$	w_{fin}/D	Type
Softenset1	1, 2, 3.3, 5, 10, 20, 50, 100	10, 20, 50	0	3	3	PIP
Softenset2	1, 2, 3.3, 5, 10, 20, 50, 100	10, 20, 50	0	0	1	PIP
Softenset3	1, 2, 3.3, 5, 10, 20, 50, 100	10, 20, 50	0	3	5	WIP
Softenset4	1, 2, 3.3, 5, 10, 20, 50, 100	10, 20, 50	0	0	5	WIP
Softenset5	1, 3.3	20	0, 1, 2, 3, 4, 5, 10, 20	3	3	PIP
Softenset6	1, 3.3	20	0, 1, 2, 3, 4, 5, 10, 20	0	1	PIP

5.5.1 Influence of strain softening on failure mechanisms

Figure 5.18 shows the variation of pipe-soil contact area A_{int} during the penetration process for embedments of less than one pipe diameter. The results obtained from soil with homogenous intact strength ($k = 0$) are presented. A_{int} was calculated based on the coordinates of the margin nodes (defined in Figure 3.3) on the rigid body. Since the pipe was modelled by 60 straight line segments rather than a perfectly circular cylinder, all the PIP curves in Figure 5.18 exhibit some 'step-type' behaviour. In reality, the evolution of A_{int} should be more smooth.

In the initial stages of penetration ($w/D \leq 0.2$) the pipe in this study (PIP) gains more contact area than that in the WIP case due to the 'wedge' effect. Beyond $w/D = 0.35$, the contact area in the PIP analysis starts to be lower than that in the WIP case. It can be seen that A_{int} almost stays unchanged at w/D below 0.2 for soils with δ_{rem} in a very wide range from 0.01 to 1. With continuing penetration ($w/D \geq 0.8$), soil with a smaller value of δ_{rem} begins to gain more contact with the pipe. This is because weak soil above the pipe centre is more likely to slip towards the pipe to generate new contact, while strong soil tends to sustain a more stable trench.

As discussed in Sections 5.2.2 and 5.4.1, the soil with a high value of γ'/k might develop a localised mechanism after the pipe is displaced by about 2-3 diameters, while that with lower γ'/k will only have a global mechanism throughout the penetration. Simulations with different combinations of $\gamma' D/s_{um}$ and kD/s_{um} in ideal soil (no softening) were carried out to ascertain the limit that differentiates the mechanism type developed by pipe penetration. A strict limit value is impractical to achieve, thus lower and upper bounds of it were derived instead. The pipe was vertically displaced by a distance of $3D$ in all the analyses, since further penetration is not relevant for field applications.

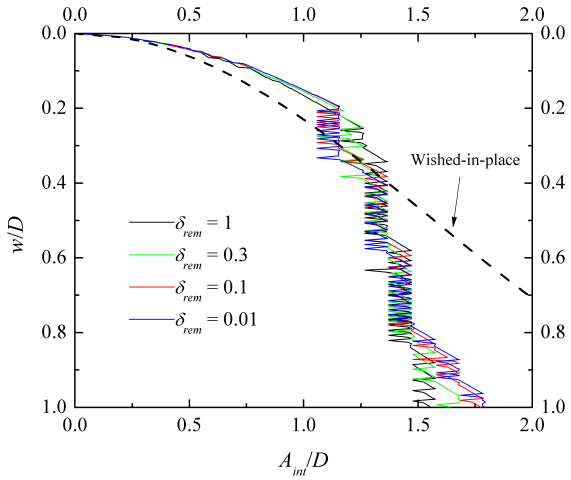

Figure 5.18 Influence of remoulded strength ratio on pipe-soil contact area. $\xi_{95} = 20$, $k = 0$ and $\gamma' D/s_{um} = 3$.

Figure 5.19 shows the lower and upper bounds for determining the failure mechanism transition for ideal soils with various $\gamma' D/s_{um}$ and kD/s_{um}. For combinations of γ' and k located above the upper line, the failure mechanism can finally become localised (see Figure 5.3c) while those below the lower line can only have a global mechanism (see Figure 5.5b). For the default $\gamma' D/s_{um}$ value of 3 used in this parametric study, soil with kD/s_{um} beyond 2 cannot develop a localised failure mechanism and a trench will be sustained throughout the penetration, which is confirmed in Figure 5.5b.

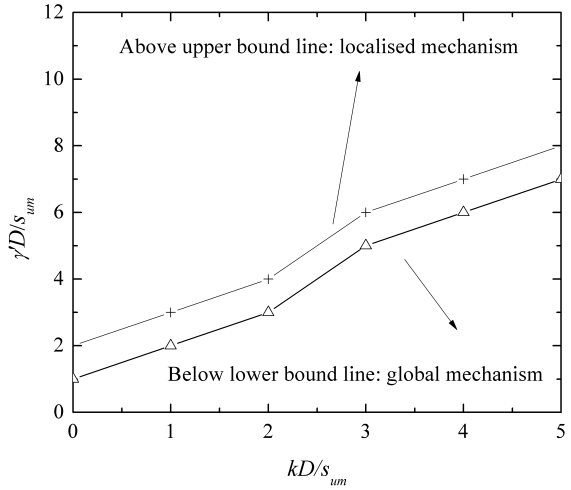

Figure 5.19 Bounds to determine the final failure mechanism ($w/D = 3$). Ideal soil.

Figures 5.20a and 5.20b show a comparison demonstrating how the strain softening effect influences the pipe penetration resistance. The values of kD/s_{um} are chosen to be 0, 1, 2, 3, 4, 5, 10 and 20 for both cases, and a decreasing trend of normalised resistance

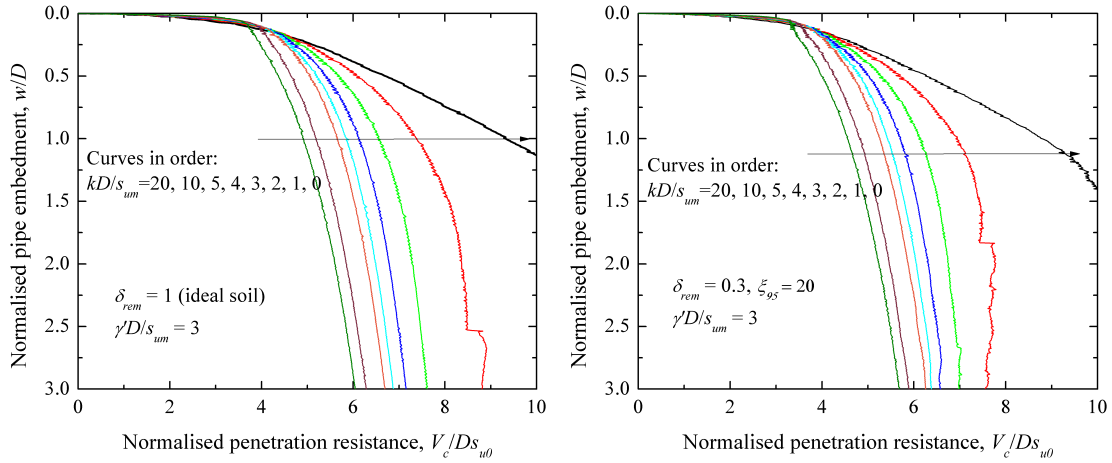

(a) Ideal soil (b) Softening soil

Figure 5.20 Influence of strength gradient on penetration resistance

with kD/s_{um} can be observed. In the ideal soil cases (Figure 5.20a) with $kD/s_{um} \leq 1$, the normalised resistance finally reaches a constant value within the displacement range investigated here, suggesting that failure mechanisms are finally developed. This is not the case for the simulations with $kD/s_{um} \geq 2$, where the penetration resistance keeps increasing, indicating that a global mechanism is sustained throughout the penetration process. These behaviours confirm the predictions made in Figure 5.19. When strain softening is taken into account, Figure 5.20b shows that all the resistance curves with kD/s_{um} below 5 can finally reach a 'residual' state and even show a slightly decreasing trend with w/D due to the fact that a localised failure mechanism has been developed. This is consistent with the previous conclusion that the softening effect tends to encourage a local failure mechanism. For a clear view of the trends of the resistance curves corresponding to large values of kD/s_{um}, all the results are presented in a relatively small scale. As a result, the curves corresponding to $kD/s_{um} = 0$ for both ideal ($\delta_{rem} = 1$) and softening ($\delta_{rem} = 0.3$) soils go off the scale in Figures 5.20a and 5.20b. The full evolution of these two curves can be seen in Figure 5.21a.

5.5.2 Typical penetration resistance

Figures 5.21 and 5.22 respectively show the influences of remoulded strength ratio (δ_{rem}) and ductility parameter (ξ_{95}) on the pipe penetration resistance. The default values of δ_{rem}

and ξ_{95} are 0.3 and 20 respectively. Other varied values of these parameters are provided in each figure. Results for soil with no softening, that is a sensitivity of unity, are also provided. Both SLA and CEL results are presented for comparison and in both cases a decreasing trend of resistance with decreasing δ_{rem} and ξ_{95} is found due to the higher rate of softening. The SLA results are found to be more stable than the CEL results though the values obtained from the two methods corresponding to a specific parameter set are very close.

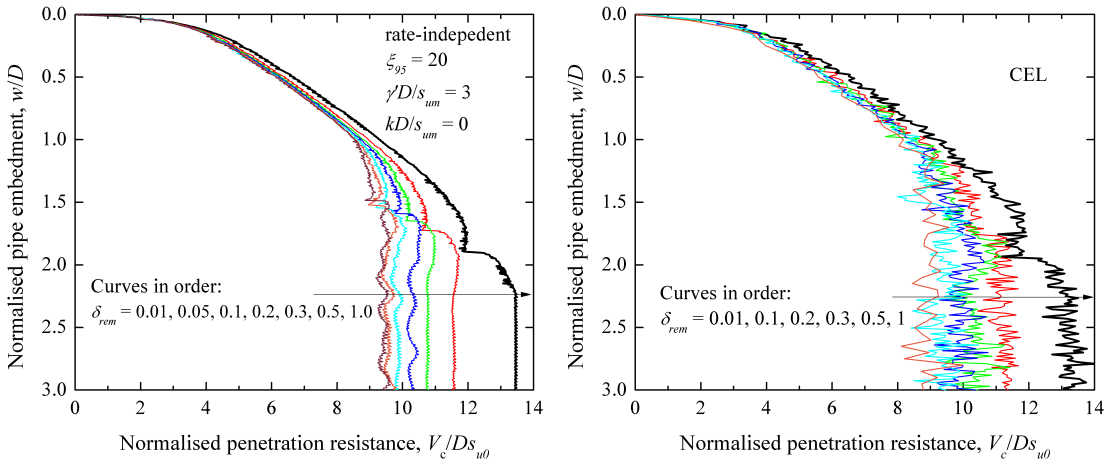

(a) SLA (b) CEL

Figure 5.21 Influence of remoulded strength ratio on penetration resistance

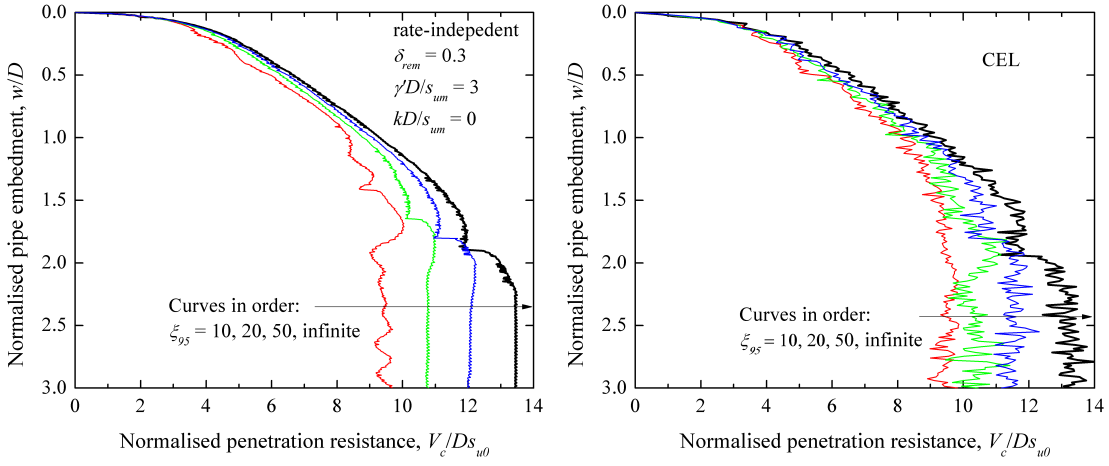

(a) SLA (b) CEL

Figure 5.22 Influence of ductility parameter on penetration resistance

Considering the default values 0.3 and 20 for δ_{rem} and ξ_{95} respectively, strain softening reduces the pipe resistance (compared with ideal soil) by about 6.5% for w/D below 1.0

and 20% for w/D beyond 2.0, as illustrated in Figures 5.21 and 5.22. The reduction in soil resistance is calculated based on total resistance. If the effect of soil buoyancy is removed, this reduction can be even more pronounced. The reason why the reduction in soil resistance becomes much more significant with further embedment is partly due to the accumulation of plastic strain in the overall soil domain. An even more important reason is that the soil near the pipe has significantly more accumulated strain than that in the remote area, resulting in a much weaker region of soil adjacent to the pipe. When the failure mechanism becomes localised after the pipe has been buried, this weak area leads to more reduction in soil resistance. The critical pipe embedment, w_{cri}, where the resistance drops to a local minimum value and increases again, increases with increasing δ_{rem} and ξ_{95}. Therefore it can be concluded from Figures 5.21 and 5.22 that a localised failure mechanism is more likely to develop when strain softening is considered, and the softening effect plays an even more significant role in reducing the penetration resistance once a local failure mechanism has been developed.

To characterise the strain softening effect on soil strength, an equivalent shear strength was proposed based on Equation 2.9 (Chatterjee *et al.*, 2012a), expressed as

$$s_{u,eq} = s_{u0}[\delta_{rem} + (1-\delta_{rem})e^{-3\xi_{eq}/\xi_{95}}] \tag{5.6}$$

in which the term ξ_{eq} reflects the equivalent plastic shear strain undergone by the soil contributing to the vertical resistance during the penetration process, which can be back-analysed from the numerical results by

$$\xi_{eq} = -\frac{\xi_{95}}{3}\ln(\frac{s_{u,eq}/s_{u0}-\delta_{rem}}{1-\delta_{rem}}) \tag{5.7}$$

where $s_{u,eq}/s_{u0}$ equals $V_g/V_{g,ideal}$, in which V_g and $V_{g,ideal}$ are the geotechnical resistance components of bearing capacity for softening and ideal soils respectively and can be quantified by reducing the total resistance V_c by the soil buoyancy term $f_b A_s \gamma'$, where f_b can be obtained from Equation 5.4.

Although the main set of simulations (Softenset1 in Table 5.5) provides all the information necessary for evaluating ξ_{eq} at both shallow and deep pipe embedment, other sets

of analyses were also performed to provide supplementary data. For quantifying ξ_{eq} when $w/D \leq 1.0$, weightless soil is used (Softenset2 in Table 5.5) to eliminate the uncertainties generated from subtracting the soil buoyancy component. At deep penetrations when the pipe has been buried by surrounding soil, WIP tests (Softenset3 and Softenset4 in Table 5.5) are carried out to help evaluate ξ_{eq} during the 'residual' loading stage without considering the effect of geometry changes at the soil surface.

5.5.3 ξ_{eq} at shallow depth: $w/D \leq 1.0$

Figures 5.23 and 5.24 illustrate the variation of equivalent plastic shear strain (ξ_{eq}) with pipe embedment at shallow depth, with the influences of δ_{rem} and ξ_{95} being examined. The results from analyses with $\gamma' D/s_{um} = 0$ and 3 are presented at the left and right sides respectively for comparison. It should be noted that for the latter case, a certain degree of inaccuracy can be generated when decoupling the soil buoyancy component from the total resistance; while for the former case, the soil mechanism is slightly different from more realistic cases with soil weight (see Figure 5.13). The average of the results obtained from these two cases is recommended for quantifying ξ_{eq}. Figures 5.23 and 5.24 show the general trend that ξ_{eq} increases linearly at first ($w/D \leq 0.2$) before reaching a stable value of $\xi_{eq,s}$ and remains constant throughout the rest of the penetration ($0.2 \leq w/D \leq 1.0$). A simple bi-linear curve is found to fit these curves satisfactorily regardless of δ_{rem} and ξ_{95}. $\xi_{eq,s}$ is calculated as the average of ξ_{eq} for $0.2 \leq w/D \leq 1.0$ and the results are presented in Figure 5.25. This figure shows the values of $\xi_{eq,s}$ for different combinations of δ_{rem} and ξ_{95}. In general, a value of 1 is recommended for $\xi_{eq,s}$ when the values presented in Figure 5.25a and Figure 5.25b are averaged.

5.5.4 ξ_{eq} at deep depth: $w/D \geq 2.0$

After the pipe is fully embedded and a local failure mechanism is mobilised, the soil around the pipe experiences further softening and finally the vertical resistance stabilises. It is worth mentioning that for very soft soil, an ideally stable state is extremely hard to attain within the displacement range ($0 \leq w/D \leq 3$) investigated in this study.

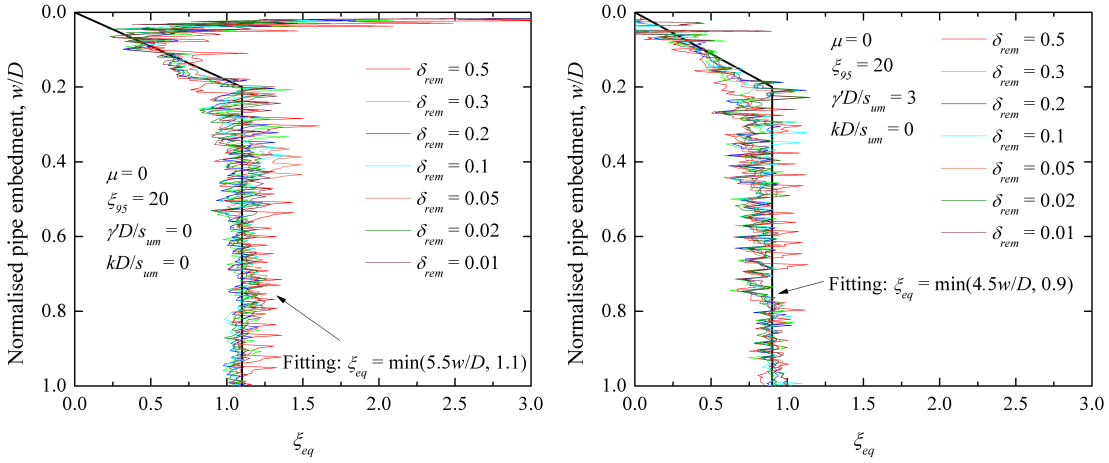

(a) $\gamma' D/s_{um} = 0$ (b) $\gamma' D/s_{um} = 3$

Figure 5.23 Influence of remoulded strength ratio on equivalent plastic shear strain at shallow embedment (PIP)

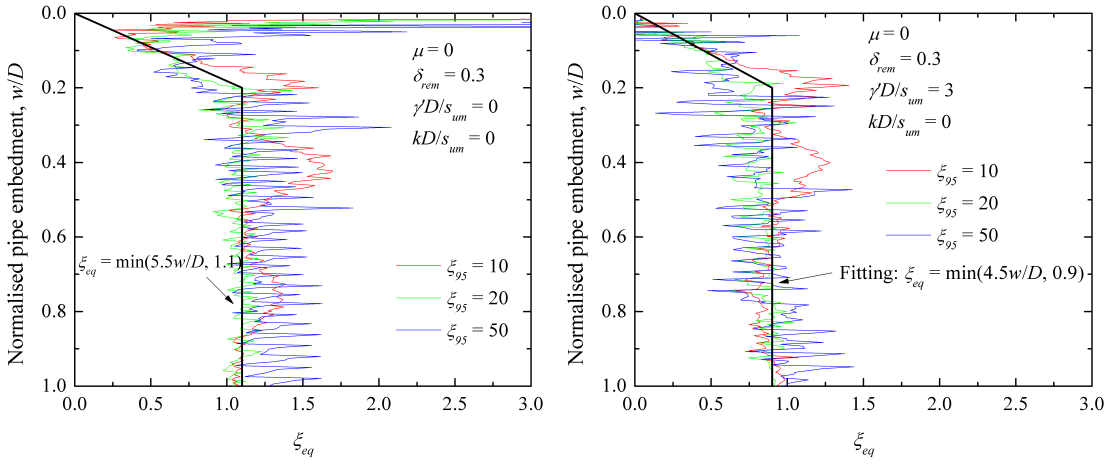

(a) $\gamma' D/s_{um} = 0$ (b) $\gamma' D/s_{um} = 3$

Figure 5.24 Influence of ductility parameter on equivalent plastic shear strain at shallow embedment (PIP)

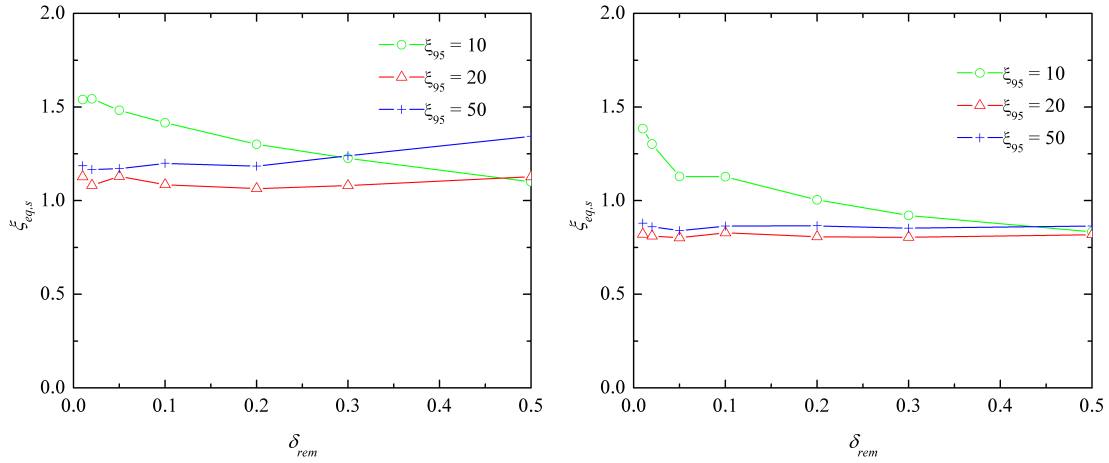

(a) $\gamma' D/s_{um} = 0$ (b) $\gamma' D/s_{um} = 3$

Figure 5.25 $\xi_{eq,s}$ for different combinations of remoulded strength ratio and ductility parameter (PIP)

To evaluate the equivalent plastic shear strain ξ_{eq} at very deep embedment, the vertical resistances in the range $2.0 \leq w/D \leq 3.0$ in the PIP tests are used, and the results are presented in Figure 5.26. It can be seen that the values of ξ_{eq} almost stay stable for w/D between 2.5 and 3.0 despite some jaggedness in the curves. Based on this finding, it is therefore assumed that a reasonably stable state can be reached after the pipe has reached an embedment of $2.5D$. The average values of ξ_{eq} at depths ranging from $2.5D$ to $3.0D$ are calculated as $\xi_{eq,d}$ and presented in Figure 5.28a, which is used to represent the ultimate ξ_{eq} value within a realistic depth of pipe penetration.

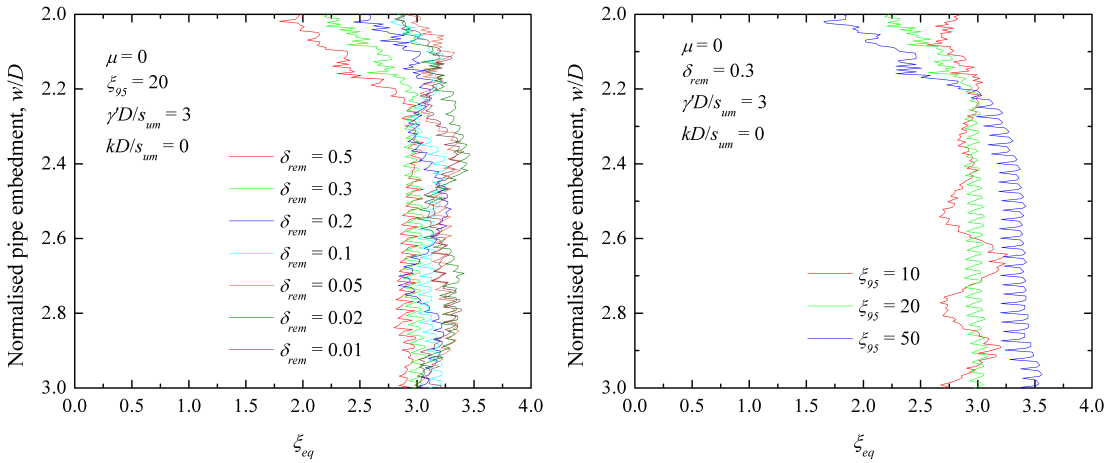

(a) Varied δ_{rem} (b) Varied ξ_{95}

Figure 5.26 Influence of strain softening parameters on equivalent plastic shear strain at deep embedment (PIP)

Another two sets of tests were performed to provide some more insights into this issue, where the pipe was pre-embedded (Softenset3 and Softenset4 in Table 5.5) deeply below the soil surface ($w = 3D$) and then vertically displaced by a further distance of $5D$ downwards. Localised soil mechanisms are developed throughout the loading, thus the influence of geometry change can be eliminated. Figure 5.27 shows the variation of ξ_{eq} with normalised penetration in the WIP case. A reasonably stable state is reached within the displacement range studied here for all the tests except that with ξ_{95} of 50. Although a more stable state might finally be achieved for this special case if the pipe traveled far beyond $5D$, this is unrealistic for field applications and the averaged values between $4D$ and $5D$ are taken as $\xi_{eq,d}$ for all the analyses. The calculated WIP results are presented in Figure 5.28b for comparison with the PIP results.

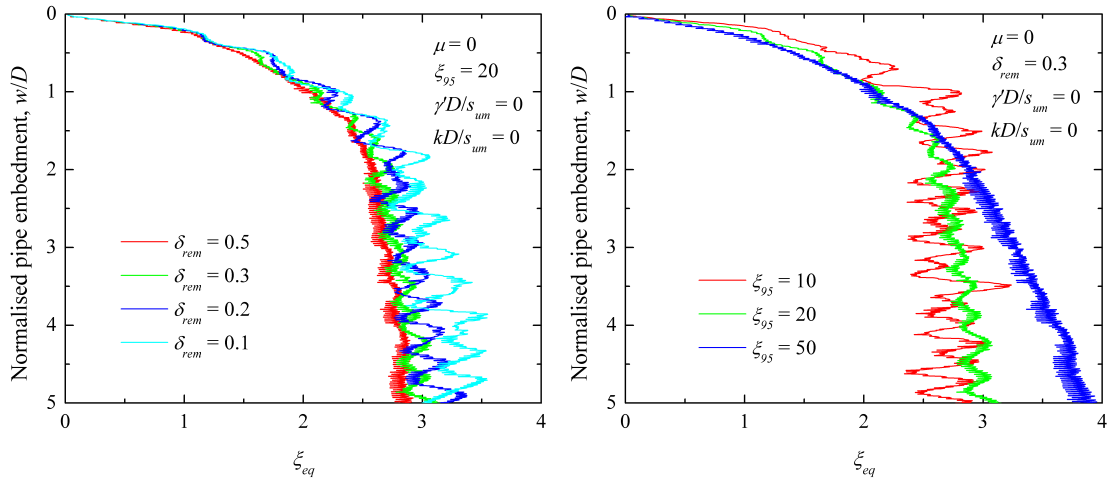

(a) Varied δ_{rem} (b) Varied ξ_{95}

Figure 5.27 Influence of strain softening parameters on equivalent plastic shear strain at deep embedment (WIP)

Figure 5.28 shows the ultimate equivalent plastic shear strain $\xi_{eq,d}$ derived from homogenous soils with various δ_{rem} and ξ_{95} values. The results obtained from PIP tests with soil weight (Softenset1), WIP tests with soil weight (Softenset3) and WIP tests without soil weight (Softenset4) are presented for comparison. Except for the soils with very large ductility parameters ξ_{95}, the derived $\xi_{eq,d}$ values from the PIP and WIP analyses are found to be very close by comparing Figures 5.28a and 5.28b. It is also observed in Figure 5.28b that the curves obtained from the WIP tests with and without soil weight almost coincide,

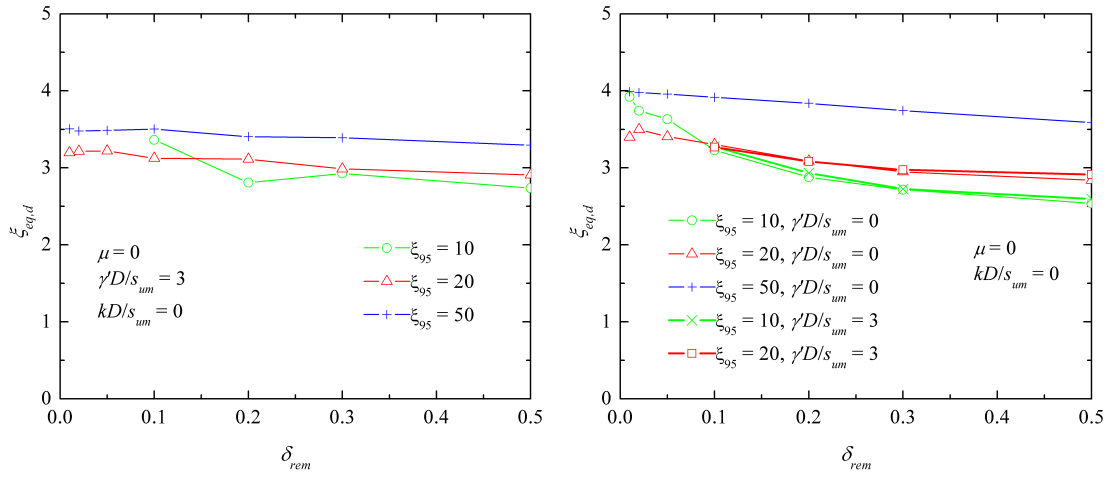

(a) PIP (b) WIP

Figure 5.28 $\xi_{eq,d}$ for different combinations of remoulded strength ratio and ductility parameter. $k = 0$.

confirming that soil weight has very limited influence on the failure mechanism at deep embedment.

5.5.5 Effect of k on ξ_{eq}

Figure 5.29 illustrates the effect of kD/s_{um} on the development of ξ_{eq} with w/D. Both the cases with (Softenset1) and without (Softenset2) soil unit weight are considered. The bi-linear trend observed from homogenous soil is reproduced here with only slightly difference in the values of $\xi_{eq,s}$, indicating that kD/s_{um} has a minor influence on ξ_{eq}.

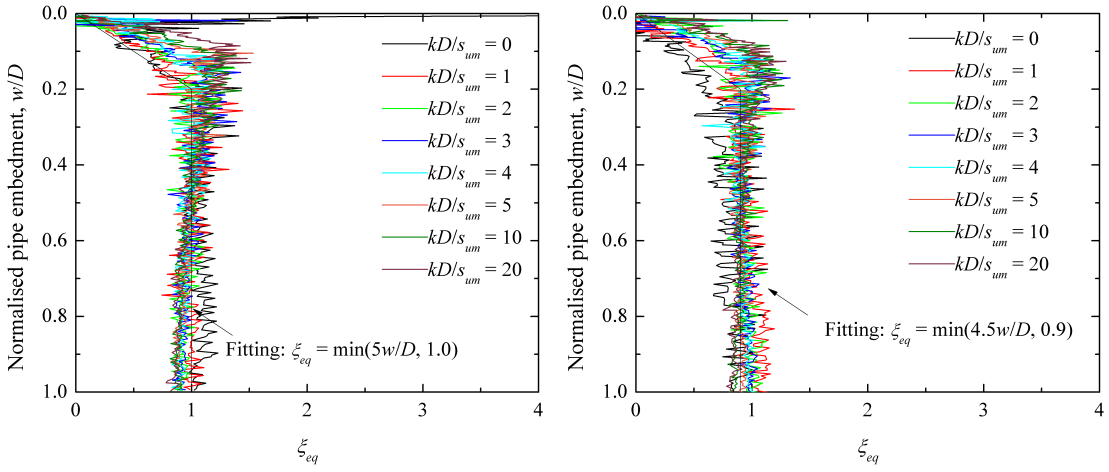

(a) $\gamma' D/s_{um} = 0$ (b) $\gamma' D/s_{um} = 3$

Figure 5.29 Influence of strength gradient on equivalent plastic shear strain at shallow embedment. $\delta_{rem} = 0.3$ and $\xi_{95} = 20$.

5.5.6 Determination of ξ_{eq}

The degradation of soil strength due to strain softening can be quantified according to Equation 5.6 above. Apart from the parameters relating to soil properties (δ_{rem}, ξ_{95} and kD/s_{um}), the equivalent plastic shear strain, ξ_{eq}, can be evaluated based on the results presented in Sections 5.5.3 to 5.5.5, and expressed as

$$\begin{aligned} \xi_{eq} &= \min(5w/D, 1) \qquad && w/D \leq 1.0 \\ \xi_{eq} &= 3 && w/D \geq 2.0 \end{aligned} \tag{5.8}$$

This equation can only be used to evaluate ξ_{eq} for a pipe at shallow ($w/D \leq 1.0$) and deep ($w/D \geq 2.0$) embedments. For the embedments in between, the softening effect influences not only the penetration resistance but also the type of soil failure mechanism; therefore a prediction model has not been proposed.

5.6 Effect of soil strength enhancement

This section aims to study the enhancement of soil strength due to strain rate during pipe penetration, and to propose an approach for quantifying it. For all the analyses conducted in this section, the effect of strain softening is ignored by choosing δ_{rem} to be 1. Soils with normalised unit weights $\gamma' D/s_{um} = 0$ and 3 are considered. In a similar way to the study on strain softening in the previous section, both PIP (default) and WIP analyses are performed. Details of the tests are summarised in Table 5.6, where Rateset1 is the main reference test set. The parameter w_{fin} in the WIP cases denotes the distance the pipe is displaced rather than the actual final embedment as in the PIP tests.

Table 5.6 Parameters chosen for investigating the effect of strain rate

Test sets	μ	$v_p/D\dot{\gamma}_{ref}$	kD/s_{um}	$\gamma' D/s_{um}$	w_{fin}/D	Type
Rateset1	0.00, 0.05, 0.10, 0.15, 0.20	100, 1000, 10000	0	3	3	PIP
Rateset2	0.00, 0.05, 0.10, 0.15, 0.20	100, 1000, 10000	0	0	1	PIP
Rateset3	0.00, 0.05, 0.10, 0.15, 0.20	100, 1000, 10000	0	3	1	WIP
Rateset4	0.00, 0.10	1000	0, 1, 2, 3, 4, 5, 10, 20	3	3	PIP
Rateset5	0.00, 0.10	1000	0, 1, 2, 3, 4, 5, 10, 20	0	1	PIP

5.6.1 Typical penetration resistance

Figure 5.30 shows some typical results demonstrating the effect of viscosity parameter μ and normalised penetration rate $v_p/D\dot{\gamma}_{ref}$ on the load-penetration response of the pipe. In general, the soil resistance increases with both μ and $v_p/D\dot{\gamma}_{ref}$ due to greater strength enhancement. The critical pipe embedment w_{cri}, at which the rate of change of soil resistance decreases to a local minimum and then achieves a recovery, also increases with both μ and $v_p/D\dot{\gamma}_{ref}$. This indicates that strain rate effects tend to prevent or postpone the occurrence of a localised failure mechanism and backfilling of the surrounding soil. Considering the default values $\mu = 0.10$ and $v_p/D\dot{\gamma}_{ref} = 1000$, the strain rate effect increases the pipe resistance (compared with ideal soil) by about 12% for w/D below 1.0 and 9% for w/D beyond 2.0. The increase in soil resistance is calculated based on total resistance, including soil buoyancy, and would be more significant if only geotechnical resistance was considered.

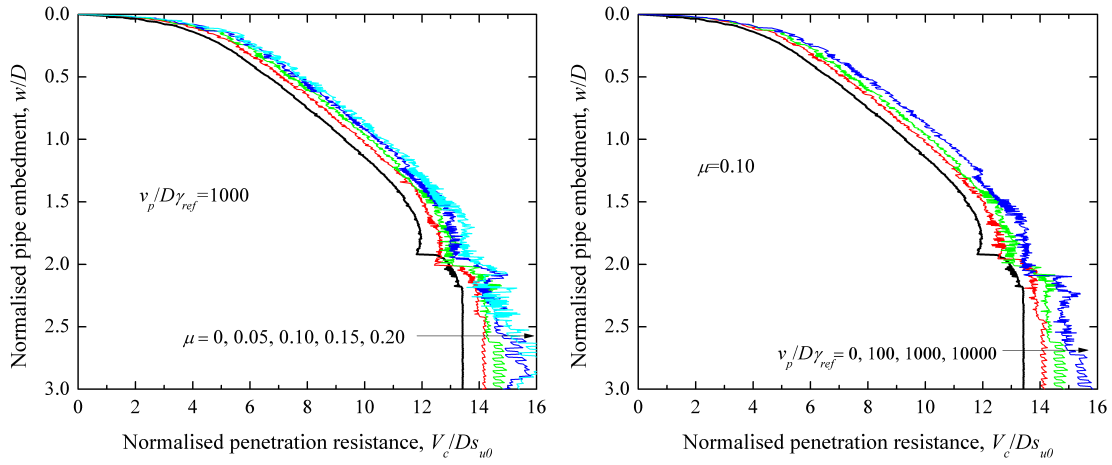

(a) Effect of viscosity parameter (b) Effect of normalised penetration rate

Figure 5.30 Influence of strain rate on penetration resistance. $\delta_{rem} = 1$, $k = 0$ and $\gamma' D/s_{um} = 3$.

To interpret the rate effect, an equivalent shear strength is used to take into account the strength enhancement based on Equation 2.9, namely

$$s_{u,eq} = s_{u0}[1 + f_r \mu \log(\frac{v_p}{D\dot{\gamma}_{ref}})] \tag{5.9}$$

where f_r reflects the equivalent strength enhancement factor of the soil contributing to the bearing capacity, and can be back-analysed from the numerical results by

$$f_r = (s_{u,eq}/s_{u0} - 1)/[\mu \log(\frac{v_p}{D\dot{\gamma}_{ref}})] \tag{5.10}$$

where $s_{u,eq}/s_{u0}$ equals $V_g/V_{g,ideal}$. V_g and $V_{g,ideal}$ are the geotechnical resistance components of bearing capacity for the strain rate-dependent and ideal soils, and can be quantified by reducing the total resistance V_c by the soil buoyancy component $f_b A_s \gamma'$, where f_b can be obtained from Equation 5.4.

5.6.2 f_r at shallow depth: $w/D \leq 1.0$

Figure 5.31 shows how the normalised penetration rate $v_p/D\dot{\gamma}_{ref}$ influences the relationship between f_r and w/D at shallow depth. Three values of $v_p/D\dot{\gamma}_{ref}$, 100, 1000 and 10000 are considered. The results calculated from soils with and without unit weight are both presented. Despite the fluctuations in the curves, it is reasonable to assume that f_r increases linearly with normalised pipe embedment at first ($w/D \leq 0.1$) and then remains constant at a stable value $f_{r,s}$ throughout the remaining penetration up to $1D$. The value of f_r is found to be independent of v_p in both Figure 5.31a and Figure 5.31b. The averaged values of f_r over the range $0.1 \leq w/D \leq 1.0$ are used to quantify $f_{r,s}$.

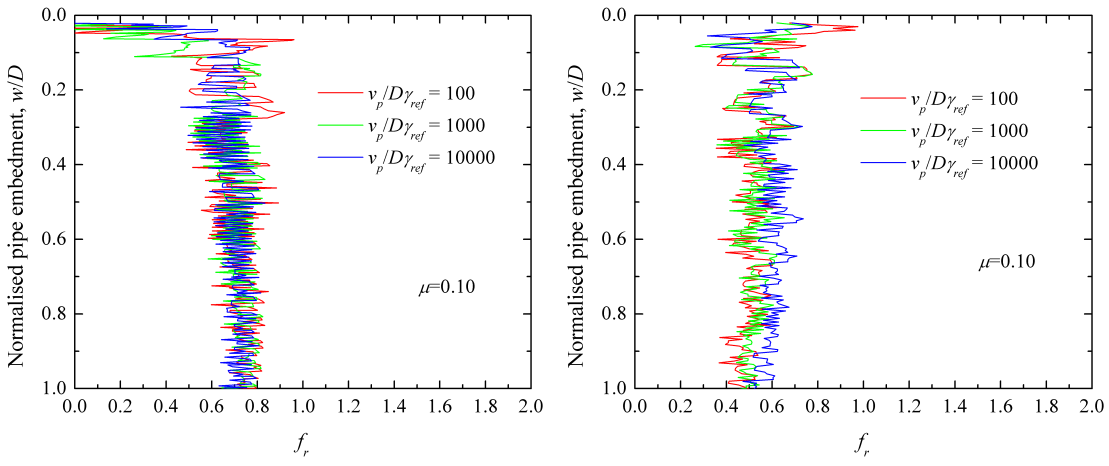

(a) $\gamma' D/s_{um} = 0$ (b) $\gamma' D/s_{um} = 3$

Figure 5.31 Influence of normalised penetration rate on equivalent strength enhancement factor at shallow embedment

Figure 5.32 shows the effect of viscosity parameter μ on f_r at shallow depth. Four values of μ, 0.05, 0.10, 0.15 and 0.20 are considered and the results obtained from soils with $\gamma' D/s_{um}$ of 0 and 3 are presented in Figure 5.32a and Figure 5.32b respectively. The general trend described above can also be seen here, though $f_{r,s}$ shows a trend of decreasing with μ.

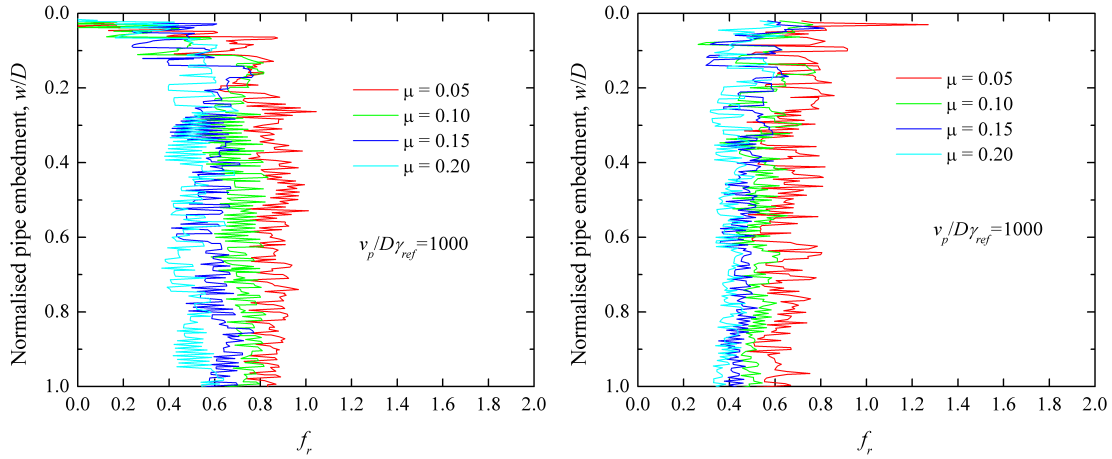

(a) $\gamma' D/s_{um} = 0$ (b) $\gamma' D/s_{um} = 3$

Figure 5.32 Influence of viscosity parameter on equivalent strength enhancement factor at shallow embedment

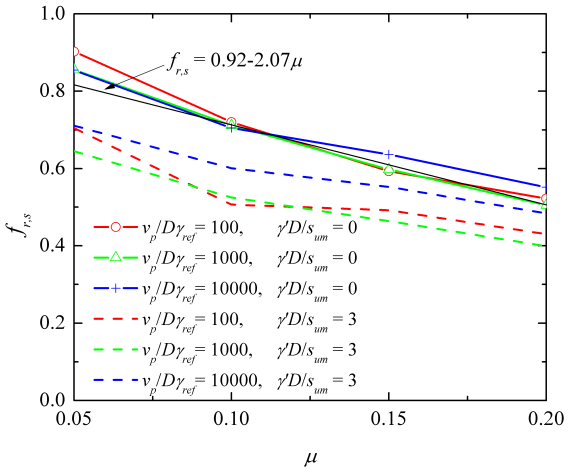

Figure 5.33 $f_{r,s}$ for different combinations of μ and $v_p/D\dot{\gamma}_{ref}$. $k = 0$.

Figure 5.33 illustrates the values of $f_{r,s}$ obtained from the analyses with different rate parameters. In weightless soil case (Rateset2) $f_{r,s}$ is found to be independent of v_p but decreases linearly with μ. A similar observation is made in the analyses with $\gamma' D/s_{um} = 3$ (Rateset1) but the penetration rate v_p has a non-negligible effect on $f_{r,s}$ here. Considering

the uncertainties generated when decoupling the soil buoyancy component from the total resistance in the latter case, the results for weightless soil are used to quantify $f_{r,s}$ hereafter, and a linear function (also presented in Figure 5.33) is found to fit the curves satisfactorily.

5.6.3 f_r at deep depth: $w/D \geq 2.0$

For homogenous soil without strain softening, the previous loading history has no effect on the soil response at very deep embedment once the pipe has been fully buried by surrounding soil. Theoretically the penetration resistance should remain constant since stable and localised mechanisms are developed. Therefore the ultimate values of f_r at depth, denoted by $f_{r,d}$, can be conveniently obtained from WIP tests (Rateset3). Since in some PIP cases the failure mechanism does not become totally localised at the final depth of $3D$ when strength enhancement is taken into account, only the results from from WIP analyses are used to derive $f_{r,d}$. Figure 5.34 shows the calculated $f_{r,d}$ values for various μ and $v_p/D\dot{\gamma}_{ref}$. A polynomial function, given in Equation 5.11 below, is used to fit these results.

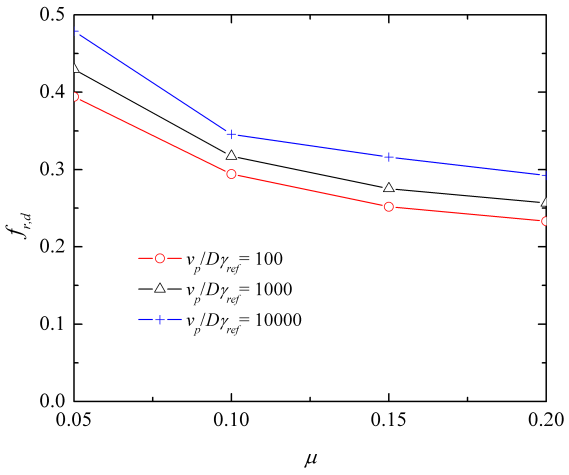

Figure 5.34 $f_{r,d}$ for different combinations of μ and $v_p/D\dot{\gamma}_{ref}$. $k = 0$ and $\gamma' D/s_{um} = 3$.

5.6.4 Influence of k on f_r

Figure 5.35a shows the effect of the normalised strength gradient kD/s_{um} on the variation of f_r with normalised pipe embedment w/D. With increasing kD/s_{um}, f_r starts to show a

trend of decreasing slightly with pipe embedment rather than remaining constant. However, it is still assumed that f_r increases linearly at first and then stays constant at shallow embedment ($w/D \leq 1$), with the value of $f_{r,s}$ varying with kD/s_{um}. The averaged values of f_r for embedment ranging from $0.1D$ to $1.0D$ are presented in Figure 5.35b as $f_{r,s}$. A linear equation is also provided to quantify the influence of kD/s_{um} on $f_{r,s}$. The calculated $f_{r,s}$ for homogenous soil with a given combination of μ and $v_p/D\dot{\gamma}_{ref}$ can be modified according to this equation to account for the effect of strength gradient.

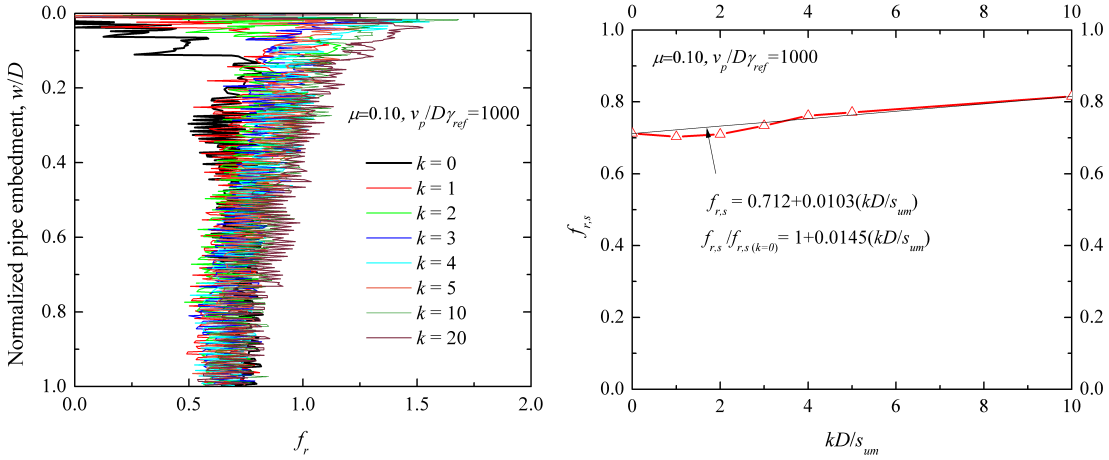

(a) Variation of f_r with w/D (b) Relation between $f_{r,s}$ and kD/s_{um}

Figure 5.35 Influence of strength gradient on equivalent strength enhancement factor. $\gamma' D/s_{um} = 0$.

5.6.5 Determination of f_r

The enhancement of soil strength due to strain rate can be evaluated according to Equation 5.9. Apart from the parameters relating to the pipe and soil properties (μ, $v_p/D\dot{\gamma}_{ref}$ and kD/s_{um}), the equivalent strength enhancement factor f_r can be evaluated based on the results presented in Sections 5.6.2 to 5.6.4, and expressed as

$$\begin{aligned} f_r &= (0.92 - 2.07\mu)[1 + 0.0145(\frac{kD}{s_{um}})] && w/D \leq 1.0 \\ f_r &= 0.582 + 0.026 \cdot \log(\frac{v_p}{D\dot{\gamma}_{ref}}) - 6.09\mu + 32.95\mu^2 - 62.91\mu^3 && w/D \geq 2.0 \end{aligned} \tag{5.11}$$

For the same reason as stated in Section 5.5.6, a model to evaluate f_r at intermediate pipe embedments ($1.0 \leq w/D \leq 2.0$) has not been proposed.

5.7 Combined effects of strain softening and strain rate

This section considers combined effects of strain softening and strain rate on the pipe penetration response, and aims to derive a model for predicting the soil resistance on the basis of the parametric studies in Sections 5.3 to 5.6. For all the simulation results presented in this section, a base case was chosen with $kD/s_{um} = 0$, $\delta_{rem} = 0.3$, $\xi_{95} = 20$, $\mu = 0.1$, and $v_p/D\dot{\gamma}_{ref} = 1000$. When the strain softening effect was examined, the parameters relating to strain rate effect were fixed; and vice versa. When the effect of the normalised strength gradient kD/s_{um} was examined, all other parameters were fixed. The full set of parameters adopted in this study are summarised in Table 5.7.

Table 5.7 Parameters chosen for investigating combined effects

Parameter	Values
kD/s_{um}	0, 1, 2, 3, 4, 5, 10, 20
δ_{rem}	1, 0.5, 0.3, 0.2, 0.1, 0.05, 0.02, 0.01
ξ_{95}	10, 20, 50, infinitely large
μ	0, 0.05, 0.10, 0.15, 0.20
$v_p/D\dot{\gamma}_{ref}$	infinitesimally small, 100, 1000, 10000

Figure 5.36 shows typical results demonstrating the effects of the various parameters on the pipe penetration resistance. For the results presented here, one parameter was varied at a time according to Table 5.7 while keeping the other parameters equal to their base case values.

5.7.1 Prediction of penetration resistance

An equation-based approach is presented here to predict the soil resistance during pipe penetration. At shallow embedments ($w/D \leq 1.0$), the geotechnical resistance $V_{g,ideal}$ of the pipe in ideal soil (i.e. rate independent, perfectly plastic soil) is calculated at first, expressed as a power law function:

$$V_{g,ideal} = a\left(\frac{w}{D}\right)^{b} \cdot s_{um} \tag{5.12}$$

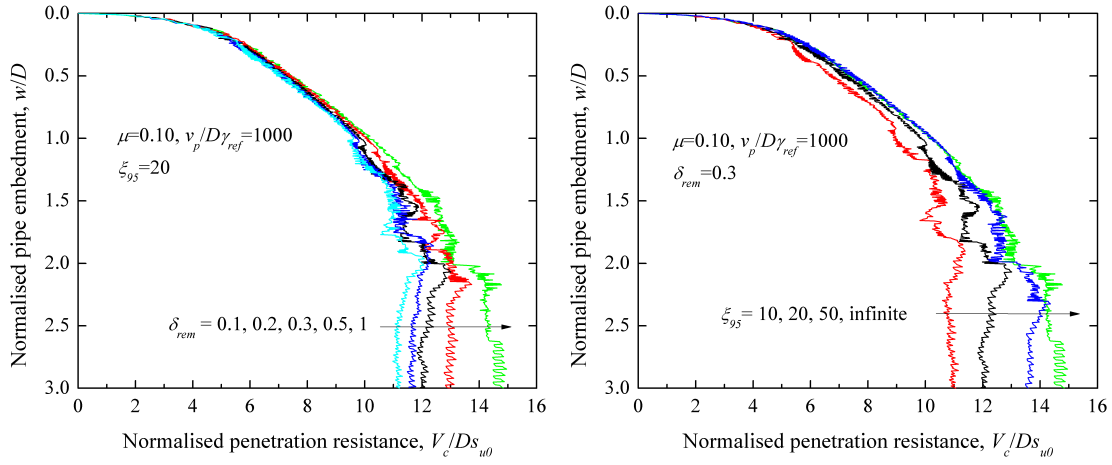

(a) Varied δ_{rem} (b) Varied ξ_{95}

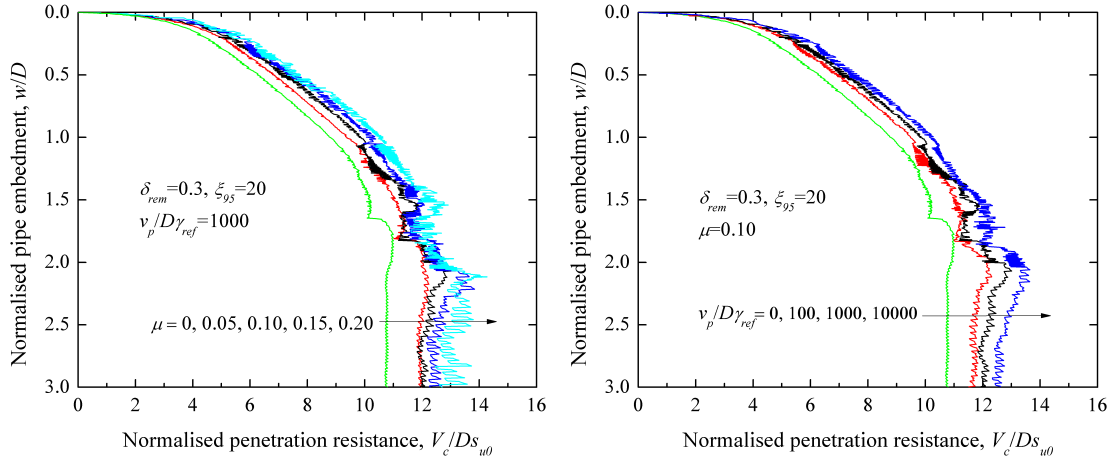

(c) Varied μ (d) Varied v_p

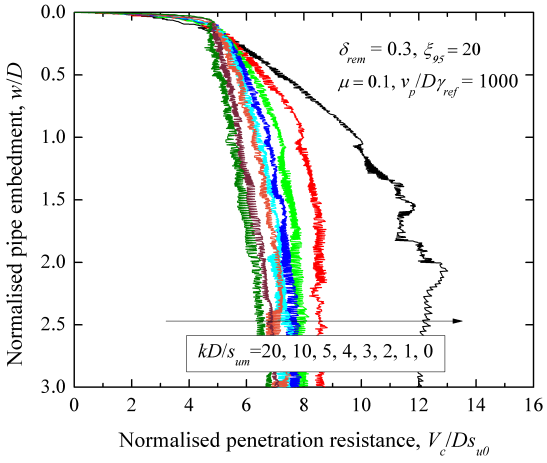

(e) Varied kD/s_{um}

Figure 5.36 Variation of normalised soil resistance with pipe embedment: effects of adjusting individual parameters.

where the coefficients a and b are determined by the interface roughness α and the normalised soil strength gradient kD/s_{um}. The relevant relations are presented in Section 5.3.3.

This 'ideal' resistance is then modified by two factors f_{soften} and f_{rate} to take into account the effects of strain softening and strain rate:

$$V_g = V_{g,ideal} \cdot f_{soften} \cdot f_{rate} \tag{5.13}$$

in which f_{soften} and f_{rate} are expressed as

$$f_{soften} = \delta_{rem} + (1 - \delta_{rem}) e^{-3\xi_{eq}/\xi_{95}} \tag{5.14}$$

$$f_{rate} = 1 + f_r \mu \log(\frac{v_p}{D\dot{\gamma}_{ref}}) \tag{5.15}$$

where ξ_{eq} and f_r represent the equivalent plastic strain and the equivalent strength enhancement factor of the soil contributing to the bearing capacity. The calculations of these two parameters are presented in Section 5.5.6 and Section 5.6.5. After accounting for these modifications of soil strength, the final bearing capacity V_c is calculated by

$$V_c = V_g + f_b A_s \gamma' \tag{5.16}$$

to include soil buoyancy. The evaluation of f_b is presented in Section 5.4.3.

The soil resistance at very deep embedment ($w/D \geq 2.5$) can also be predicted by the process described above. However, the influence of kD/s_{um} on the penetration resistance at this stage was not quantified in this study. $V_{g,ideal}$ of a pipe at very deep embedment ($w/D \geq 2.5$) in homogenous soil can be expressed as $N_c s_{um}$, where N_c is the bearing capacity factor of the pipe, which depends on the roughness factor α. The values of N_c corresponding to α of 0.0, 0.5 and 1.0 are 9.20, 11.06 and 11.94 as discussed in Section 5.3.1. For other values of α, N_c can be obtained by quadratic interpolation.

5.7.2 Comparison between predicted results with numerical data

The validity of the SLA model in predicting the pipe penetration resistance has been established in Chapter 4 in three different cases. Therefore, the proposed model (Equations

5.12 to 5.16) is not validated here against physical modelling results. More importantly, the parameters relating to the strain softening and strain rate effects (δ_{rem}, ξ_{95} and μ) vary for different soils, and very few physical modelling studies are available to give details of them. Instead of using different arbitrary parameter sets to fit these model test results, this section aims to show that this model can be used to quantify satisfactorily the variations of penetration resistance caused by strain softening and strain rate. The predicted results obtained from Equations 5.12 to 5.16, $V_{c,pre}$, are compared with the numerical results used to perform the calibration, $V_{c,cal}$. Since the effects of strain softening and strain rate have been quantified separately in the previous sections, this study also provides some insights into how much error this model generates when they are combined.

It is noteworthy that using a simple power law equation to quantify $V_{g,ideal}$ leads to a certain degree of inaccuracy, especially for the high values of kD/s_{um}. Although using other nonlinear fits for $V_{g,ideal}$ can produce more satisfactory results, this issue is not pursued further since the main focus of this chapter is to investigate the variation of soil strength caused by strain softening and strain rate effects rather than to quantify the bearing capacity of ideal soil. Another method to evaluate $V_{g,ideal}$ is also used, which is to adopt the numerical results obtained from ideal weightless soil as base line curves. These curves are then used instead of Equation 5.12 to quantify $V_{g,ideal}$, and are then modified according to Equations 5.13 to 5.16 to take into account the variation of soil strength and soil buoyancy to produce $V_{c,pre}$.

Figure 5.37 shows the ratio of $V_{c,pre}$ to $V_{c,cal}$ at shallow embedment for different values of kD/s_{um}. The results obtained from using the power law equation and the base curves to generate $V_{g,ideal}$ are both presented. Ignoring the inaccuracy caused by adopting the power law expression (Figure 5.37a), very satisfactory predictions are obtained for the resistance curves (Figure 5.37b).

For the presentation of a large amount of data relating to the prediction error of V_c, a parameter *err* is introduced, expressed as

$$err = \frac{\sum |V_{c,pre} - V_{c,cal}|}{\sum V_{c,cal}} \tag{5.17}$$

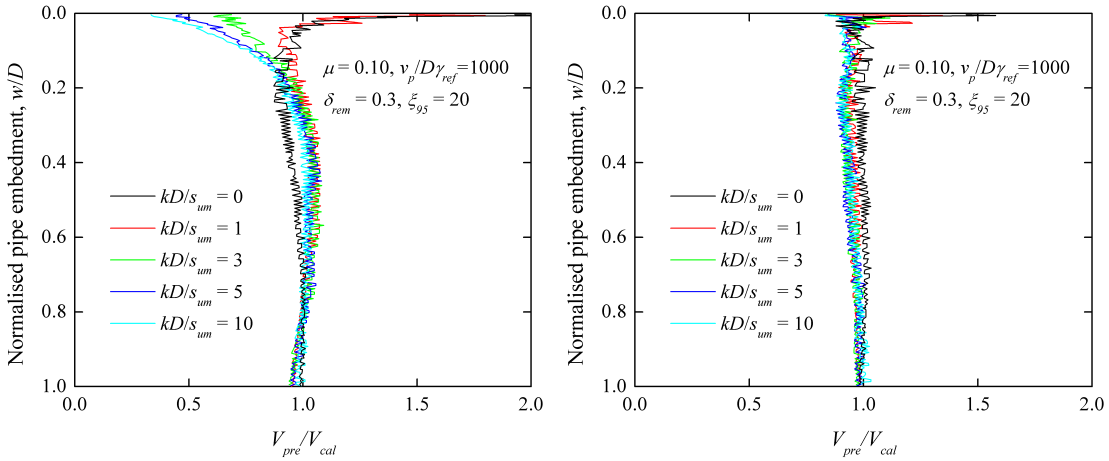

(a) $V_{g,ideal}$ from power law equation (b) $V_{g,ideal}$ from numerical results

Figure 5.37 $V_{c,pre}/V_{c,cal}$ at shallow embedment: effect of kD/s_{um}.

According to this definition, it can be seen that *err* denotes the weighted average of the prediction error, within a certain depth range. The reason why a weighted average is chosen is to weaken the influence of prediction errors at the initial stages of penetration, where the power law equation produces the severest inaccuracy for predicting $V_{g,ideal}$.

Figure 5.38 presents the values of *err* for different combinations of soil parameters for shallow embedments ($w/D \leq 1.0$). When the resistance curve obtained from the SLA simulation with ideal weightless soil is used to provide $V_{g,ideal}$, the prediction error is satisfactorily limited to 3%.

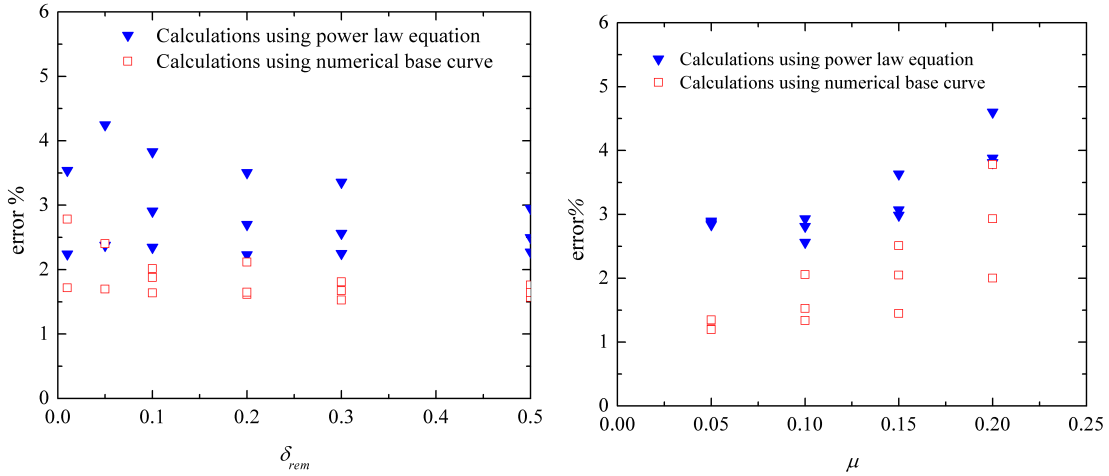

(a) Varied δ_{rem} and ξ_{95} (b) Varied μ and $v_p/D\dot{\gamma}_{ref}$

Figure 5.38 Weighted average of prediction error at shallow embedments ($w/D \leq 1.0$)

Figure 5.39 presents the values of *err* for different combinations of soil parameters for deep embedments ($2.5 \leq w/D \leq 3.0$). Here a considerable discrepancy between $V_{c,pre}$ and $V_{c,cal}$ at deep embedment is observed. It is noteworthy that strength degradation and enhancement are quantified separately in Sections 5.5 and 5.6 respectively, without taking into account the combined effects. This might lead to differences in the type and extent of the failure mechanism as well as the accumulated shear strain, compared with analyses where both effects are considered simultaneously. This issued is discussed in Section 5.7.3.

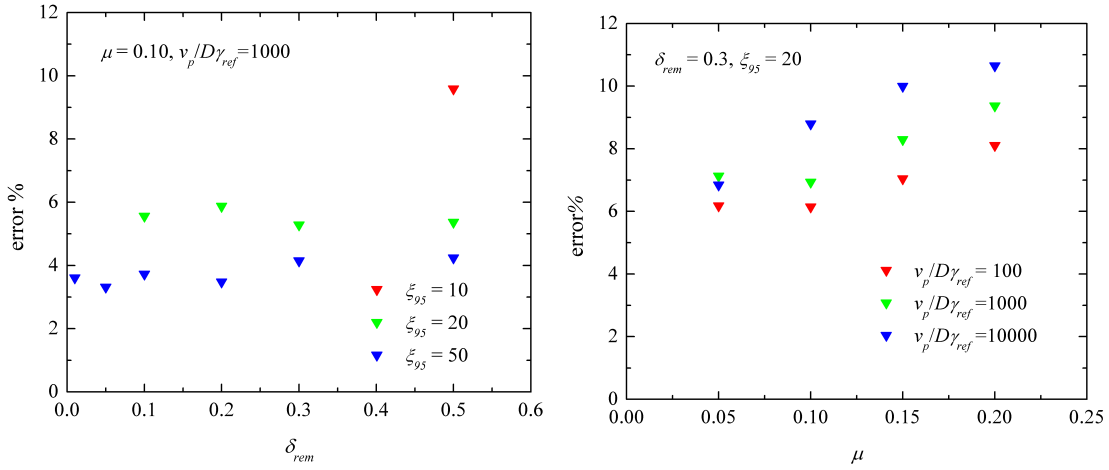

(a) Varied δ_{rem} and ξ_{95} (b) Varied μ and $v_p/D\dot{\gamma}_{ref}$

Figure 5.39 Weighted average of prediction error at deep embedments ($2.5 \leq w/D \leq 3.0$)

5.7.3 Effect of rate-dependence on strain softening

Figure 5.40 presents a comparison of the softening factor distribution between rate-dependent and rate-independent analyses. WIP analysis is performed to eliminate the influence of geometry change at the soil surface. The initial embedment of the pipe is chosen to be $3D$ to ensure that a localised mechanism is developed throughout the analysis. Typical parameters are used to consider the softening effect, namely $\delta_{rem} = 0.3$ and $\xi_{95} = 20$ (Randolph, 2004). The rate-dependent case is analysed with $\mu = 0.1$ and $v_p/D\dot{\gamma}_{ref} = 1000$ while the rate-independent case is analysed with $\mu = 0$. The presented field variables are obtained from results at $w/D = 2.0$ and 3.0, where w/D denotes the vertical distance that the pipe is displaced from its initial WIP position (see the dashed lines in Figure 5.40). It is found that after a movement of $2D$, the softening factor distributions in

the two cases show a very similar pattern, especially for the soil in the vicinity of the pipe. However, minor differences can also be observed. The rate-dependent soil case shows another area experiencing a slight softening effect away from the pipe vicinity, which might be caused by the larger mechanism size compared to that in the rate-independent case.

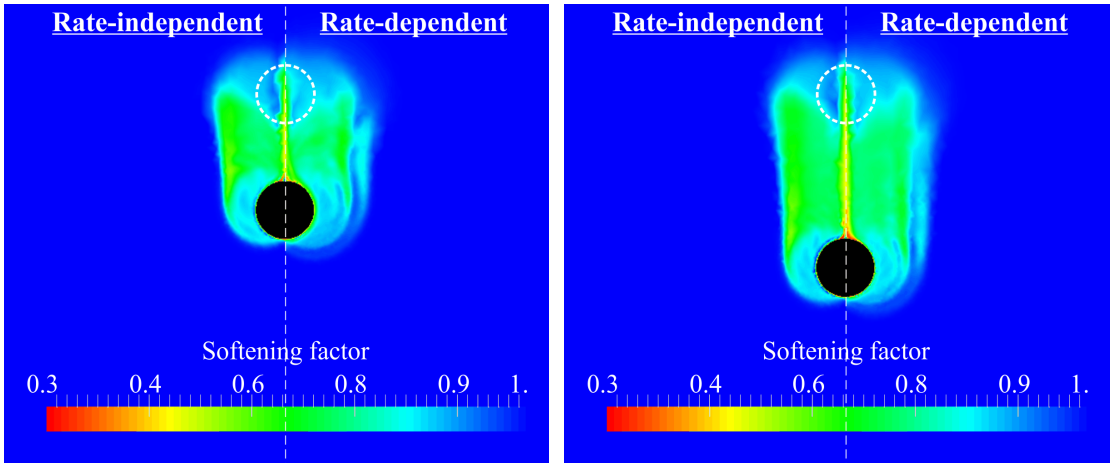

(a) $w/D = 2.0$ (b) $w/D = 3.0$

Figure 5.40 Comparison of softening factor between rate-dependent and rate-independent WIP analyses. $k = 0$, $\delta_{rem} = 0.3$ and $\xi_{95} = 20$.

In SLA modelling, the areas in which the strength is enhanced due to the strain rate effect is determined by the shear strain rate distribution obtained from the previous increment, which means the currently enhanced area does not necessarily coincide with the regions experiencing the highest strain rates in the current increment. When a particular area is enhanced, the sliplines of the failure mechanism tend to 'jump' to some other area with relatively 'weaker' strength; and in the next increment, these sliplines will 'jump' back when rate-dependent strength enhancement is applied to the current 'weaker' area. With repeated sequential analyses the sliplines will tend to oscillate between these areas, which is a disadvantage of using SLA to model strain rate effects. The drastic change in mechanism size between two consecutive analysis increments can be observed by comparing the right halves of Figure 5.41a and Figure 5.41b. However, global numerical stability can still be maintained, which can be confirmed by checking the degree of jaggedness in the penetration resistance curves shown in Figure 5.30. It is also seen in Figure 5.41b that the mechanism moves into a much less softened area compared with the vicinity of the pipe

(see Figure 5.40b). When the resistances obtained from the two consecutive increments are averaged, the softening factor will be moderately underestimated.

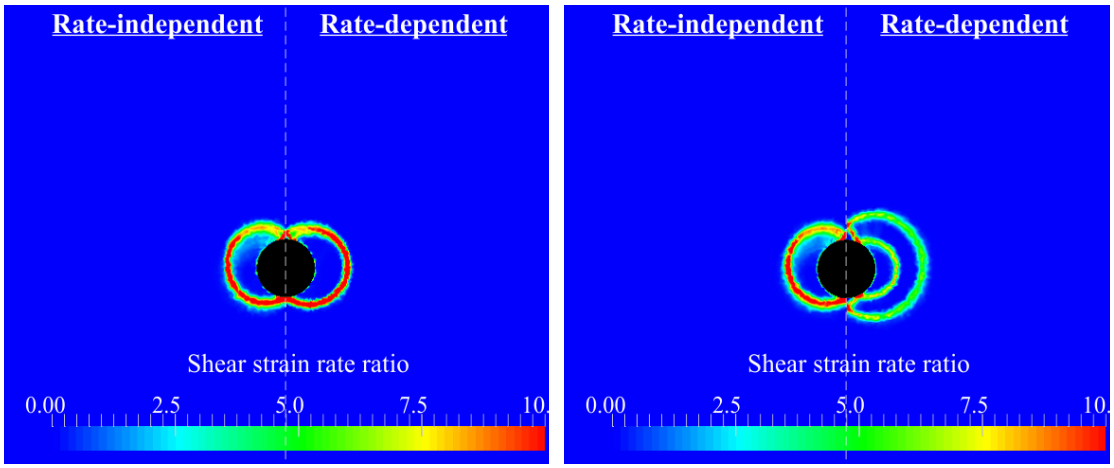

(a) 599th increment (b) 600th increment

Figure 5.41 Comparison of soil failure mechanisms (showing $\dot{\gamma}_{max}D/v_p$) between rate-dependent and rate-independent WIP analyses. $k = 0$, $\delta_{rem} = 0.3$ and $\xi_{95} = 20$.

5.8 Summary

This chapter has presented a numerical study into the vertical penetration behaviour of a rigid pipe into soft clay. The SLA and CEL methods were employed to explore the main features of this problem, and the parametric study results obtained from SLA are interrogated in detail. The pipe is penetrated from the soil surface to an embedment of three pipe diameters, in order to capture the pipe behaviour as a function of depth, particularly to explore different failure mechanisms. The influence of strength gradient, soil unit weight and parameters related to strain rate and remoulding effects, on the failure mechanism, as well as the penetration resistance, is examined. The main findings of this chapter are:

- At a shallow pipe embedment, typically below $0.8D$, soil deformation mechanisms extending to the soil surface are developed. With further penetration, the soil in the berms next to the pipe tends to slip towards the pipe. A transition of failure mechanism takes place at this stage, and after the pipe has reached a critical embedment, w_{cri}, of about $2D$, the soil around the pipe starts to flow around to gradually backfill the void above the pipe crown. This leads to a sharp reduction in the penetration

resistance. With further embedment, the soil surfaces at the two faces of the trench above the pipe gradually come into contact. Finally the failure mechanism becomes totally localised around the pipe. The transition of failure mechanism is found to take place much earlier if the strain softening effect of the soil is considered. The entire loading sequence, with extremely large deformations and strains, can be successfully modelled by both SLA and CEL methods.

- As the pipe penetrates the soil at shallow embedment the soil near the pipe ('adjacent soil') experiences much more plastic strain compared to that in areas remote to the pipe ('remote soil'). At deeper embedments, when the failure mechanism becomes more localised, only the 'adjacent soil' contributes to the bearing capacity. This leads to the consequence that at deep embedment, when a localised mechanism is induced, strain softening effects result in more reduction in soil resistance compared with that at shallow embedment.

- The local failure mechanism is more likely to occur when strength remoulding effects are considered, and as above this leads to a reduced rate of increase of bearing resistance. Typical values of the strain softening parameters, $\delta_{rem} = 0.3$ and $\xi_{95} = 20$ (Randolph, 2004), give a strain softening effect that reduces the total pipe resistance by about 6.5% at a pipe embedment below $1D$ and 20% at embedments beyond $2D$ (by comparison with ideal soil). If the soil buoyancy is neglected this change can be even more pronounced.

- Typical values of strain rate parameters $\mu = 0.1$ and $v_p/D\dot{\gamma}_{ref} = 1000$ (Biscontin and Pestana, 2001; Chatterjee *et al.*, 2012a) lead to strain rate effects that increase the total pipe resistance by about 12% at a pipe embedment below $1D$ and 9.2% at embedments beyond $2D$.

- A new calculation approach was proposed for assessing the penetration resistance of a pipeline (Equations 5.12 to 5.16). The geotechnical resistance in ideal weightless soil is calculated first, which takes into account the effect of the roughness of pipe-soil interface, α, and the soil strength gradient, k. After that any change to the soil

strength caused by strain softening and strain rate effects are considered, modifying the initial soil strength to an 'operative shear strength'. Soil buoyancy is included in the last step to produce the total soil resistance. Comparisons between the predictions made using this approach and numerical simulations demonstrate that this model satisfactorily quantifies the different and competing effects.

Chapter 6

Lateral pipe-soil interaction: monotonic

The design of untrenched pipelines for controlled buckling requires comprehensive understanding of the pipe-soil interaction behaviour, especially in the lateral direction (Bruton *et al.*, 2005, 2007). Accurate assessment of the soil resistance on the pipeline during lateral movements is required to ensure that lateral buckles form as planned. This chapter presents a detailed investigation into the monotonic lateral loading response of a pipe section under large deformations. The amplitude of the lateral pipe movement in this study is up to eight pipe diameters.

Both sequential limit analysis (SLA) and the coupled Eulerian-Lagrangian (CEL) method are used, although for the sake of clarity only the parametric study results obtained from SLA modelling are presented. Validation studies comparing the two methods have already been presented in Chapter 4. For the problem investigated in this chapter, further careful comparisons between the two methods are made before the parametric study results are presented. In order to provide a clearer insight into the pipe-soil interaction, yield envelopes at different loading stages have been derived in addition to the fundamental outputs of interest: pipe invert trajectory and lateral soil resistance.

6.1 Description of the numerical model

6.1.1 Problem definition

The problem as considered in the analysis is illustrated in Figure 6.1. A pipe of diameter D, shallowly embedded into the seabed by w_{ini}, is displaced laterally under a constant

vertical load representing its weight W. Solutions have been computed for w_{ini} ranging from $0.1D$ to $0.5D$, which is the typical range of initial embedment in the field (Westgate *et al.*, 2009; Westgate *et al.*, 2010). The pipe is considered as being infinitely long so that plane-strain conditions can be assumed. The soil has submerged unit weight γ' and its initial shear strength is determined by $s_{u0} = s_{um} + kz$, where s_{um} is the initial strength at the mudline, k is the strength gradient and z is the depth. A soil berm is formed ahead of the pipe as it scrapes across the soil surface, and this material comes into progressively increasing contact with the pipe as the analysis proceeds. The pipe is assumed not to rotate as it moves laterally because in practice the torsional rigidity of the pipe is likely to be sufficient to restrain it against rotation within a buckle. The transient suction generated at the rear side of the pipe is neglected, and thus no tensile force is permitted at the pipe-soil interface. Large deformations and strains are developed in the loading process and the soil around the pipe experiences severe remoulding, leading to degradation of the operative shear strength s_u. The loading rate has an influence of enhancing s_u due to the strain rate effect (viscosity).

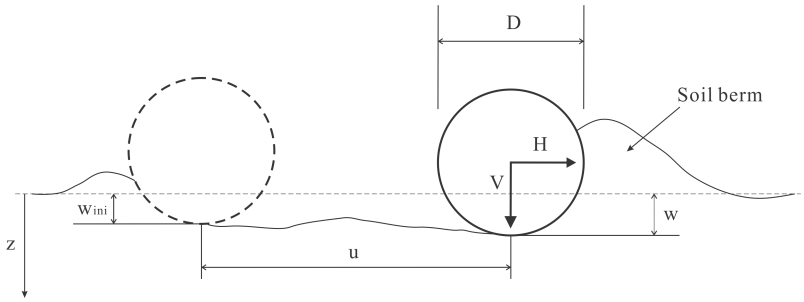

Figure 6.1 Problem definition: monotonic lateral loading

6.1.2 Numerical details of the SLA model

A two-dimensional plane strain model was used in the SLA simulation. The main details of the model are as provided in Section 4.7.1.1. The configuration and boundary conditions of the model are illustrated in Figure 4.27. For this study, B_1 and B_2 were chosen to be $3D$ and $16D$ respectively, and h was set as $5D$. This dimension was chosen based on preliminary studies to ensure that the zones of plastic shearing were contained within the model boundaries throughout the simulation. A typical initial mesh for this problem can

be seen in Figure 6.2a. The values of the normalised incremental displacement $\delta d/D$ were chosen to be 0.0025 and 0.005 for the installation and lateral loading processes respectively. The minimum element size A_{min} was set as $0.00025D^2$. These values of $\delta d/D$ and A_{min} have been proven to yield reliable results, as discussed in Chapter 4 where studies of benchmark problems are presented. A no-tension condition was imposed at the pipe-soil interface to allow for separation of the pipe from the soil. The shear strength of the pipe-soil interface was modelled as $\tau_{int} = \alpha s_u$, with α chosen as 0.5 by default. Other values of the soil and pipe parameters used in the study are listed in Table 6.1. The simulation procedure can be described as follows.

Table 6.1 Parameter values used for investigating the loading behaviour of a pipe

Parameter	Default value	Other values
Pipe diameter, D: m	1.0	-
Shear strength of soil at mudline, s_{um}: kPa	1.0	-
Shear strength gradient, k: kPa/m	2	0, 1, 3, 5, 10
Submerged unit weight of soil, γ': kN/m^3	3	0, 1, 5, 10, 20
Roughness of pipe/soil interface, α	0.5	0.0, 0.2, 1.0
Initial pipe embedment, w_{ini}: m	0.2	0.1, 0.3, 0.4, 0.5
Maximum lateral displacement of the pipe, u_{fin}: m	8.0	-
Remoulded strength ratio, $\delta_{rem} = 1/S_t$	0.3	1, 0.8, 0.6, 0.5, 0.4, 0.2, 0.1
Ductility parameter of soil, ξ_{95}	10	2, 5, 20, 30, 40, 50
Viscosity parameter of soil, μ	0	0.05, 0.10, 0.15, 0.20
Pipe displacement rate, v_p: m/s	0.003	0.0003, 0.03
Reference shear strain rate, $\dot{\gamma}_{ref}$: s^{-1}	3×10^{-6}	-

- The pipe was pre-embedded into the soil at a very shallow depth of $0.001D$ and then pushed under displacement control to desired initial embedment depth, w_{ini}, which in the default case of the parametric study was $0.2D$. The effects of strain softening and rate dependence of the soil were not considered during this installation process, and the cumulative shear strain of the soil domain was reset to zero before the start of the lateral loading step. This was to ensure that all the differences resulting from the effects of strain softening and strain rate was generated from the lateral loading step rather than the initial penetration stage.

- Once the installation process had been completed, a downward vertical load representing the pipe weight was applied and kept constant while the pipe was displaced

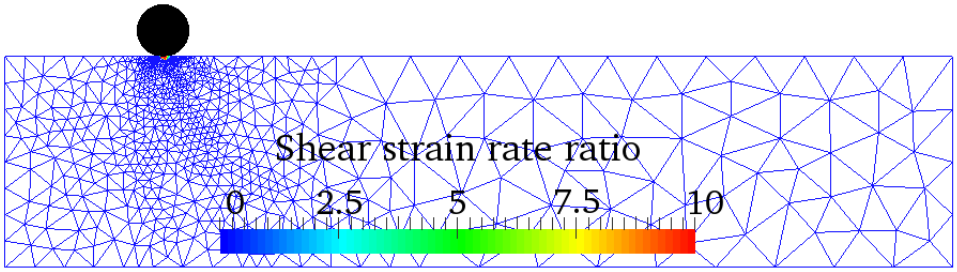

(a) Initial position

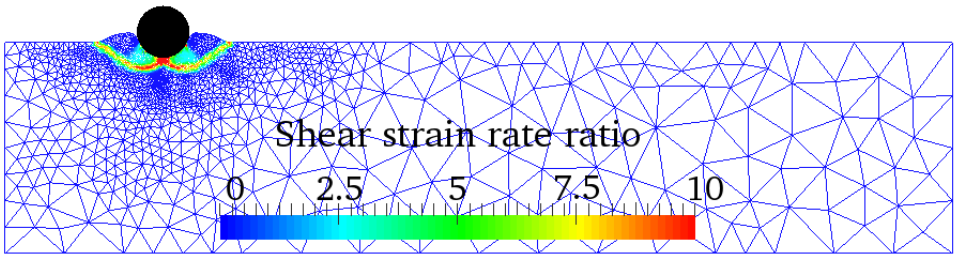

(b) $\bar{u} = 0.0$

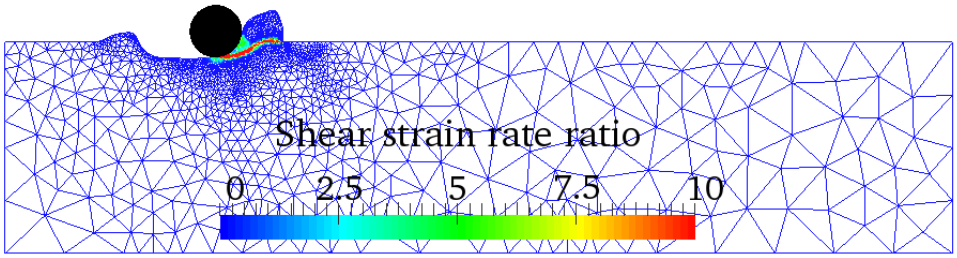

(c) $\bar{u} = 1.0$

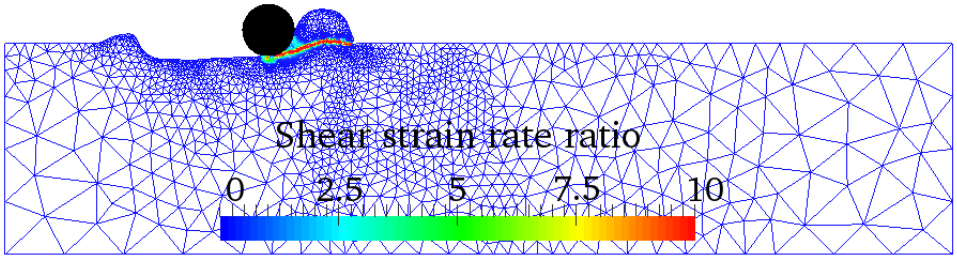

(d) $\bar{u} = 2.0$

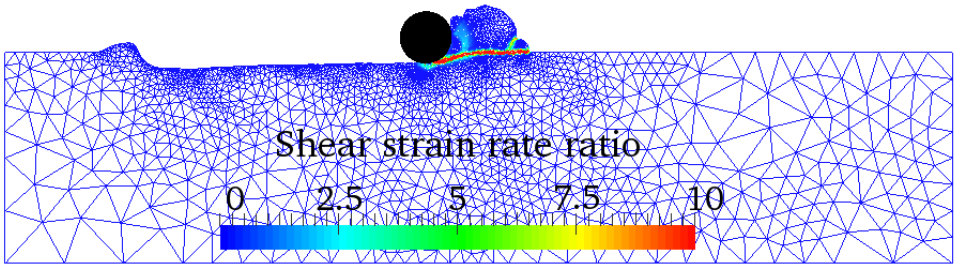

(e) $\bar{u} = 5.0$

Figure 6.2 Soil failure mechanisms (showing $\dot{\gamma}_{max}D/v_p$) during lateral loading in SLA modelling. $kD/s_{um} = 2$, $\delta_{rem} = 0.3$, $\xi_{95} = 10$, $w_{ini}/D = 0.3$, $W/Ds_{um} = 3.2$.

laterally to a final horizontal displacement of $8D$. The loading process is illustrated in Figure 6.2 for a pipe weight $W = 3.2Ds_{um}$.

During the lateral movement, the analyses were terminated if the soil berm ahead of the pipe grew so big that it covered the pipe crown, even if the target displacement had not been reached. Because once that happened, severe numerical instability would be introduced; and more importantly, heavy pipe behaviour with overtopping was not the focus of this study.

6.1.3 Numerical details of the CEL model

The main details of the CEL model for this problem are as provided in Section 4.7.1.2. The configuration and boundary conditions of the model are illustrated in Figure 4.28. B_1 and B_2 were chosen to be $3D$ and $12D$ respectively and h was set as $4.2D$. This dimension was chosen based on preliminary studies to eliminate boundary effects. The minimum mesh size of the model was $0.025D \times 0.025D \times 0.025D$ and the Eulerian domain had a total number of 58800 elements. The simulations were conducted in the following four steps.

- Restrain the Eulerian material from flowing outside the predefined dimensions. The velocity was set to zero in the perpendicular direction at the bottom and all planar boundaries of the soil extending to the top of the Eulerian domain, while the top surface of the soil was left free to move within the void.

- Apply a body force representing the submerged unit weight of the soil, and at the same time restrain the movement of the pipe in all directions.

- Penetrate the pipe at a given velocity (v_p) of $0.05D$/s to the required position w_{ini}. As in the SLA modelling the soil was considered as ideal (perfectly plastic, rate-independent) within this step and the cumulative shear strain was reset to zero after the installation was completed.

- Release the vertical constraint on the pipe and apply a constant downward vertical load to it. Then laterally displace the pipe, without rotation, at constant velocity (v_p)

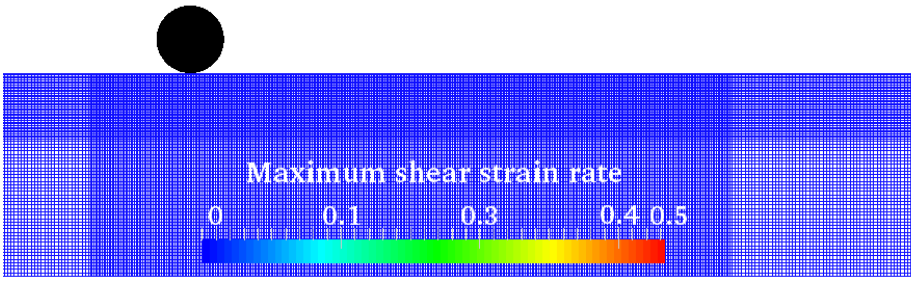

(a) Initial position (with mesh)

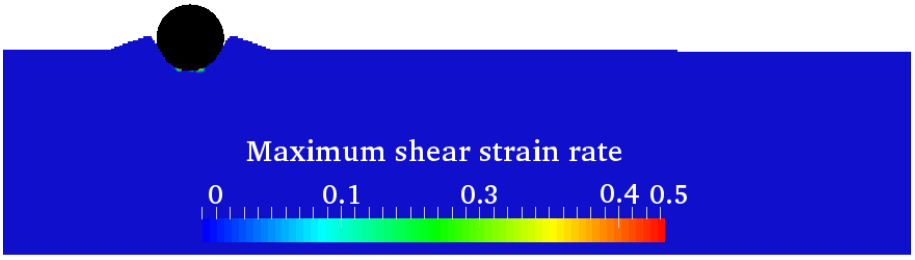

(b) $\bar{u} = 0.0$

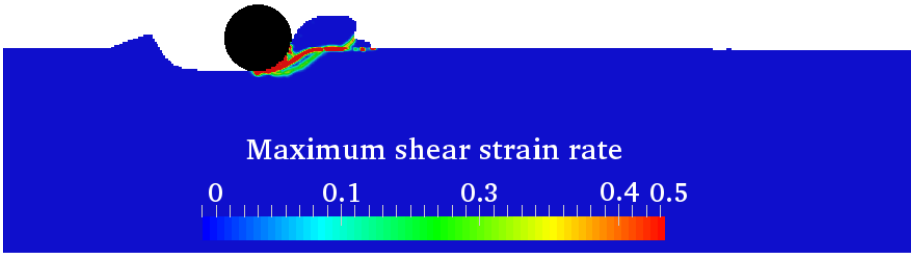

(c) $\bar{u} = 1.0$

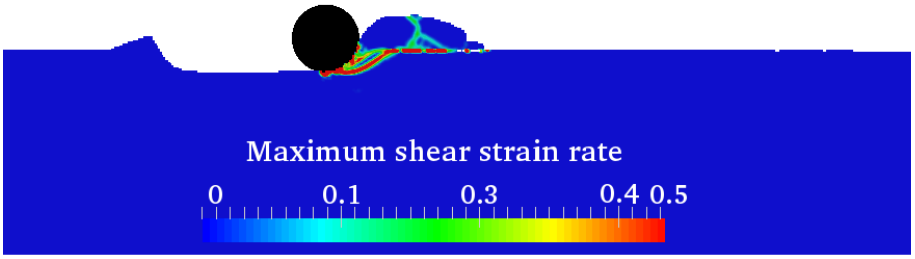

(d) $\bar{u} = 2.0$

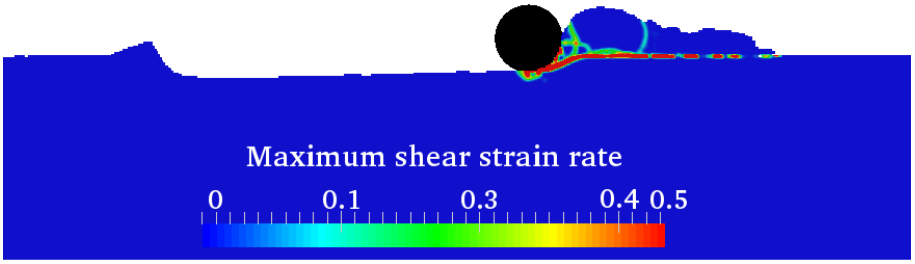

(e) $\bar{u} = 5.0$

Figure 6.3 Soil failure mechanisms (showing $\dot{\gamma}_{max}$) during lateral loading in CEL modelling. $kD/s_{um} = 2$, $\delta_{rem} = 0.3$, $\xi_{95} = 10$, $w_{ini}/D = 0.3$, $W/Ds_{um} = 3.2$.

of $0.05D$/s through a distance of $5D$ (Figure 6.3). The enhancement and degradation of the soil strength due to loading rate and strain softening were taken into account in this step.

6.2 Comparison between typical SLA and CEL results

Three types of soil were used in the comparison between SLA and CEL analysis: homogenous ideal soil ($kD/s_{um} = 0$ and $\delta_{rem} = 1.0$), homogenous softening soil ($kD/s_{um} = 0$ and $\delta_{rem} = 0.3$) and non-homogeneous softening soil ($kD/s_{um} = 2$ and $\delta_{rem} = 0.3$). The initial embedment of the pipe before the lateral loading was $0.3D$. Other parameters were chosen to be the same as the default case, as given in Table 6.1. The normalised vertical penetration resistances V_c/Ds_{um} of the pipe at the depth of $0.3D$ were 5.43 and 8.01 for the homogenous and non-homogeneous soil respectively. Three levels of overloading W/V_c, of 0.1, 0.2 and 0.4 were considered here for comparison.

Figures 6.4 to 6.6 show the invert trajectory as well as the equivalent 'friction factor' H/W, where H is the lateral soil resistance experienced by the pipe. Good agreement between SLA and CEL results is apparent for most of the loading cases, covering both light and heavy pipe behaviour. It is noteworthy that the loading case with $W/V_c = 0.2$ in non-homogeneous softening soil (see Figure 6.6) has not been completed in CEL modelling. This is probably due to the fact that the Eulerian volume fractions (EVF) of the CEL model in the region where the active soil berm makes contact with the original soil surface is less than one, resulting in a mechanically weak and unstable region. This phenomenon can be observed in almost all the CEL simulations of lateral loading of a pipe with light or moderate weight (see Figure 6.7).

In general, CEL generates slightly larger pipe embedment but lower soil resistance than SLA. The increase in H to a peak value within a very short displacement caused by soil suction, as observed in physical modelling results (e.g. Dingle *et al.*, 2008, Rismanchian, 2014), cannot be observed in either the SLA and CEL results. This is because separation at the rear of the pipe took place immediately after the lateral movement began, due to the prescribed absence of tension at the pipe-soil interface. Therefore, both SLA and

CEL underestimate the breakout response of the pipe to some degree. In the parametric study results presented in Section 6.3, interface tensile capacity was taken into account when deriving the yield envelopes of the pipe before lateral loading. A more reasonable prediction of the breakout resistance H_{brk} could be made by seeking a value between the results obtained with and without the tensile capacity.

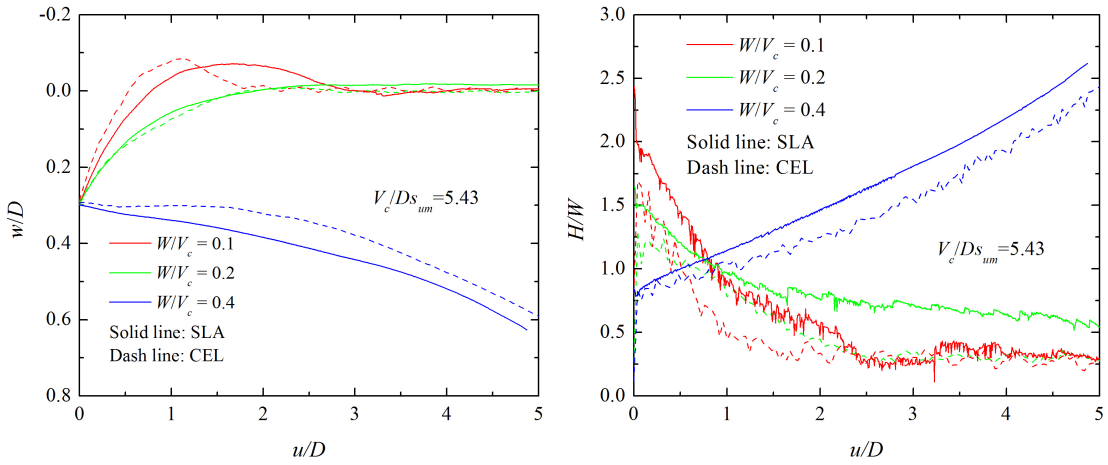

(a) Invert trajectory (b) Equivalent friction factor

Figure 6.4 Comparison between SLA and CEL results using homogenous ideal soil. $kD/s_{um} = 0$, $\mu = 0$, $\delta_{rem} = 1.0$.

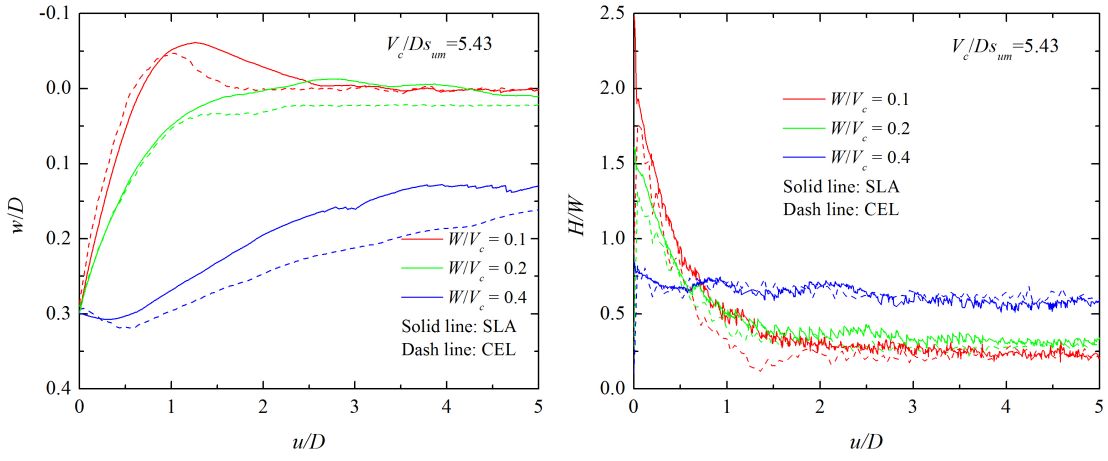

(a) Invert trajectory (b) Equivalent friction factor

Figure 6.5 Comparison between SLA and CEL results using homogenous softening soil. $kD/s_{um} = 0$, $\mu = 0$, $\delta_{rem} = 0.3$, $\xi_{95} = 10$.

Table 6.2 shows a comparison of computing time between the SLA and CEL analyses. Only the results obtained from the soils with softening effects being considered are provided for comparison. The computing time of the SLA analyses increases with W/V_c because

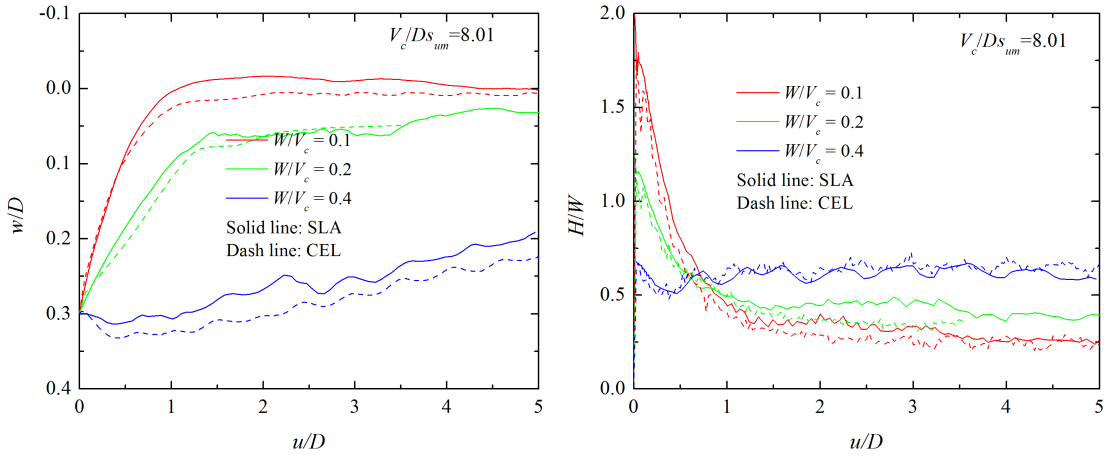

(a) Invert trajectory (b) Equivalent friction factor

Figure 6.6 Comparison between SLA and CEL results using non-homogeneous softening soil. $kD/s_{um} = 2$, $\mu = 0$, $\delta_{rem} = 0.3$, $\xi_{95} = 10$.

Table 6.2 Computing time for SLA and CEL analyses

Soil type	W/V_c	Time (SLA): h:m:s [1]	Time (CEL): h:m:s [2]
Homogenous softened soil	0.1	02:53:39	07:53:16
	0.2	03:49:19	07:46:29
	0.4	06:41:55	07:57:40
Linear softened soil	0.1	02:41:24	12:11:09
	0.2	03:36:10	-
	0.4	05:38:33	11:59:54

[1] 4 core PC, 3 to 4 analyses running in parallel
[2] 32 core supercomputer, 1 analysis at a time

more elements become involved in the simulation as the pipe with heavier weight dives deeper into the soil. This is not the case in the CEL analyses as the number of elements remains the same throughout the simulation. On average, the computing time of the SLA analyses presented here is about 40% of the CEL analyses. However, it is noteworthy that second order elements are used in SLA, which indicates more reliable treatment of field variables than in CEL. Moreover, the SLA analyses were performed on a 4-processor desktop and typically 3-4 parallel analyses were carried out at the same time, while the CEL analyses were run on a supercomputer with full use of 32 processors.

Figures 6.2 and 6.3 illustrate the soil failure mechanisms during lateral loading in the SLA and CEL analyses. The soil in this loading case was non-homogeneous softening soil ($kD/s_{um} = 2$ and $\delta_{rem} = 0.3$) and the overloading ratio (W/V_c) was 0.4. The variable $\dot{\gamma}_{max}D/v_p$ in Figure 6.2 is visualised on the scale of 10 while $\dot{\gamma}_{max}$ in Figure 6.3 is visualised

on the scale of 0.5. Considering that the loading rate (v_p) in the CEL modelling was chosen to be $0.05D$/s, these results are ready for direct comparison. By comparing the shape of soil berm between Figures 6.2 and 6.3, it can be inferred that the soil in the CEL analysis is much softer than that in SLA throughout the simulation. The reason for such different behaviour lies in the fact that the region where the soil berm makes contact with the original soil surface is not fully filled by soil material (EVF<1, see Figure 6.7), which creates a mechanically very weak region. During the analysis, intense shearing always takes place in the weakest area of the soil and thus the unrealistic weak region in CEL analysis leads to underestimated soil resistance. This reveals a drawback of CEL in handling the evolution of self-contacting free surfaces. Figures 6.8a and 6.8b show the softening factor of the soil in the SLA and CEL simulations. The results obtained at $u/D = 5.0$ are presented. In both analyses, the soil within the active berm experiences different levels of softening. Some of the soil becomes fully remoulded while some remains intact even after a displacement of five pipe diameters. The shape of the soil berm obtained from SLA simulation has been compared with that from centrifuge modelling (Dingle *et al.*, 2008) in Section 4.7.2, and reasonably good agreement has been achieved.

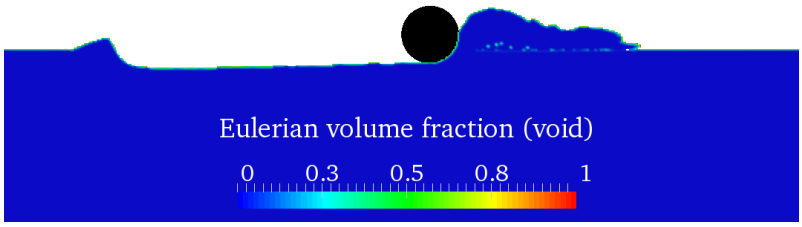

Figure 6.7 Eulerian volume fractions (EVF) of the CEL model at $u/D = 5.0$. $kD/s_{um} = 2$, $\delta_{rem} = 0.3$, $\xi_{95} = 10$ and $W/Ds_{um} = 3.2$. Only part of the soil domain is shown.

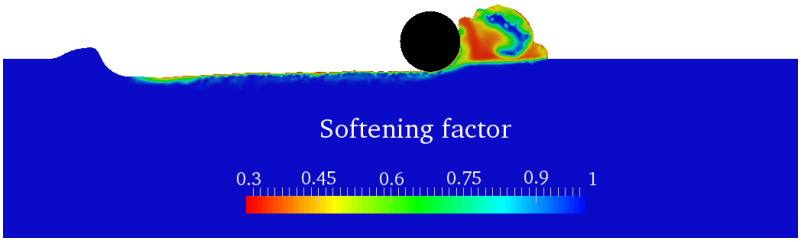

(a) SLA

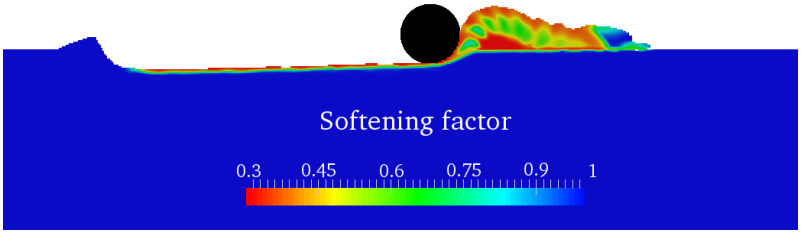

(b) CEL

Figure 6.8 Softening factor of the soil at $u/D = 5.0$. $kD/s_{um} = 2$, $\delta_{rem} = 0.3$, $\xi_{95} = 10$ and $W/Ds_{um} = 3.2$. Only part of the soil domain is shown.

6.3 Parametric study

The default pipe and soil parameters representing a typical soft clay seabed in the parametric study are given in Table 6.1, where the other parameters adopted are also illustrated. In each set of analyses, one parameter was changed while keeping all others the same as the default case. All of the results are presented in normalised form and can therefore be generalised to other parameter values. The normalised pipe weight (W/Ds_{um}) was chosen to be in the range 0.8 to 6.4 to investigate the behaviour of both light and heavy pipes. The bearing capacity of the pipe (V_c) was calculated as $6.45Ds_{um}$, at the default initial embedment of $0.2D$. It it noteworthy that V_c was quantified from displacement-controlled penetration into ideal soil where no strain softening or rate dependence was considered. This is for the sake of consistency when the effects of softening and rate dependence during the lateral displacement phase are to be studied.

6.3.1 Effect of pipe weight, W

6.3.1.1 Soil mechanism

Figure 6.9 shows typical soil failure mechanisms of three pipes of light, moderate and heavy weight, after being displaced by $5D$. All parameters apart from the pipe weight have their default values as in Table 6.1.

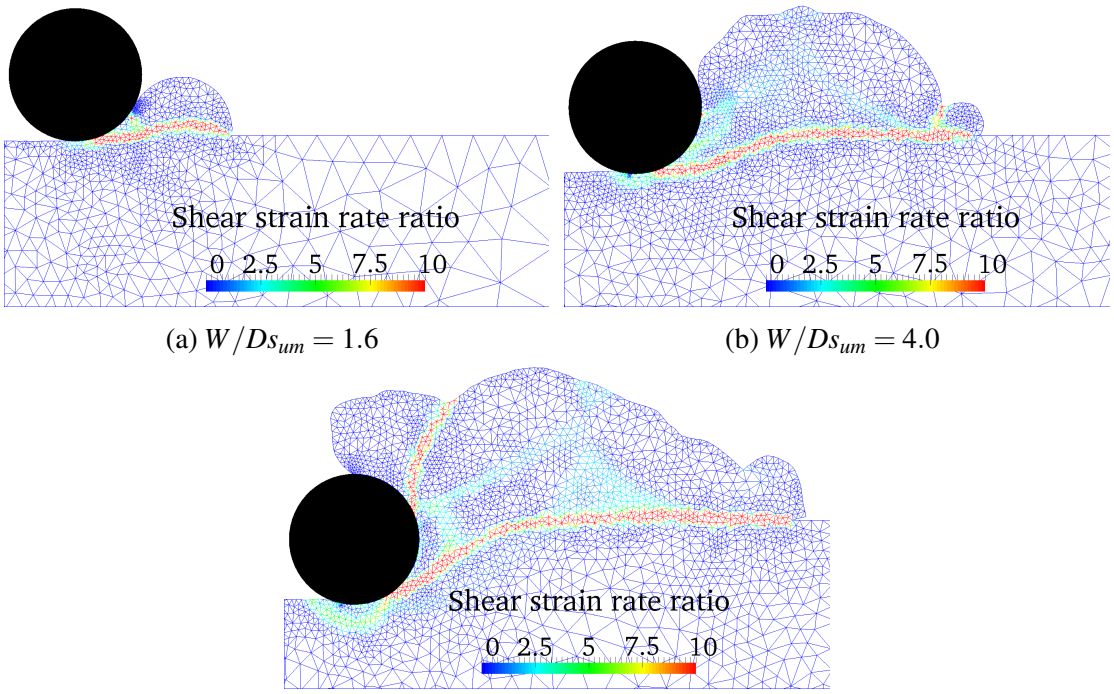

(a) $W/Ds_{um} = 1.6$ (b) $W/Ds_{um} = 4.0$

(c) $W/Ds_{um} = 5.6$

Figure 6.9 Soil failure mechanisms (showing $\dot{\gamma}_{max}D/v_p$) for pipes with different weights at $u/D = 5.0$

It can be seen Figure 6.9a that the light pipe scrapes across the soil surface at very shallow depth, with a small berm ahead of it moving essentially as a rigid block. Shear deformation takes places almost horizontally at the elevation of the original soil surface. A similar mechanism can be seen in Figure 6.9b, where the pipe is of moderate weight and the soil berm of a larger size because the pipe has been scraping at a deeper embedment. The heavy pipe (Figure 6.9c) ploughs at a depth over half its diameter, and multiple sliplines can be observed within the soil berm, which grows so big that it even covers part of the pipe crown. The soil above the pipe crown exerts a downward force on the pipe (see the slip line above the pipe) and encourages it to dive further into the soil, which can be seen

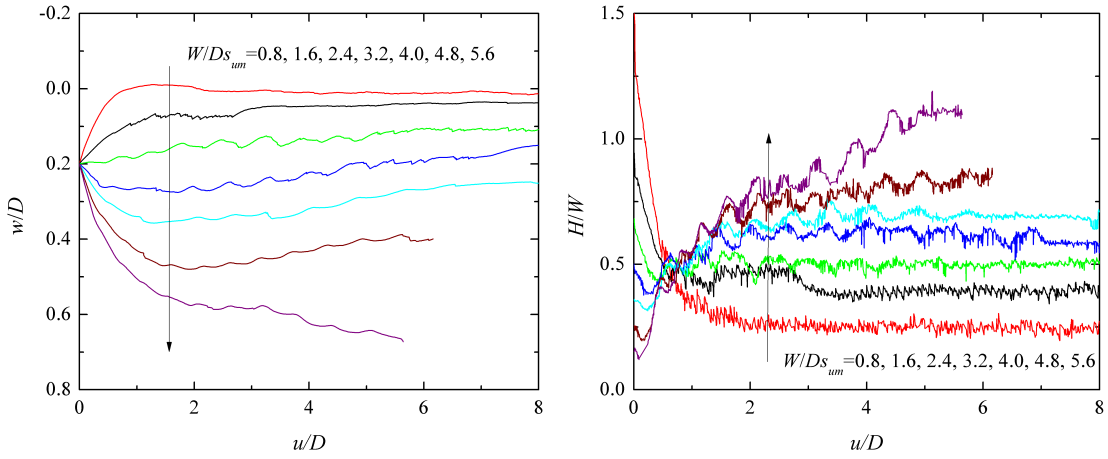

(a) Invert trajectory (b) Equivalent friction factor

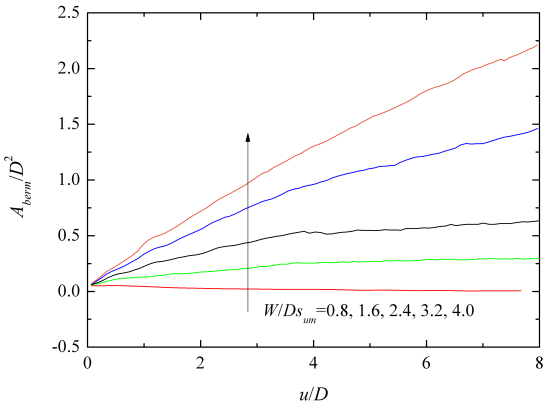

(c) A_{berm}

Figure 6.10 Effect of pipe weight on lateral loading behaviour. $kD/s_{um} = 2$, $\delta_{rem} = 0.3$, $\xi_{95} = 10$, $\mu = 0$

in the pipe trajectory curve for $W/Ds_{um} = 5.6$ in Figure 6.10a. In most cases, it can be assumed that once the embedment of the pipe exceeds half its diameter, it will never move upward again, even considering the increase in soil strength with depth and the growth of the softened soil berm.

6.3.1.2 Loading response under large displacement

Figures 6.10a to 6.10c show the loading responses of pipes with different weights, in terms of invert trajectory, equivalent friction factor and soil berm size. The berm area was obtained based on integration of the vertical coordinates of the surface nodes of the berm. Three types of behaviour can be observed:

1) For pipes with light weight ($W/Ds_{um} = 0.8$, 1.6 and 2.4), upward movement occurs immediately when the lateral movement begins. After a lateral displacement of about $3D$,

the vertical displacement stabilizes and the berm size remains almost constant until the final displacement of $8D$. As a result, the lateral resistance drops sharply after the initial breakout and then reaches a relatively stable residual value. Thus a very reasonable 'steady state' can be achieved by these light pipes. A similar phenomenon has been reported by Wang *et al.* (2010) and Chatterjee *et al.* (2012a), that a steady state can be reached by a light pipe after being displaced by about $2.2D$.

2) The pipes with moderate weight ($W/Ds_{um} = 3.2$, 4.0 and 4.8) move downwards at first and then experience a rebound in the invert elevation due to the growth of the soil berm ahead. After that both the invert elevation and the berm size keep increasing gradually. Due to these counterbalancing effects, the lateral resistance of the pipe stays almost constant during the residual loading stage. In this study, the response of these pipes with moderate weight can also be categorized eventually as light pipe behaviour, even though the pipes move downward at the initial stage.

3) The pipe with heavy weight ($W/Ds_{um} = 5.6$) keeps diving into the soil to an embedment of over half a diameter and never experiences a rebound of invert elevation, resulting in a continuous increase in the lateral resistance. In this scenario a steady residual resistance cannot be reached within the displacement range considered in this study.

Of interest in Figure 6.10b is that the breakout friction factor, H_{brk}/W, decreases significantly with increase of the pipe weight, but this trend is reversed quickly with further lateral movement. Acceptable fluctuations are observed in the resistance curves. However, for better visualization, the load-displacement results presented hereafter are smoothed by taking the average of every ten consecutive data points.

6.3.1.3 Evolution of yield envelopes

Figures 6.11a to 6.11c show the evolution of the $V-H$ yield envelope for three pipes of different weight during lateral loading. The yield envelopes at a given model configuration were obtained by applying radial loading probes at fixed intervals, chosen as 1° in this study. The initial yield envelopes before the lateral movement are identical in all three cases and have a symmetric form. Since no tension is allowed at the pipe-soil interface,

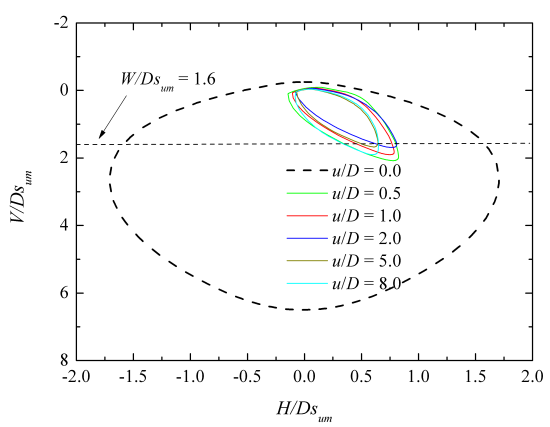

(a) $W/Ds_{um} = 1.6$

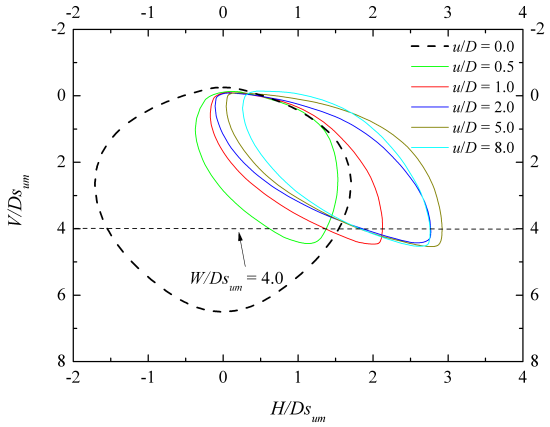

(b) $W/Ds_{um} = 4.0$

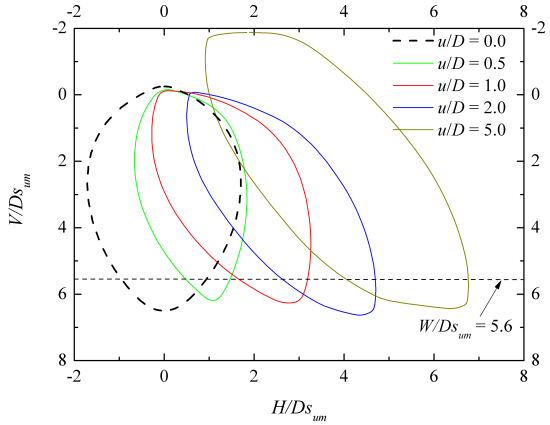

(c) $W/Ds_{um} = 5.6$

Figure 6.11 Evolution of $V-H$ yield envelope for pipes with different weights. $w_{ini} = 0.2$, $kD/s_{um} = 2$, $\delta_{rem} = 0.3$, $\xi_{95} = 10$, $\mu = 0$

breakout of the pipe from the soil in the active area takes place immediately after the lateral movement is imposed. This leads to a rapid change in the shape of the yield envelopes.

Figure 6.11a shows the yield envelope evolution of a pipe with light weight ($W/Ds_{um} = 1.6$) at different loading stages. The envelope size experiences severe shrinking during the first half diameter of lateral displacement, then reaches a relatively stable state after being displaced by about $5D$. This finding is consistent with the observations in Figure 6.10b.

Figure 6.11b shows the evolution of yield envelopes of a pipe with moderate weight ($W/Ds_{um} = 4.0$). Less shrinkage in the envelope size can be observed, although the envelope shape changes considerably. The envelope expands in the H direction at first within a pipe displacement of $2D$, then experiences very limited change in both size and shape.

Figure 6.11c shows the yield envelopes of a pipe with heavy weight ($W/Ds_{um} = 5.6$) at different stages of the lateral loading. The envelope size keeps growing after the initial breakout stage, and the expansion takes place mostly in the H direction. It is interesting to note that V_{max} stays almost unchanged throughout the analysis no matter how the shape and size of the envelope vary. After a pipe displacement of $5D$, the uplift capacity of the pipe improves markedly, even though no tension is allowed at the interface. This is because the soil berm grows extremely large and exerts a downward force on the pipe (see Figure 6.9c).

The yield envelopes described above were derived based on the assumption that the pipe-soil interface has zero tension capacity. This has been proved to underestimate the breakout response of the pipe, as discussed in Section 4.7.2. When evaluating the breakout resistance H_{brk} prior to the lateral movement, it is useful to take into account the influence of the soil suction on the rear of the pipe. In the results presented hereafter, yield envelopes for assessing the breakout resistance are obtained from analyses both with and without tensile capacity at the pipe-soil interface. A realistic value should lie in the band bracketed by the results obtained for these two conditions.

6.3.2 Effect of initial pipe embedment, w_{ini}

A set of simulations was conducted examining the effect of initial embedment on the lateral loading behaviour of pipes. Five values of initial embedment ($w_{ini}/D = 0.1$, 0.2, 0.3, 0.4 and 0.5) and six levels of overloading ($W/Ds_{um} = 0.8$, 1.6, 2.4, 3.2, 4.0 and 4.8) were considered. Other soil parameters were kept as the default values given in Table 6.1.

6.3.2.1 Loading response at break-out

Figure 6.12 shows the yield envelopes of pipes with different initial embedments (w_{ini}), before the lateral loading. As stated before, the effect of strain softening was ignored during the initial penetration phase and thus the yield envelopes presented here were derived with ideal soil. It can be seen that w_{ini} has a fundamental influence on the breakout resistance of the pipe; that is, for a given pipe weight, more lateral resistance can be mobilised

with deeper initial embedment, which is confirmed in Figure 6.14b. The effect of tensile capacity at the pipe-soil interface is also illustrated in Figure 6.12. The enhancement of lateral resistance caused by the tensile capacity becomes much more significant as the pipe weight reduces, which can be easily checked by adopting an extreme value of $V = 0$ in Figure 6.12.

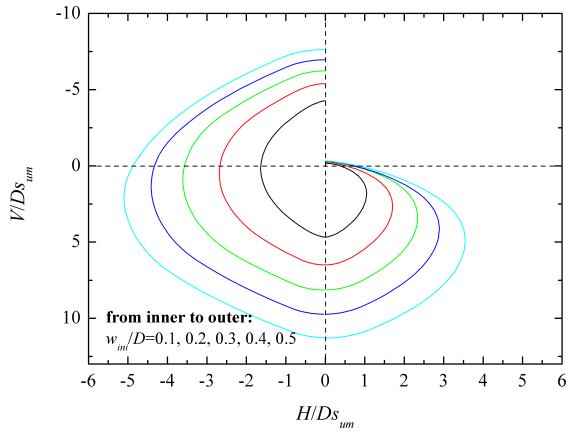

Figure 6.12 Effect of initial embedment on $V-H$ yield envelope at the breakout stage. Left half is with full tension at the pipe-soil interface and right half is without tension. $kD/s_{um} = 2$, $\gamma' D/s_{um}$, ideal soil.

6.3.2.2 Loading response under large displacement

Figures 6.13a and 6.13b illustrate the effect of w_{ini} on the yield envelopes of the pipe at lateral displacements of $5D$ and $8D$. It can be seen, especially in Figure 6.13b, that both the shape and size of the yield envelopes are very close for the analyses starting from different values of w_{ini}, indicating limited influence of the initial embedment on the residual response of the pipe.

Figures 6.14a to 6.14d show the effect of w_{ini} on the lateral loading response of a light pipe ($W/Ds_{um} = 1.6$). It can be observed in Figure 6.14b that H_{brk}/W increases significantly from 0.65 to 1.77 as w_{ini}/D ranges from 0.1 to 0.5. Two reasons contribute to this significant difference. One is that the yield envelope of a pipe (wished-in-place) expands considerably with its nominal embedment, as reported by Merifield *et al.* (2008b) and Martin and White (2012). Another reason is that in the deeper embedment case, more soil is displaced during the penetration process (pushed-in-place) to form bigger

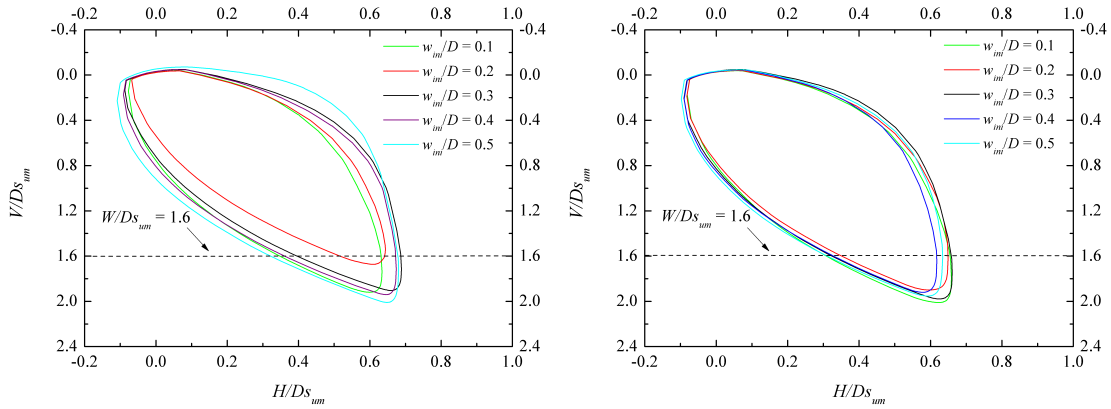

(a) $u/D = 5.0$ (b) $u/D = 8.0$

Figure 6.13 Effect of initial embedment on $V-H$ yield envelope at the residual stage. $kD/s_{um} = 2$, $\delta_{rem} = 0.3$, $\xi_{95} = 10$, $\mu = 0$.

berms beside the pipe, which provides more resistance to the pipe when it moves laterally. These two factors also explain why the light pipe with deeper w_{ini} moves upward more rapidly compared to that with shallow w_{ini} during the initial loading stage, as illustrated in Figure 6.14a. After the initial lateral breakout, the influence of w_{ini} on the lateral response diminishes with further displacement. As shown in Figures 6.14a and 6.14b, both the invert trajectory and the friction factor of the pipe converge very closely. A moderate difference is found in the size of the soil berm illustrated in Figure 6.14c; however, a trend of converging is also present.

According to the concept of effective embedment proposed by Wang *et al.* (2010), the lateral resistance of a pipe depends strongly on the effective embedment, w', as shown in Figure 2.11 and defined as

$$\frac{w'}{D} = \frac{w}{D} + \frac{h'_{berm}}{D} = \frac{w}{D} + \frac{1}{S_t D}\sqrt{\frac{A_{berm}}{\eta}} \tag{6.1}$$

in which A_{berm} is the area of the soil berm, idealized as a rectangle with aspect ratio η. Since the parameter η also varies for different loading cases, precise values of w' derived from Equation 6.1 are not presented here. Instead, w' was obtained by measuring the vertical coordinate of the leftmost node on the surface of the active soil berm relative to that of the pipe invert. The variation of w' with lateral movement is shown in Figure 6.14d, where a closer match can be observed compared with that of A_{berm} as illustrated in Figure 6.14c.

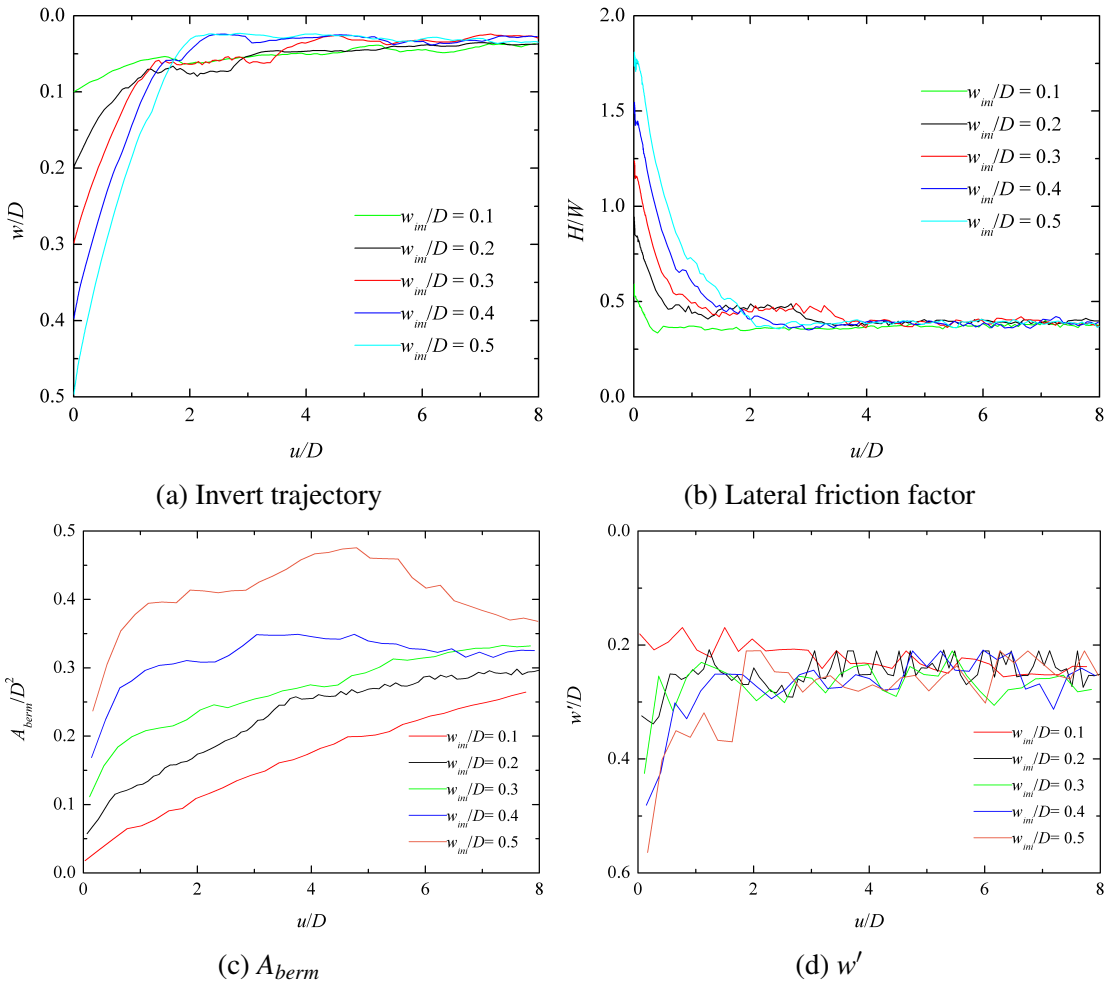

(a) Invert trajectory

(b) Lateral friction factor

(c) A_{berm}

(d) w'

Figure 6.14 Effect of initial embedment on lateral loading behaviour of a light pipe. $W/Ds_{um} = 1.6$, $kD/s_{um} = 2$, $\delta_{rem} = 0.3$, $\xi_{95} = 10$, $\mu = 0$.

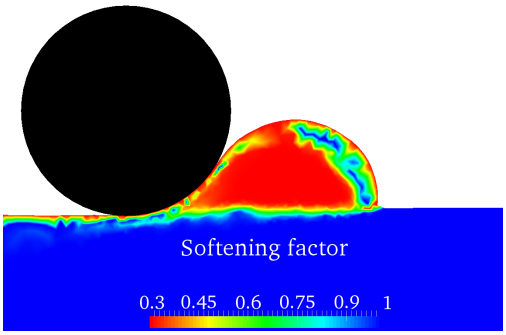

(a) $w_{ini}/D = 0.1$

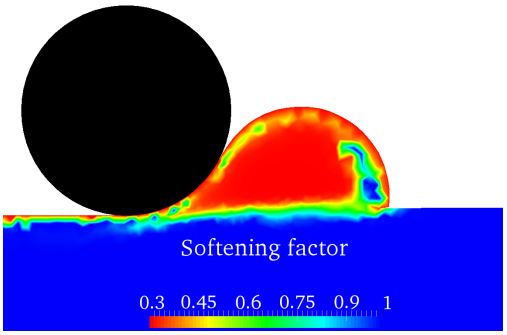

(b) $w_{ini}/D = 0.2$

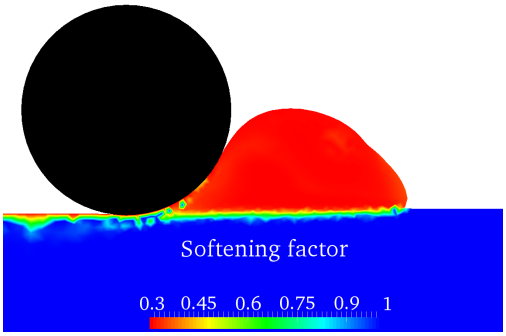

(c) $w_{ini}/D = 0.3$

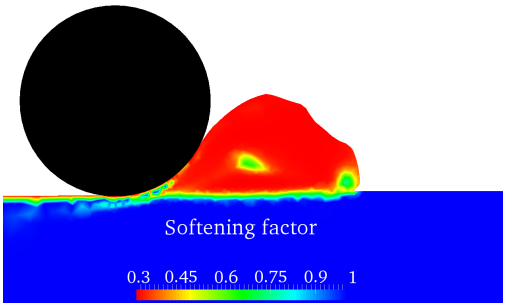

(d) $w_{ini}/D = 0.4$

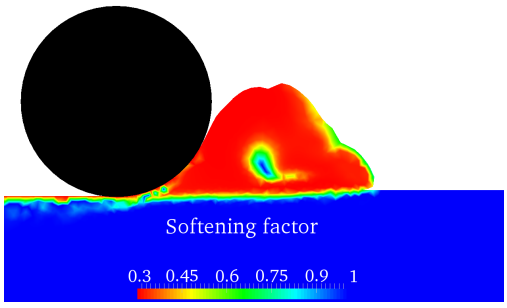

(e) $w_{ini}/D = 0.5$

Figure 6.15 Effect of initial embedment on the softening factor of the soil at $u/D = 8.0$. $kD/s_{um} = 2$, $\delta_{rem} = 0.3$, $\xi_{95} = 10$, $\mu = 0$.

Figure 6.15 illustrates the distribution of the softening factor at the end of loading for different w_{ini}/D. A very similar pattern can be observed despite the fact that the berm shape in the case of $w_{ini}/D = 0.5$ shows some difference from the others. It is also found that the soil within the berm experiences the most softening (nearly fully-remoulded) while that beneath the pipe invert suffers far less from softening.

6.3.2.3 Quantification of residual soil resistance

Although a perfect 'steady' state cannot be reached even for very light pipes, it is useful to introduce a parameter H_{res} to characterize the residual lateral resistance of the pipe. Based on the results presented so far, it is in general reasonable to assume that the residual state of a light pipe has been reached after a lateral displacement of $4D$. Hence, H_{res} is quantified as the average of H evaluated within the lateral displacement range of $4D$ to $5D$, which is also denoted by $H_{4.5D}$. Another parameter λ is also introduced, denoting the variation rate of the equivalent friction factor (H/W) with normalised lateral displacement (u/D), expressed as:

$$\lambda = \frac{D}{W} \cdot \frac{(H_{7.5D} - H_{4.5D})}{(3D)} \tag{6.2}$$

where $H_{7.5D}$ is evaluated as the average H in the lateral displacement range $7D$ to $8D$.

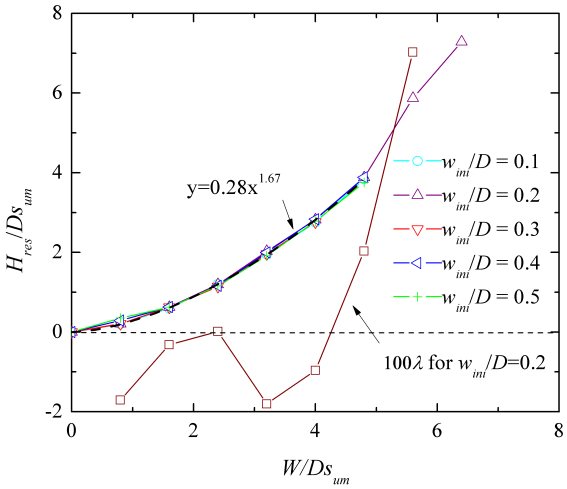

Figure 6.16 Variation of residual lateral resistance with pipe weight. $kD/s_{um} = 2$, $\delta_{rem} = 0.3$, $\xi_{95} = 10$, $\mu = 0$.

Figure 6.16 shows the variation of normalised residual resistance (H_{res}/Ds_{um}) with normalised pipe weight (W/Ds_{um}). The results obtained from all values of w_{ini} fall in an

extremely narrow band, suggesting that for light pipes the influence of initial embedment on the residual response is rather limited. It is thus assumed hereafter that the effect of w_{ini} can be eliminated when evaluating the pipe response during the residual stage. A power law function is found to fit the results in Figure 6.16 satisfactorily:

$$\frac{H_{res}}{Ds_{um}} = a(\frac{W}{Ds_{um}})^b \tag{6.3}$$

where $a = 0.28$ and $b = 1.67$. Figure 6.16 also presents the values of λ quantified from the analyses with $w_{ini}/D = 0.2$. For the default soil type investigated here, the pipes with W/Ds_{um} below 4.8 can reach a satisfactorily steady state with λ being within $\pm 2\%$.

6.3.3 Effect of soil strength gradient, k

Since the normalised shear strain gradient kD/s_{um} is the dominant factor in determining the initial soil strength s_{u0} of the soil, it dominates the type of pipe behaviour, light or heavy, for a given pipe weight. This section presents a study into the influence of kD/s_{um} on the behaviour of a pipe during breakout as well as the residual loading stage. The critical pipe weight W_{cri} that determines the type of pipe behaviour, light or heavy, is discussed and the influence of kD/s_{um} is examined.

6.3.3.1 Loading response at breakout

Figures 6.17a and 6.17b show the influence of normalised soil strength gradient (kD/s_{um}) on the breakout response of a pipe initially penetrated to embedments of $0.2D$ and $0.5D$ respectively. The values of kD/s_{um} used in this study are 0, 1, 2, 5 and 10. Two extreme bond conditions at the pipe-soil interface are considered by assuming unlimited or no tensile capacity. For both pipe embedments and both bond conditions, a considerable increase in the envelope size with kD/s_{um} is observed, especially where heavy pipe behaviour is expected. For the case of purely vertical pushing kD/s_{um} has the most significant influence on the loading response of the pipe.

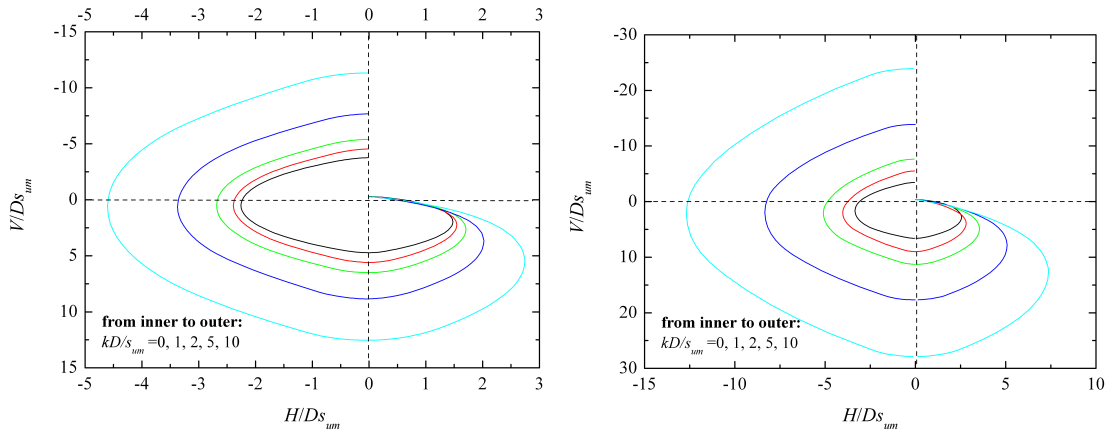

(a) $w_{ini}/D = 0.2$ (b) $w_{ini}/D = 0.5$

Figure 6.17 Effect of strength gradient on $V-H$ yield envelope at the breakout stage. Left half is with full tension at the pipe-soil interface and right half is without tension. Ideal soil, $kD/s_{um} = 2$, $\gamma' D/s_{um}$.

6.3.3.2 Loading response under large displacement

Figures 6.18a and 6.18b show the effect of kD/s_{um} on the yield envelopes at the residual stage ($u/D = 5.0$) of two pipes with light ($W/Ds_{um} = 1.6$) and moderate ($W/Ds_{um} = 4.0$) weight respectively. Comparing with Figure 6.17, it is interesting to find that the influence of kD/s_{um} on the loading behaviour of the pipe has been reversed during the lateral movement. A decreasing trend in the envelope size with kD/s_{um} is observed in general. The envelope corresponding to $kD/s_{um} = 1$ in Figure 6.18b is shifted towards the right and gains the largest resistance. The yield envelope in the case of $kD/s_{um} = 0$ is not drawn in Figure 6.18b since the pipe dived into the soil very rapidly and the analysis was terminated before the pipe reached a displacement of $5D$. The yield envelope in the case of $kD/s_{um} = 10$ is not provided either, because for the lateral loading of a pipe, some simulations with high values of kD/s_{um} cannot be completed due to numerical instability.

Figures 6.19 shows the influence of kD/s_{um} on the loading response of a pipe with $W/Ds_{um} = 3.2$ during the lateral movement phase. The elevation of the pipe invert increases significantly with kD/s_{um}, since less embedment is needed to support the pipe weight when stronger soil is beneath the pipe as well as within the soil berm. Consistent with the findings in Figures 6.17 and 6.18, kD/s_{um} has a positive influence on the lateral resistance at the initial breakout stage and then exhibits a contrasting trend. In the sim-

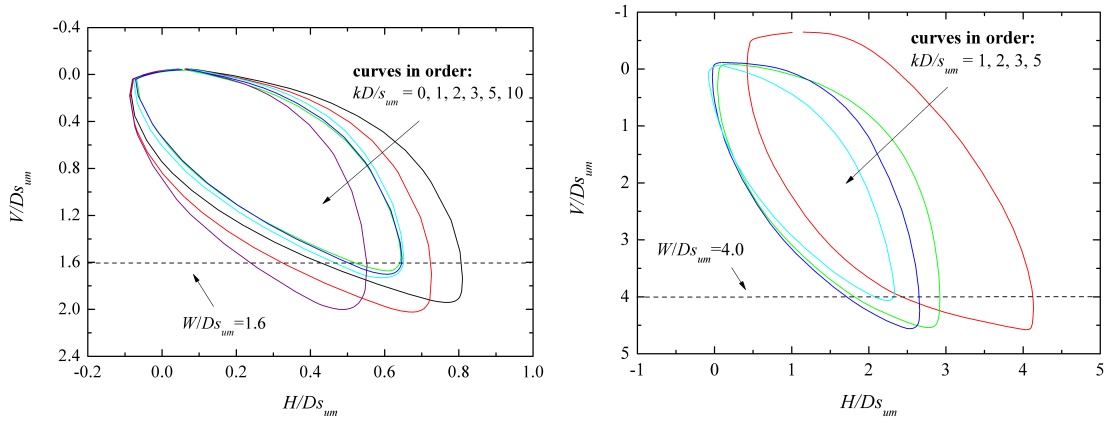

(a) $W/Ds_{um} = 1.6$ (b) $W/Ds_{um} = 4.0$

Figure 6.18 Effect of strength gradient on $V-H$ yield envelope at the residual stage. $w_{ini}/D = 0.2$, $u/D = 5$, $\delta_{rem} = 0.3$, $\xi_{95} = 10$, $\mu = 0$.

ulations with larger values of kD/s_{um}, the smaller embedment results in a considerable reduction in soil resistance. In the extreme case of $k = 0$, heavy pipe behaviour can even be observed, where the pipe keeps ploughing deeper into the soil (over $0.5D$) and gains a continuous increase in resistance. A gradual transition from heavy to light pipe behaviour can be expected with increasing kD/s_{um}, as shown in Figure 6.19.

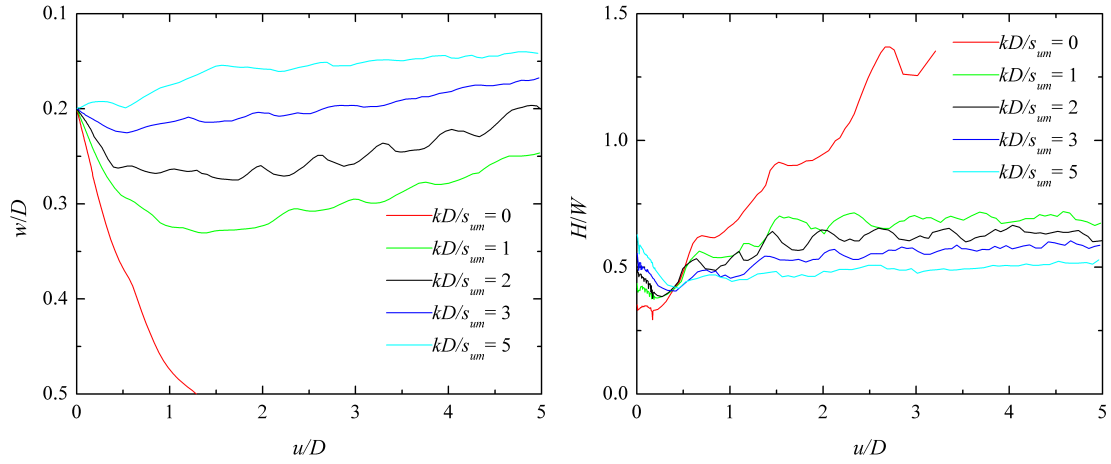

(a) Invert trajectory (b) Equivalent friction factor

Figure 6.19 Effect of strength gradient on lateral loading behaviour. $W/Ds_{um} = 3.2$, $w_{ini}/D = 0.2$, $\delta_{rem} = 0.3$, $\xi_{95} = 10$, $\mu = 0$.

Figure 6.20a shows the variation of H_{res} with kD/s_{um}, with different levels of normalised pipe weight (W/Ds_{um}) being considered. A parameter f_k is introduced here to evaluate the influence of kD/s_{um} on H_{res}, which is the ratio of H_{res} quantified for an arbitrary value of kD/s_{um} to that evaluated for $kD/s_{um} = 2$ (default case). The relation-

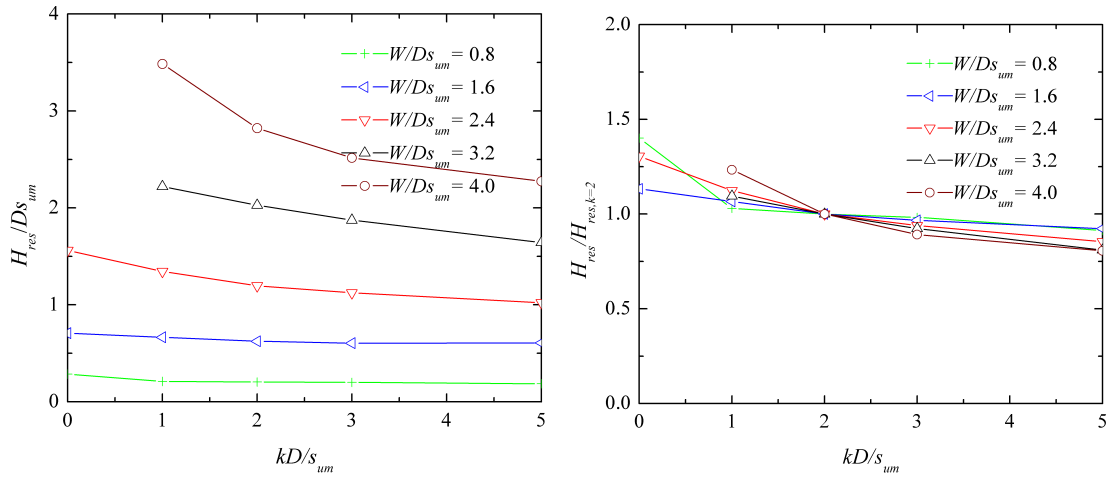

(a) H_{res} (b) f_k

Figure 6.20 Effect of strength gradient on normalised residual resistance H_{res}. $w_{ini}/D = 0.2$, $\delta_{rem} = 0.3$, $\xi_{95} = 10$, $\mu = 0$.

ship between f_k and kD/s_{um} is depicted in Figure 6.20b where an approximately linear decreasing trend in f_k with kD/s_{um} can be observed.

6.3.3.3 Critical pipe weight to differentiate light and heavy pipes

One of the main objectives of this chapter is to find a critical weight W_{cri} that differentiates light and heavy pipe behaviours. Ideally, a pipe with weight below W_{cri} can finally reach an essentially steady state within the displacement range considered ($8D$); otherwise a steady state can never be achieved. Whether a pipe moves upward or downward in the initial stage of lateral movement depends on the overloading ratio, W/V_c, where V_c depends strongly on the initial pipe embedment w_{ini}; that is, the same pipe could be recognized as a light pipe or a heavy one when it starts from different initial embedments. As discussed before, the influence of w_{ini} diminishes with further displacement and thus it is recommended that the type of pipe behaviour should be decided based on its response during the residual stage. For example, the curves corresponding to normalised pipe weights W/Ds_{um} of 3.2, 4.0 and 4.8 in Figure 6.10a exhibit light pipe behaviour at the residual stage even though these pipes move downward initially, which is the 'normally-penetrated' response reported by Cheuk *et al.* (2008). Typically when a pipe ploughs deep enough (over $0.5D$) into the soil, the soil berm will cover the pipe crown and exert an additional downward force on

the pipe (see the mechanism in Figure 6.9c). Once that takes place, a rebound of the pipe trajectory is very unlikely to happen and the pipe will keep diving. Since finding a strict value of W_{cri} is extremely difficult and unnecessary, indicative lower and upper bounds are derived instead and the results are presented in Figure 6.21.

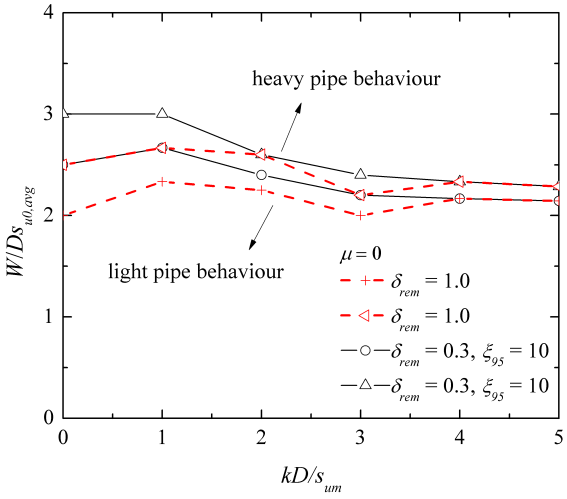

Figure 6.21 Lower and upper bounds of pipe weight to differentiate light and heavy pipe behaviour at the residual stage

Both ideal soil and the more realistic softening soil (the default case in this chapter) are considered. Since quantification of the soil strength at mudline can be unreliable in the field (Bruton *et al.*, 2006), the pipe weight is normalised by $Ds_{u,avg}$ instead of Ds_{um}. The parameter $s_{u,avg}$, calculated as $s_{u,avg} = s_{um} + 0.5kD$, is the initial shear strength of the soil at a depth of half a pipe diameter. Above the upper bound line, the pipe will keep diving into the soil and never reach a steady state within the displacement range considered, while below the lower bound line, the pipe will eventually show light pipe behaviour after being displaced by at most 2-3D. Figure 6.21 also indicates that strain softening does not have a major effect on the behaviour type, even considering that it may have some moderate or significant influence on the berm resistance. More discussions of this issue are presented in Section 6.3.5.

6.3.4 Effect of soil unit weight, γ'

The influence of soil unit weight on the lateral loading behaviour of a pipe is investigated in this section. Values of $\gamma' D/s_{um} = 0$, 1, 3, 5, 10 and 20 were considered.

6.3.4.1 Loading response at breakout

Figures 6.22a and 6.22b show the yield envelopes of a pipe penetrated to $0.2D$ (default value) and $0.5D$ respectively in soils with different $\gamma' D/s_{um}$. Two extreme bond conditions, with unlimited or no tensile capacity at the pipe-soil interface, are considered and the results are shown in the left and right halves of each figure.

When no tension is allowed at the interface, the yield envelope is found to expand with increasing $\gamma' D/s_{um}$, mainly in the vertical (V) direction. Therefore, soil buoyancy has a much more significant influence on the lateral breakout resistance of heavy pipes than of light ones. When full tension is assumed, the yield envelope simply shifts downwards in the V direction with increasing $\gamma' D/s_{um}$. In this case, $\gamma' D/s_{um}$ has a very limited effect on the peak breakout resistance of the pipe, though the pipe weight needed to mobilise this peak resistance increases greatly with increasing $\gamma' D/s_{um}$. This can be easily observed by checking the leftmost points of all the envelope curves.

For the case with very high unit weight ($\gamma' D/s_{um} = 20$), the soil in the active area tends to collapse onto the pipe rear to prevent the occurrence of a crack, maintaining a 'bonded' condition even when gapping at the pipe rear is allowed. In such a scenario, the yield envelopes show a trend to become symmetric. This is confirmed by the curve for $\gamma' D/s_{um} = 20$ in Figure 6.22b. The curves corresponding to $\gamma' D/s_{um} = 20$ in Figure 6.22a and $\gamma' D/s_{um} = 10$ in Figure 6.22b show similar behaviour, although the trend is less profound. Also of interest is that the curve for $\gamma' D/s_{um} = 20$ in Figure 6.22b exhibits a totally different pattern from the others, where the uppermost point moves below the origin. This indicates that a weightless pipe in such a weak soil would be expelled from the soil as a result of soil buoyancy.

6.3.4.2 Loading response under large displacement

Figures 6.23a and 6.23b show the effect of soil unit weight on the yield envelopes at the residual stage ($u/D = 5.0$) of two pipes with small ($W/Ds_{um} = 1.6$) and moderate ($W/Ds_{um} = 4.0$) weight respectively. In a similar way to the effect of kD/s_{um}, the positive influence of $\gamma' D/s_{um}$ on the soil resistance at the breakout stage is reversed with large pipe

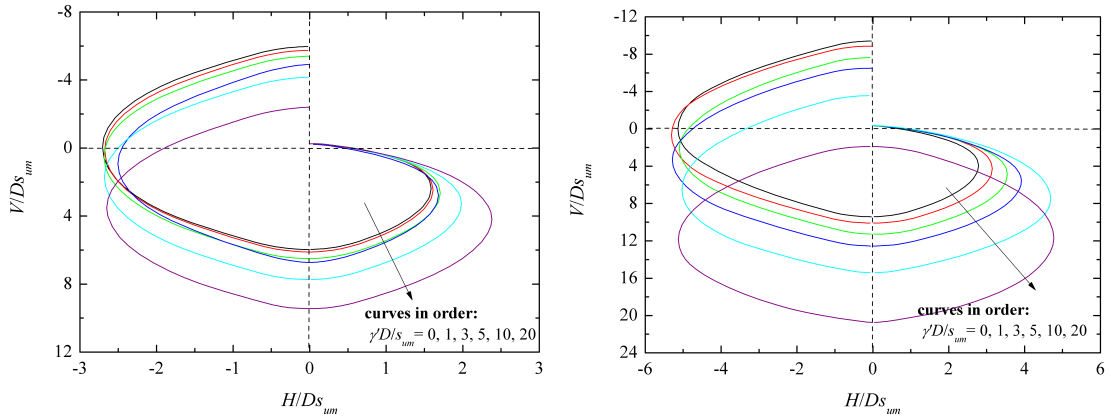

(a) $w_{ini}/D = 0.2$ (b) $w_{ini}/D = 0.5$

Figure 6.22 Effect of unit weight on $V-H$ yield envelope at the breakout stage. Left half is with full tension at the pipe-soil interface and right half is without tension. Ideal soil, $kD/s_{um} = 2$.

movements. The yield envelopes of the light pipe (Figure 6.23a) are of different shape but similar size; while the yield envelopes for the pipe with moderate weight (Figure 6.23b) are different in both shape and size. For a given pipe weight, the lateral resistance is found to decrease with $\gamma' D/s_{um}$ in both Figures 6.23a and 6.23b if the pipe keeps moving towards the right. If the direction of lateral movement is subsequently reversed, the influence $\gamma' D/s_{um}$ on the lateral resistance is also reversed as shown in Figure 6.23a. This trend is less profound in 6.23b.

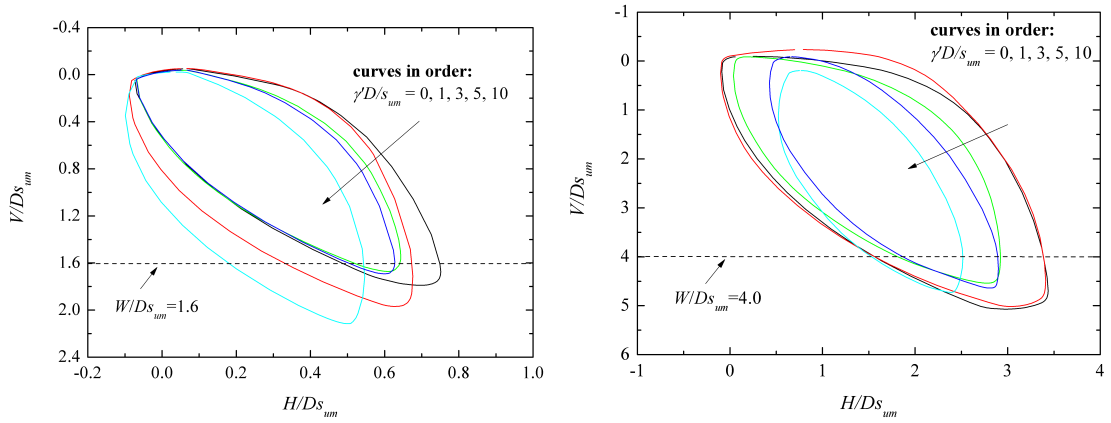

(a) $W/Ds_{um} = 1.6$ (b) $W/Ds_{um} = 4.0$

Figure 6.23 Effect of unit weight on $V-H$ yield envelope at the residual stage. $w_{ini}/D = 0.2$, $u/D = 5$, $kD/s_{um} = 2$, $\delta_{rem} = 0.3$, $\xi_{95} = 10$, $\mu = 0$.

Figures 6.24a and 6.24b illustrate the effect of $\gamma' D/s_{um}$ on the response of a pipe during lateral loading, in terms of the pipe invert trajectory and equivalent friction factor. The

elevation of the pipe invert increases moderately with $\gamma' D/s_{um}$, since less embedment is needed to support the pipe weight due to larger soil buoyancy. As a consequence, a moderate reduction in lateral soil resistance with increasing $\gamma' D/s_{um}$ is observed in Figure 6.24b. In a similar way to the findings on the effect of kD/s_{um}, the normalised unit weight $\gamma' D/s_{um}$ has a positive influence on the lateral resistance at the initial breakout stage and then exhibits a contrasting trend at the residual stage, which can be confirmed by comparing Figure 6.22 with Figure 6.23. However, the influence of $\gamma' D/s_{um}$ in determining the pipe behaviour type (light or heavy) is much less significant than that of kD/s_{um}.

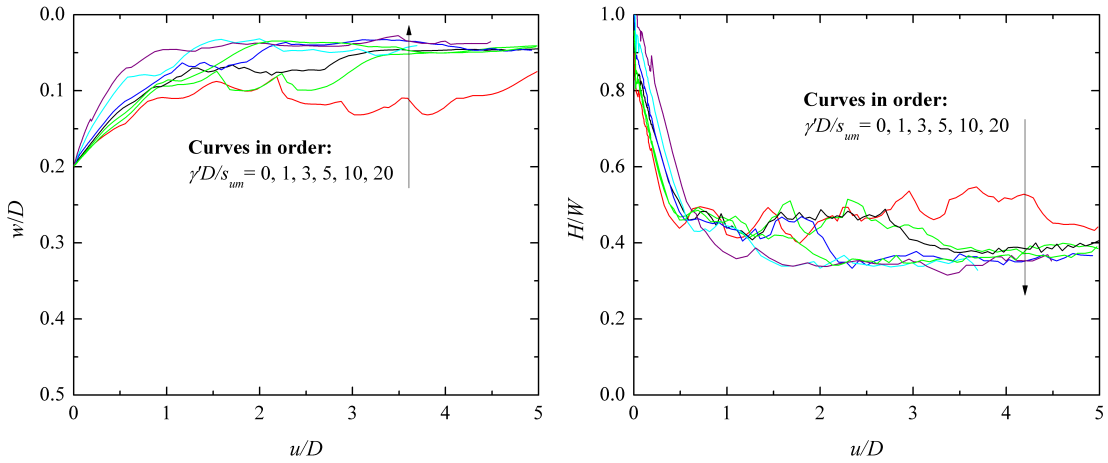

(a) Invert trajectory (b) Equivalent friction factor

Figure 6.24 Effect of unit weight on the lateral loading behaviour of a light pipe. $W/Ds_{um} = 1.6$, $kD/s_{um} = 2$, $\delta_{rem} = 0.3$, $\xi_{95} = 10$, $\mu = 0$.

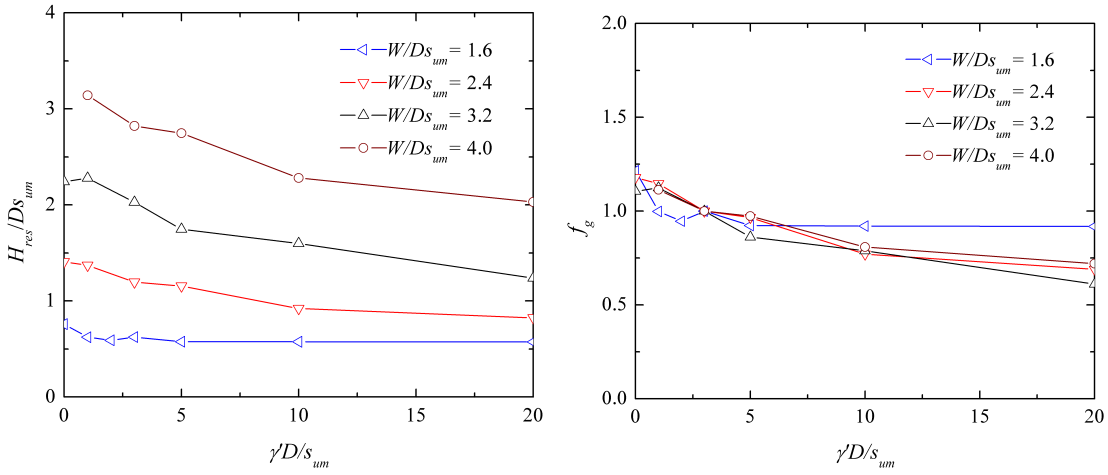

(a) H_{res} (b) f_g

Figure 6.25 Effect of unit weight on residual resistance H_{res}. $w_{ini}/D = 0.2$, $kD/s_{um} = 2$, $\delta_{rem} = 0.3$, $\xi_{95} = 10$, $\mu = 0$.

Figure 6.25a shows the variation of H_{res}/Ds_{um} with $\gamma' D/s_{um}$ for different levels of pipe weight. The influence of $\gamma' D/s_{um}$ on H_{res}/Ds_{um} can be characterised by introducing a parameter f_g, which is the ratio of H_{res} quantified for a arbitrary value of $\gamma' D/s_{um}$ to that evaluated for $\gamma' D/s_{um} = 3$ (default case). The relationship between f_g and $\gamma' D/s_{um}$ is depicted in 6.25b, where an approximately linear decreasing trend can be observed.

6.3.5 Effect of strain softening

In this section, the effect of soil strength degradation on the lateral loading response of a pipe is studied. The parameters used for the large displacement analyses in this section are listed in Table 6.3. All other parameters were kept the same as the default values in Table 6.1. The different pipe weights in Table 6.3 were chosen to investigate the influence of remoulding on the lateral resistance as well as the pipe behaviour type (light or heavy).

Table 6.3 Parameter values used for investigating the effect of strain softening

W/Ds_{um}	δ_{rem}	ξ_{95}
1.6	0.1 to 1.0 by an interval of 0.1	10
	0.3	2, 5, 10, 20, 50
2.4	0.1, 0.2, 0.3, 0.5, 0.8, 1.0	10
	0.3	2, 5, 10, 20, 50
3.2	0.1, 0.2, 0.3, 0.5, 0.8, 1.0	10
	0.3	2, 5, 10, 20, 50
4.0	0.1, 0.2, 0.3, 0.5, 0.8, 1.0	10
	0.3	2, 5, 10, 20, 50

As discussed in Section 6.1.2 where the details of the loading process were introduced, the strain softening effect was taken into account only after the lateral movement began for most of the simulations presented in this section. This was to ensure that all the difference was generated from the lateral loading step rather than the initial penetration stage. All the results concerning the lateral loading behaviour at large displacement in this section were obtained from this type of analysis. However, for the results pertaining to the breakout response (Figures 6.26 and 6.31), another set of analyses was conducted where the pipe was penetrated into soil with the softening effect considered. No lateral loading was performed in this set of analyses because the configuration after the vertical loading provided enough information to derive the yield envelopes.

6.3.5.1 Effect of δ_{rem} on loading response at breakout

Figures 6.26a and 6.26b show the effect of remoulded strength ratio ($\delta_{rem} = 1/S_t$) on the breakout resistance of pipes embedded at $0.2D$ and $0.5D$ respectively. The results for unlimited tensile capacity at the pipe-soil interface are presented in the left half of each figure, while those for no tensile capacity are in the right half. It is found that the size of the envelope shrinks considerably with decreasing δ_{rem}, suggesting a great difference in the lateral breakout resistance. However, according to the associated flow rule, the critical pipe weight, W_{cri}, to differentiate light and heavy pipe behaviour at the breakout stage (see the parallel points) does not change very much. This critical pipe weight is approximately $2.5Ds_{um}$ (Figure 6.26a) and $4Ds_{um}$ (Figure 6.26b) for the pipes with normalised embedments of 0.2 and 0.5 respectively when no tension is allowed at the interface.

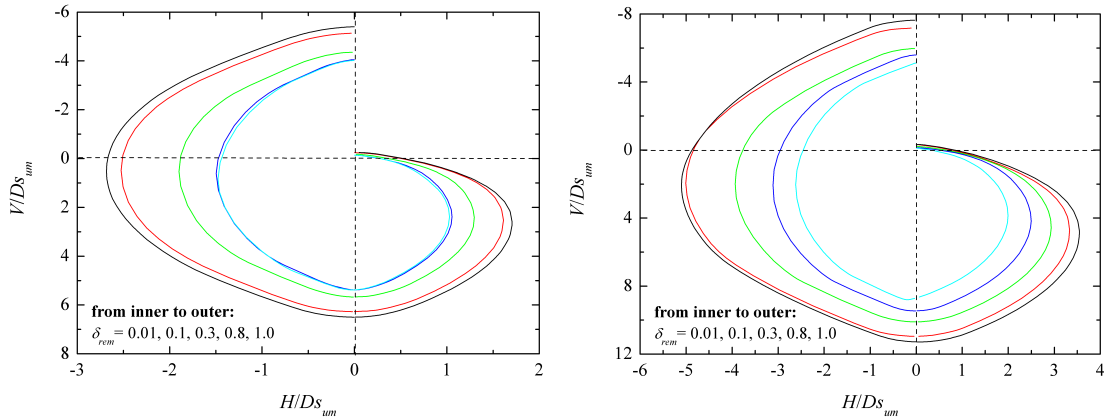

(a) $w_{ini}/D = 0.2$ (b) $w_{ini}/D = 0.5$

Figure 6.26 Effect of remoulded strength ratio δ_{rem} on $V-H$ yield envelope at the breakout stage. Left half is with full tension at the pipe-soil interface and right half is without tension. $kD/s_{um} = 2$, $\xi_{95} = 10$, $\mu = 0$.

6.3.5.2 Effect of δ_{rem} on loading response under large displacement

Figures 6.27a and 6.27b illustrate the effect of remoulded strength ratio ($\delta_{rem} = 1/S_t$) on the yield envelopes at the residual stage ($u/D = 5$) of two pipes with normalised weights $W/Ds_{um} = 1.6$ and 4.0 respectively. In general, the size of the envelope increases considerably with δ_{rem} and the envelope derived for the ideal soil case is about two times

the size of that derived for soils with δ_{rem} below 0.5. However, it can be seen that for a typical seabed soil with δ_{rem} ranging from 0.2 to 0.5 (Randolph, 2004), both the shape and the size of the envelopes are very similar. This observation is consistent with the results presented later in Figures 6.28b and 6.28d.

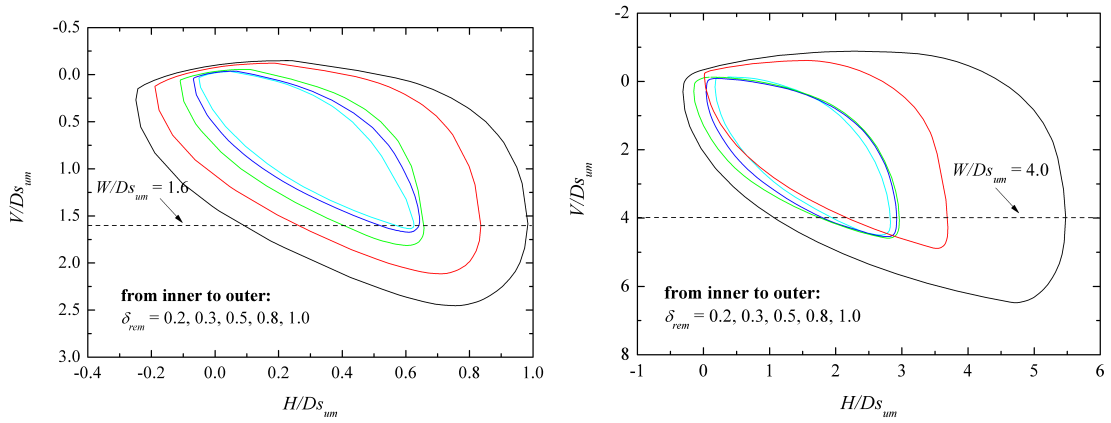

(a) $W/Ds_{um} = 1.6$ (b) $W/Ds_{um} = 4.0$

Figure 6.27 Effect of remoulded strength ratio on $V-H$ yield envelope at the residual stage. $w_{ini}/D = 0.2$, $u/D = 5$, $kD/s_{um} = 2$, $\xi_{95} = 10$, $\mu = 0$.

Figure 6.28 shows the effect of δ_{rem} on the lateral loading response in terms of the invert trajectory and equivalent friction factor. Two separate cases with $W/Ds_{um} = 1.6$ and 4.0 are considered to cover pipes with small and moderate weight. In both cases, the depth at which the pipe scrapes across the soil surface decreases with increasing δ_{rem}, since more resistance can be provided by the soil berm with larger δ_{rem}. This leads to smaller pipe embedment as well as smaller soil berm size. However, the soil with higher δ_{rem} still provides higher lateral resistance to the pipe, as illustrated in Figures 6.28b and 6.28d. For typical values of soil sensitivity of 2-5 (Randolph, 2004), which implies δ_{rem} in the range 0.2 to 0.5, all the residual resistances are very close. It is noteworthy that the normalised weight of 4.0 is close to the upper bound illustrated in Figure 6.21 (5.2 for $kD/s_{um} = 2$) and is thus at risk of turning from a light pipe to a heavy one if the soil strength is weakened. However, with decreasing δ_{rem}, a transition from light to heavy behaviour is not observed in Figure 6.28c, suggesting that the soil sensitivity has limited influence on determining the behaviour type of the pipe. Of interest in Figure 6.28c is that the pipe in the ideal soil case ($\delta_{rem} = 1.0$) ploughs much deeper than others (except the

very soft soil with $\delta_{rem} = 0.1$) and even shows a trend of diving into the soil (see Figure 6.29f).

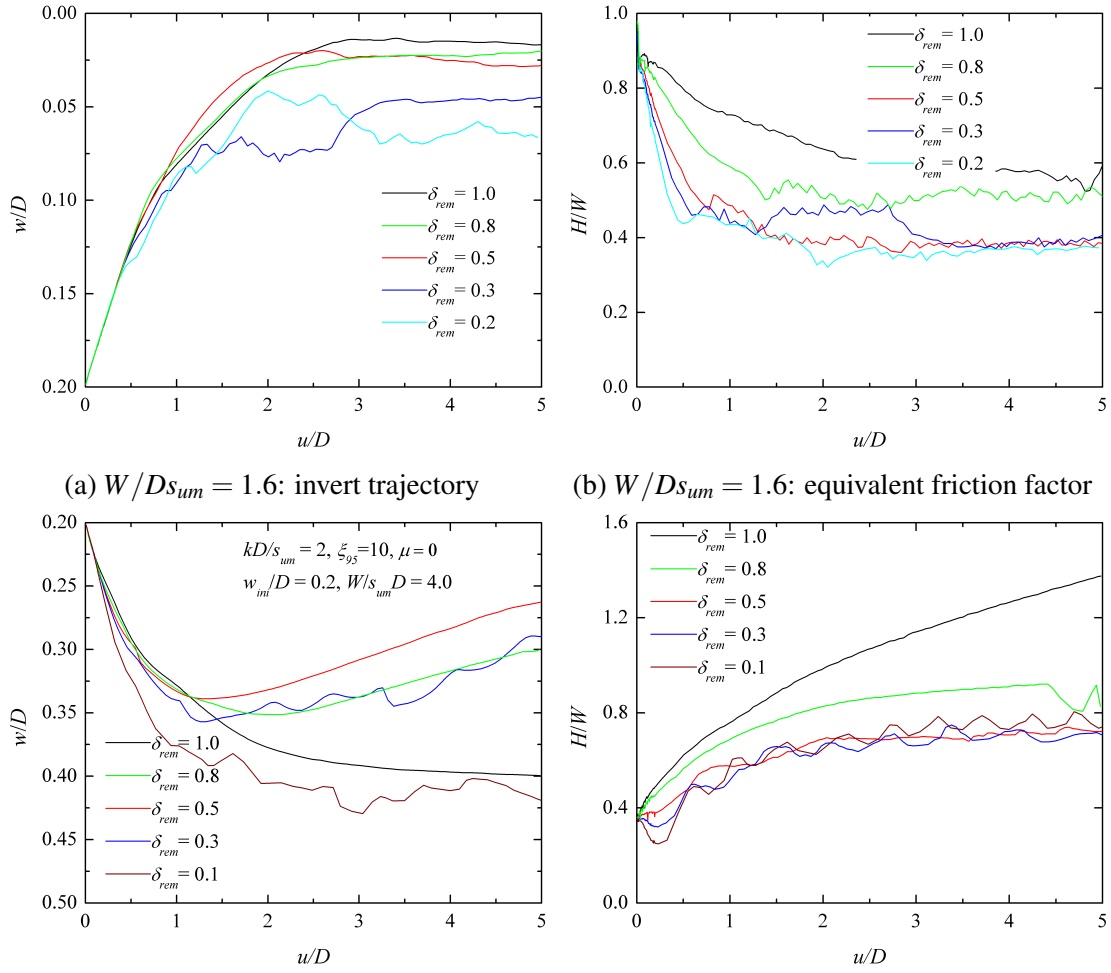

(a) $W/Ds_{um} = 1.6$: invert trajectory

(b) $W/Ds_{um} = 1.6$: equivalent friction factor

(c) $W/Ds_{um} = 4.0$: invert trajectory

(d) $W/Ds_{um} = 4.0$: equivalent friction factor

Figure 6.28 Effect of remoulded strength ratio on lateral loading behaviour. $kD/s_{um} = 2$, $\xi_{95} = 10$, $\mu = 0$.

Figure 6.29 shows the cumulative shear strain ξ in the soil at a lateral pipe displacement of $5D$. The results obtained from soils with different δ_{rem} of 0.1, 0.2, 0.3, 0.5, 0.8 and 1.0, are illustrated and the normalised pipe weight W/Ds_{um} is 4.0 in the cases presented. It can be observed that the area experiencing the most shear strain, and thus the most softening, is within the soil berm rather than the soil beneath the pipe invert. The scale used to visualise ξ is 10, which is exactly the value of ductility parameter ξ_{95} for all the cases. Therefore it can be concluded that the soil with higher values of δ_{rem} not only has higher remoulded strength but also experiences a lower degree of softening during the simulation. By comparing Figures 6.29a to 6.29f, it is found that the soil with higher δ_{rem}

sustains a stiffer berm in the passive area, leading to higher residual resistance. The berm in the ideal soil case (Figure 6.29f) even grows high enough to cover the pipe crown, which is likely to exert a downward force on the pipe. This explains why the pipe in the ideal soil case ploughs at a relatively large depth as illustrated in Figure 6.28c, even considering that the strength in the berm is much greater than in the softening soil cases.

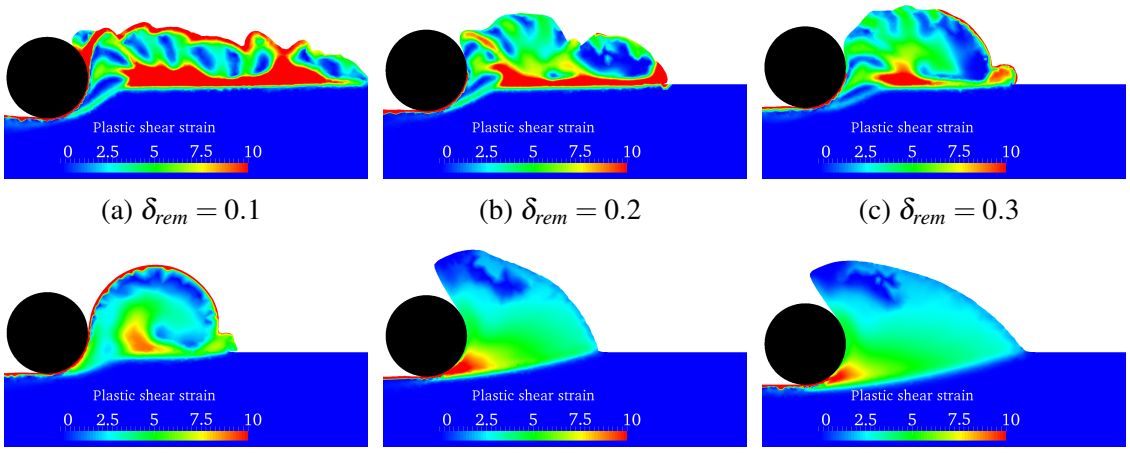

(a) $\delta_{rem} = 0.1$ (b) $\delta_{rem} = 0.2$ (c) $\delta_{rem} = 0.3$

(d) $\delta_{rem} = 0.5$ (e) $\delta_{rem} = 0.8$ (f) $\delta_{rem} = 1.0$

Figure 6.29 Effect of remoulded strength ratio on plastic shear strain of the soil. $w_{ini}/D = 0.2$, $u/D = 5.0$, $kD/s_{um} = 2$, $\xi_{95} = 10$, $\mu = 0$.

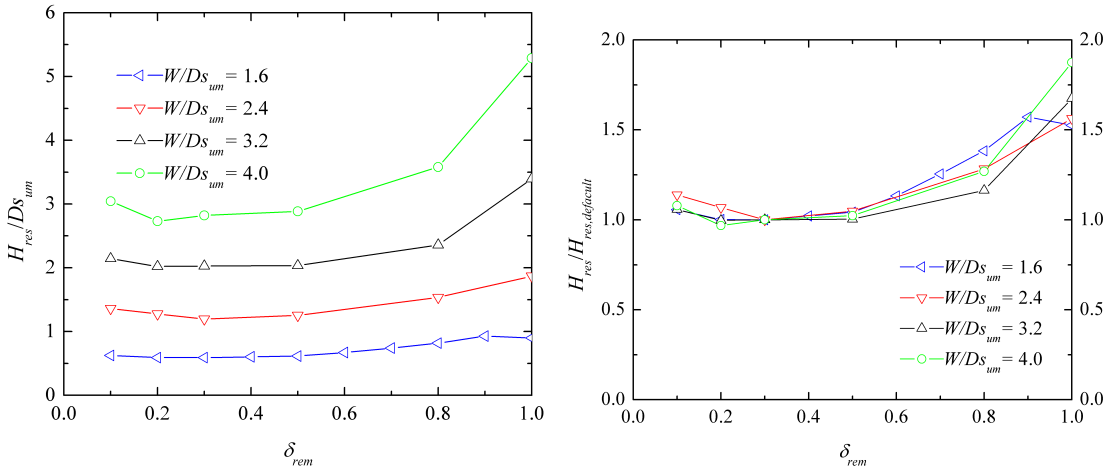

(a) H_{res}/Ds_{um} (b) f_δ $(H_{res}/H_{res,default})$

Figure 6.30 Effect of remoulded strength ratio on residual resistance H_{res}. $w_{ini}/D = 0.2$, $kD/s_{um} = 2$, $\xi_{95} = 10$, $\mu = 0$.

Figure 6.30a shows the variation of H_{res} with δ_{rem} for different pipe weights. A parameter f_δ is used to evaluate the effect of δ_{rem} on H_{res}, which is the ratio of H_{res} to its reference value quantified at $\delta_{rem} = 0.3$ (default case). The results are illustrated in Figure

6.30b. For typical values of δ_{rem} ranging from 0.2 to 0.5 (Randolph, 2004), the calculated values of f_δ lie in a very narrow band for all the pipe weights considered here, indicating that varying δ_{rem} within a reasonable range has limited influence on H_{res}.

6.3.5.3 Effect of ξ_{95} on loading response at breakout

Figure 6.31 shows the influence of the ductility parameter ξ_{95}, ranging from 2 to infinity (ideal soil), on the breakout response of pipes embedded at $0.2D$ and $0.5D$. In both cases, the envelope expands considerably with ξ_{95} but the difference becomes less significant with larger pipe embedment. Figure 6.31b even illustrates that the curves corresponding to ξ_{95} of 2 and 5 become extremely close when no tension is allowed at the pipe-soil interface. This is because the shear strain of the surrounding soil that contributes to the lateral bearing capacity surpasses 5 at a pipe penetration of half a diameter, resulting in similarly softened soil for ξ_{95} of 2 and 5.

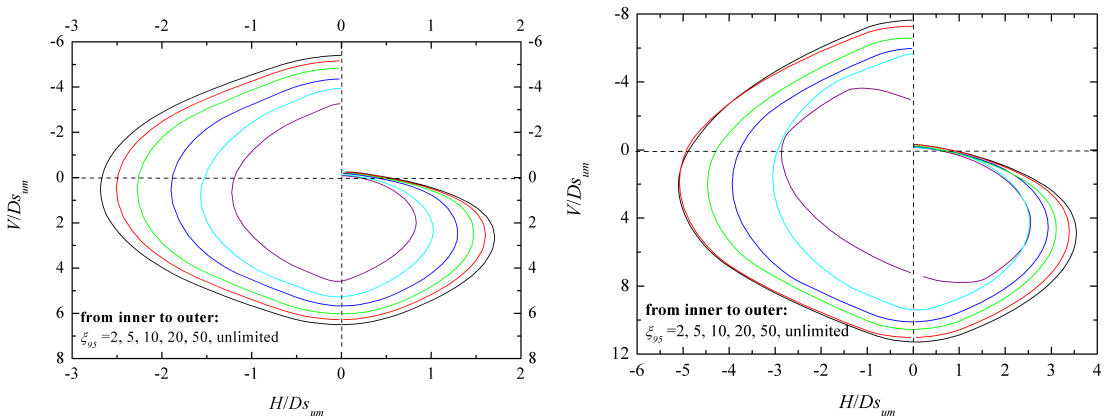

(a) $w_{ini}/D = 0.2$ (b) $w_{ini}/D = 0.5$

Figure 6.31 Effect of ductility parameter on $V-H$ yield envelope at the breakout stage. Left half is with full tension at the pipe-soil interface and right half is without tension. $kD/s_{um} = 2$, $\delta_{rem} = 0.3$, $\mu = 0$.

6.3.5.4 Effect of ξ_{95} on loading response under large displacement

Figure 6.32 shows yield envelopes at the residual stage in soils with different ξ_{95}. Both a light pipe ($W/Ds_{um} = 1.6$) and a moderately heavy one ($W/Ds_{um} = 4.0$) are analysed. Except for the ideal soil case, all the other yield envelopes are of similar shape and size. By comparing Figures 6.32a and 6.32b, it is found that the effect of ξ_{95} becomes more

pronounced with increased pipe weight. This is reasonable since in the light pipe case, the pipe tends to move upward more to reduce the area of shearing where stronger soil is present (with large ξ_{95}). This trend is less likely with a heavy pipe, the extreme case of which is vertical penetration, where the effect of strain softening on the soil resistance becomes most significant.

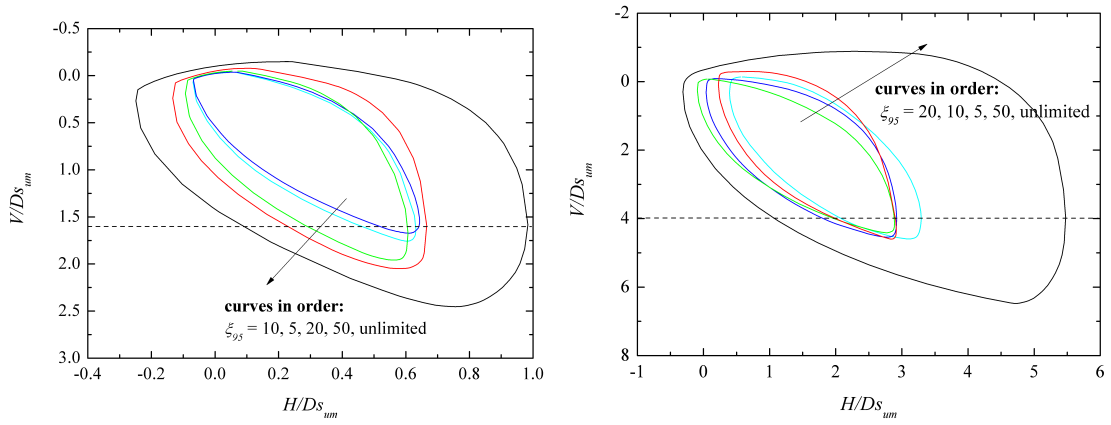

(a) $W/Ds_{um} = 1.6$ (b) $W/Ds_{um} = 4.0$

Figure 6.32 Effect of ductility parameter on $V-H$ yield envelope at the residual stage. $w_{ini}/D = 0.2$, $u/D = 5$, $kD/s_{um} = 2$, $\delta_{rem} = 0.3$, $\mu = 0$.

Figure 6.33 shows the evolution of invert trajectory and equivalent friction factor for two pipes of light and moderate weight. It is interesting to find that in both cases, although the strongest soil provides the highest resistance throughout the loading process, it does not necessarily lead to the shallowest pipe embedment. Figure 6.33a shows that the scraping depth of a light pipe during the residual stage generally decreases significantly with increasing ξ_{95} while the resulting resistances are very close in Figure 6.33b except for the most brittle ($\xi_{95} = 2$) and most ductile ($\xi_{95} = \infty$) soil. The trajectories of the pipe with moderate weight, as illustrated in Figure 6.33c, are not so conclusive as those in Figure 6.33a. However, similar observations regarding lateral resistance (Figure 6.33d) can be made as with the light pipe (Figure 6.33b). Considering that typically ξ_{95} varies in the range 10-50 as suggested by Randolph (2004), the ductility parameter ξ_{95} has far less influence on the lateral resistance than on the invert trajectory of a pipe.

For the default soil (normalised strength gradient $kD/s_{um} = 2$), W/Ds_{um} of 4.0 in the moderately heavy pipe case denotes a $W/Ds_{u,avg}$ of 2.0, which is close to the upper

bound value of 2.6 shown in Figure 6.21. Thus this pipe is at risk of exhibiting heavy pipe behaviour when the soil is further weakened by adopting smaller values of ξ_{95}. However, this is not observed in Figure 6.33c, indicating that the ductility parameter ξ_{95} hardly affects the behaviour type of a pipe. This finding is similar to that concerning the influence of remoulded strength ratio δ_{rem}, as illustrated in Figure 6.28c.

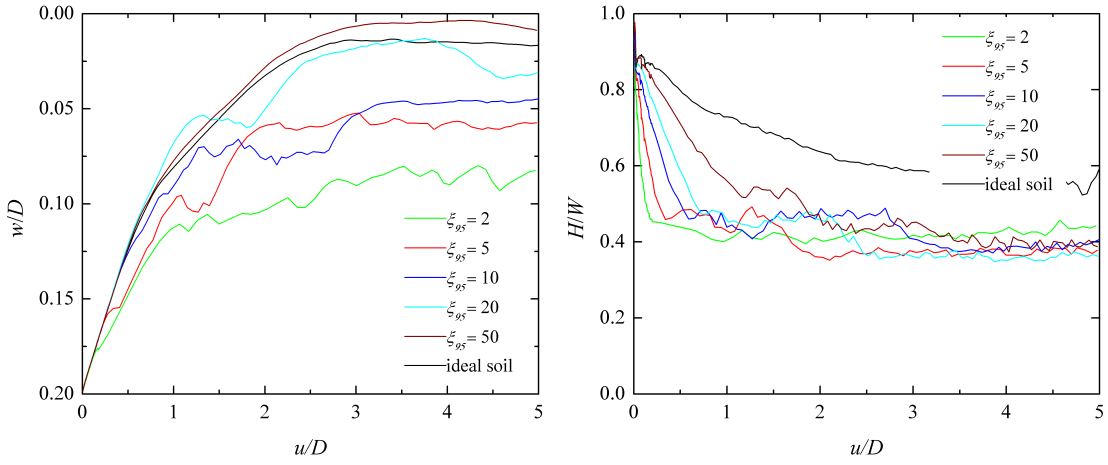

(a) $W/Ds_{um} = 1.6$: invert trajectory

(b) $W/Ds_{um} = 1.6$: equivalent friction factor

(c) $W/Ds_{um} = 4.0$: invert trajectory

(d) $W/Ds_{um} = 4.0$: equivalent friction factor

Figure 6.33 Effect of ductility parameter on lateral loading behaviour. $kD/s_{um} = 2$, $\delta_{rem} = 0.3$, $\mu = 0$.

Figure 6.34 shows the softening factor of the soil after the pipe has been laterally displaced by $5D$ under a normalised weight W/Ds_{um} of 4.0. The results obtained from analyses with six values of ξ_{95} (2, 5, 10, 20, 50 and infinite) are presented here. It is found that the more ductile soil with larger ξ_{95} experiences less softening, as expected, and thus has a stiffer soil berm ahead of the pipe. An extremely steep slope is observed in the case with $\xi_{95} = 50$, as shown in Figure 6.34e, and the soil tends to cover the pipe crown, which

is similar to the behaviour in the ideal soil case (Figure 6.34f). This explains why the pipes in these two cases plough at relatively deeper depths and have much higher resistances than the others as illustrated in Figure 6.33c.

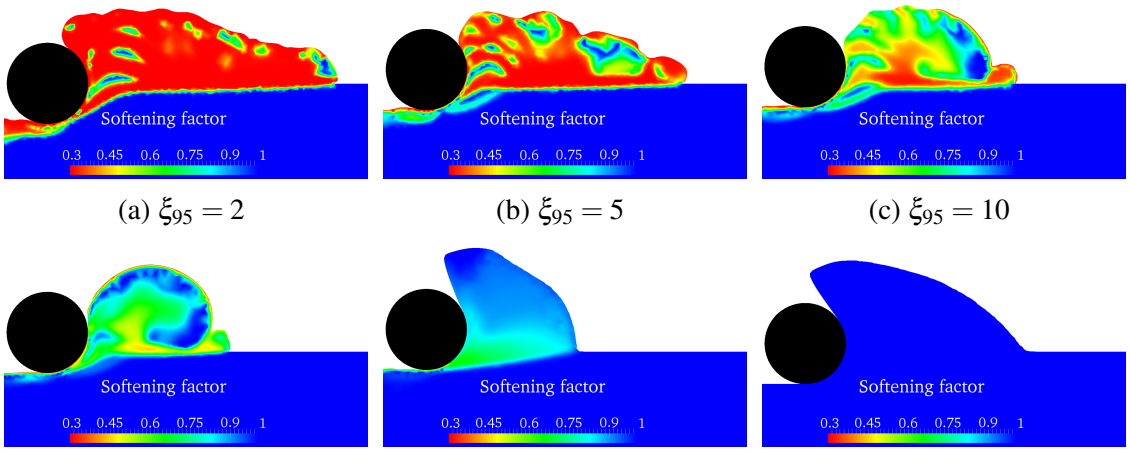

(a) $\xi_{95} = 2$ (b) $\xi_{95} = 5$ (c) $\xi_{95} = 10$

(d) $\xi_{95} = 20$ (e) $\xi_{95} = 50$ (f) $\xi_{95} =$ infinite

Figure 6.34 Effect of ductility parameter on softening factor of the soil. $w_{ini}/D = 0.2$, $u/D = 5.0$, $kD/s_{um} = 2$, $\delta_{rem} = 0.3$, $\mu = 0$.

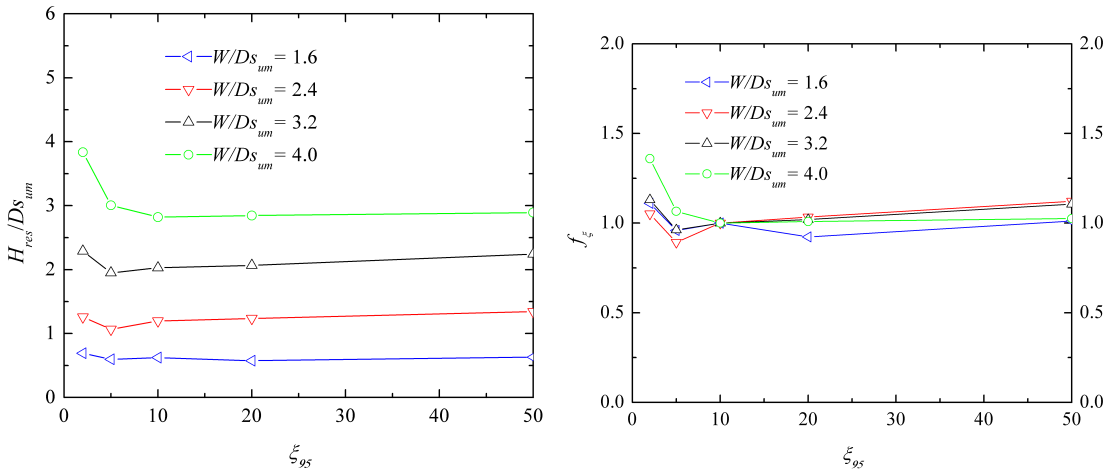

(a) H_{res}/Ds_{um} (b) f_ξ

Figure 6.35 Effect of ductility parameter on residual resistance. $w_{ini}/D = 0.2$, $\delta_{rem} = 0.3$, $\mu = 0$.

Figure 6.35 shows the variation of the residual lateral resistance H_{res} with ξ_{95} for different pipe weights. A parameter f_ξ is introduced to evaluate the effect of ξ_{95} on H_{res}, which is the ratio of the calculated value of H_{res} to that quantified at $\xi_{95} = 10$ (default case). The relationship between f_ξ and ξ_{95} is depicted in Figure 6.35b. In general, for pipes of light to moderate weight ($W/Ds_{um} \leq 2.4$), the calculated f_ξ increases approximately

linearly from 1.0 to 1.1 as ξ_{95} increases from 10 to 50, which is the typical range of ξ_{95} suggested by Randolph (2004).

6.3.6 Effect of rate dependence

The effect of rate-dependent soil strength on the pipe behaviour is examined in this section and the parameters investigated are listed in Table 6.4. Other parameters were kept the same as the default values given in Table 6.1. Two pipes with light and moderate weights were chosen for this study to investigate the influence of rate effects on the lateral resistance as well as the pipe behaviour type (light or heavy). Soils with remoulded strength ratios δ_{rem} of 1.0 and 0.3 were adopted to investigate how the rate effect could influence the pipe-soil interaction with and without the strain softening effect being considered.

Table 6.4 Parameter values used for investigating the effect of strain rate

δ_{rem}	μ	$v_p/D\dot{\gamma}_{ref}$	W/Ds_{um}
0.3	0.05	1000	1.6, 4.0
	0.10	100, 1000, 10000	1.6, 4.0
	0.15	1000	1.6, 4.0
	0.20	10000	1.6, 4.0
1.0	0.05	1000	1.6
	0.10	100, 1000, 10000	1.6
	0.15	1000	1.6
	0.20	10000	1.6

6.3.6.1 Soil deformation

Figure 6.36 shows both the softening and rate factors of the soil, which are the second and third parts of Equation 2.9 respectively, after the pipe has been displaced laterally by $5D$. In this loading case, $\mu = 0.10$, $v_p/D\dot{\gamma}_{ref} = 1000$, $\delta_{rem} = 0.3$, $\xi_{95} = 10$ and $W/Ds_{um} = 1.6$. The soil parameters concerning the effects of strain rate and strain softening chosen here are typical values recommended by Randolph (2004). It is observed that the influencing area of strain rate is smaller than that of strain softening since only the region with intense shearing can be enhanced by the rate effect (Figure 6.36a) while the whole soil berm suffers various degrees of softening (Figure 6.36b) since this depends on the cumulative shear strain. By checking the minimum and maximum values of the combined factor illustrated

in Figure 6.36c, it can be seen that the effect of strain softening is also more important than that of strain rate when the typical parameter values are chosen.

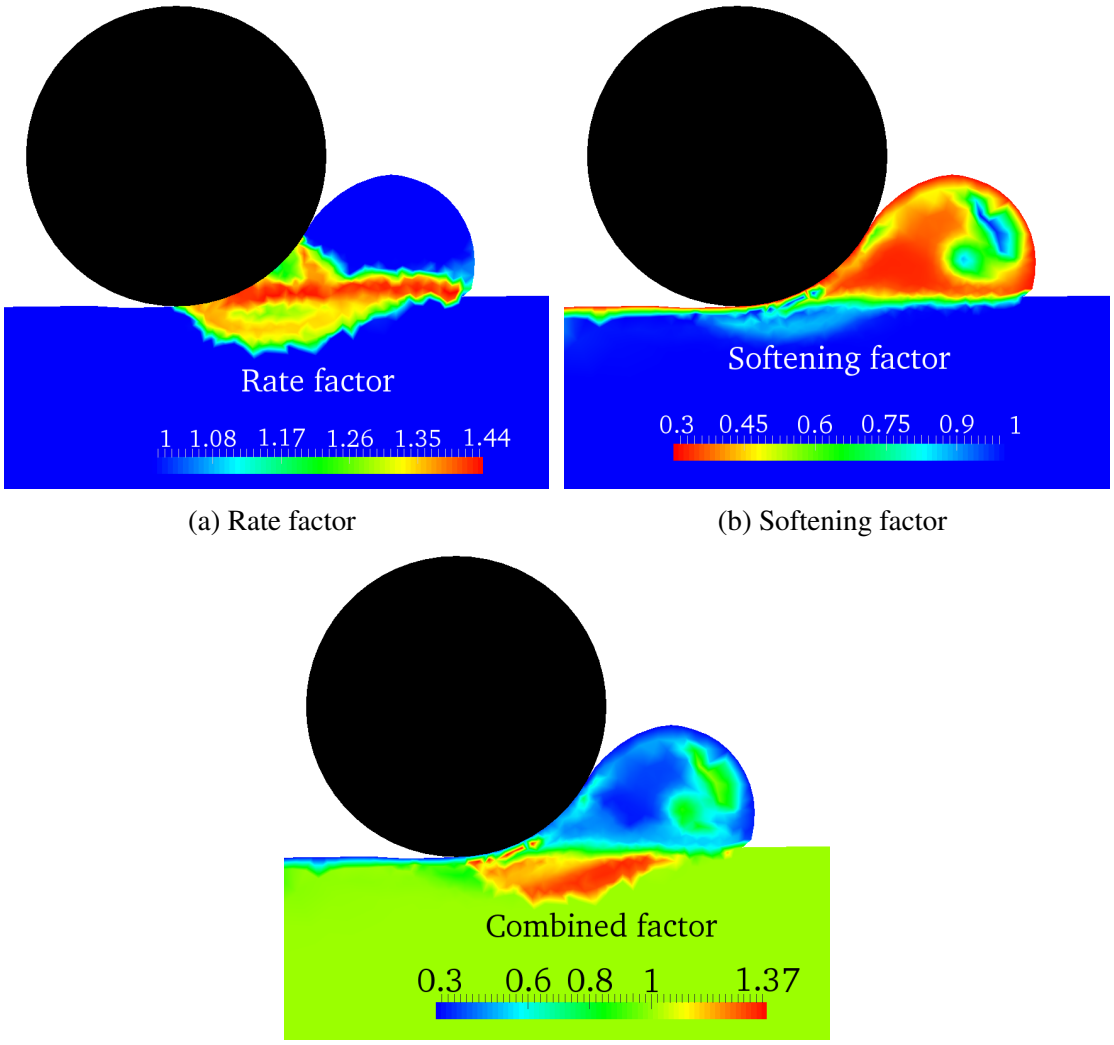

(a) Rate factor

(b) Softening factor

(c) Combined factor

Figure 6.36 Rate and softening factors. $w_{ini}/D = 0.2$, u/D =5, $\mu = 0.10$, $v_p/D\dot{\gamma}_{ref}$ =1000, $\delta_{rem} = 0.3$, $\xi_{95} = 10$.

6.3.6.2 Effect of μ on loading response under large displacement

Figure 6.37 shows the effect of the viscosity parameter μ on the lateral loading response of a light pipe in terms of pipe invert trajectory and equivalent friction factor. Results for two types of soil, with and without strain softening, are presented. For both soil cases, it is found that the evolution of invert trajectory is not conclusive, as the elevation of the pipe invert does not necessarily increase with μ, as shown in Figure 6.37a and 6.37c. In general, the adoption of a larger value of μ results in higher lateral resistance at the initial

loading stage, within a lateral pipe displacement of one diameter. Subsequently, this trend is only obvious in the case of soil without strain softening (see Figure 6.37b). In Figure 6.37d, the analysis with $\mu = 0.05$ generates the lowest resistance, even lower than the rate-independent case.

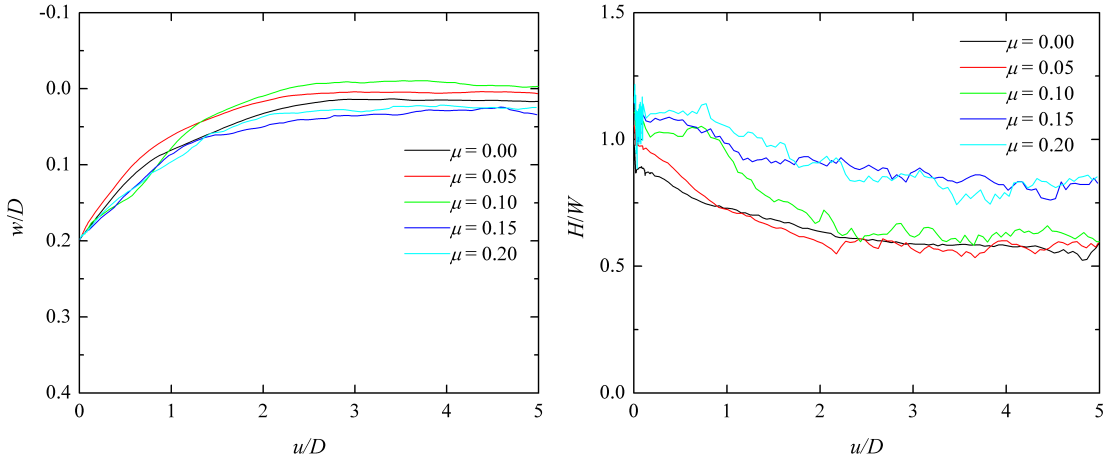

(a) $\delta_{rem} = 1.0$: invert trajectory

(b) $\delta_{rem} = 1.0$: equivalent friction factor

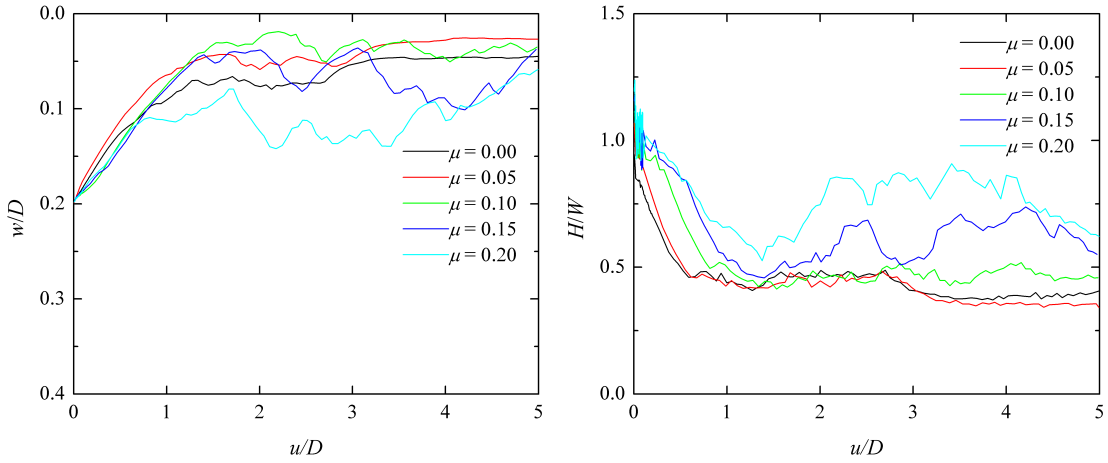

(c) $\delta_{rem} = 0.3$: invert trajectory

(d) $\delta_{rem} = 0.3$: equivalent friction factor

Figure 6.37 Effect of viscosity parameter on lateral loading behaviour of a light pipe. $W/Ds_{um} = 1.6$, $w_{ini}/D = 0.2$, $v_p/D\dot{\gamma}_{ref}$ =1000, $\xi_{95} = 10$.

Figure 6.38 shows the effect of μ on the behaviour of a pipe of moderate weight ($W/Ds_{um} = 4.0$). As discussed before, this pipe is near the upper bound of the critical pipe weight W_{cri} shown in Figure 6.21. With large values of μ, the pipe dives into the soil (see Figure 6.38a), resulting in a continuous increase of resistance (see Figure 6.38b). In such a scenario, heavy pipe behaviour is observed, indicating that μ has a non-negligible influence on deciding the behaviour type (light or heavy) of a pipe. This is attributable to the fact that a steep slope might be developed during the lateral sweep of the pipe as the

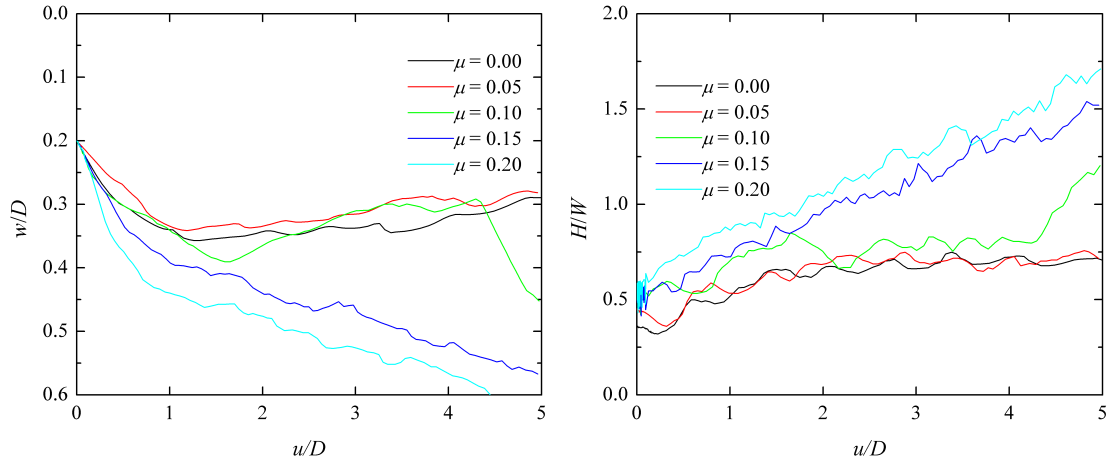

(a) Invert trajectory (b) Equivalent friction factor

Figure 6.38 Effect of viscosity parameter on lateral loading behaviour of a pipe with moderate weight. $W/Ds_{um} = 4.0$, $w_{ini}/D = 0.2$, $v_p/D\dot{\gamma}_{ref}$ =1000, $\delta_{rem} = 0.3$, $\xi_{95} = 10$.

soil strength in the active berm is enhanced with increasing μ. This steep slope tends to change the mechanism type and exerts a downward force on the pipe crown to drive it to embed further (see Figure 6.39). This observation is similar to that made in studying the effect of stain softening, in that a stronger soil berm increases the lateral resistance but does not necessarily guarantee light pipe behaviour (see Figure 6.29).

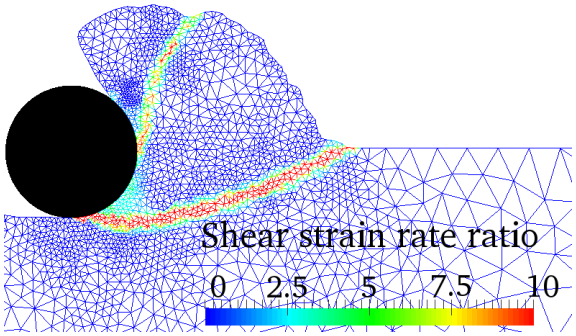

Figure 6.39 Heavy pipe behaviour caused by loading rate effect. $W/Ds_{um} = 4.0$, $w_{ini}/D = 0.2$, $u/D = 3$, $\mu = 0.20$, $v_p/D\dot{\gamma}_{ref} = 1000$, $\delta_{rem} = 0.3$, $\xi_{95} = 10$.

6.3.6.3 Effect of v_p on loading response under large displacement

Figure 6.40 shows the effect of the normalised lateral loading rate $v_p/D\dot{\gamma}_{ref}$ on the behaviour of a light pipe. Higher resistance is observed in the cases with faster loading rate v_p during the initial lateral pipe displacement of one diameter in both soil cases with remoulded strength ratios δ_{rem} of 1.0 and 0.3, as illustrated in Figures 6.40b and 6.40d,

respectively. Very slight differences in the elevation levels of the pipe are observed during this stage (see Figures 6.40a and 6.40c). After this initial loading phase, the pipe tends to move upward more in the simulation with a faster loading rate, to reduce the extent of the region with intense shearing. This generates a smaller soil berm, which is a key element in providing the lateral resistance. As a result, all the resistance curves almost converge in Figure 6.40b. Extreme observations can be made in Figure 6.40d, where the fastest loading rate yields the lowest soil resistance, with the corresponding pipe elevation being above all the other curves as illustrated in Figure 6.40c.

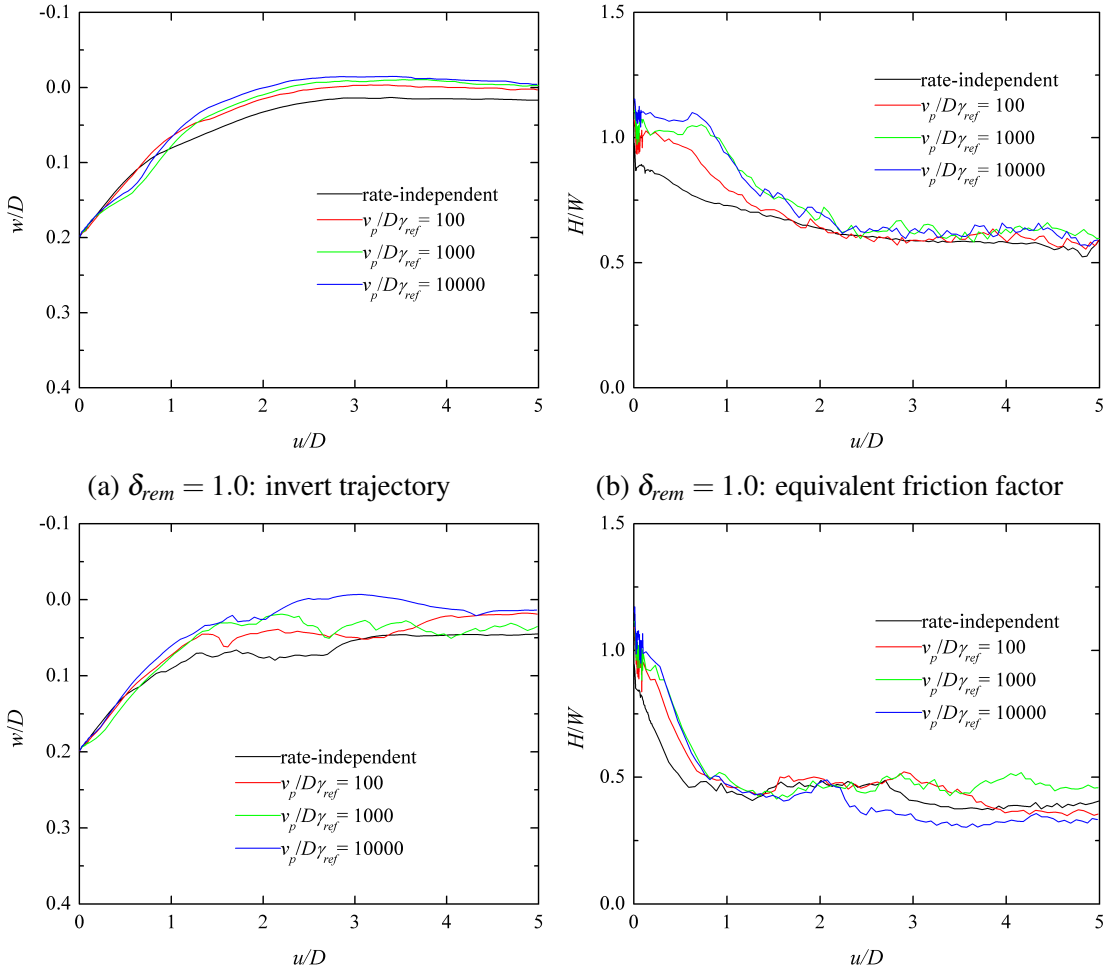

(a) $\delta_{rem} = 1.0$: invert trajectory

(b) $\delta_{rem} = 1.0$: equivalent friction factor

(c) $\delta_{rem} = 0.3$: invert trajectory

(d) $\delta_{rem} = 0.3$: equivalent friction factor

Figure 6.40 Effect of loading rate on lateral loading behaviour of a light pipe. $W/Ds_{um} = 1.6$, $w_{ini}/D = 0.2$, $\mu = 0.10$, $\xi_{95} = 10$.

Figure 6.41 shows the effect of $v_p/D\dot{\gamma}_{ref}$ on the behaviour of a moderately heavy pipe ($W/Ds_{um} = 4.0$). The pipe with the fastest loading rate ($v_p/D\dot{\gamma}_{ref} = 10000$) tends to exhibit some heavy pipe behaviour, with the corresponding lateral resistance still showing

an increasing trend at the end of loading (Figure 6.41b). This confirms the previous findings with varying μ, that the enhanced strength of the soil within the active berm may lead to heavy pipe behaviour.

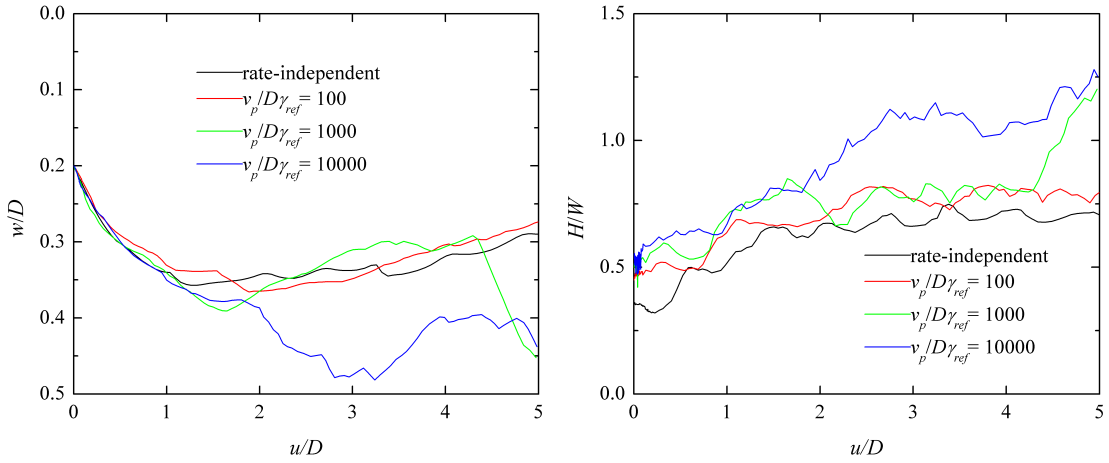

(a) Invert trajectory (b) Equivalent friction factor

Figure 6.41 Effect of loading rate on the lateral loading behaviour of a pipe with moderate weight. $W/Ds_{um} = 4.0$, $w_{ini}/D = 0.2$, $\mu = 0.10$, $\delta_{rem} = 0.3$, $\xi_{95} = 10$.

6.4 Summary

This chapter has presented a detailed numerical investigation into the monotonic lateral loading response of a shallowly embedded pipe undergoing large lateral movements, up to eight pipe diameters in distance. The main findings of this study, and the guidance for design, are summarised below:

- Lower and upper bounds for the critical pipe weight, W_{cri}, that differentiates light pipe behaviour from heavy pipe behavior, were derived (Figure 6.21) and took account of the influence of soil strength gradient k. The two bounds can be expressed as:

$$W_u = (3 - 0.14\frac{kD}{s_{um}})(s_{um} + 0.5kD)D \tag{6.4}$$

$$W_l = (2.5 - 0.07\frac{kD}{s_{um}})(s_{um} + 0.5kD)D \tag{6.5}$$

  A pipe with weight above W_u will exhibit heavy behaviour with continuous increase in lateral resistance during lateral loading, while a pipe with weight below W_l will

eventually exhibit light behaviour, and reach a steady residual stage. The effects of strain softening and strain rate were found to have limited influence in determining the pipe behaviour type (light or heavy), if the parameter values adopted are within the typically range. Therefore, Equations 6.4 and 6.5 can be used to assess pipe behaviour type during early design.

- The initial pipe embedment is found to have negligible effect on the residual lateral resistance H_{res}. An equation quantifying H_{res} for a light pipe is derived as

$$\frac{H_{res}}{Ds_{um}} = 0.28(\frac{W}{Ds_{um}})^{1.67} \tag{6.6}$$

This equation is obtained based on default soil properties (see Table 6.1) used in the parametric study. Two additional parameters, f_k and f_g, were introduced to modify the calculation of H_{res} (using Equation 6.6) to account for the influence of normalised soil strength gradient kD/s_{um} (from 1 to 5) and normalised soil unit weight $\gamma' D/s_{um}$ (from 0 to 10). These parameters were expressed as

$$f_k = 1.12 - 0.06\frac{kD}{s_{um}} \tag{6.7}$$

$$f_g = 1.105 - 0.035\frac{\gamma' D}{s_{um}} \tag{6.8}$$

The influence of the remoulded strength ratio, δ_{rem}, (from 0.2 to 0.5) on H_{res} was found to be very limited. The influence of the ductility parameter ξ_{95} (from 10 to 50) could be quantified for light pipes ($W/Ds_{um} \leq 2.4$) as

$$f_\xi = 0.0025\xi + 0.975 \tag{6.9}$$

Equations 6.6 to 6.9 can be used to assess the residual lateral resistance of a light pipe with constant effective weight W under lateral loading, taking into account the effects of soil unit weight, soil strength gradient and parameters related to strain softening. Although the effect of strain rate dependence is also examined in the study, the influence of rate is not quantified because the parametric study results are

less conclusive. However, it has been found that rate has a minor influence on H_{res}, unless extremely large values of the rate parameters are adopted.

- At the breakout stage of lateral loading, the absence of tensile capacity at the pipe-soil interface leads to a lower-bound on the breakout resistance for the pipe, as expected. When full tension capacity is allowed the breakout resistance typically increases by 50%.

- Consideration of the strain softening effect significantly reduces the residual lateral resistance H_{res} of a pipe by almost 40% compared to that quantified with ideal soil, although changing the relevant parameters in the given range recommended by Randolph (2004) is found to have very limited effect on H_{res}. It is therefore recommended that further research concerning the lateral loading behaviour of a pipe should take into account the strain softening effect, but focus on quantifying the influence of soil strength gradient, soil unit weight and the parameters related to the strain rate effect.

Chapter 7

Lateral pipe-soil interaction: cyclic

In the area of pipe-soil interaction during large-amplitude cyclic movements, a number of experimental studies (e.g. Cheuk *et al.*, 2007; Dingle *et al.*, 2008; Lee, 2012; Rismanchian, 2014) have provided insights into the soil mechanisms. However, a better understanding of the cyclic load-displacement response requires parametric studies based on robust numerical modelling. Such numerical simulations should consider the effect of remoulding of the soil around the pipe caused by large strains, since this greatly affects the lateral resistance.

The aim of this chapter is to use the sequential limit analysis (SLA) tool introduced in Chapter 3 to study pipe-soil interaction under cyclic lateral motions, as well as demonstrating an important application of this tool in geomechanics. Validations against centrifuge modelling results reported by Rismanchian (2014), including various different types of cyclic loading history, are presented first, followed by a numerical parametric study investigating the influence of loading history and soil strength properties on pipe-soil interaction during cyclic lateral displacements.

7.1 Problem definition

This study focuses on simulating the behaviour of a pipeline undergoing lateral sweeps across a soft clay seabed, caused by cyclic thermal loading/unloading. The problem is idealized in plane strain conditions by using a section from a pipeline with typical outside diameter in the range 0.1 to 0.75m as illustrated in Figure 7.1. Undrained conditions that generally prevail during pipe movements on fine-grained soils in deep water (Chatterjee

et al., 2013) are assumed in the analyses. The pipe is assumed not to rotate as it moves laterally because in practice the torsional rigidity of the pipe is likely to be sufficient to restrain it against rotation within a buckle. The transient suction generated at the rear side of the pipe is neglected, and thus no tensile force is permitted at the pipe-soil interface. Consolidation effects and the effect of waves and currents on the seabed topography around the pipeline are beyond the scope of the present study.

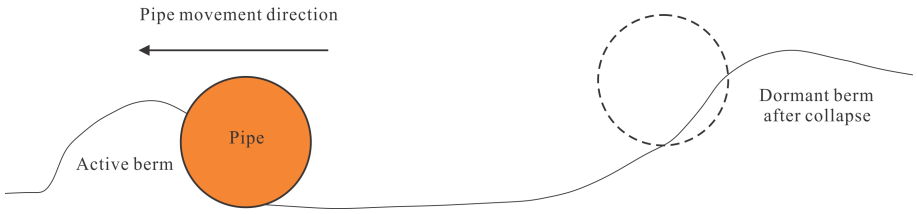

(a) A dormant berm left by previous sweeps

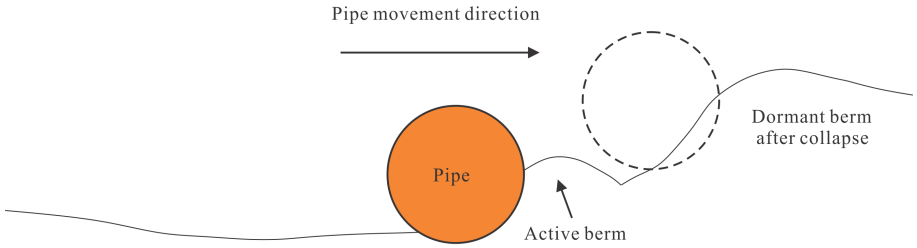

(b) Merging of an active berm and a dormant berm

Figure 7.1 Problem definition: cyclic lateral loading

During the cyclic loading, soil berms are created by the sweeps of the pipe (see Figure 7.1). A berm that is left by previous sweeps is called a 'dormant' berm and the one currently being pushed by the pipe is called an 'active' berm. When the active berm interacts with a dormant one, the pipe will achieve a rise of lateral resistance until it scrapes across/over the dormant berm (typically for a light pipe). Large deformations and strains are developed in the loading process and the soil around the pipe experiences severe remoulding, leading to degradation of the operative shear strength s_u.

The key elements affecting the force-displacement response of the pipe are identified as: (1) lateral resistance against a steadily growing active berm during large-amplitude movement at an essentially steady pipe embedment; 2) progressive mobilization of berm resistance during collection of a pre-existing dormant berm; 3) increase in berm resistance

as the size of the berm grows with multiple lateral sweeps; 4) influence of cyclic loading history on the pipe response after it encroaches beyond the previous displacement limits.

7.2 Numerical simulation of experiments

7.2.1 Summary of physical model tests

A set of centrifuge model tests studying the cyclic lateral loading behaviour of a pipe section was reported by Rismanchian (2014). All the tests were conducted under an acceleration level of 25g. The pipe and soil parameters provided by Rismanchian (2014) are summarised in Table 7.1, where all the values are given at prototype scale. In the current study, the first few lateral sweeps of these centrifuge tests are simulated. The details of these sweeps are given in Table 7.2.

Table 7.1 Pipe and soil parameters in tests by Rismanchian (2014)

Parameter	Value
Pipe diameter, D: m	0.5
Initial shear strength of soil at mudline, s_{um}: kPa	3.0
Shear strength gradient, k: kPa/m	6.5
Saturated unit weight of soil, γ_{sat}: kN/m^3	16.1+0.1z

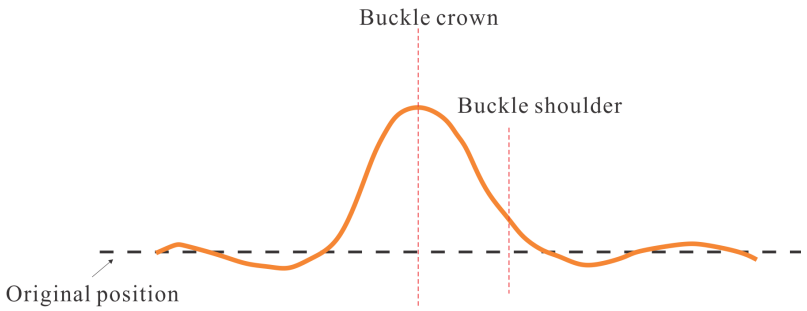

Figure 7.2 Different sections along a buckle

Tests A and B were designed to mimic the behaviour of pipe sections close to the crown of a lateral buckle (see Figure 7.2). The vertical load during sweeps 1-2 of these two tests spanned a relatively wide range (2.05 kN/m and 4.05 kN/m) but was the same (1.25 kN/m) during sweep 3. Test C was also chosen to examine the pipe behaviour close to a buckle crown, but all three sweeps were performed under different vertical loads to consider a

Table 7.2 Summary of first few sweeps in centrifuge tests Rismanchian (2014)

Test	Initial embedment	Summary of the first few sweeps
A	$0.15D$	sweep 1: $V = 2.05$ kN/m, $\Delta u = 8D(+)$ sweep 2: $V = 2.05$ kN/m, $\Delta u = 7D(-)$. Consolidation after this sweep sweep 3: $V = 1.25$ kN/m, $\Delta u = 8D(+)$
B	$0.45D$	sweep 1: $V = 4.05$ kN/m, $\Delta u = 6D(+)$ sweep 2: $V = 4.05$ kN/m, $\Delta u = 5D(-)$. Consolidation after this sweep sweep 3: $V = 1.25$ kN/m, $\Delta u = 6D(+)$
C	$0.45D$	sweep 1: $V = 3.00$ kN/m, $\Delta u = 8D(+)$. Consolidation after this sweep sweep 2: $V = 0.65$ kN/m, $\Delta u = 7D(-)$. Consolidation after this sweep sweep 3: $V = 1.25$ kN/m, $\Delta u = 8D(+)$
D	$0.15D$	sweep 1: $V = 1.35$ kN/m, $\Delta u = 6D(+)$ sweep 2: $V = 1.35$ kN/m, $\Delta u = 5D(-)$. Consolidation after this sweep sweeps 3-12: $V = 1.35$ kN/m, constant at $0.6D$ but encroaching by $0.2D$ at the positive extremity and retreating by $0.2D$ at the negative extremity of each cycle
E	$0.45D$	sweep 1: $V = 5.35$ kN/m, $\Delta u = 6D(+)$ sweep 2: $V = 5.35$ kN/m, $\Delta u = 5D(-)$. Consolidation after this sweep sweeps 3-12: $V = 5.35$ kN/m, constant at $0.6D$ but encroaching by $0.2D$ at the positive extremity and retreating by $0.2D$ at the negative extremity of each cycle

possible variation of contact force during cyclic buckling as a result of three-dimensional effects (variation of elevation along the pipe). The vertical load in sweep 3 of Test C was the same as that of Tests A and B. Therefore, the influence of previous loading history can be studied by comparing the results of the three tests in the last sweep. Tests D and E represent hypothesized modes of behaviour relevant to pipe sections near the buckle shoulders (see Figure 7.2). A cycle of lateral motion with large amplitude, followed by progressive movements with small amplitudes in one direction were applied to the pipe in these two tests, to study the encroaching/retreating behaviour of pipelines.

7.2.2 Numerical modelling with SLA

The configuration and boundary conditions of the SLA model are as illustrated in Figure 4.27. The typical soil domain for this study was chosen to be $5D$ in depth (h) and its left and right edges were $3D$ (B_1) and $12D$ (B_2) away from the initial position of the pipe. For better visualisation of the results, the dimensions were not necessarily kept the same for all simulations, but were always kept large enough to contain the zones of plastic shearing throughout the simulations. The pipe-soil interface was modelled as fully smooth

($\alpha = 0$), as assumed by Rismanchian (2014), and no tensile capacity was allowed at the interface ($T = 0$). The effect of rate-dependent strength was not taken into account, but the softening behaviour was considered according to Equation 2.9 (Einav and Randolph, 2005; Zhou and Randolph, 2007). The remoulded strength ratio, δ_{rem}, and ductility parameter, ξ_{95} of the soil were chosen to be 0.3 and 10 respectively, both being within the range recommended by Randolph (2004) and Wang *et al.* (2010). Other parameters relating to the pipe and soil were chosen according to Table 7.1. Although a quadratic variation of s_{u0} with depth was supported in the SLA modelling, which offers a more reasonable fit to the T-bar results provided by Rismanchian (2014), a linear variation was adopted here as it is more commonly used in practice. The simulations were performed in the following two steps:

- The pipe was pre-embedded into the soil by $0.001D$ and then pushed under displacement control to the desired depth w_{ini} (see Table 7.2). This process differs from that in the centrifuge model tests, where the pipe was dynamically laid using small amplitude lateral oscillations. A simple vertical penetration method was chosen here to eliminate uncertainties caused by the dynamic embedment process. During this installation step the soil was taken as an ideal Tresca material without considering the remoulding effect.

- Once the installation had been completed, the cumulative shear strain of the soil domain was reset to zero. Cyclic lateral movement was then applied to the pipe and it was allowed to move upward or downward freely, depending on the applied vertical load. Rotation was not allowed during the cyclic lateral loading process. The degradation of soil strength caused by strain softening was taken into account during this step.

More details of SLA modelling can be found in Section 4.7.1.1, where a general modelling procedure for lateral loading behaviour of a pipe is established.

7.2.3 Numerical simulations of experiments

Section 6.3.3 presents an approach for predicting the pipe behaviour type (heavy or light) during lateral movement. The lower bound value of the critical normalised pipe weight, $W/Ds_{u,0.5D}$, for the soil properties studied here can be extracted from Figure 6.21 and a value of 2.6 is obtained, which generates a critical pipe weight of 6.0kN/m. All of the vertical loads in Table 7.2 are below this value and thus light pipe behaviour is expected for all the simulations in the residual stage.

Figure 7.3 shows the yield envelopes of two pipes following penetration to embedments of $0.15D$ and $0.45D$, considering different conditions of interface tension. Only the right half of the envelopes are illustrated due to symmetry. The breakout resistances obtained in the centrifuge model tests are also plotted. The points corresponding to tests B and E are found to be outside the numerical envelope even when interface tension is considered. According to available physical modelling results (e.g. Dingle *et al.*, 2008; Rismanchian, 2014), breakaway of the pipe from the soil takes place immediately after lateral loading is imposed. Therefore, it is reasonable to use the yield envelopes derived with no interface tension to predict the pipe motion in the initial lateral loading stage. Based on the associated flow rule, the pipes in tests A, B, C and D would be expected to have upward movement once they are displaced laterally, while the pipe in test E might move downward at first (see Figure 7.3). These predictions are consistent with the centrifuge results presented below.

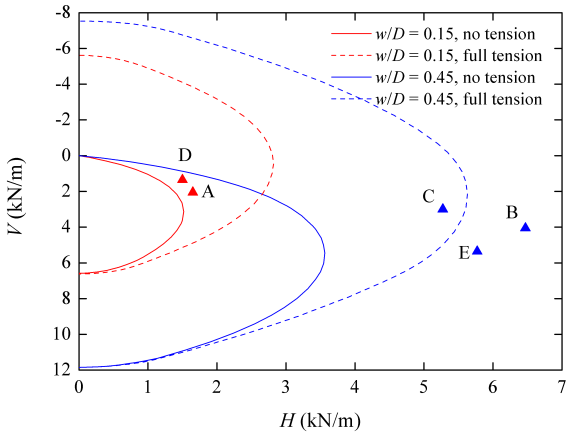

Figure 7.3 Yield envelopes at the breakout stage, with experimental breakout data.

Comparisons between SLA and the centrifuge test results, in terms of the pipe invert trajectory and equivalent friction factor, are presented in Figures 7.4, 7.8, 7.12, 7.13 and 7.18. Very good agreement can be observed in general. It is noteworthy that it is impractical to match the numerical results with centrifuge data for all the loading tests by using the same soil parameters, considering the divergence in soil properties related to each test (Rismanchian, 2014). However, for the sake of consistency, the initial soil strength profile in all the SLA simulations was kept the same as the representative profile given in Table 7.1.

7.2.3.1 Test A

Figures 7.4a and 7.4b show the invert trajectory and the lateral resistance respectively of the pipe in Test A. During sweep 1 in the centrifuge test, break-out of the pipe from the soil takes place almost immediately when the loading begins, resulting in a peak followed by a sharp drop in the lateral resistance. After that, both lateral soil resistance and the pipe embedment gradually decrease with lateral pipe displacement, which denotes typical 'light pipe' behaviour. A steady plateau stage is then reached after the pipe is displaced by about $3D$. When the loading direction is reversed and sweep 2 begins, the pipe ploughs slightly deeper into the seabed. After a further distance of $1D$, a steady state is achieved again. Similar observations can be made in the initial and middle parts of sweep 3. At a lateral pipe displacement of $8D$ during sweep 3, the pipe approaches the soil berm left by sweep 1 (see Figure 7.6c) and a sharp increase in soil resistance is observed.

Overall, SLA produces reasonable pipe-soil response compared with the centrifuge test results, although the lateral resistance in sweep 2 is moderately underestimated. Moreover, the centrifuge curve shown in Figure 7.4b exhibits a small peak at the beginning of sweep 3, which is not observed in the SLA curve. Since there is no peak at the beginning of sweep 2 in centrifuge test, it can be speculated that this peak response may be attributable to consolidation of the soil during the resting period prior to sweep 3 (see Table 7.2), which leads to a certain enhancement in soil strength. Moreover, during this resting period, the pipe gains more contact with the soil and suction can be mobilised when a subsequent

'new' lateral loading is applied to the pipe. The breakout suction and the consolidation of soil cannot be modelled by the SLA method proposed here. However, in general, the main features of pipe behaviour during a typical buckling event when little or no consolidation takes place can be captured satisfactorily.

The pipe motion was reversed at $u = 8D$ during sweep 3 in the centrifuge test and the remaining sweeps were not modelled in SLA. Instead, the pipe in the SLA simulation was further displaced to scrape across/over the berm left by sweep 1 to study the encroaching behaviour. After the pipe scrapes across/over the berm (see Figures 7.6d and 7.6e) there is considerable rebound in the elevation of the pipe invert as shown in Figure 7.4a, and a drop in soil resistance is achieved.

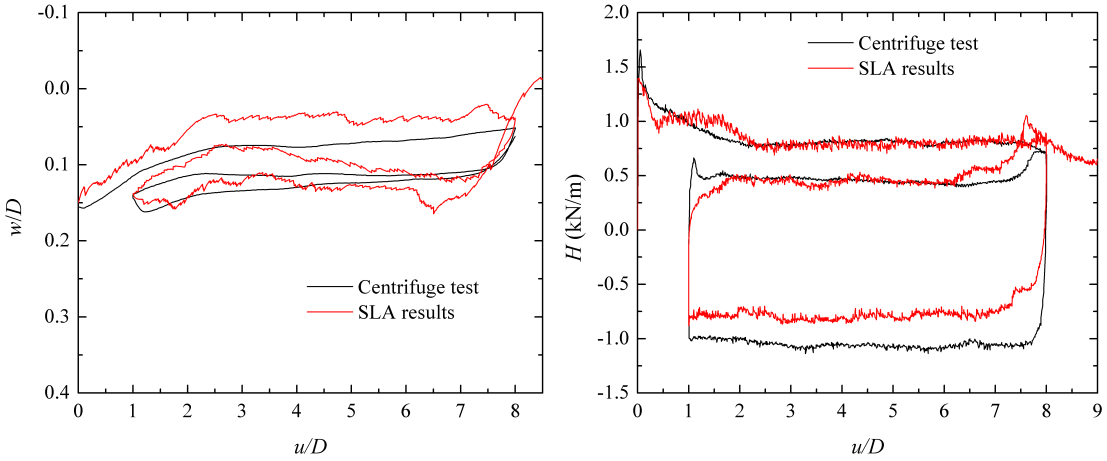

(a) Invert trajectory (b) Lateral resistance

Figure 7.4 Invert trajectory and lateral resistance in test A

Figure 7.5 shows the evolution of the $V - H$ yield envelope of the pipe during cyclic lateral loading. The results are consistent with the resistance curve in Figure 7.4b, but provide more information on the likely pipe behaviour if different pipe weight or moving direction is involved. All the envelopes show a trend of rotation towards the sweep direction. The expansion and shrinkage of the yield envelope near the end of sweep 3, when the pipe moves toward a previous berm and scrapes over it, can be observed in Figure 7.5c.

Figures 7.6a to 7.6e shows the soil failure mechanisms as well as the mesh of the SLA model during the cyclic loading process. For a clearer view of the sliplines as well as the mesh near the pipe, only part of the domain near the deforming region is presented.

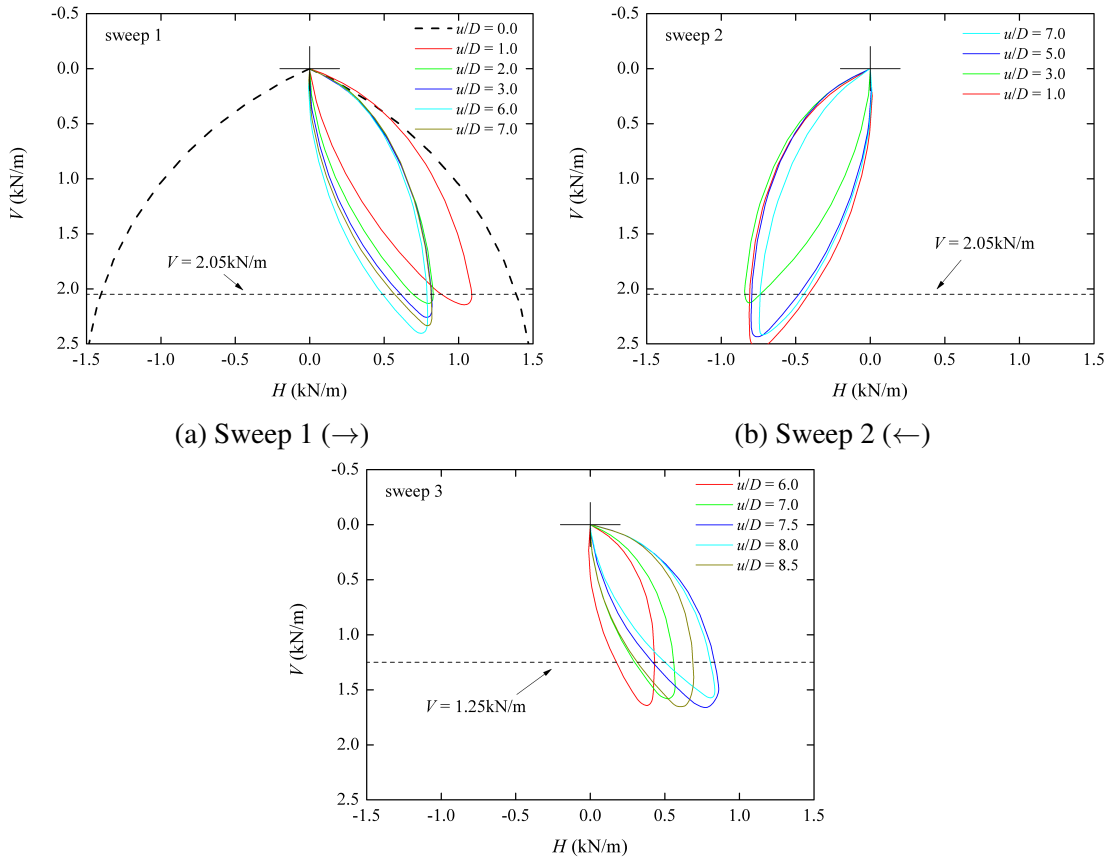

(a) Sweep 1 (→)

(b) Sweep 2 (←)

(c) Sweep 3 (→)

Figure 7.5 Evolution of $V-H$ yield envelope in test A

Figures 7.6a and 7.6b show typical mechanisms of a light pipe during the residual stage, while Figures 7.6c to 7.6e illustrate the merging of the current active berm and the dormant one left by the previous sweep.

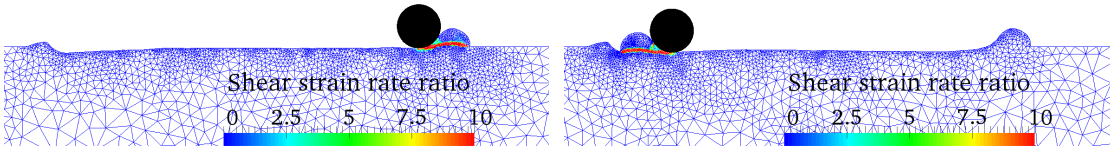

(a) sweep 1 ($\rightarrow$), $u/D = 8.0$

(b) sweep 2 ($\leftarrow$), $u/D = 1.0$

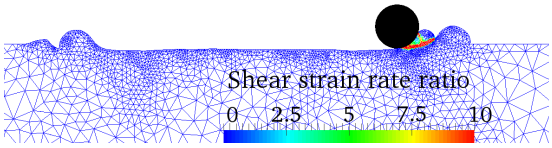

(c) sweep 3 ($\rightarrow$), $u/D = 7.5$

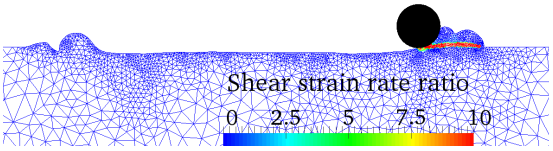

(d) sweep 3 ($\rightarrow$), $u/D = 8.0$

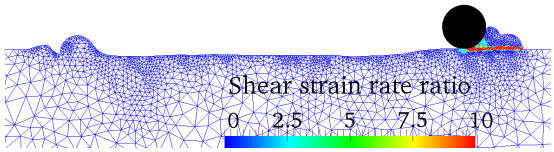

(e) sweep 3 ($\rightarrow$), $u/D = 9.0$

Figure 7.6 Soil failure mechanisms (showing $\dot{\gamma}_{max}D/v_p$) during Test A

Figure 7.7 illustrates the distribution of the softening factor in the soil near the end of loading. Three different soil berms are observed, the current active one and another two at the leftmost and rightmost positions. It is found that the soil within all the berms is almost fully remoulded, while that between these berms is far less softened. This confirms that the shearing deformations mainly take place as the soil is being scraped from the intact soil into the berm.

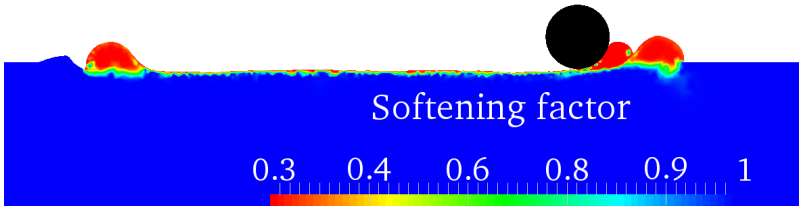

Figure 7.7 Softening factor in Test A: $u/D = 7.5$ in sweep 3

7.2.3.2 Test B

Figure 7.8 shows the response of the pipe in Test B. Very good agreement between the numerical and centrifuge results can be found again, despite the fact that SLA overestimates

the pipe embedment by about $0.1D$ during sweeps 2-3. The peak of lateral resistance in the centrifuge results at the start of sweep 1 cannot be captured by SLA modelling, due to the absence of soil suction at the pipe rear in the numerical model. In a similar way to the findings in centrifuge Test A, the peak response observed at the beginning of sweep 3 (with consolidation) cannot be seen at the same stage of sweep 2 (without consolidation). It is therefore further indicated that this peak response is likely to be attributable to consolidation, which enhances the soil strength as well as increasing the development of soil suction at the breakout stage during a subsequent 'new' sweep. Of course, this consolidation-induced peak behaviour cannot be captured by SLA modelling.

When the loading direction is reversed at the right extremity, the lateral resistance drops immediately in both the numerical and centrifuge results, then increases to a stable value after about one pipe diameter, when a plateau is achieved. Such plateaus are found in Figure 7.8b for all the three sweeps, suggesting that an essentially steady residual stage can always be reached for a light pipe during cyclic lateral movement, provided there is enough distance between the two extremities of motion.

A sharp increase in lateral resistance as the pipe approaches a dormant berm can be found at the end of sweeps 2 and 3 in both the SLA and centrifuge results. In the SLA simulation, after the pipe has pushed into the berm at the end of sweep 3, its invert reaches a very high level that is above the original soil surface. This is accompanied by a rapid drop in soil resistance. Such behaviour is not observed in the centrifuge test since the pipe was not displaced this far. Note that the vertical load on the pipe was much smaller in sweep 3 than in sweeps 1 and 2 (See Table 7.2).

Figure 7.9 shows the evolution of the yield envelope of the pipe during different sweeps, to complement the SLA resistance curve in Figure 7.8b. It can be observed that the yield envelopes in a given plateau stage are of similar shape and size, which is most clear in Figure 7.9a. The envelopes in Figure 7.9b show a very obvious trend of rotating clockwise as the pipe moves away from the soil berm at the right extremity (see Figures 7.10a-c).

Figure 7.10 shows the soil failure mechanisms as well as the mesh of the SLA model during the cyclic loading. The behaviour is similar to that in Test A, though much bigger

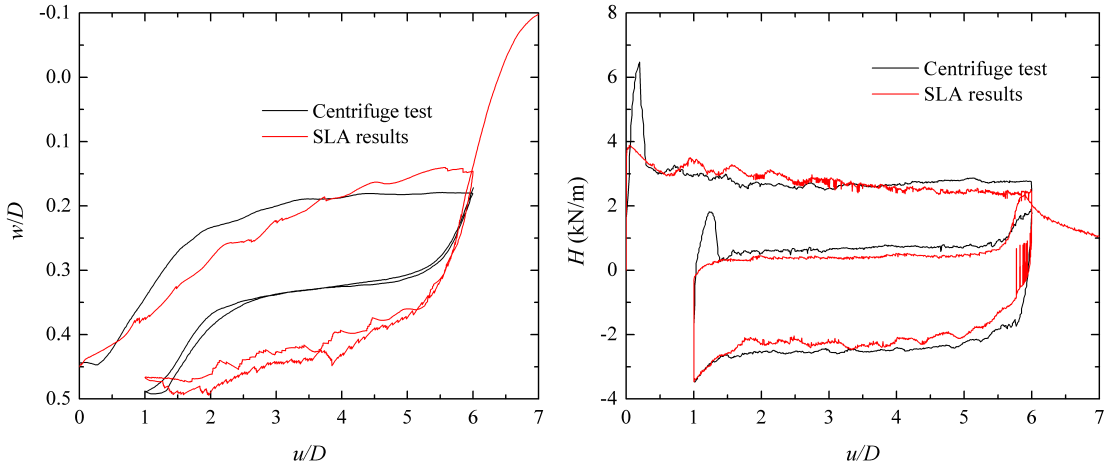

(a) Invert trajectory (b) Lateral resistance

Figure 7.8 Invert trajectory and lateral resistance in Test B

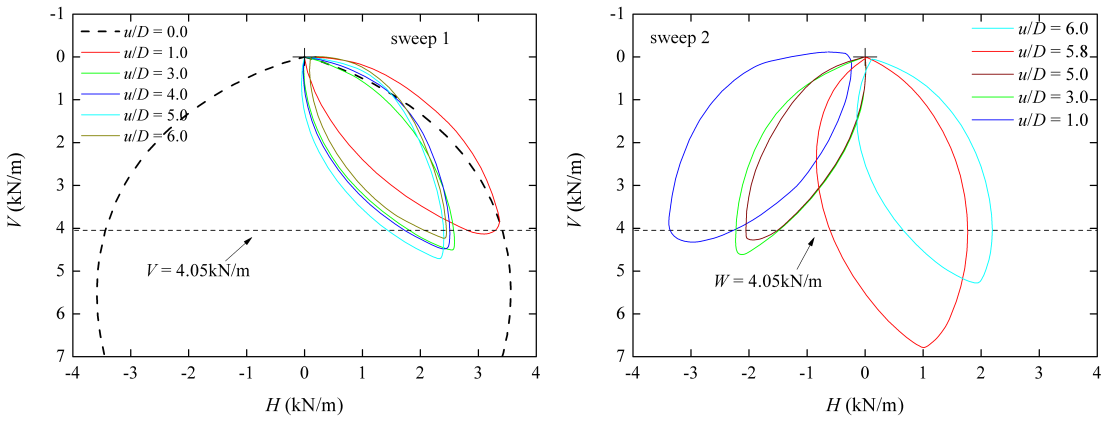

(a) Sweep 1 (→) (b) Sweep 2 (←)

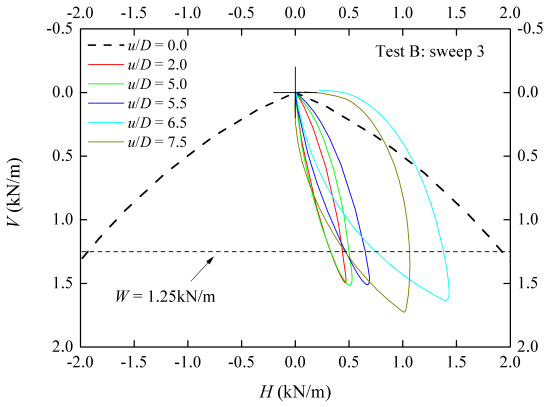

(c) Sweep 3 (→)

Figure 7.9 Evolution of $V-H$ yield envelope in Test B

berms caused by the heavier pipe weight and deeper initial pipe embedment are developed. Of interest is that when the pipe has moved back by a distance of $0.2D$ away from the right extremity (see Figure 7.10b), the soil in the active area collapses and moves with the pipe, resulting in an additional 'driving' force on it. This behaviour significantly decreases the net lateral resistance when the pipe motion is reversed. Figures 7.10e to 7.10g illustrate the process of the pipe approaching the berm created by sweep 1 and then pushing up and into it. The corresponding expansion and shrinkage of yield surface can be seen in Figure 7.9c.

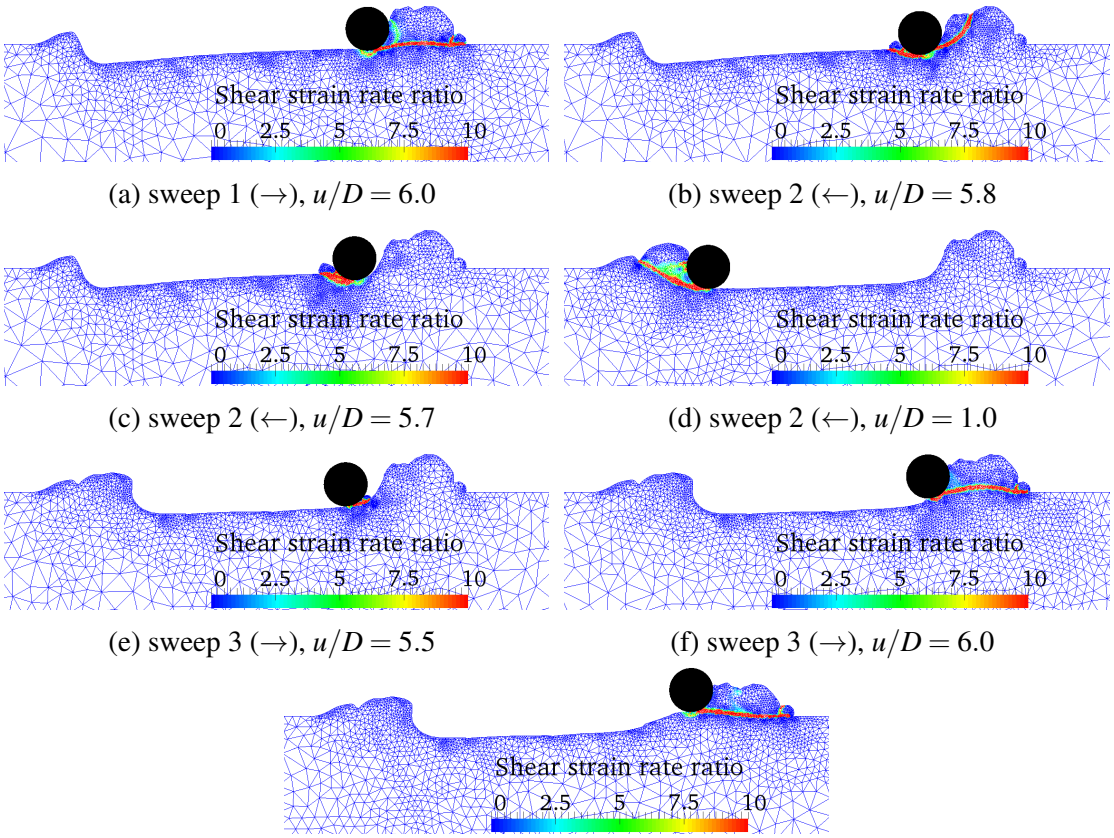

(a) sweep 1 ($\rightarrow$), $u/D = 6.0$

(b) sweep 2 ($\leftarrow$), $u/D = 5.8$

(c) sweep 2 ($\leftarrow$), $u/D = 5.7$

(d) sweep 2 ($\leftarrow$), $u/D = 1.0$

(e) sweep 3 ($\rightarrow$), $u/D = 5.5$

(f) sweep 3 ($\rightarrow$), $u/D = 6.0$

(g) sweep 3 ($\rightarrow$), $u/D = 7.0$

Figure 7.10 Soil failure mechanisms (showing $\dot{\gamma}_{max}D/v_p$) during Test B

Figures 7.11a and 7.11b illustrate the softening factor of the soil at the end of sweep 1 and sweep 2 respectively. The soil within the berms experiences different degrees of softening, with some being fully remoulded and some undisturbed. However, intense shearing (see the sliplines in Figures 7.10a and 7.10d) always takes place in the weakest region of the berm, and in a simpler (non-sequential) analysis it would be reasonable to

assume fully remoulded strength throughout the whole berm when evaluating the lateral resistance.

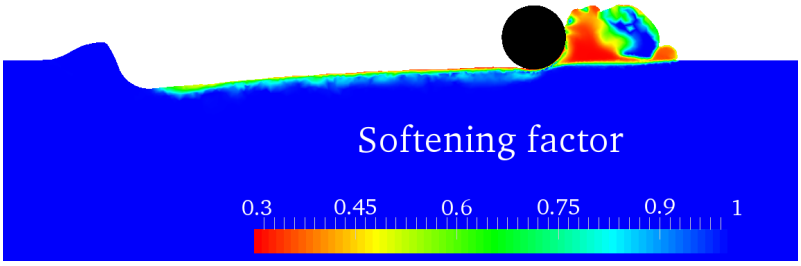

(a) sweep 1 ($\rightarrow$), $u/D = 6.0$

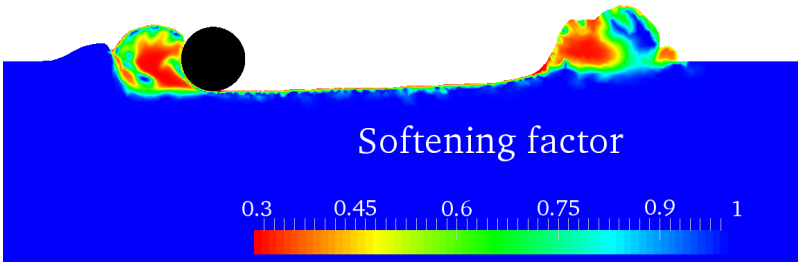

(b) sweep 2 ($\leftarrow$), $u/D = 1.0$

Figure 7.11 Softening factor in Test B

7.2.3.3 Test C

Figure 7.12 shows the comparison between the SLA and centrifuge model test results of test C. Highly satisfactory agreement can be observed in both the invert trajectory and the lateral resistance. As noted in Table 7.2, before each sweep in the centrifuge test, the pipe was rested to allow for consolidation. As a result, the peak in lateral resistance observed at the beginning of each sweep in the centrifuge data is absent in the numerical results, due to the assumption of no tension at the pipe-soil interface as well as the inability of SLA to model the consolidation behaviour.

7.2.3.4 Test D

Figure 7.13 shows the invert trajectory and lateral resistance during test D obtained from SLA and the centrifuge modelling. Unlike Tests A-C, the centrifuge data in test D exhibits greater lateral resistance than the SLA results (see Figure 7.13b) and higher pipe embedment for the whole of the first loading cycle (sweeps 1 and 2). This might be caused

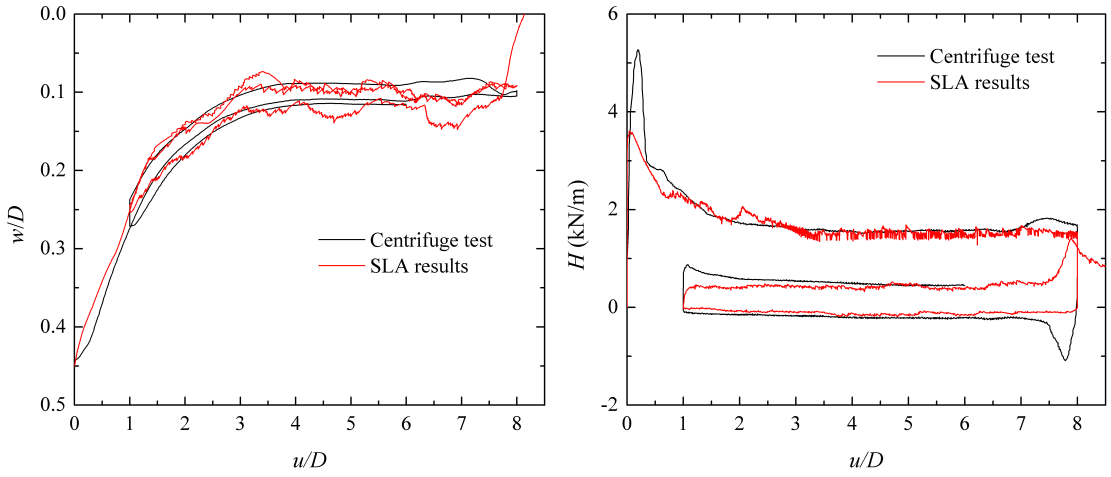

(a) Invert trajectory (b) Lateral resistance

Figure 7.12 Invert trajectory and lateral resistance in Test C

by the fact that the soil strength profile adopted in the SLA modelling is stronger than the real soil strength in centrifuge Test D. It is worth mentioning that the SLA model uses the same soil strength profile to simulate all the five centrifuge tests, without considering the discrepancies of soil samples for the sake of consistency. Higher pipe embedment as well as higher lateral resistance can be gained from the SLA analyses by adopting smaller values of s_{um} or k to match the centrifuge data.

During the encroaching/retreating cycles (sweeps 3-12) as shown in Figure 7.13b, the SLA results exhibit significantly smaller lateral resistance at first due to the absence of the consolidation which was allowed in the centrifuge test. The amplitude of the lateral resistance cycles increases to a certain level after several cycles, as the pipe becomes more embedded, but the resistance is still much lower than that of the centrifuge results. However, the trajectory of the pipe invert agrees well with the centrifuge data.

Figures 7.14 and 7.15 show the yield envelopes of the pipe in the first loading cycle and the encroaching/retreating cycles respectively. For the light pipe used here, all the yield envelopes during the cyclic loading show rotation towards the direction of lateral displacement. This behaviour is not so pronounced for a pipe with moderate weight, as will be discussed below for Test E.

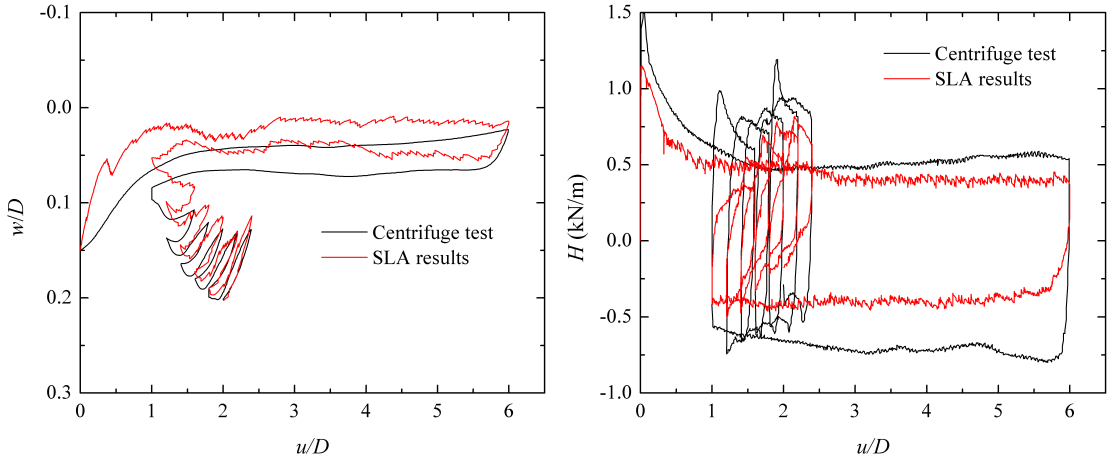

(a) Invert trajectory (b) Lateral resistance

Figure 7.13 Invert trajectory and lateral resistance in Test D

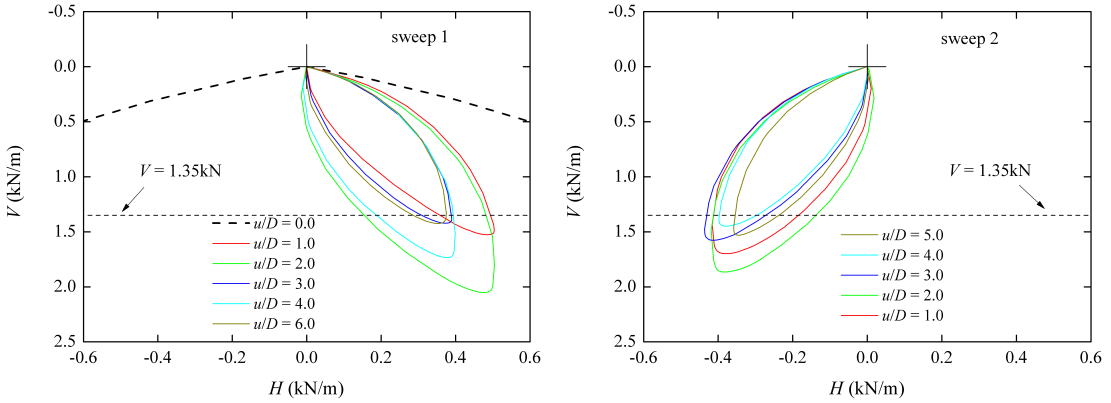

(a) Sweep 1 (→) (b) Sweep 2 (←)

Figure 7.14 Evolution of $V-H$ yield envelope in Test D. Sweeps 1-2

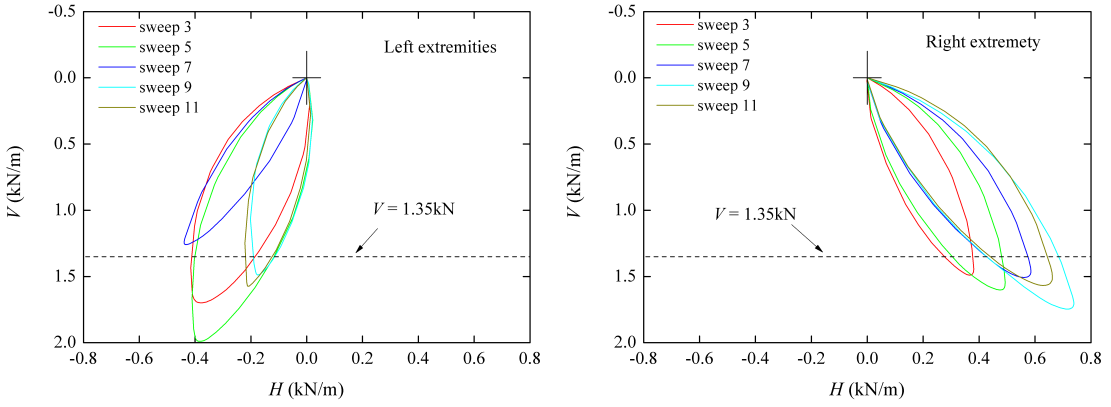

(a) Left extremities (b) Right extremities

Figure 7.15 Evolution of $V-H$ yield envelope in Test D. Sweeps 3-12

Figure 7.16 shows the soil failure mechanism near the end of cyclic loading in test D, and Figure 7.17 shows the softening factor of the soil at the end of sweep 11, where the soil within all the berms is found to be fully remoulded.

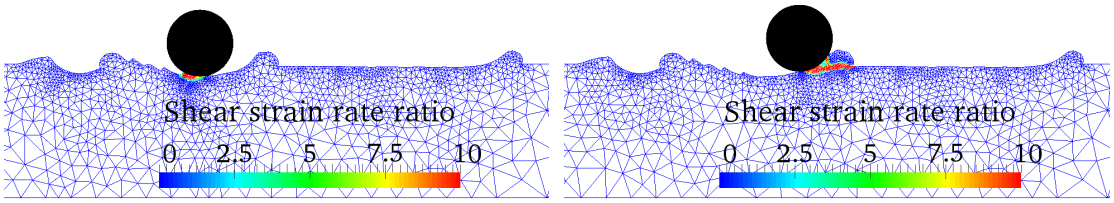

(a) sweep 10 (←), left extremity (b) sweep 11 (→), right extremity

Figure 7.16 Soil failure mechanisms (showing $\dot{\gamma}_{max}D/v_p$) during Test D

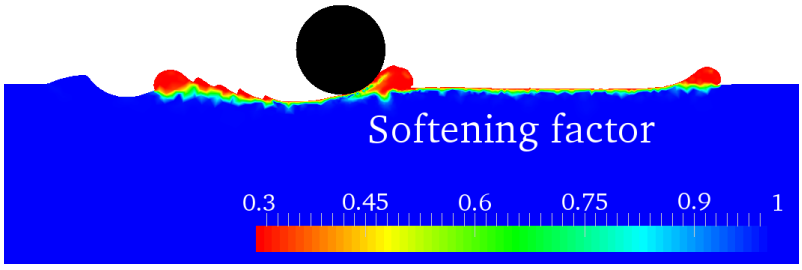

Figure 7.17 Softening factor in Test D at the end of sweep 11 (→)

7.2.3.5 Test E

Figure 7.18 shows the comparison between SLA and centrifuge results in Test E. very satisfactory agreement can be seen during the first cycle of motion. During the remaining cycles, SLA predicts reliable pipe embedment in general, while it moderately underestimates/ overestimates the lateral resistance during the encroaching/retreating stages.

Figure 7.19 presents the $V-H$ yield envelopes of the pipe at the extremities during the encroaching/retreating stage. It is interesting to find in Figure 7.19b that some yield envelopes still show deviation towards the left, even when the pipe moves to the right extremity, which is quite different from Figure 7.15b.

Figures 7.20a-g show the soil failure mechanism as well as the SLA mesh at different stages in Test E. Only part of the soil domain is illustrated. Figures 7.20c and 7.20e show the mechanism when the pipe reaches its right extremity in sweeps 3 and 5. The soil on the active side (the left) moves with the pipe and no gapping occurs, leading to additional

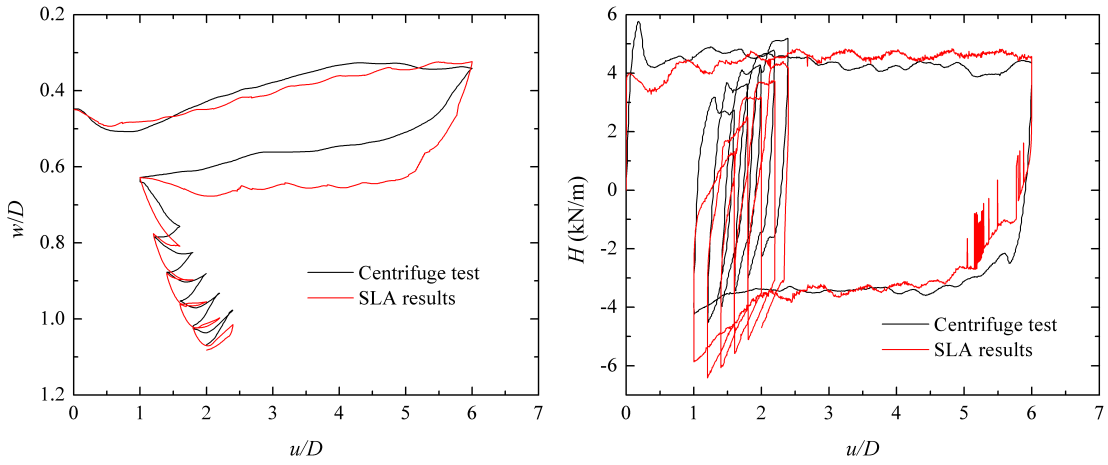

(a) Invert trajectory (b) Lateral resistance

Figure 7.18 Invert trajectory and lateral resistance in Test E

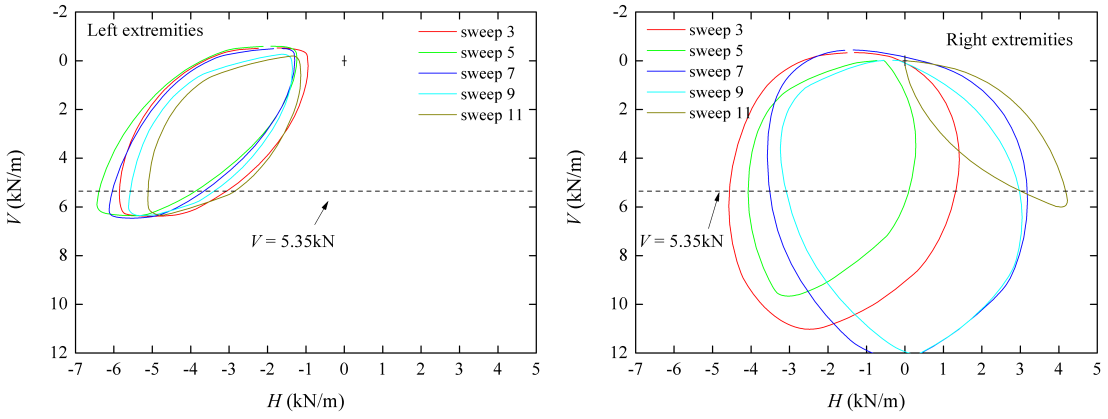

(a) Left extremities (b) Right extremities

Figure 7.19 Evolution of $V-H$ yield envelope in Test E: sweeps 3-12

'driving' force pushing the pipe to the right. As a consequence, more force is needed to displace the pipe to the left direction than to the right in these small cycles, as shown in Figure 7.19b. This behaviour ceases after the pipe is driven far enough towards the right as illustrated in Figure 7.20g, where a crack on the left of the pipe is observed.

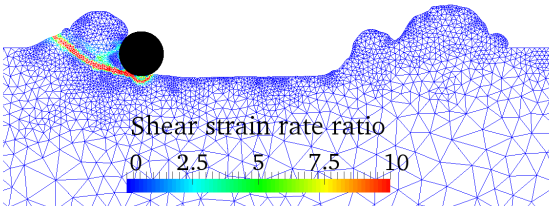

(a) sweep 2 (←), left extremity

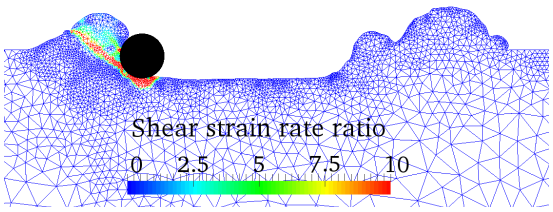

(b) sweep 3 (→), left extremity

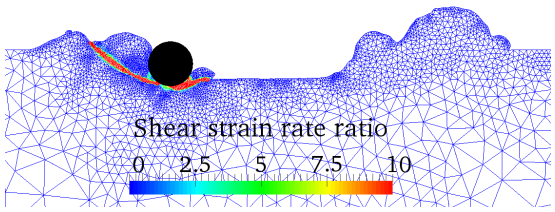

(c) sweep 3 (→), right extremity

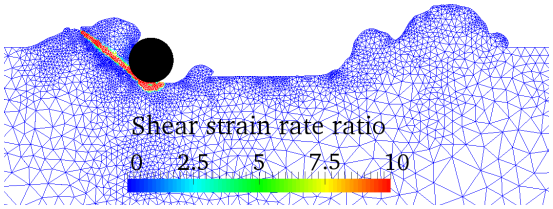

(d) sweep 5 (→), left extremity

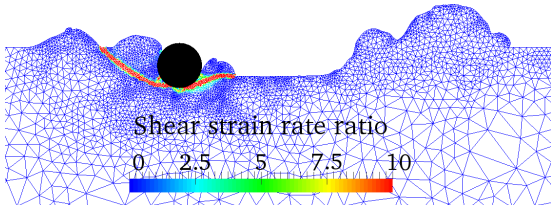

(e) sweep 5 (→), right extremity

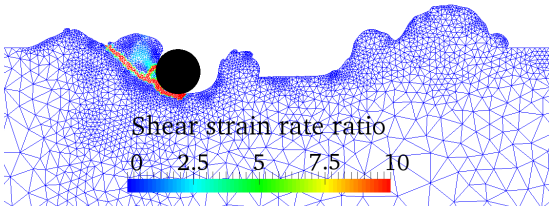

(f) sweep 11 (→), left extremity

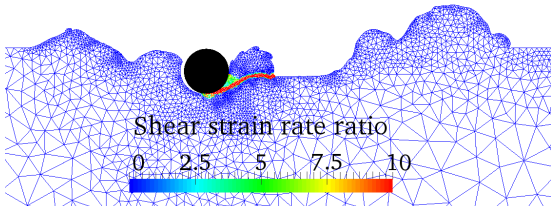

(g) sweep 11 (→), right extremity

Figure 7.20 Soil failure mechanisms (showing $\dot{\gamma}_{max}D/v_p$) during Test E

Figures 7.21a and 7.21b show the distribution of the softening factor at the end of sweeps 2 and 11 in Test E. The softening factor within the right soil berm exhibits very limited change between the two figures, revealing the reliability of SLA in dealing with remeshing and interpolation of field variables, since no shearing takes place in this region after sweep 2. Of interest in Figure 7.21b is that the region experiencing the largest softening effect is within the berm at the left side of the pipe, rather than the one created by the rightward encroaching motions. This can be explained by the mechanisms shown in

Figures 7.20a-f, where shear deformations always take place on the left side of the pipe whatever the loading direction is.

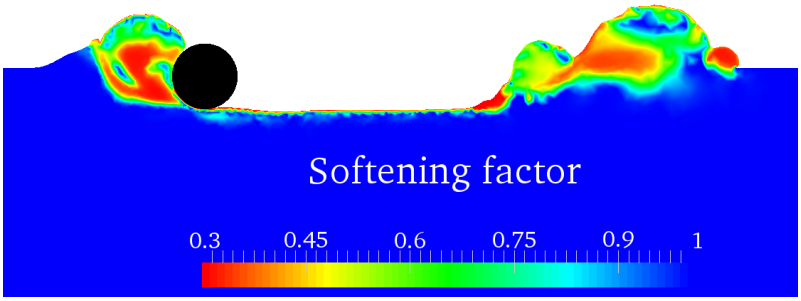

(a) sweep 2 (←), left extremity

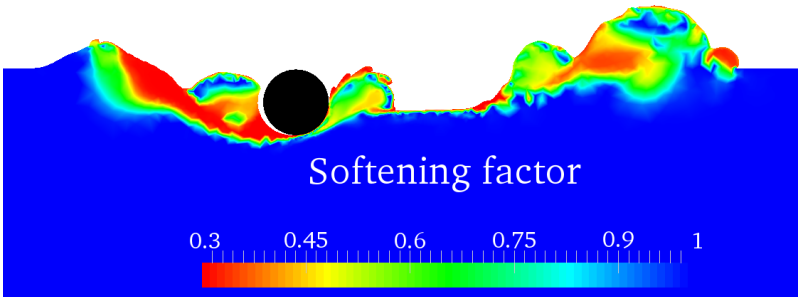

(b) sweep 11 (→), left extremity

Figure 7.21 Softening factor in Test E

7.2.4 Discussion

The centrifuge/numerical tests illustrated in Table 7.2 cannot be directly compared to provide a parametric study. Taking Test A, Test B and Test C for example, the vertical loads during sweep 3 are the same in the three tests, which means the influence of the vertical loading history (during sweeps 1 and 2) can be examined for comparison. However, apart from the vertical loads, the initial pipe embedments and the amplitudes of lateral displacement are also different in these tests. For comparison of these tests, auxiliary numerical tests have to be performed. Section 7.2.4.1 presents a brief parametric study on the influence of initial embedment and lateral displacement amplitude on the pipe behaviour. The vertical loading history in this study is the same as that of Test A. This serves as a basis for the study presented in Section 7.2.4.2, where the influence of vertical loading history on the pipe behaviour is briefly discussed. The displacement sequence applied to the pipe for the tests presented in Section 7.2.4.2 is the same as that of Test B.

7.2.4.1 Effect of lateral displacement history

For the results presented in this section, the horizontal position where the lateral loading direction is reversed are u_r and u_l for sweep 1 and sweep 2 respectively. The constant vertical load representing the unit pipe weight at the i^{th} sweep is denoted by V_i.

Figure 7.22 illustrates the influence of u_r/D on the pipe response. Four values of u_r/D, 2.0, 4.0, 6.0 and 8.0 are considered, with u_l/D kept constant at 1. When the pipe motion is reversed from the rightmost position of sweep 1, it takes about one diameter for the resistance curve to reach a relatively stable value, as shown in Figure 7.22b. The case with $u_r/D = 2$ cannot achieve a stable resistance since the travel distance in sweep 2 is too short. For the remaining cases, all the resistance curves show a very similar trend. After the pipe motion is reversed again and sweep 3 begins, the resistances for all the four cases keep increasing during the initial travel distance of about one pipe diameter, as the pipe dives deeper into the soil (see Figure 7.22a), and then reach very close residual values. As the pipe approaches the dormant berm left by sweep 1, a peak in lateral resistance can be seen for all the cases as expected. After that, the resistances drop to new residual values which vary for each case and show a trend of increasing slightly with u_r. Note that the vertical load is reduced for sweep 3 compared with sweep 1, so the residual resistance is lower.

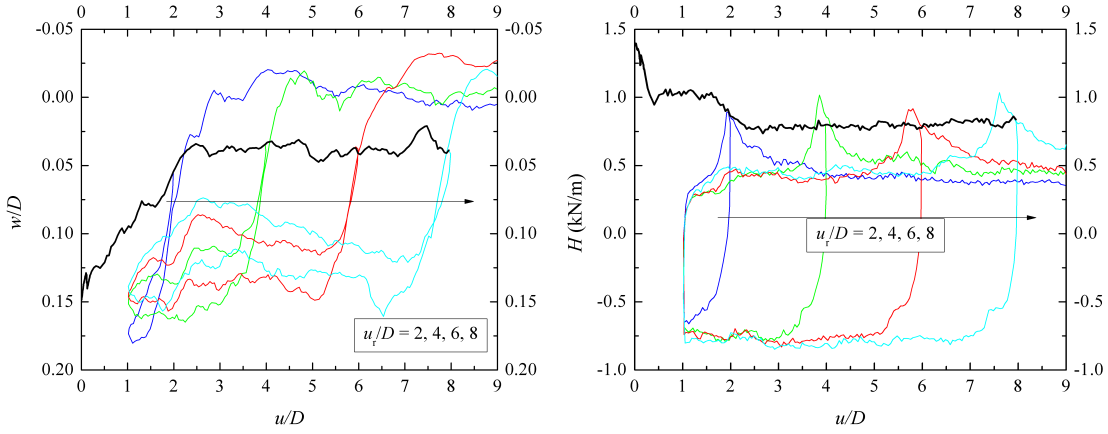

(a) Invert trajectory (b) Lateral resistance

Figure 7.22 Effect of u_r on cyclic lateral loading. $V_1 = V_2 = 2.05$ kN/m, $V_3 = 1.25$ kN/m.

Figure 7.23 shows the effect of initial embedment, which in general diminishes with the lateral distance travelled. During sweep 1, the pipe with deeper w_{ini} finally ends up with

higher elevation (less embedment) but slightly larger resistance, indicating a bigger size of active berm ahead of the pipe. The resistances obtained from both cases are extremely close during the residual stage of sweeps 2 and 3 within the displacement range of $2D$ to $6D$. Very satisfactory agreement between the two cases can be noted even in the initial part of sweep 2, where drastic changes in both soil resistance and pipe embedment can be observed. The peak resistance near the end of sweep 3, where the pipe pushes into the dormant berm from sweep 1, increases with w_{ini} due to the bigger size of soil berm created by previous sweeps.

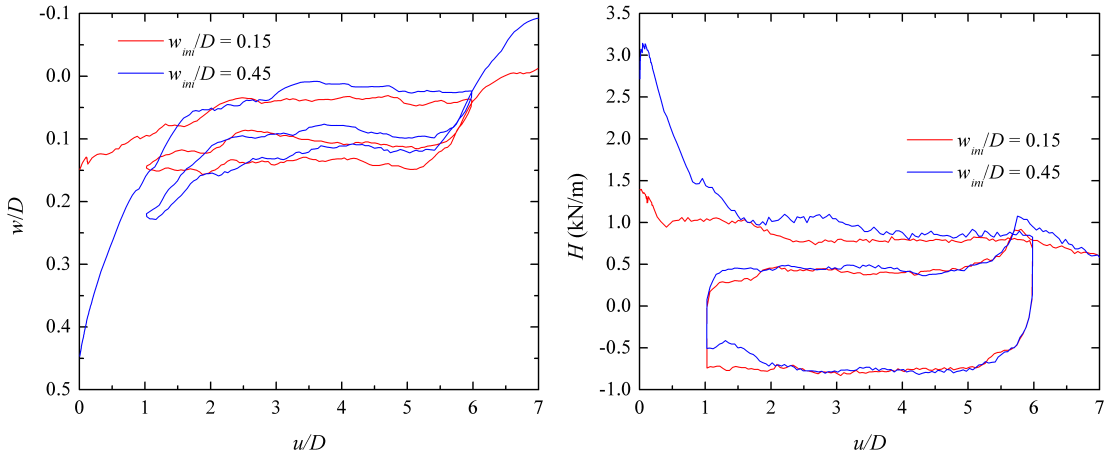

(a) Invert trajectory (b) Lateral resistance

Figure 7.23 Effect of initial pipe embedment on cyclic lateral loading. $V_1 = V_2 = 2.05$ kN/m, $V_3 = 1.25$ kN/m.

7.2.4.2 Effect of vertical loading history

This section presents a brief study on the influence of the vertical loading history on the pipe behaviour during sweep 3. The displacement sequence applied to the pipe was the same as that of Test B in Table 7.2. Two different conditions are considered by choosing V_3 to be the smallest (over-penetrated) or largest (normally-penetrated) value during all sweeps (V_1, V_2 and V_3). The values of V_i were chosen according to those have been adopted in centrifuge Tests A-C (see Table 7.2), and are presented in Table 7.3.

Figure 7.24 shows the influence of vertical load on the response of a pipe subject to one cycle of lateral motion. The lateral resistance in the second sweep is lower than that in the first for all the cases, due to the fact that the berm beside the pipe in sweep 1, created

Table 7.3 Parameters used for investigating the influence of pipe weight

Pipe type	$V_1 = V_2$: kN/m	V_3: kN/m
Over-penetrated	1.25	1.25
	2.05	1.25
	3.00	1.25
	4.05	1.25
Normally-penetrated	1.25	4.05
	2.05	4.05
	3.00	4.05
	4.05	4.05

by the pushed-in-place installation process, is absent in sweep 2. This also leads to an increase in pipe embedment since the pipe has to embed deeper to gain enough vertical resistance to support its weight.

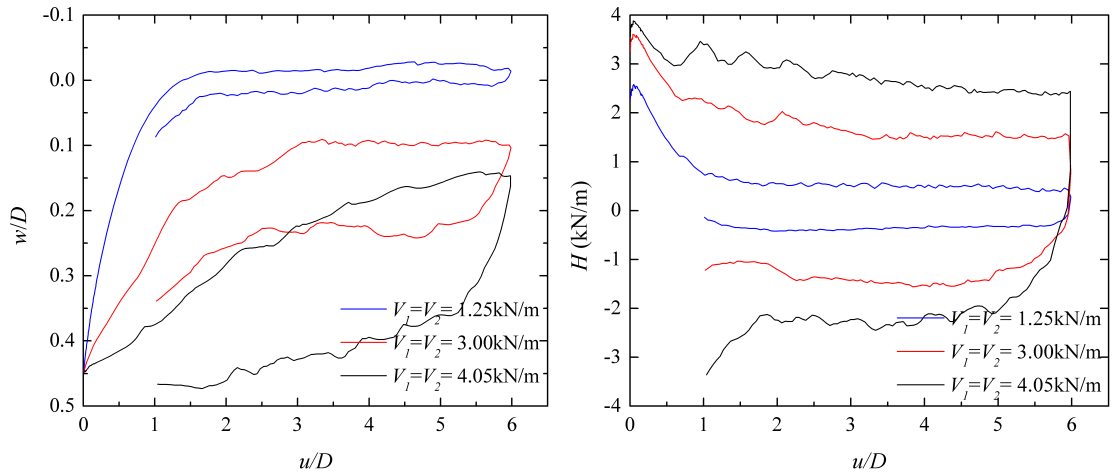

(a) Invert trajectory (b) Lateral resistance

Figure 7.24 Effect of current pipe weight on cyclic lateral loading during sweeps 1-2

The vertical load not only influences the current behaviour of the pipe, but may also affect the subsequent behaviour due to the change in soil geometry and strength. Figures 7.25 and 7.26 illustrate how the vertical load during sweeps 1-2 affects the pipe behaviour during sweep 3, which may involve a change of vertical load in each case. Figure 7.25 shows the results of the over-penetrated case. It is found that the soil resistances during the plateau stage for all four loading cases are very close, indicating limited influence of the previous vertical load on the current vertical load, even considering that current pipe embedments vary over a wide range. As the pipe approaches and pushes into the dormant berm, the corresponding peak and residual resistance both increase with the largest previous/historical vertical load V_{pre} due to the larger size of berm ahead of the

pipe. Similar observations can be made in Figure 7.26. Exceptions are that the pipe in the normally-penetrated condition does not reach such a stable state during sweep 3, and a drop in resistance after encountering the dormant berm is not obvious.

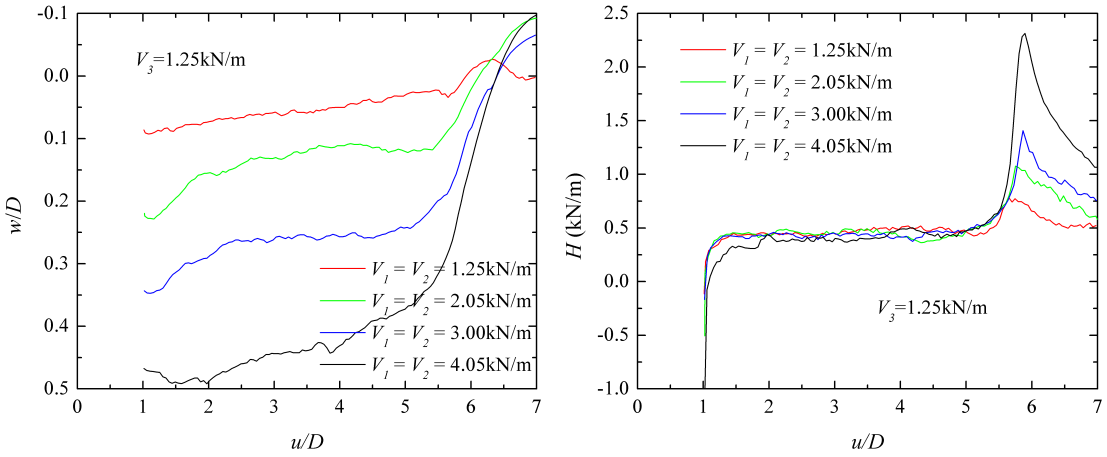

(a) Invert trajectory (b) Lateral resistance

Figure 7.25 Effect of previous pipe weight on cyclic lateral loading during sweep 3: over-penetrated

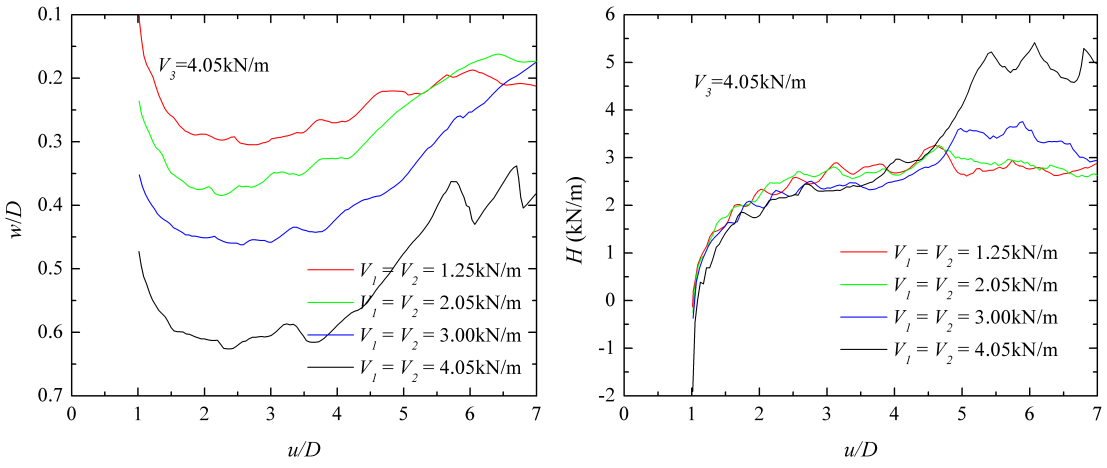

(a) Invert trajectory (b) Lateral resistance

Figure 7.26 Effect of previous pipe weight on cyclic lateral loading during sweep 3: normally-penetrated

Figure 7.27 shows a direct comparison of Tests A and C (see Table 7.2) during sweep 3, where both w_{ini} and V_{pre} (V_1 and V_2) vary in a wide range. Reasonably good agreement can still be observed between the two cases in invert trajectory as well as lateral resistance.

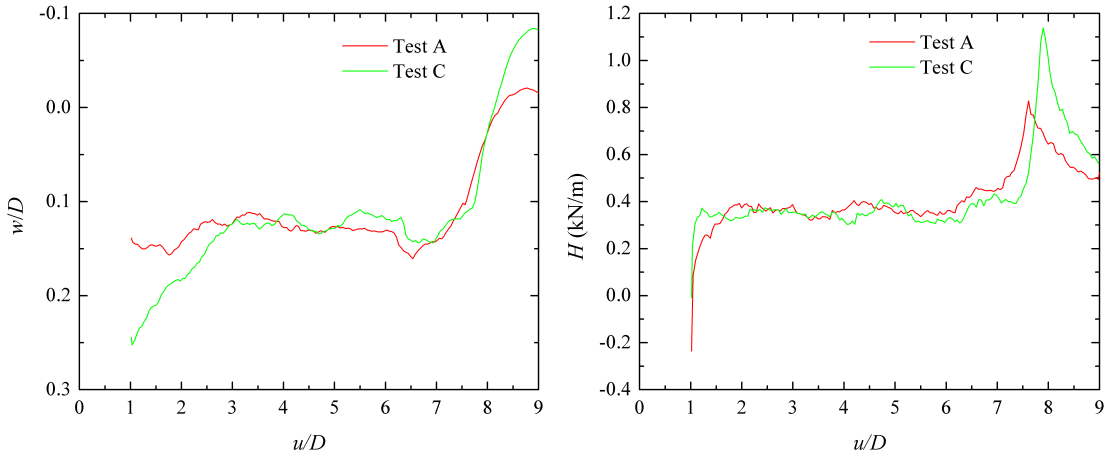

(a) Invert trajectory (b) Lateral resistance

Figure 7.27 Direct comparisons between SLA simulations of Test A and Test C during sweep 3

7.3 Numerical parametric study

In this parametric study, the pipe was laterally displaced by $3D$ after being penetrated to a required depth w_{ini}, then subjected to several (0-3) cycles between the horizontal positions of $1D$ and $3D$. After that, another large cycle of motion was imposed to push the pipe across/over the soil berm created by the preceding sweeps, to a farthest position of $6D$. In some cases the pipe was finally reversed to $-1D$. The complete lateral displacement history of the pipe is illustrated in Figure 7.28. The annotations, p1, p2, ..., denote positions where yield envelopes were derived. The default pipe and soil parameters are the same as those used in Chapter 6, as given in Table 6.1. The results are presented in normalised form and thus can be generalized to other combinations of parameters.

7.3.1 Typical results

Figures 7.29a and 7.29b show the lateral loading response in a typical analysis. As illustrated in Figure 7.29a, the pipe moves upward and reaches a relatively stable elevation during sweep 1, then ploughs quickly into the soil immediately after the motion is reversed. Obvious downward motion occurs each time the motion is reversed at the extremity points, while upward motion occurs when the pipe approaches the soil berm at righthand side created by preceding sweeps. After three cycles of loading, the greatest rebound in elevation

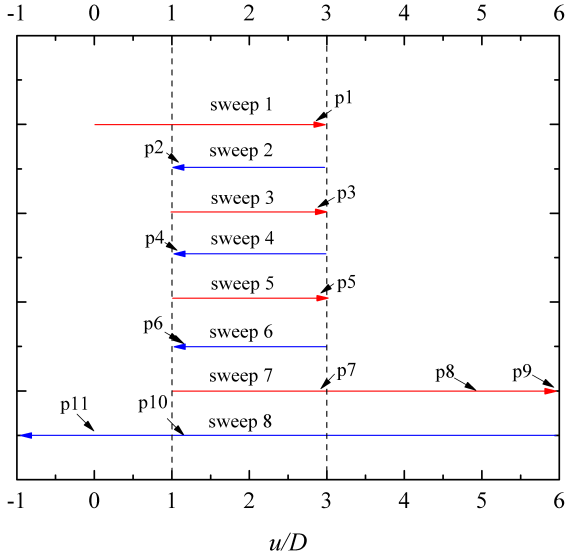

Figure 7.28 Complete sequence of lateral sweeps in parametric study

is achieved during sweep 7 when the pipe moves towards and into the predominant soil berm. As depicted in Figure 7.29b, the largest soil resistance is mobilised at the initial breakout stage. After that, a peak value in the lateral resistance for each sweep can be observed near the end of the sweep, where the pipe approaches the soil berm. This peak value is found to increase greatly with the number of loading cycles, as the pipe penetrates more deeply. When the pipe rises up through intact soil and into the accumulated berm during sweep 7, a sharp drop in lateral resistance can be observed.

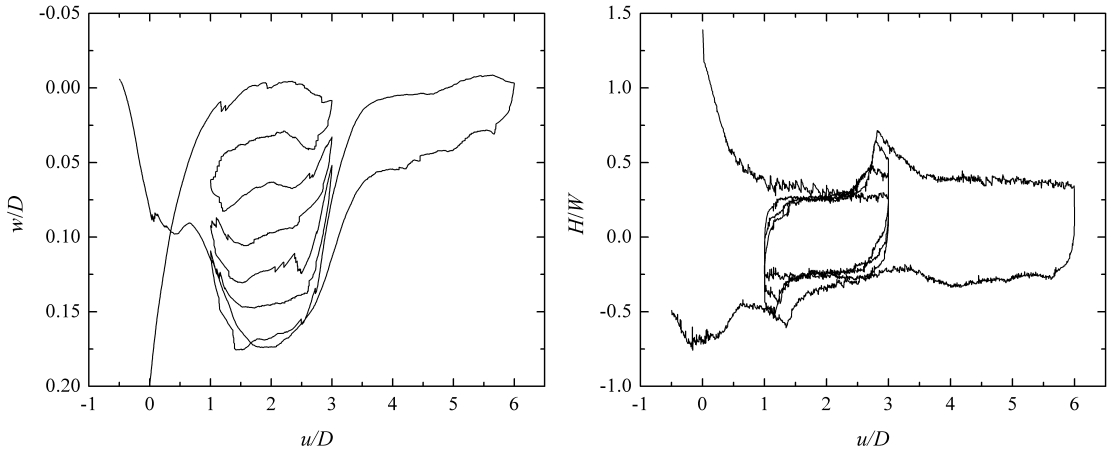

(a) Invert trajectory (b) Equivalent friction factor

Figure 7.29 Invert trajectory and 'friction' factor for base case. $W/Ds_{um} = 1.0$, $\delta_{rem} = 0.3$, $\xi_{95} = 10$, $kD/s_{um} = 2$.

Figure 7.30 shows the evolution of the yield envelope of the pipe during the cyclic loading. The positions where these yield envelopes were evaluated are illustrated in Figure 7.28 (p1, p2, ...). Every time the loading cycle is repeated, the yield surface expands towards the direction of the pipe motion. According to these envelopes, the lateral resistance of the pipe at the extremity points can be enlarged by a factor of about 2-3 over three cycles of loading. This confirms the findings in Figure 7.29b.

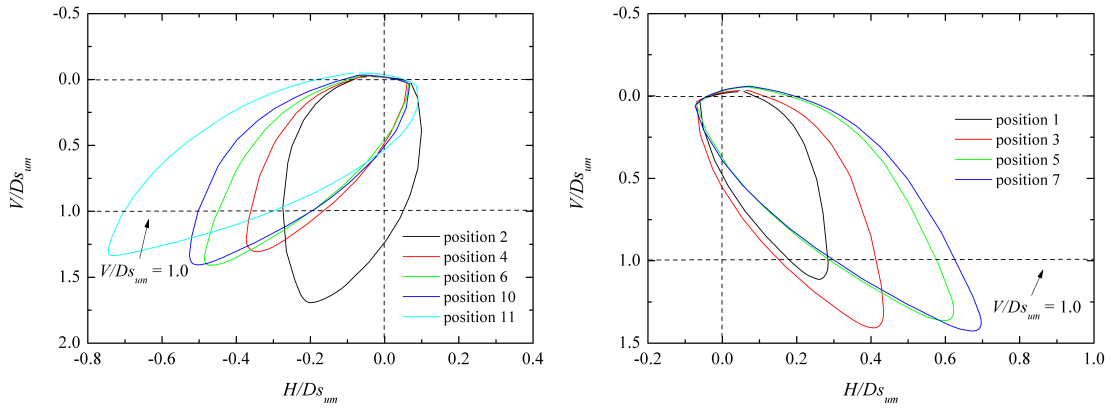

(a) Left extremity (b) Right extremity

Figure 7.30 Yield envelopes at extremity points during cyclic lateral loading. $W/Ds_{um} = 1.0$, $w_{ini}/D = 0.2$, $\delta_{rem} = 0.3$, $\xi_{95} = 10$, $kD/s_{um} = 2$.

7.3.2 Effect of pipe weight

Figure 7.31 shows the response of the pipe under different levels of vertical load. As expected, heavier pipes achieve deeper embedment as well as higher lateral resistance throughout the loading process. However, it is interesting to find that the pipe with normalised weight (W/Ds_{um}) of 2 exhibits a trend of turning into a heavy one after three cycles of motion, with its embedment approaching half a pipe diameter (see Figure 7.31a). This level of vertical load is categorised as very light as discussed in Chapter 6, where the parametric study has the same default soil and pipe parameters as used in this section.

7.3.3 Effect of initial pipe embedment

Figure 7.32 confirms the general expectation that the influence of the initial pipe embedment diminishes with the lateral traveling distance of the pipe. All the resistance

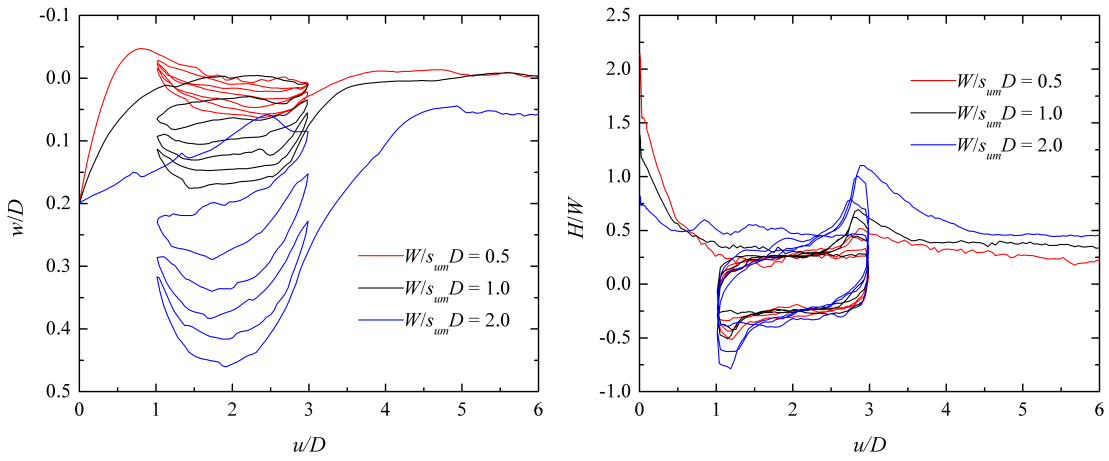

(a) Invert trajectory (b) Equivalent friction factor

Figure 7.31 Effect of pipe weight on cyclic lateral loading. $\delta_{rem} = 0.3$, $\xi_{95} = 10$, $kD/s_{um} = 2$.

curves corresponding to a given pipe weight almost converge after the first reversal point, indicating that initial embedment has a very small influence on the behaviour of pipes under large cyclic lateral movements. After the pipe finally passes the berm created by previous sweeps (1-6), the residual resistances also show some convergence. Exceptions can be found in Figure 7.32b where the curve corresponding to $w_{ini}/D = 0.4$ is moderately higher than the other two converged curves. The same observations cannot be made in Figure 7.32d, which may indicate that a heavier pipe weight helps to achieve a converged stable state for the pipe.

7.3.4 Effect of lateral displacement

Figure 7.33 shows the influence of cyclic lateral displacement history on the pipe behaviour. The number of loading cycles between the lateral positions of $1D$ and $3D$ is chosen to be in the range 0 to 3 here. Three types of soil, homogeneous without softening ($kD/s_{um} = 0$ and $\delta_{rem} = 1.0$), homogeneous with softening ($kD/s_{um} = 0$ and $\delta_{rem} = 0.3$) and non-homogeneous with softening ($kD/s_{um} = 2$ and $\delta_{rem} = 0.3$), are presented. The first case is chosen to ensure that the loading history only has an effect on the boundary geometry of the model.

For all the cases considered here, the peak lateral resistance and the subsequent residual resistance, as the pipe approaches and scrapes over the dormant berm (at $3D$), increase

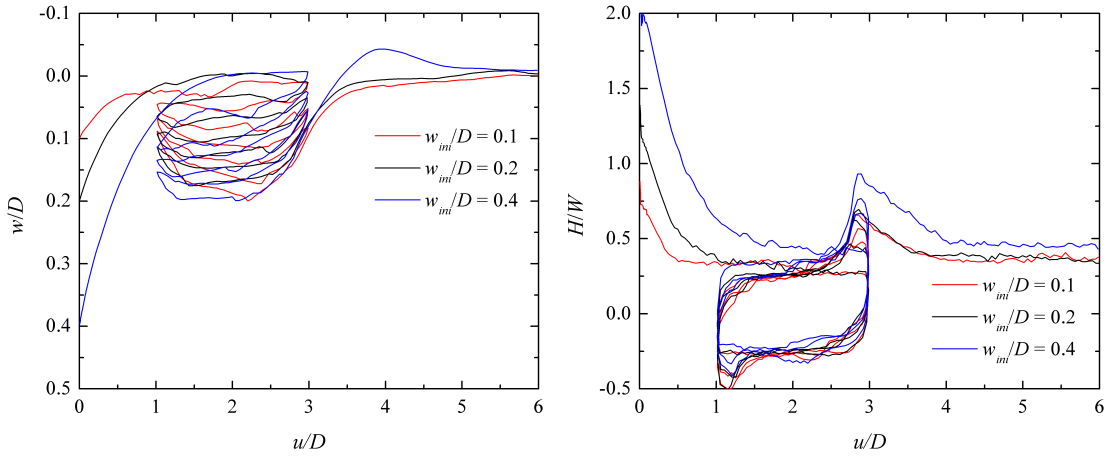

(a) $W/Ds_{um} = 1.0$: invert trajectory

(b) $W/Ds_{um} = 1.0$: equivalent friction factor

(c) $W/Ds_{um} = 2.0$: invert trajectory

(d) $W/Ds_{um} = 2.0$: equivalent friction factor

Figure 7.32 Effect of initial pipe embedment on cyclic lateral loading. $\delta_{rem} = 0.3$, $\xi_{95} = 10$, $kD/s_{um} = 2$.

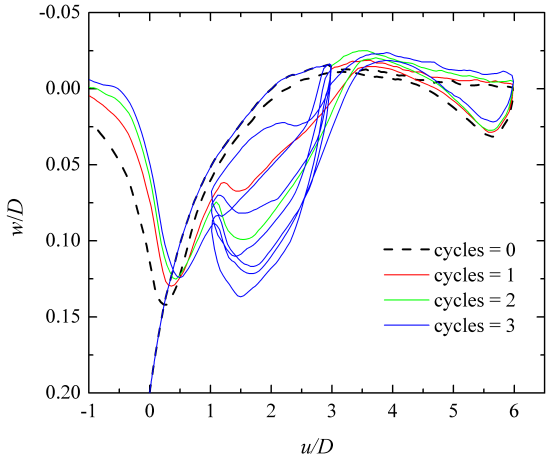

(a) $kD/s_{um} = 0$ and $\delta_{rem} = 1.0$: w/D

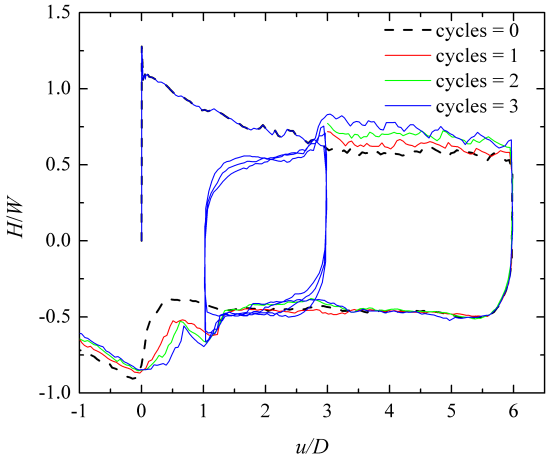

(b) $kD/s_{um} = 0$ and $\delta_{rem} = 1.0$: H/W

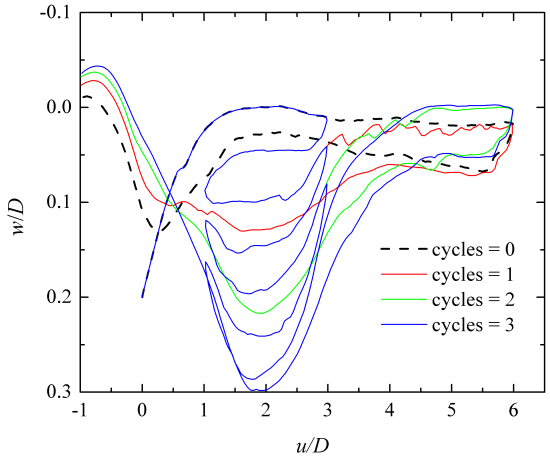

(c) $kD/s_{um} = 0$ and $\delta_{rem} = 0.3$: w/D

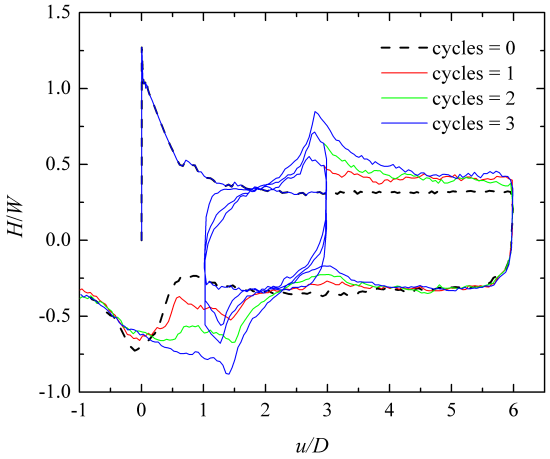

(d) $kD/s_{um} = 0$ and $\delta_{rem} = 0.3$: H/W

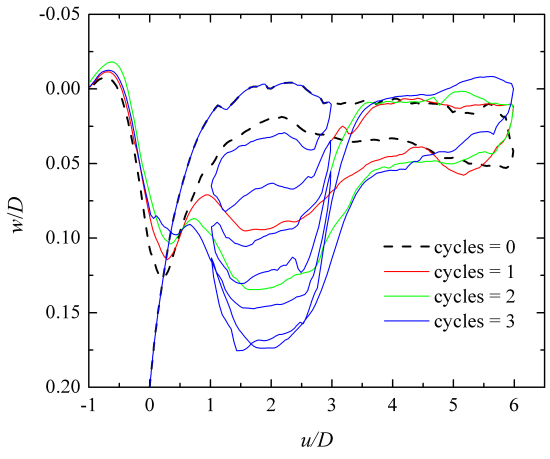

(e) $kD/s_{um} = 2$ and $\delta_{rem} = 0.3$: w/D

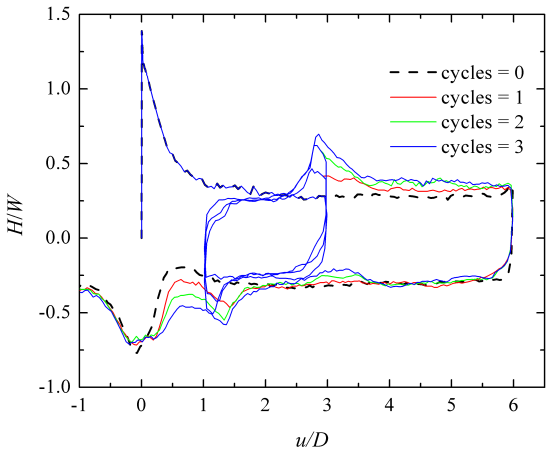

(f) $kD/s_{um} = 2$ and $\delta_{rem} = 0.3$: H/W

Figure 7.33 Effect of displacement history on cyclic lateral loading. $W/Ds_{um} = 1.0$, $\xi_{95} = 10$.

with the number of previous loading cycles (between $1D$ and $3D$). This behaviour is more pronounced when strain softening has been taken into account. When the pipe motion is reversed from the rightmost extremity (at $6D$), the resistance curves almost coincide, indicating very limited influence of the displacement history on the pipe behaviour during the current sweep. This residual behaviour ceases when the pipe reaches a lateral displacement of about $3.5D$, which might well be attributable to the collection of the dormant berm (at $3D$) by the active berm. Again, when the pipe approaches the leftmost dormant berm (at $0D$) during the last sweep, the peak and the following residual resistances increase considerably with the number of previous cycles. After the pipe has travelled over this berm, a sharp drop of resistance is observed, and the resistance curves start to converge.

7.3.5 Effect of soil strength gradient

Figure 7.34 shows the influence of strength gradient on the behaviour of the pipe. As expected, the embedment of the pipe decreases considerably with increasing kD/s_{um}. The pipe in the soil with $kD/s_{um} = 0$ gains an embedment almost two times that in the soil with $kD/s_{um} = 2$. As a result, higher lateral resistance can be achieved by the pipe in the soil with smaller kD/s_{um}.

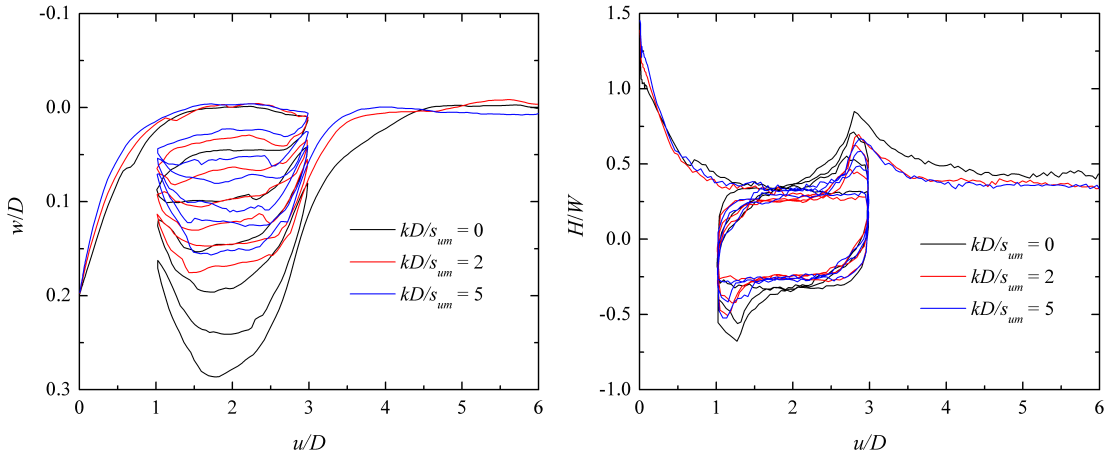

(a) Invert trajectory (b) Equivalent friction factor

Figure 7.34 Effect of soil strength gradient on cyclic lateral loading. $W/Ds_{um} = 1.0$, $\delta_{rem} = 0.3$, $\xi_{95} = 10$.

7.3.6 Effect of strain softening

Figure 7.35 shows how the remoulded strength ratio δ_{rem} influences pipe embedment as well as lateral resistance during the cyclic loading. Considerable accumulated embedment can be gained by the pipe with $W/Ds_{um} = 2$ if strain softening is taken into account. Compared with the monotonic loading results discussed in Section 6.4, the effect of strain softening becomes much more significant when the pipe moves back to plough across the scraped soil surface created by the preceding lateral sweep. Due to the accumulation of pipe embedment, the lateral soil resistance increases greatly with further loading cycles. This behaviour is less pronounced in the ideal soil case with no softening ($\delta_{rem} = 1.0$).

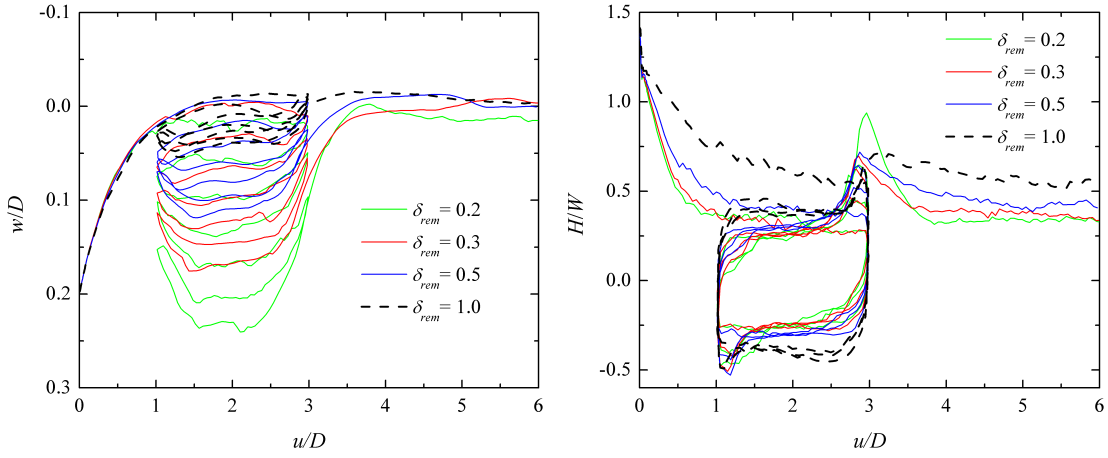

(a) $W/Ds_{um} = 1.0$: invert trajectory

(b) $W/Ds_{um} = 1.0$: equivalent friction factor

(c) $W/Ds_{um} = 2.0$: invert trajectory

(d) $W/Ds_{um} = 2.0$: equivalent friction factor

Figure 7.35 Effect of remoulded strength ratio on cyclic lateral loading. $\xi_{95} = 10$, $kD/s_{um} = 2$.

Figure 7.36 shows that the ductility parameter ξ_{95} of the soil hardly affects the lateral resistance after the first reversal point under cyclic loading conditions, if the value of ξ_{95} is chosen within the recommended range of 10-50 (Randolph, 2004). However, the rate at which the pipe embedment develops is found to decrease with increasing ξ_{95}.

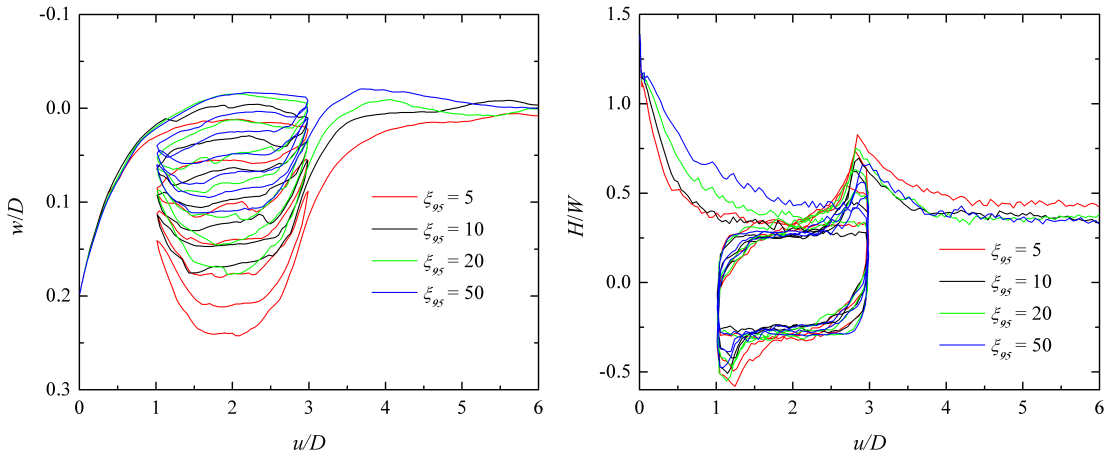

(a) Invert trajectory (b) Equivalent friction factor

Figure 7.36 Effect of ductility parameter on cyclic lateral loading. $W/Ds_{um} = 1.0$, $\delta_{rem} = 0.3$, $kD/s_{um} = 2$.

7.4 Summary

This chapter has presented a numerical study using SLA, principally to explore lateral pipe-soil interactions under cyclic movements, and to assist the development of force resultant plasticity models. The numerical model considers the remoulding effect of the soil around the pipe caused by large strains. Validation studies, involving comparisons with centrifuge model test results, were performed, followed by a brief parametric study that provided insights into the influence of loading history and soil strength properties on the pipe-soil interactions. During the analyses, the pipe was displaced by up to eight pipe diameters and for several cycles of motion. Yield envelopes, as well as displacement trajectories and lateral resistance, for the pipe at different loading stages were derived to provide a comprehensive understanding for large cyclic movements. The main findings of the study were:

- The merging of an active berm into a pre-existing berm during the cyclic loading was satisfactorily modelled by the SLA approach. Very good agreement between numerical modelling and centrifuge results, for several different loading cases, was achieved, even given very complex loading histories in the pipe model tests. The prediction of the residual response of the pipe was very satisfactory. The increase in soil resistance as the pipe approaches a pre-existing berm, and the drop in resistance when the pipe scrapes over or moves away from the berm, was also accurately captured.

- The SLA method does not appear to appropriately model the pipe response following a short period of consolidation. This was highlighted by the mismatch between the peak response observed in centrifuge tests and that from the SLA calculations. This peak response is attributed to the soil suction at the pipe rear as well as the soil strength enhancement due to consolidation. The SLA is not able to deal with the tensile capacity of the pipe-soil interface for large deformation analyses and consolidation of the soil is beyond the scope of this research. Therefore, the break-out pipe-soil response, both at the beginning of initial sweep and at each subsequent sweep after consolidation, cannot be accurately replicated by the SLA model.

- The loading history (displacement and load) appears to have very limited influence on the pipe resistance during the subsequent motions. The effects of loading history on the soil-interactions only became significant when the pipe moved towards an extremity point, berm or trench, left by previous sweeps.

Chapter 8

Conclusions

8.1 Introduction

This thesis reports a computational study exploring the interactions between untrenched subsea pipelines and undrained clay, with the aim of gaining insights into the behaviour of pipelines that undergo lateral buckling. A novel numerical technique based on the sequential limit analysis (SLA) has been developed, providing the tool to enable an extensive set of parametric studies to be completed. This method was chosen because of the high computing efficiency of limit analysis in solving plasticity problems. The following sections outline the major contributions that have been made in the work as well as recommendations for further research.

8.2 Original contributions

This thesis has made the following contributions to knowledge:

8.2.1 Methodology

- This is the first attempt to apply sequential limit analysis as a method for solving large deformation problems involving soil-structure interactions. The SLA method has been previously used to explore relatively simple structural problems, such as frames and plates (e.g. Yang, 1993, Raithatha and Duncan, 2008), where no contact or interface conditions need to be handled. The thesis describes how to extend the SLA method to deal with the updating of model geometry and material properties in

the context of a two dimensional (plane strain) continuum analysis, using the finite element limit analysis (FELA) software Oxlim (Makrodimopoulos and Martin, 2006, 2007, 2008) as the core solver.

- The commonly used coupled Eulerian-Lagrangian (CEL) method, as implemented in Abaqus, was employed as a complementary tool to demonstrate the robustness of SLA in dealing with changes to model geometry and field variables through a series of comparisons. The constitutive model used in the SLA method was implemented into the CEL model via a user subroutine VUMAT to ensure comparability of results.

- A detailed benchmarking study has shown that the SLA model generates robust solutions by comparison with known plasticity solutions. In conjunction with an appropriately chosen soil constitutive model (Einav and Randolph, 2005) it also captures appropriate pipe-soil interaction behaviour on undrained clay (e.g. strain rate and strain softening effects), and can achieve good comparisons with centrifuge model test data (Table 4.7). The benchmarking study also demonstrated the capability of the SLA approach to simulate monotonic and cyclic pipe-soil interactions under large-amplitude vertical and lateral movements.

8.2.2 Vertical pipe-soil interaction

- The effect of remoulding on soil strength was found to have a very significant influence on the vertical resistance experienced by a pipe during penetration. The soil failure mechanism transitions from a global mechanism at shallow embedment to a fully localised mechanism at deep embedment. The localised failure mechanism occurs more quickly if strain softening effects are accounted for; and when a localised mechanism is induced, strain softening effects result in more reduction in soil resistance compared with that at shallow embedment.

- A new approach (Equations 5.12 to 5.16) for evaluating the vertical resistance of a pipe during penetration was proposed, based on the results of an extensive parametric study. The geotechnical resistance in ideal weightless soil is first calculated, taking

account of the effect of pipe interface roughness, α, and soil strength gradient, k. Then the change of soil strength caused by strain softening and strain rate effects is considered, leading to a modification of the initial soil strength to an 'operative shear strength'. Soil buoyancy is included in the last step to produce the total soil resistance. Comparisons between the predictions made using this approach and numerical simulations demonstrate that this model satisfactorily quantifies the different and competing effects.

8.2.3 Lateral pipe-soil interaction

- An extensive parametric study led to the development of empirical equations (Equations 6.6 to 6.9) for evaluation of the lateral soil resistance experienced by a pipe during the steady-state residual stage (H_{res}) of a large lateral displacement. The influence of a range of parameters on H_{res} was quantified; including pipe weight, initial pipe embedment, soil strength gradient, soil unit weight and finally strain softening effects.

- Lower and upper bound estimates for the critical pipe weight, W_{cri}, differentiating light pipe behaviour from heavy pipe behavior, were derived (Equations 6.4 and 6.5). A pipe with weight above the upper bound value will exhibit heavy (diving) behaviour while a pipe with weight below the lower bound value will eventually exhibit light behaviour, and reach a steady residual stage. The effects of strain softening and strain rate were examined and found to have limited influence in determining pipe behaviour, if parameter values within the typical range are adopted. These equations can be used to assess the likely pipe behaviour type during early stage design.

- At the breakout stage of lateral loading, the absence of tensile capacity at the pipe-soil interface leads to a lower bound on the breakout resistance for the pipe, as expected. When full tension capacity is allowed, the breakout resistance typically increases by about 50%.

- This thesis has explored the evolution of the $V-H$ yield envelope for the pipe during lateral movement, accounting for geometry changes and strength remoulding effects. Previous work that has explored the lateral loading response of a pipe has assumed that either the vertical load or the vertical position of the pipe remains constant. These envelopes add to the understanding of the pipe-soil interaction when a change of vertical load occurs, adding to the database that can be used for developing macro-element models for pipelines on clay.

- A detailed numerical study of the cyclic loading behaviour for a pipe subjected to large-amplitude lateral movements on undrained clay has been conducted. The merging of an active berm into a pre-existing berm during the cyclic loading appeared to be satisfactorily modelled by the SLA approach. Very good agreement between numerical modelling and centrifuge model test results, for several different loading cases, was achieved, even given very complex loading histories in the model tests. The increase in soil resistance as the pipe approaches a pre-existing berm, and the drop in resistance as the pipe scrapes over or moves past a berm, was also accurately captured. The loading history was found to have very limited influence on the pipe resistance during subsequent motions. The effects of loading history on the pipe-soil interactions only became significant when the pipe moved towards an extremity point, either a berm or a trench, left by the previous sweeping motions. The evolution of soil failure mechanism and $V-H$ yield envelope has been presented to assist the development of macro-element plasticity models.

8.3 Recommendations for future research

This thesis has, for the first time, illustrated the capability of the SLA method to model continuum soil-structure problems involving large deformations and strains. This approach was successfully applied to the analysis of offshore pipelines on soft undrained clay under both monotonic and cyclic loading, for both vertical and lateral loading conditions.

However, there is still room for further improvements and future research. The limitations of this study, together with recommendations for future work, are presented here.

8.3.1 Analysis of offshore pipelines

- In the analyses concerning pipe-soil interaction after installation, the pipe was assumed to be pushed into the soil to the desired depth. In reality the pipeline is laid in a dynamic manner with both horizontal and vertical oscillations, which cause the soil to experience much more accumulated strain than for the purely vertical, monotonically pushed-in process. Therefore the numerical analysis in this thesis has largely underestimated the remoulding effect caused by strain softening during initial laydown; that is, the real pipe embedment at a given vertical load should be greater than the numerical results obtained from pushed-in penetration. Although this thesis has demonstrated the capability of SLA for modeling the accumulated vertical settlements induced by cyclic loading, detailed study is needed to explore this issue further. The range of the dynamic lay effect parameter, f_{dyn}, should be further assessed based on the results of a parametric study.

- A brief study on the cyclic vertical loading behaviour of a pipeline has been presented and the results agree very satisfactorily with centrifuge model test data. However a further and more detailed parametric study is needed to assist the development of a hysteretic macro-element pipe-soil model that can be used to predict the pipe embedment in the context of 3D problems such as steel catenary riser analysis.

- The consolidation of the soil has been neglected in this thesis since SLA is unable to deal directly with such behaviour. Validation against centrifuge model testing shows that the strength enhancement caused by consolidation could have a significant influence on the pipe-soil interactions at the break-out stage. For accurate assessment of the peak lateral resistance during pipe movements, consolidation should be accounted for by using a combination of numerical approaches.

- Cyclic lateral displacement analyses should be performed to investigate the pipe response for longer sequences of cycles, as offshore on-bottom pipelines might undergo lateral displacements of up to 10 or 20D, for up to 1000 cycles over their lifetime.

- Most of the current research on lateral pipe-soil interaction assumes that the pipe experiences either a constant vertical load or a constant vertical elevation, which neglects the global response along a length of pipeline. A 3D model that takes into account the global response would be useful to provide valuable information on the lateral buckling behavior of pipelines, particularly the loading and displacement paths at different cross-sections within a lateral buckle. Considering the tremendous computational cost related to a full 3D numerical model, analyses using a 3D pipeline model with a series of '2D' soil slices would be more attractive and practical. Such a numerical model using the CEL method has been demonstrated by Martin *et al.* (2013) and proven to be viable. This promising idea is still at an early stage, but further studies using this model or a similar approach would provide greater insight into the behaviour of offshore pipelines undergoing thermally-induced lateral buckling.

8.3.2 Improvement and further application of the SLA method

- The typical incremental displacement used to update the model configuration in the studies presented in this thesis was 0.5% of the pipe diameter. Although this time step yielded reliable results for the problems investigated, adopting a smaller value is still more tempting and theoretically correct. However this will lead to a greater number of analyses that must be completed for a single problem. The additional computational cost related to remeshing, along with the potential for cumulative error of the field variables, might be large and perhaps not viable. One practical way might be to remesh only around the vicinity of the pipe, leaving the remainder of the domain untouched. The treatment of field variables is likely to be more accurate

and the sequence of analyses will be processed in a more efficient manner. As a consequence the finer mesh may be able to yield more accurate results.

- The adaptive remeshing strategy used for the SLA modelling in this thesis depends to an extent on the experience of the user. The generalisation of this method to other geotechnical problems calls for a more robust remeshing strategy, such as that used by Martin (2011). This approach relies on developing a relationship between the target element size (i.e. mesh density) and the shear strain rate within a given deforming region. More refined meshes are produced in areas that experience very high shear strain rates.

- The SLA approach in this thesis was mainly used to analyse pipe-soil interactions for surface pipelines on clay, and also for the modelling of buried pipelines. The penetration and extraction behaviour of shallow foundations, which can often be idealised as plane-strain problems, can also be explored using this method. By extending the software to the axi-symmetric case, the approach could be readily applied to other problems, such as the penetration and extraction behavior of a ball penetrometer or spudcan footing.

- Although the core solver used in the SLA model is OxLim, the method developed and applied in this thesis can be readily generalised to other FELA software.

References

Abadalla, B., Pike, K., Eltaher, A., Jukes, P., and Duron, B. (2009). Development and validation of a coupled eulerian lagrangian finite element ice scour model. In *Proceedings of the ASME 28th International Conference on Ocean, Offshore and Arctic Engineering*, volume OMAE2009-79553, Honolulu, Hawaii.

Almeida, M. S. S., Costa, A. M., Amaral, C. S., Benjamin, A. C., Noronha Jr, D. B., Futai, M. M., and Mello, J. R. (2001). Pipeline failure on very soft clay. In *Proceedings of the 3rd International Conference on Soft Soil Engineering*, pages 131–138, Balkema, Hong Kong.

Andresen, L. and Khoa, H. D. V. (2013). *LDFE analysis of installation effects for offshore anchors and foundations*. Installation Effects in Geotechnical Engineering. Taylor & Francis Group, London.

Ansari, Y., Kouretzis, G. P., and Sheng, D. (2014). An effective stress analysis of partially embedded offshore pipelines: Vertical penetration and axial walking. *Computers and Geotechnics*, 58:69–80.

Aubeny, C. P., Shi, H., and Murff, J. D. (2005). Collapse loads for a cylinder embedded in trench in cohesive soil. *The International Journal of Geomechanics*, 5(4):320–325.

Augarde, C. E., Lyamin, A. V., and Sloan, S. W. (2003). Prediction of undrained sinkhole collapse. *Journal of Geotechnical and Geoenvironmental Engineering*, 129(3):197–205.

Ayachit, U. (2015). *The ParaView Guide: A Parallel Visualization Application*. Kitware Inc.

Beaubouef, B. (2014). Operators planning more than 7,000 miles of offshore pipelines through 2018. *Offshore Magazine*, 74(8).

Biscontin, G. and Pestana, J. M. (2001). Influence of peripheral velocity on vane shear strength of an artificial clay. *Geotech. Test. J.*, 24(4):423–429.

Borel, D., Puech, A., Dendani, H., and Colliat, J.-H. (2005). Deepwater geotechnical site investigation practice in gulf of guinea. In *Proceedings of International Symposium on Frontiers in Offshore Geotechnics*, pages 921–926, Perth, Australia.

Brennodden, H., Sveggen, O., Wagner, D. A., and Murff, J. D. (1986). Full-scale pipe–soil interaction tests. In *Proceedings of 18th Annual Offshore Technology Conference*, pages 433–440, Houston, Texas.

Bridge, C. D. and Howells, H. A. (2007). Observations and modelling of steel catenary riser trenches. In *Seventeenth (2007) International offshore and polar engineering conference*, Lisbon, Portugal. The International Society of Offshore and Polar Engineers (ISOPE).

Bruton, D., Carr, M., Carawford, M., and Poiate, E. (2005). The safe design of hot on-bottom pipelines with lateral buckling using the design guidance developed by the SAFEBUCK Joint Industry Project. In *Deep Offshore Technology Conference*, Vitoria, Espirito Santo, Brazil.

Bruton, D., Carr, M., and White, D. J. (2007). The influence of pipe-soil interaction on lateral buckling and walking of pipelines: the SAFEBUCK JIP. In *Proceedings of 6th International Conference on Offshore Site Investigation and Geotechnics*, pages 133–150, London.

Bruton, D., White, D. J., Cheuk, C. Y., Bolton, M. D., and Carr, M. C. (2006). Pipe-soil interaction behaviour during lateral buckling, including large amplitude cyclic displacement tests by the SAFEBUCK JIP. In *Offshore Technology Conference*, Houston, Texas.

Cardoso, C. O. and Silveira, R. M. S. (2010). Pipe-soil interaction behavior for pipelines under large displacements on clay soils: a model for lateral residual friction factor. In *Offshore Technology Conference*, Houston,Texas, USA. Offshore Technology Conference.

Cathie, D. N., Jaeck, C., Ballard, J. C., and Wintgens, J. F. (2005). Pipeline geotechnics –state-of-the-art. In *Proceedings of International Symposium on Frontiers in Offshore Geotechnics*, pages 95–114, Perth, Australia.

Chakrabarti, S. (2005). *Handbook of offshore engineering*, volume 1. Elsevier.

Chatterjee, S. (2012). *Numerical modelling of pipe-soil interactions*. PhD thesis, The University of Western Australia.

Chatterjee, S., Randolph, M. F., and White, D. J. (2012a). The effects of penetration rate and strain softening on the vertical penetration resistance of seabed pipelines. *Géotechnique*, 62(7):573–582.

Chatterjee, S., White, D. J., and Randolph, M. F. (2012b). Numerical simulations of pipe-soil interaction during large lateral movements on clay. *Géotechnique*, 62(8):693–705.

Chatterjee, S., White, D. J., and Randolph, M. F. (2013). Coupled consolidation analysis of pipe-soil interactions. *Canadian Geotechnical Journal*, 50(6):609–619.

Chatterjee, S., Yan, Y., Randolph, M. F., and White, D. J. (2012c). Elastoplastic consolidation beneath shallowly embedded offshore pipelines. *Géotechnique Letters*, 2:73–79.

Cheuk, C. Y. (2005). *Soil-pipeline interaction at the seabed*. PhD thesis, University of Cambridge.

Cheuk, C. Y. and White, D. J. (2009). Modelling the dynamic embedment of seabed pipelines. *Géotechnique*, 61(1):39–57.

Cheuk, C. Y., White, D. J., and Bolton, M. D. (2007). Large-scale modelling of soil-pipe interaction during large amplitude cyclic movements of partially embedded pipelines. *Canadian Geotechnical Journal*, 44:977–996.

Cheuk, C. Y., White, D. J., and Dingle, D. J. (2008). Upper bound plasticity analysis of a partially-embedded pipe under combined vertical and horizontal loading. *Soils and Foundations*, 48(1):133–140.

Courant, R., Friedrichs, K., and Lewy, H. (1967). On the partial differential equations of mathematical physics. *IBM Journal of Research and Development*, 11(2):215–234.

Dassault Systémes (2011). *Abaqus analysis users' manual*. Simula Corp, Providence, RI, USA.

Dingle, H. R. C., White, D. J., and Gaudin, C. (2008). Mechanisms of pipe embedment and lateral breakout on soft clay. *Canadian Geotechnical Journal*, 45:636–652.

DNV (2007). *Global buckling of submarine pipeline: Structural design due to high temperature/high pressure*. Recommended Practice DNV-RP-F110. Det Norske Veritas, Oslo, Norway.

DNV (2010). *On-bottom stability design of submarine pipelines*. Recommended Practice DNV-RP-F109. Det Norske Veritas, Oslo, Norway.

Drucker, D. C., Prager, W., and Greenberg, H. J. (1952). Extended limit design theorems for continuous media. *Quarterly of Applied Mathematics*, 9:381–389.

Dutta, S., Hawlader, B., and Phillips, R. (2012). Finite element modeling of vertical penetration of offshre pipelines using coupled eulerian lagrangian approach. In *Proceedings of the Twenty-second (2012) International Offshore and Polar Engineering Conference*, Rhodes, Greece.

Dutta, S., Hawlader, B., and Rhillips, R. (2015). Finite element modeling of partially embedded pipelines in clay seabed using Coupled Eulerian-Lagrangian method. *Canadian Geotechnical Journal*, 52:58–72.

Dutta, S. and Phillips, R. (2013). Numerical investigation of dynamic embedment of offshore pipelines. In *Proceedings of the 18th International Conference on Soil Mechanics and Geotechnical Engineering*, Paris.

Einav, I. and Randolph, M. F. (2005). Combining upper bound and strain path methods for evaluating penetration resistance. *International Journal for Numerical Methods in Engineering*, 63(14):1991–2016.

Grabe, J., Henke, S., Pucker, T., and Hamann, T. (2013). *CEL: Simulations for soil plugging, screwed pile installation and deep vibration compaction*. Installation Effects in Geotechnical Engineering. Taylor & Francis Group, London.

Gvozdev, A. A. (1960). The determination of the value of the collapse load for statically indeterminate systems undergoing plastic deformation (in Russian). *International Journal of Mechanical science*, 1(4):322–335.

Hawlader, B., Dutta, S., Fouzder, A., and Zakeri, A. (2015). Penetration of steel catenary riser in soft clay seabed: Finite-element and finite-volume methods. *International Journal of Geomechanics*, 15(6).

Hazell, E. (2008). *Numerical and experimental studies of shallow cone penetration in clay*. DPhil thesis, University of Oxford.

Hesar, M. (2004). Pipeline-seabed interaction in soft clay. In *Proc. 23rd Int. Conf. on Offshore Mechanics and Arctic Eng.*, pages 225–232, Vancouver.

Hill, R., Lee, E. H., and Tupper, S. J. (1945). The theory of wedge indentation of ductile materials. In *Proceedings of the Royal Society of London Series A - Mathematical and Physical Sciences*, volume 188, pages 273–290.

Hodder, M. S. and Cassidy, M. J. (2010). A plasticity model for predicting the vertical and lateral behaviour of pipelines in clay soils. *Géotechnique*, 60(4):247–263.

Hu, H. J. E., Leung, C. F., Chow, Y. K., and Palmer, A. C. (2011). Centrifuge modelling of SCR vertical motion at touchdown zone. *Ocean Engineering*, 38:888–899.

Hu, Y. and Randolph, M. F. (1998). A practical numerical approach for large deformation problems in soil. *International Journal for Numerical and Analytical Methods in geomechanics*, 22:327–350.

Konuk, I. and Yu, S. (2007). Continuum FE modelling of lateral buckling: study of soil effects. In *Proceedings of the 26th International Conference on Offshore Mechanics and Arctic Engineering*, Houston, Texas.

Krost, K., Gourvenec, S., and White, D. J. (2011). Consolidation around partially embedded seabed pipelines. *Géotechnique*, 61(2):167–173.

Lee, Y. S. (2012). *Physical and numerical modelling of pipe-soil interaction in clay*. PhD thesis, The University of Sheffield.

LimitState (2009). *LimitState:GEO Manual VERSION 2.0*. Sept 3 ed. LimitState Ltd.

Lund, K. M. (2000). Effect of increase in pipeline soil penetration from installation. In *Proceedings of ETCE/OMAE2000 Joint Conference Energy for the New Millennium*, pages 14–17, New Orleans, LA,.

Lunne, T. and Anderson, K. H. (2007). Soft clay shear strength parameters for deepwater geotechnical design. In *Proc. 6th Int. Offshore Site Investigation Geotech. Conf.: Confronting New Challenges and Sharing Knowledge*, volume 1, pages 151–176, London, UK.

Lyamin, A. V. and Sloan, S. W. (2002). Upper bound limit analysis using linear finite elements and non-linear programming. *International Journal for Numerical and Analytical Methods in Geomechanics*, 26:181–216.

Macaro, G. (2015). *Distinct element modelling of pipe-soil interaction for offshore pipelines on granular soils*. DPhil thesis, University of Oxford.

Maenchen, G. and Sack, S. (1964). The tensor code. *Methods in Computational Physics*, 3.

Makrodimopoulos, A. and Martin, C. M. (2006). Lower bound limit analysis of cohesive frictional materials using second-order cone programming. *International Journal for Numerical Methods in Engineering*, 66(4):604–634.

Makrodimopoulos, A. and Martin, C. M. (2007). Upper bound limit analysis using simplex strain elements and second-order cone programming. *International Journal for Numerical and Analytical Methods in Geomechanics*, 31:835–865.

Makrodimopoulos, A. and Martin, C. M. (2008). Upper bound limit analysis using discontinuous quadratic displacement fields. *Communications in Numerical Methods in Engineering*, 24:911–927.

Martin, C. M. (2011). The use of adaptive finite-element limit analysis to reveal slip-line fields. *Géotechnique Letters*, 1:23–29.

Martin, C. M., Kong, D., and Byrne, B. W. (2013). 3D analysis of transverse pipe-soil interaction using 2D soil slices. *Géotechnique Letters*, 3:119–123.

Martin, C. M. and Randolph, M. F. (2006). Upper bound analysis of lateral pile capacity in cohesive soil. *Géotechnique*, 56(2):141–145.

Martin, C. M. and White, D. J. (2012). Limit analysis of the undrained bearing capacity of offshore pipelines. *Géotechnique*, 62(9):847 –863.

Merifield, R. S., White, D. J., and Randolph, M. F. (2008a). The effect of pipe-soil interface conditions on the undrained breakout resistance of partially-embedded pipelines. In *The 12th International Conference of International Association for Computer Methods and Advances in Geomechanics (IACMAG)*, pages 4249–4256, Goa, India.

Merifield, R. S., White, D. J., and Randolph, M. F. (2008b). The ultimate undrained resistance of partially embedded pipelines. *Géotechnique*, 58(6):461–470.

Merifield, R. S., White, D. J., and Randolph, M. F. (2009). Effect of surface heave on response of partially embedded pipelines on clay. *Journal of Geotechnical and Geoenvironmental Engineering*, 135(6):819–829.

Morris, D. V., Yen, T., and Dunlap, W. A. (1988). Self-burial of laterally loaded offshore pipelines in weak sediments. In *Offshore Technology Conference*, volume OTC5855, Houston, Texas.

MOSEK APS (2010). *The MOSEK optimization tools manual, Version 5*.

Murff, J. D., Wanger, D. A., and Randolph, M. F. (1989). Pipe penetration in cohesive soil. *Géotechnique*, 39(2):213–229.

Oliveira, J. R. M. S., Almeida, M. S. S., ASCE, M., Almeida, M. C. F., and Borges, R. G. (2010). Physical modeling of lateral clay-pipe interaction. *Journal of Geotechnical and Geoenvironmental Engineering*, 136:950–956.

Prandtl, L. (1921). Über die Eindringungsfestigkeit Plastischer Baustoffe und die Festigkeit von Schneiden. *Z. Angew. Math. Mech*, 1:15–20.

Qiu, G. and Grabe, J. (2011). Explicit modeling of cone and strip footing penetration under drained and underained conditions using a visco-hypoplastic model. *Geotechnik*, 34:205–217.

Qiu, G. and Grabe, J. (2012). Numerical simulation of the deep penetration process of spudcans into sand overlying clay using the extended hypoplastic models. In *Proceedings of the Twenty-second (2012) International Offshore and Polar Engineering Conference*, Rhodes, Greece.

Qiu, G., Henke, S., and Grabe, J. (2009). Applications of Coupled Eulerian-Lagrangian method to geotechnical problems with large deformations. In Conference, S. C., editor, *SIMULIA Customer Conference*. SIMULIA Customer Conference.

Raithatha, A. and Duncan, S. R. (2008). Rigid plastic model of incremental sheet deformation using second-order cone programming. *International Journal for Numerical Methods in Engineering*, 78:955–979.

Randolph, M. F. (2004). Characterization of soft sediments for offshore applications. In *Proc. 2nd Int. Conf. on Site Characterization*, pages 209–231, Porto, Portugal.

Randolph, M. F. and Gourvenec, S. (2011). *Offshore geotechnical engineering*. Spon Press, Taylor and Francis Group, New York.

Randolph, M. F. and Houlsby, G. T. (1984). The limiting pressure on a circular pile loaded laterally in cohesive soil. *Géotechnique*, 34(4):613–623.

Randolph, M. F., Wang, D., Zhou, H., Hossain, M. S., and Hu, Y. (2008). Large deformation finite element analysis for offshore applications. In *Proceedings of the 12th International Conference of International Association for Computer Methods and Advances in Geomechanics*, pages 3307–3318, Goa, India.

Randolph, M. F. and White, D. J. (2008a). Pipeline embedment in deep water: processes and quantitative assessment. In *Offshore Technology Conference*, Houston, Texas, USA.

Randolph, M. F. and White, D. J. (2008b). Upper-bound yield envelopes for pipelines at shallow embedment in clay. *Géotechnique*, 58(4):297–301.

Rismanchian, A. (2014). *Pipe-soil interaction during lateral buckling of marine pipelines*. PhD thesis, The University of Western Australia.

Rowe, R. K. and Davis, E. H. (1982). The behaviour of anchor plates in clay. *Géotechnique*, 32(1):9–23.

Sabetamal, H. (2014). *Finite element algorithms for dynamic analysis of geotechnical problems*. PhD thesis, University of Newcastle, Australia.

Schotman, G. J. M. and Stork, F. G. (1987). Pipe-soil interaction: A model for laterally loaded pipelines in clay. In *Offshore Technology Conference*, Houston, Texas. Offshore Technology Conference.

Shewchuk, J. R. (2002). Delaunay refinement algorithms for triangular mesh generation. *Computational Geometry*, 47:741–778.

Tani, K. and Craig, W. H. (1995). Bearing capacity of circular foundations on soft clay of strength increasing with depth. *Soils and Foundations*, 35(4):21–35.

TECPLOT (1992). *version 5 Users Manual, Amtec Engineering*. Western Australia.

Tho, K. K., Leung, C. F., Chow, Y. K., and Somsak, S. (2013). Eulerian finite elements simulation of spudcan-pile interaction. *Canadian Geotechnical Journal*, 50(6):595–608.

Verley, R. and Lund, K. M. (1995). A soil resistance model for pipelines placed on clay soils. In *Proceedings of the International Conference on Offshore Mechanics and Arctic Engineering*, volume 5, pages 225–232.

Wang, D., Hu, Y., and Randolph, M. F. (2010). Three-dimensional large deformation finite-element analysis of plate anchors in uniform clay. *Journal of Geotechnical and Geoenvironmental Engineering*, 136(2):355–365.

Wang, D., White, D. J., and Randolph, M. F. (2009). Large-deformation finite element analysis of pipe penetration and large-amplitude lateral displacement. *Canadian Geotechnical Journal*, 47:842–856.

Wang, L., Zhang, J., Yuan, F., and Kai, L. (2014). Interaction between catenary riser and soft seabed: Large-scale indoor tests. *Applied Ocean Research*, 45:10–21.

Westgate, Z. J., Randolph, M. F., White, D. J., and Li, S. (2010). The influence of sea state on as-laid pipeline embedment: A case study. *Applied Ocean Research*, 32(3):321–331.

Westgate, Z. J., White, D. J., and Randolph, M. F. (2009). Video observations of dynamic embedment during pipelaying on soft clay. In *ASME 2009 28th International Conference on Ocean, Offshore and Arctic Engineering*, volume 3, pages 699–707.

White, D. J. and Cheuk, C. Y. (2008). Modelling the soil resistance on seabed pipelines during large cycles of lateral movement. *Marine Structures*, 21:59–79.

White, D. J. and Randolph, M. F. (2007). Seabed characterisation and models for pipeline-soil interaction. In *Proceedings of the 17th International Offshore and Polar Engineering Conference*, pages 758–769.

Wilkins, M. (1964). Calculation of elastoplastic flows. *Methods in Computational Physics*, 3:211–263.

Yang, W. H. (1993). Large deformation of structures by sequential limit analysis. *International Journal of Solids and Structures*, 30(7):1001–1013.

Youssef, B., Tian, Y., and Cassidy, M. J. (2013). Centrifuge modelling of an on-bottom pipeline under equivalent wave and current loading. *Applied Ocean Research*, 40:14–25.

Yu, S. and Konuk, I. (2007). Continuum FE modelling of lateral buckling. In *Offshore Technology Conference*, Houston.

Zhang, J., Stewart, D. P., and Randolph, M. F. (2002a). Kinematic hardening model for pipeline-soil interaction under various loading conditions. *International Journal of Geomechanics*, 2(4):419–446.

Zhang, J., Stewart, D. P., and Randolph, M. F. (2002b). Modeling of shallowly embedded offshore pipelines in calcareous sand. *Journal of Geotechnical and Geoenvironmental Engineering*, 128(5):363–371.

Zhou, H. and Randolph, M. F. (2007). Computational techniques and shear band development for cylindrical and spherical penetrometers in strain-softening clay. *International Journal of Geomechanics*, 7(4):287–295.

Appendix A

VUMAT source code of the Tresca-based soil model

```
!DEC$ FREEFORM
module mymod
!implicit none
integer,parameter::Q=8
real(Q),parameter::zero=0.D0,one=1.D0,two=2.D0,three=3.D0,four=4.D0,&
                   ref=3.D-6
contains
subroutine ElasticMatrix(E,v,M)
    real(Q),intent(out),dimension(6,6):: M
    real(Q),intent(in)::E,v
    M(1,1:6)=(/one-v,v,v,zero,zero,zero/)
    M(2,1:6)=(/v,one-v,v,zero,zero,zero/)
    M(3,1:6)=(/v,v,one-v,zero,zero,zero/)
    M(4,1:6)=(/zero,zero,zero,one-two*v,zero,zero/)
    M(5,1:6)=(/zero,zero,zero,zero,one-two*v,zero/)
    M(6,1:6)=(/zero,zero,zero,zero,zero,one-two*v/)
    M=M*E/((one+v)*(one-two*v))
end subroutine ElasticMatrix

subroutine Matrix_inverse(M,Inve)
        real(Q),intent(in),dimension(3,3)::M
    real(Q),intent(out),dimension(3,3)::Inve
    real(Q),dimension(3,3)::temp
        integer::i,j
```

```
      real(Q)::Det
      temp(1,1)=M(2,2)*M(3,3)-M(2,3)*M(3,2)
      temp(2,1)=M(2,3)*M(3,1)-M(2,1)*M(3,3)
      temp(3,1)=M(2,1)*M(3,2)-M(2,2)*M(3,1)
      temp(3,2)=M(1,2)*M(3,1)-M(1,1)*M(3,2)
      temp(2,2)=M(1,1)*M(3,3)-M(1,3)*M(3,1)
      temp(3,3)=M(1,1)*M(2,2)-M(1,2)*M(2,1)
      temp(1,2)=M(1,3)*M(3,2)-M(1,2)*M(3,3)
      temp(1,3)=M(1,2)*M(2,3)-M(1,3)*M(2,2)
      temp(2,3)=M(1,3)*M(2,1)-M(1,1)*M(2,3)
      Det=M(1,1)*temp(1,1)+M(1,2)*temp(2,1)+M(1,3)*temp(3,1)
      Inve=temp/Det
end subroutine Matrix_inverse

subroutine returntoplane(p,s)
real(Q),intent(inout)::p
real(Q),intent(in)::s
real(Q)::a,b,c,d,t
dimension::p(3),s(4)
      t=-(s(1)*p(1)+s(2)*p(2)+s(3)*p(3)+s(4))/two!!!!(a**2+b**2+c**2)
      p(1)=s(1)*t+p(1)
      p(2)=s(2)*t+p(2)
      p(3)=s(3)*t+p(3)
end subroutine returntoplane

subroutine returntoline(p,l)
real(Q),intent(inout)::p
real(Q),intent(in)::l
real(Q)::t
dimension::p(3),l(3)
      t=(p(1)+p(2)+p(3)-l(1)-l(2)-l(3))/three
      p(1:3)=(/t+l(1),t+l(2),t+l(3)/)
end subroutine returntoline

subroutine modi_pstress(s,c)
```

```
!s is the pstress, c is su
integer::rp
real(Q),intent(inout),dimension(3)::s
real(Q),intent(in)::c
real(Q)::plane,line,f1,f2,f3,f4,f5,f6,two3,four3
dimension::plane(4),line(6)
    two3=c*two/three
    four3=c*four/three
    f1=s(1)-s(2)-c*2.D0; f2=s(2)-s(1)-c*2.D0
    f3=s(2)-s(3)-c*2.D0; f4=s(3)-s(2)-c*2.D0
    f5=s(3)-s(1)-c*2.D0; f6=s(1)-s(3)-c*2.D0
    if ((f1 >= f4*2.D0) .and. (f1 >= f6*2.D0) .and. (f1>=0.D0)) then
        plane(1:4)=(/one,-one,zero,-c*two/)
        call returntoplane(s,plane)
    else if ((f2>=f3*2.D0) .and. (f2>=f5*2.D0) .and. (f2>=0.D0)) then
        plane(1:4)=(/-one,one,zero,-c*two/)
        call returntoplane(s,plane)
    else if ((f3>=f2*2.D0) .and. (f3>=f6*2.D0) .and. (f3>=0.D0)) then
        plane(1:4)=(/zero,one,-one,-c*two/)
        call returntoplane(s,plane)
    else if ((f4>=f1*2.D0) .and. (f4>=f5*2.D0).and. (f4>=0.D0)) then
        plane(1:4)=(/zero,-one,one,-c*two/)
        call returntoplane(s,plane)
    else if ((f5>=f2*2.D0) .and. (f5>=f4*2.D0).and. (f5>=0.D0)) then
        plane(1:4)=(/-one,zero,one,-c*two/)
        call returntoplane(s,plane)
    else if ((f6>=f3*2.D0) .and. (f6>=f1*2.D0).and. (f6>=0.D0)) then
        plane(1:4)=(/one,zero,-one,-c*two/)
        call returntoplane(s,plane)
    else if ((f1<f4*2.D0) .and. (f4<f1*2.D0).and. (f1>=0.D0)) then
        line(1:3)=(/two3,-four3,two3/)
        call returntoline(s,line)
    else if ((f4<f5*2.D0) .and. (f5<f4*2.D0).and. (f4>=0.D0)) then
        line(1:3)=(/-two3,-two3,four3/)
        call returntoline(s,line)
```

```
    else if ((f2<f5*2.D0) .and. (f5<f2*2.D0).and. (f2>=0.D0)) then
        line(1:3)=(/-four3,two3,two3/)
        call returntoline(s,line)
    else if ((f2<f3*2.D0) .and. (f3<f2*2.D0).and. (f3>=0.D0)) then
        line(1:3)=(/-two3,four3,-two3/)
        call returntoline(s,line)
    else if ((f3<f6*2.D0) .and. (f6<f3*2.D0).and. (f6>=0.D0)) then
        line(1:3)=(/two3,two3,-four3/)
        call returntoline(s,line)
    else if ((f6<f1*2.D0) .and. (f1<f6*2.D0).and. (f6>=0.D0)) then
        line(1:3)=(/four3,-two3,-two3/)
        call returntoline(s,line)
    end if
end subroutine modi_pstress

subroutine getnewstress(Ematrix,Pstress,newstress)
real(Q),intent(out),dimension(6)::newstress
real(Q)::Ematrix,Pstress,inve,temp
dimension::Ematrix(3,3),Pstress(3),inve(3,3),temp(3,3)

    call Matrix_inverse(Ematrix,Inve)
    Ematrix(1:3,1)=Ematrix(1:3,1)*Pstress(1)
    Ematrix(1:3,2)=Ematrix(1:3,2)*Pstress(2)
    Ematrix(1:3,3)=Ematrix(1:3,3)*Pstress(3)
    temp=matmul(Ematrix,Inve)
    newstress(1:3)=(/temp(1,1),temp(2,2),temp(3,3)/)
    newstress(4:6)=(/temp(1,2),temp(2,3),temp(1,3)/)
end subroutine getnewstress
end module mymod
!*****************************************************************
!*****************************************************************

subroutine vumat(nblock, ndir, nshr, nstatev, nfieldv, nprops, lanneal,&
                 stepTime, totalTime, dt, cmname, coordMp, charLength, &
                 props, density, strainInc, relSpinInc,tempOld,       &
```

```
     stretchOld, defgradOld, fieldOld, stressOld, stateOld, &
     enerInternOld, enerInelasOld, tempNew, stretchNew, &
     defgradNew, fieldNew, stressNew, stateNew, &
     enerInternNew, enerInelasNew )
use Mymod
include 'vaba_param.inc'

dimension props(nprops), density(nblock), coordMp(nblock,*), &
 charLength(nblock), strainInc(nblock,ndir+nshr), &
 relSpinInc(nblock,nshr), tempOld(nblock), enerInelasNew(nblock), &
 stretchOld(nblock,ndir+nshr), enerInelasOld(nblock), &
 defgradOld(nblock,ndir+nshr+nshr), fieldOld(nblock,nfieldv), &
 stressOld(nblock,ndir+nshr), stateOld(nblock,nstatev), tempNew(nblock),&
 enerInternOld(nblock), stretchNew(nblock,ndir+nshr), &
 defgradNew(nblock,ndir+nshr+nshr), stateNew(nblock,nstatev), &
 fieldNew(nblock,nfieldv), stressNew(nblock,ndir+nshr), &
 enerInternNew(nblock)
character*80 cmname
!**********************************************************************
!**********************************************************************
real(Q)::E_r,nam,su_mud,k,rem,kesai95,mu,amp,su0,f1,f2,c,shear,dpshear,&
        E,kesai,rate,temp1,&
        DELAS,dstrain,pstrain,tstress,pstress,pvec,p,Ematrix,newstress
integer::bi
logical::yield
dimension:: DELAS(6,6),dstrain(nblock,6),pstrain(nblock,3),&
            tstress(nblock,6),pstress(nblock,3),pvec(nblock,3,3),&
            p(3),Ematrix(3,3),newstress(6)
!-----------------------------------------------------------------
! get soil properties
E_r=props(1);nam=props(2);su_mud=props(3);k=props(4)
rem=props(5);kesai95=props(6);mu=props(7);amp=props(8)

!-----------------------------------------------------------------
! initialize all the history and field valiables
```

```
if (totalTime==0.D0) then
    do 200 bi=1,nblock
        temp1=max(su_mud,su_mud-k*coordMp(bi,3))
        stateold(bi,1:8)=(/zero,zero,zero,zero,zero,zero,zero,temp1/)
    200 continue
end if
!-------------------------------------------------------------------------------
    dstrain=strainInc
do 300 bi=1,nblock
    E=E_r*stateold(bi,8)
    call ElasticMatrix(E,nam,DELAS)
    tstress(bi,1:6)=stressOld(bi,1:6)+ matmul(DELAS,dstrain(bi,1:6))
300 continue
    call vsprind(nblock,tstress,pstress,pvec,3,3)
    call vsprinc(nblock,dstrain,pstrain,3,3)
!-----------------Begin the main loop-------------------------------------------
do 100 bi=1,nblock
! to get maximum incremental shear strain
    p(1:3)=pstrain(bi,1:3)
    shear=max(max(p(1),p(2),p(3))-min(p(1),p(2),p(3)),zero)
    su0=stateold(bi,8); rate=amp*shear/dt; kesai=stateold(bi,3)
    f1=one+mu*log10(max(rate,ref)/ref)
    f2=rem+(one-rem)*exp(-three*kesai/kesai95)
    c=f1*f2*su0
! to check if yield
    p(1:3)=pstress(bi,1:3)
    yield=(max(abs(p(1)-p(2)),abs(p(2)-p(3)),abs(p(3)-p(1)))>=c*2.D0)
    dpshear=zero
    if ((yield==.False.).or.(Totaltime==0.D0)) then
        stressNew(bi,1:6)=tstress(bi,1:6)
    else
        !drag the point to yield surface
        call modi_pstress(p,c)
        !from principle stress to stress
        call getnewstress(pvec(bi,1:3,1:3),p,newstress)
```

```
            stressNew(bi,1:6)=newstress(1:6)
            dpshear=shear
        end if
! update SDVs
        statenew(bi,1)=shear/dt
        statenew(bi,2)=dpshear/dt
        if (Totaltime>1.D0) then ! ignore the strain in the initial step for gravity
            statenew(bi,3)=stateold(bi,3)+dpshear
        else
            statenew(bi,3)=zero
        end if
        statenew(bi,4)=f1
        statenew(bi,5)=f2
        statenew(bi,6)=c
        if (yield==.True.) then
            statenew(bi,7)=one
        else
            statenew(bi,7)=zero
        end if
        statenew(bi,8)=stateold(bi,8)
100 continue
return
end
```